

Development of Catalysts and Catalyst Supports for Polymer Electrolyte Fuel Cells

Noramalina Binti Mansor

A thesis submitted to University College London
for the degree of Doctor of Philosophy

Department of Chemical Engineering
Torrington Place, WC1E 7JE

October 2014

Declaration

I, Noramalina Mansor, confirm that the work presented in this thesis is my own. Where information has been derived from other sources, I confirm that this has been indicated in the thesis.

Signature

October 2014

Abstract

Polymer Electrolyte Membrane fuel cells (PEMFC) are clean and efficient electrochemical energy converters that can be adapted to a wide range of domestic and automotive applications. However, large-scale commercialisation is hindered by issues of cost and durability relating to the catalyst layer. This work aims to address the need for cheaper and durable catalysts through the development of novel catalyst and catalyst support.

The initial aim of this work is to investigate the potential application of Pd-based alloy catalyst in PEMFC. Pd is about 42% cheaper than Pt and 50 times more abundant on earth. Previous studies have shown that there is a correlation between electronic structure and catalytic activity of Pd binary alloys, and therefore it is possible to design a highly efficient Pd-based alloy catalyst. In this work, Pd-based catalyst was synthesised and characterized electrochemically in *ex-situ* and *in-situ* configurations to determine their activity and durability. It was found that Pd-based catalyst could potentially replace Pt as a low-cost anode catalyst.

The second part of this work investigated the potential application of graphitic carbon nitride materials as catalyst support. Carbon black is the most widely used catalyst support for state-of-the-art PEMFCs even though it is known to undergo carbon corrosion during operation. Graphitic carbon nitride could offer enhanced durability and activity due to their graphitic structure and intrinsic catalytic properties. In addition, graphitic carbon nitride is low-cost, fairly simple to synthesise and highly tunable. In this work, various graphitic carbon nitride materials were prepared and characterised using accelerated carbon corrosion protocol. They were found to be more electrochemically stable compared to conventional carbon black. Superior methanol oxidation activity is also observed for graphitic carbon nitride supported Pt catalysts on the basis of the catalyst electrochemical surface area. However further work is needed to optimise the deposition and utilisation of metal catalyst on graphitic carbon nitride materials.

Acknowledgements

Firstly, I would like to thank my supervisor, Dan Brett, for his constant support, guidance and encouragement, and without whom this thesis will not be possible.

I am indebted to the following people: Chris, Rhodri and Simon for their valuable input and discussions contributing to the progress of the work; Ana for her contributions to the carbon nitride work, and helpful comments and suggestions; Quentin for the countless hours of discussions and help on various aspects of the work (often at ridiculous hours!); Toby for his generosity and assistance; and Jay for his help especially during the initial stage of this work.

I would like to thank the members of the Electrochemical Innovation Lab for their kindness and assistance during my PhD. Thank you to Flora, Ishanka, and Mithila for their constant support inside and outside the lab. To everyone in UB4: Aliya, Dave, Lawrence, Mayowa, Phil, - for making the office a nice environment. To the staff at the department of Chemical Engineering: Simon and Mike for their technical assistance; Agata, Pattie and Mae in the departmental office for sorting out much of my student related admin matters.

Last but not least, I am grateful to my family, especially my parents, for their unconditional love and support throughout my PhD. To Shane for always being there.

List of Publications

Journal Paper

N. Mansor, A. Jorge, F. Corà, C. Gibbs, R. Jervis, P. McMillan, X. Wang, D. Brett. Performance of Graphitic-Carbon Supported Catalysts for Polymer Electrolyte Fuel Cells. *J. Phys. Chem. C*, **2014**, *118* (13), pp 6831–6838

R. Jervis, N. Mansor, C. Gibbs, C. Murray, C. Tang, D. Brett. Hydrogen Oxidation Reaction on PdIr/C Catalysts in Alkaline Media. *J. Electrochem. Soc.*, 2014, *161*, 4, F458-F463

Conference Paper

N. Mansor, A. Jorge, F. Corà, C. Gibbs, R. Jervis, P. McMillan, X. Wang, D. Brett. Development of Graphitic-Carbon Nitride Materials as Catalyst Supports for Polymer Electrolyte Fuel Cells, *J. Electrochem. Soc. Trans.* 2013, *58*, 1767-1778

R. Jervis, N. Mansor, C. Gibbs, C. Murray, C. Tang, D. Brett. Novel PdIr/C Catalysts for the Hydrogen Oxidation Reaction in Alkaline Media, *J. Electrochem. Soc. Trans.* 2013, *58*, 637-650

Patents

D. Brett, C. Gibbs, R. Jervis, N. Mansor. Electrolysis Electrocatalysts, WO2014045049 A1.

D. Brett, C. Gibbs, R. Jervis, N. Mansor. Fuel Cell, WO2013093449 A2.

Conferences Attended

Materials Research Exchange 2014, Coventry. Poster: *Graphitic Carbon Nitrides for Energy Applications*.

H2FC Supergen 2013, Birmingham. Poster: *Development of Graphitic-Carbon Nitride as Catalyst Supports for Polymer Electrolyte Fuel Cell*

ECS 224th Meeting 2013, San Francisco. Presentation: *Development of Graphitic-Carbon Nitride as Catalyst Supports for Polymer Electrolyte Fuel Cell*.

Celebration of Catalysis 2012, Imperial College London. Presentation: *Anode Catalyst Development for Alkaline Fuel Cells*

iChemE Catalysis for Energy University of Birmingham 2012. Poster: *Anode Catalyst Development for Polymer Electrolyte Membrane Fuel Cells*

London and South East Region Postgraduate Electrochemistry Meeting and ISE Satellite Student Regional Symposium on Electrochemistry 2012. Presentation: *Novel Anode Catalyst Development for PEM Fuel Cells*

London Catalysis Winter Seminar 2012 at Imperial College London.

Hydrogen & Fuel Cell - Zing Conference 2011, Mexico. Poster: *A novel, low-cost, high efficiency anode catalyst for alkaline fuel cells*

Electrochemical Horizons 2011, Bath. Poster: *Electrocatalytic activity of a low-cost, high-efficiency anode catalyst for alkaline fuel cells*

Abbreviations & Symbols

α	Transfer coefficient
A (cm ²)	Area
AC	Alternating current
AST	Accelerated Stress Test
AFC	Alkaline fuel cell
b (mV decade ⁻¹)	Tafel slope
BET	Brunauer-Emmet-Teller
C (mol dm ⁻³)	Reaction concentration
C_{dl}	Double-layer capacitance
CNC	Carbon nanocoil
CNF	Carbon nanofiber
CNH	Carbon nanohorn
CNT	Carbon nanotube
CPE	Constant phase element
CV	Cyclic voltammogram
D (cm ² s ⁻¹)	Diffusion coefficient
DCDA	Dicyandiamide
DEFC	Direct Ethanol Fuel Cell
DFT	Density functional theory
DMFC	Direct Methanol Fuel Cell
DOE	The US Department of Energy
E (V)	Electrode potential

ECSA ($\text{m}^2 \text{g}^{-1}$)	Electrochemical Surface Area
EDX	Energy-dispersive X-ray spectroscopy
EIS	Electrochemical Impedance Spectroscopy
f (rpm s^{-1})	Revolutions per second
F (C mol^{-1})	Faraday constant (96485 C mol^{-1})
GC	Glassy carbon
GDE	Gas diffusion electrode
GDL	Gas diffusion layer
GE	General Electric Company
GO	Graphene Oxide
H_{upd}	Underpotential deposited hydrogen
HER	Hydrogen evolution reaction
HOR	Hydrogen oxidation reaction
i (A)	Current
ICE	Internal combustion engine
j (A cm^{-2})	Current density
k (sec^{-1})	Rate constant
L ($\mu\text{g cm}^{-2}$)	Metal loading on electrode
LSV	Linear sweep voltammetry
MA	Mass activity
MCFC	Molten Carbonate Fuel Cell
MEA	Membrane electrode assembly
MOR	Methanol oxidation reaction
MWCNT	Multi-walled carbon nanotube

η	Overpotential
n	Number of electron
NASA	The National Aeronautics and Space Administration
OCV	Open-circuit voltage
OMC	Ordered mesoporous carbon
ORR	Oxygen reduction reaction
PAFC	Phosphoric Acid Fuel Cell
PEMFC	Polymer Electrolyte Membrane Fuel Cell
PGM	Platinum metal group
PTFE	Polytetrafluoroethylene
PVP	Polyvinylpyridine
Q (C)	Charge
R_Q (Ω)	Ohmic resistance
R_{anode} (Ω)	Anode charge transfer resistance
$R_{cathode}$ (Ω)	Cathode charge transfer resistance
R ($J K^{-1} mol^{-1}$)	The gas constant ($8.314 J K^{-1} mol^{-1}$)
R_f	Roughness factor
rds	Rate determining step
RDE	Rotating-disc electrode
RHE	Reversible Hydrogen Electrode
rpm	Revolutions per minute
SA	Specific Activity
SWCNT	Single-walled carbon nanotube
SXPD	Synchrotron X-ray powder diffraction

T (K)	Temperature
TEM	Transmission electrons microscopy
TGA	Thermogravimetric analysis
TPB	Triple phase boundary
U	Catalyst utilisation
ν (cm ² s ⁻¹)	Kinematic viscosity
XANES	X-ray absorption near edge structure
XPS	X-ray photoelectron spectroscopy
XRD	X-ray diffraction
ω (rad s ⁻¹)	Angular frequency
\hat{Z}	Complex impedance

Table of Contents

Declaration	ii
Abstract	iii
Acknowledgements	iv
List of Publications	v
Abbreviations & Symbols	vii
Table of Contents.....	xi
List of Figures	xvi
List of Tables.....	xxiii
Chapter 1	1
1 Introduction.....	1
1.1 Motivation	1
1.2 Fuel cells	2
1.3 Types of fuel cells.....	3
1.4 Introduction to PEMFC	4
1.5 Thermodynamics	5
1.6 Fuel cell polarisation curves	7
1.6.1 Mixed-potential losses	8
1.6.2 Activation overpotential.....	9
1.6.3 Ohmic overpotential.....	12
1.6.4 Concentration overpotential	12

1.7 Commercialisation barriers	12
1.7.1 Cost and durability	13
1.8 Aims	15
 Chapter 2	 16
 2 PEMFC Catalyst Layers.....	 16
2.1 Anode catalyst layers.....	16
2.1.1 Anode catalyst layer degradation	22
2.1.1.1 CO contamination.....	24
2.1.2 Methanol Oxidation Reaction	26
2.2 Cathode catalyst layer	29
2.2.1 Cathode catalyst layer degradation	32
2.2.1.1 Cathode failure mode.....	36
2.3 Alternative Carbon Support	38
2.3.1 Carbon nanotubes (CNT)	39
2.3.2 Carbon nanofiber (CNF)	41
2.3.3 Ordered mesoporous carbon (OMC).....	42
2.3.4 Graphene and Graphene oxide (GO).....	43
2.3.5 Graphitic Carbon Nitride.....	45
2.4 Summary	48
 Chapter 3	 49
 3 Methodology: Electrochemical Characterisation Techniques	 49
3.1 Ex-situ characterisation.....	49
3.1.1 Cyclic voltammetry	49
3.1.2 Electrochemical surface area.....	51
3.1.3 CO-stripping voltammetry	52
3.1.4 Methanol oxidation	52
3.1.5 Kinetic analysis using the rotating-disk electrode (RDE)	53
3.2 In-situ characterisation	56
3.2.1 Polarisation curve.....	57
3.2.2 Electrochemical Impedance Spectroscopy (EIS)	58

3.2.2.1	Equivalent circuits	61
3.2.3	CO tolerance	64
3.3	Durability Studies	65
3.4	Summary	68
Chapter 4	69
4	Preparation and Characterisation of Pd-alloy Anode Catalyst	69
4.1	Materials and methods	69
4.1.1	Hardware	69
4.1.2	Materials	70
4.1.3	Synthesis of catalysts	70
4.1.4	Glassware cleaning.....	71
4.1.5	Working electrolyte and temperature	71
4.1.6	Preparation of working electrodes.....	72
4.1.7	Reference electrode.....	72
4.1.8	Physical characterisation.....	72
4.1.9	Electrochemical measurements	73
4.1.10	Durability Testing.....	74
4.2	Results and discussions.....	74
4.2.1	Materials characterisation	74
4.2.2	CO-stripping voltammetry	79
4.2.3	Hydrogen Oxidation Reaction.....	80
4.2.4	Methanol oxidation reaction.....	82
4.2.5	Durability	84
4.3	Conclusions	86
5	In-situ Testing	87
5.1	Materials and methods	87
5.1.1	MEA fabrication	87
5.1.2	Single-cell PEMFC testing.....	87
5.2	Results and discussions.....	88
5.2.1	Performance analysis	88
5.2.2	Performance optimisation	95

5.2.3	CO tolerance	101
5.3	Conclusions	104
Chapter 6	106
6	Alternative Catalyst Supports: Graphitic-Carbon Nitrides.....	106
6.1	Background	106
6.2	Experimental.....	106
6.2.1	Synthesis of Graphitic Carbon Nitride	106
6.2.2	Synthesis of Pt/gCNM.....	106
6.2.3	Structural and Compositional Characterization.....	107
6.2.4	Electrochemical Characterisation.....	107
6.3	Results and discussions.....	108
6.3.1	Synthesis and chemical characterisation	108
6.3.1.1	gCNM.....	108
6.3.1.2	Pt/gCNM.....	109
6.3.2	Durability studies	111
6.3.3	Electrocatalytic Activity.....	114
6.3.4	Synthesis optimisation	117
6.3.4.1	Higher pH conditions and low metal loading	117
6.3.4.2	Addition of spacer material	119
6.3.4.3	Protonated gCNM.....	120
6.3.4.4	Future work: exfoliated and protonated gCNM.....	122
6.4	Conclusions	122
7	Modified Graphitic Carbon Nitride as Catalyst Support.....	124
7.1	Background	124
7.2	Experimental.....	124
7.2.1	Synthesis of PTI-Li ⁺ Cl ⁻	124
7.2.2	Synthesis of B-gCNM	124
7.2.3	Post-mortem analysis	125
7.3	Results and discussions.....	125
7.3.1	Synthesis and chemical characterisation	125

7.3.1.1	PTI-Li ⁺ Cl ⁻	125
7.3.1.2	B-gCNM	126
7.3.2	Characterisation of supported catalysts	127
7.3.3	Durability Studies	129
7.3.4	Post-mortem analysis	132
7.3.5	Electrocatalytic activity	134
7.4	Conclusions	135
Chapter 8	137
8	Conclusions and Future Work.....	137
References	140

List of Figures

Figure 1.1: Basic operation of a typical PEMFC	4
Figure 1.2: A typical PEMFC polarisation curve showing the various irreversible voltage losses.	8
Figure 1.3: Theoretical polarisation curves according to the Butler-Volmer equation with $\alpha=0.5$ for two exchange current densities: (a) $j_0 = 10^{-9} \text{A cm}^{-2}$ and (b) $j_0 = 10^{-6} \text{A cm}^{-2}$. Reproduced from reference 5 and 6. ^{8,9}	11
Figure 1.4. Breakdown of fuel cell stack cost based on projected scale-up of 1000 and 500,000 systems per year. Reproduced from reference 7. ¹⁰	14
Figure 2.1: A plot of $\log j_0$ versus metal-hydrogen bond energy for various metal catalysts, showing the volcano-like dependency. ²⁷	19
Figure 2.2: Schematic illustration of the formation of a chemical bond between an adsorbate and the s and d states of a transition metal. ^{28,29}	20
Figure 2.3: (a) Linear relationship between the d -band centre and the percentage of Pd, and (b) HOR exchange current density on PdIr electrode as a function of d -band centres and percentage of Pd. ³¹	21
Figure 2.4: Time-dependent changes in the anode and cathode potential during a voltage reversal experiment. ³⁹	23
Figure 2.5: Allowable accumulated time during a voltage reversal experiment for a Pt/C catalyst at a carbon loading of 0.2 mg cm^{-2} based on two scenarios: (a) 10% of the cell current is supplied by anode carbon corrosion, and (b) 100% of the cell current is supplied by anode carbon corrosion. Note: red arrows added as guidance. ⁴⁰	23

Figure 2.6: Reaction scheme of methanol oxidation reaction, showing all the possible pathways. ⁶⁹	27
Figure 2.7: Volcano plot of oxygen reduction reaction activity plotted as a function of the oxygen binding energy (ΔE_O). ⁸⁵	30
Figure 2.8: Regions of stability for platinum vs potential and pH (Pourbaix Diagram). Diagram reproduced from reference 100. ¹⁰⁰	32
Figure 2.9. Typical automotive fuel cell vehicle drive cycle showing average cell voltage over time. ⁴⁰	34
Figure 2.10: Cell voltage loss versus carbon weight loss measured at 0.8 A cm ⁻² for KB (Ketjen black), Vulcan, Gr-KB (Graphitized Ketjen black) and Gr-Vulcan (Graphitized Vulcan XC-72C). The inset shows the carbon weight loss versus time at 1.2 V. ¹⁰⁴	35
Figure 2.11: The schematic diagram of a PEMFC start-up experiencing start-up/shutdown and all electrochemical reactions involved. ORR: oxygen reduction reaction, COR: carbon oxidation reaction, HOR: hydrogen oxidation reaction and OER: oxygen evolution reaction. Reproduced from reference 104. ¹⁰⁴	37
Figure 2.12: (a) Schematic illustrations of the three different structures of single-walled carbon nanotubes (SWCNTs). (b) Structure of a multi-walled carbon nanotube (MWCNT) made up of a three shells of differing chirality. ¹²⁸	39
Figure 2.13: Schematic representation of the three structures of CNFs. ¹⁴²	41
Figure 2.14: Schematic diagram explaining the conversion of adsorbed CO _{ads} species to CO ₂ on Pt/GO catalysts. Diagram adapted from reference 175. ¹⁷⁵	44
Figure 2.15: Schematic diagram of possible bifunctional ORR and MOR mechanisms involving oxophilic C–N defects near Pt/C catalyst. The adsorbed oxygen containing surface species facilitate reaction of poisoning intermediate reaction species that would otherwise block catalyst active sites, thereby increasing electrochemical reaction. Diagram reproduced from reference 186. ¹⁸⁶	45

Figure 2.16. Structural motifs found in graphitic carbon nitrides. (a) Liebig's melon ($[\text{C}_6\text{N}_7(\text{NH}_2)(\text{NH})]_n$) contains zig-zag chains of heptazine (tri-s-triazine) units linked by bridging -NH- groups and decorated on their edges by N-H groups, (b) fully condensed C_3N_4 layer based on heptazine units, and (c) graphitic carbon nitride based on triazine ring units.²⁰⁶47

Figure 3.1: CV of Pt/C (40 wt% Alfa Aesar) at 20 mV s^{-1} in N_2 saturated 0.1 M HClO_4 . The shaded region shows the area integrated for hydrogen adsorption.50

Figure 3.2: (a) Schematic of the RDE experimental setup as part of a three-electrode cell; (b) rotating electrode showing the mass transport characteristic flow lines.....53

Figure 3.3. (a) A single-cell hardware (Fuel Cell Technologies) showing the different components; (b) a torque screwdriver is used to compress the cell to the required pressure. .56

Figure 3.4: Typical polarisation curve of a PEMFC showing the cell voltage and power density as a function of current density.57

Figure 3.5: Applied sinusoidal current and resulting sinusoidal voltage response in a linear system.58

Figure 3.6. A typical Nyquist plot (left) for a Randle circuit with a resistor and capacitor in parallel (right) with frequencies between 10 kHz and 0.01 Hz60

Figure 3.7: An example of the Bode plot showing the (a) phase response, and (b) magnitude response as a function of frequency.....60

Figure 3.8: (a) Transmission line model of the Warburg circuit element and (b) typical Nyquist plot response of an equivalent circuit with Warburg impedance.62

Figure 3.9: General equivalent circuit model and Nyquist plot for (a) an electrochemical interface, and (b) for a PEMFC at low current densities.63

Figure 3.10: Polarisation curves of a PEMFC with Pt/Vulcan (40 wt%) anode and cathode (a) using H_2/CO fuel gas (25 to 250 ppm), and (b) in $\text{H}_2/100 \text{ ppm CO}$ during the poisoning period with steady-state achieved after 210 minutes.⁴⁸64

Figure 3.11. US DOE ex-situ AST potential cycle used to test catalyst durability. Reproduced from 211. ²³⁶	68
Figure 4.1: Experimental setup for ex-situ electrocatalyst characterisation	70
Figure 4.2: (a) TEM image of Pt supported on carbon and (b) histogram showing the particle size distribution with an average size of 4.2 nm.	75
Figure 4.3: The cyclic voltammogram of Pt/C on glassy carbon in 0.1 M HClO ₄ at 25°C. Scan rate: 20 mV s ⁻¹	76
Figure 4.4: (a) EDX spectrum and (b) SXPD pattern for PdIr alloy catalyst.	77
Figure 4.5: (a) TEM image of PdIr supported on carbon and (b) histogram showing the particle size distribution with an average size of 9.6 nm.	77
Figure 4.6: The cyclic voltammogram of PdIr, Pd and Ir in N ₂ -saturated 0.1 M HClO ₄ at 25°C. For clarity, the Pd cyclic voltammogram is only shown from 0.05 V. Scan rate: 20 mV s ⁻¹	78
Figure 4.7: CO-stripping voltammogram of Pt, PtRu and PdIr/C, and in 0.1 M HClO ₄ at 25°C.....	79
Figure 4.8: The HOR linear sweep voltammogram for carbon supported Pt, PdIr, Pd and Ir in H ₂ -saturated 0.1 M HClO ₄ at 1600 rpm. Inset: Tafel plot based on Butler-Volmer fit for each catalyst.	81
Figure 4.9: Methanol oxidation voltammogram of Pt/C, PdIr/C and PtRu/C in 1 M CH ₃ OH + 0.1 M HClO ₄ at 25°C. Inset: Close-up of the hydrogen region showing hydrogen desorption peak for PdIr.	83
Figure 4.10: A comparison of the methanol oxidation voltammetry for PdIr and Pd in 1 M CH ₃ OH + 0.1 M HClO ₄ at 25°C.	84
Figure 4.11: (a-c) The CV of Pt/Vulcan, Pt/Ketjen, and PdIr/Ketjen during the ex-situ AST potential cycling (1.0 – 1.5 V) and (d) the change in ECSA of the catalysts as a result of AST potential cycling.....	85

Figure 5.1: Polarisation curves of a single-cell operating at 80°C with PdIr, Pd and Ir as anode catalysts. Conditions: 5.29 cm ² cell, 100% relative humidity anode and cathode, 1 atm. Load-based stoichiometry: Anode = 2.0; Cathode = 6.5 based on O ₂ in air.	89
Figure 5.2: Polarisation curves of single-cell operating at 80°C with Pt (JM), PtRu (Alfa Aesar) and PdIr as anode catalysts. Conditions: 5.29 cm ² cell, 100% relative humidity anode and cathode, 1 atm. Load-based stoichiometry: Anode = 2.0; Cathode = 6.5 based on O ₂ in air.	90
Figure 5.3: Nyquist plot showing the EIS data at 100 mA cm ² for all MEAs.....	91
Figure 5.4: Equivalent circuit element fitted values for (a) ohmic resistance, (b) anode charge transfer resistance, (c) cathode charge transfer resistance, and (d) the sum of ohmic, cathode and anode charge transfer resistances for EIS data obtained at 100 mA cm ⁻²	93
Figure 5.5: Nyquist plot showing the EIS data at 500 mA cm ⁻² for all MEAs.....	94
Figure 5.6: The cyclic voltammograms of PdIr-40 (40 wt% on pre-treated carbon) and PdIr-20 (20 wt% on pre-treated carbon) measured using RDE in N ₂ -saturated 0.1 M HClO ₄ electrolyte at 25°C.....	96
Figure 5.7. TEM images and histograms showing the particle size distribution of (a) PdIr-40 (40 wt%), and (b) PdIr-20 (20 wt%).	97
Figure 5.8: Polarisation curves of a single-cell operating at 80°C with Pt (JM) and PdIr as anode catalysts. Conditions: 5.29 cm ² cell, 100% relative humidity anode and cathode, 1 atm. Load-based stoichiometry: Anode = 2.0; Cathode = 6.5 based on O ₂ in air.	98
Figure 5.9: Nyquist plot of EIS data obtained at 100 mA cm ⁻² for Pt and PdIr anode catalysts	98
Figure 5.10 The resulting equivalent circuit element fitted values of the EIS data obtained at 100 mA cm ⁻² for Pt and PdIr anode catalyst MEAs showing the (a) ohmic resistance, (b) anode charge transfer resistance, (c) cathode charge transfer resistance, and (d) the sum of ohmic and charge transfer resistances.....	100

Figure 5.11: CO polarisation curves for (a) Pt and (b) PtRu MEAs operating with H ₂ /CO fuel with various CO concentrations in a single-cell operating at 80°C. Conditions: 5.29 cm ² cell, 100% relative humidity anode and cathode, 1 atm. Stoichiometry: Anode = 2.0, constant flow rate; Cathode = 6.5 based on O ₂ in air, load-based.....	102
Figure 5.12: CO polarisation curves for Pt, PtRu and PdIr MEAs operating with H ₂ /CO fuel with various CO concentrations in a single-cell operating at 80°C. Conditions: 5.29 cm ² cell, 100% relative humidity anode and cathode, 1 atm. Stoichiometry: Anode = 2.0, constant flow rate; Cathode = 6.5 based on O ₂ in air, load-based.....	103
Figure 6.1: X-ray diffraction pattern (a) and SEM image (b) of a typical layered carbon nitride prepared by thermal condensation of DCDA/melamine 1:1 molar ratio.	108
Figure 6.2: (a) TEM image and (b) particle size distribution of Pt/gCNM	110
Figure 6.3: X-ray diffraction pattern of (a) Pt/Vulcan (Alfa Aesar) and (b) Pt/gCNM.....	111
Figure 6.4: The evolution of cyclic voltammograms of (a) Vulcan, and (b) gCNM during the accelerated carbon corrosion cycling.....	112
Figure 6.5: Change in double-layer capacitance (at 0.40 V) of the support materials as a result of accelerated carbon corrosion cycling.	112
Figure 6.6: The evolution of cyclic voltammograms of (a) Pt/Vulcan, and (b) Pt/gCNM during the accelerated carbon corrosion cycling.	113
Figure 6.7. The change in ECSA (calculated from hydrogen adsorption/desorption) of the supported Pt electrocatalysts as a result of accelerated carbon corrosion cycling.	114
Figure 6.8. (a) Oxygen reduction reaction polarisation curves at 1600 rpm in O ₂ -saturated 0.1 M HClO ₄ , and (b) Levich-Koutecky plot at 0.90 V for Pt/Vulcan and Pt/gCNM.....	115
Figure 6.9. Methanol oxidation reaction of Pt/Vulcan and Pt/gCNM electrocatalyst in 1 M CH ₃ OH + 0.1 M HClO ₄ at 25°C.....	116
Figure 6.10. The TEM images particle size distribution of Pt/gCNM at various metal loadings: (a) 5 wt% Pt, (b) 10 wt% Pt, and (c) 20 wt% Pt.....	118

Figure 6.11. Schematic diagram of Pt/gCNM at (a) high metal loading, and (b) low metal loading.....	119
Figure 6.12. Pt supported on gCNM with the addition of spacers.....	120
Figure 6.13. TEM image and particle size distribution of Pt/gCNM-H ⁺ Cl ⁻ at (a) 10 wt% Pt and (b) 20 wt% Pt.	121
Figure 7.1. X-ray diffraction pattern (a) and SEM image (b) of a poly(triazine)imide carbon nitride prepared by ionothermal route.....	125
Figure 7.2. X-ray diffraction pattern (a) and SEM image (b) of B-gCNM doped with 10 wt% B.....	126
Figure 7.3. X-ray diffraction patterns of supported Pt electrocatalysts. Peaks for nanocrystalline Pt are significantly stronger than gCNM features. Inset: Magnification of the XRD pattern of Pt/PTI-Li ⁺ Cl ⁻ confirming the presence of PTI-Li ⁺ Cl ⁻	127
Figure 7.4. (a) HR-TEM image and (b) particle size distribution of Pt/PTI-Li ⁺ Cl ⁻	128
Figure 7.5. (a) HR-TEM image and (b) particle size distribution of Pt/B-gCNM.....	128
Figure 7.6. Change in double-layer capacitance (at 0.40 V) of the graphitic carbon nitride materials as a result of accelerated carbon corrosion cycling.....	130
Figure 7.7. The change in ECSA (calculated from hydrogen adsorption/desorption) of the supported Pt electrocatalysts as a result of accelerated carbon corrosion cycling.	132
Figure 7.8. Pre and post-AST TEM images for (a) Pt/gCNM, (b) Pt/PTI-Li ⁺ Cl ⁻ , and (c) Pt/B-gCNM.	133
Figure 7.9. Methanol oxidation reaction of supported Pt electrocatalysts in 1 M CH ₃ OH + 0.1 M HClO ₄ at 25°C with a scan rate of 2 mV s ⁻¹	134

List of Tables

Table 1.1: Major types of fuel cells	3
Table 1.2: Status and targets for PEMFC performance based on 80 kW direct hydrogen integrated PEMFC system suitable for automotive applications as reported by the US Department of Energy. ¹⁰⁻¹² ^a Durability based on 10% voltage degradation in a DOE automotive drive cycles. ^b Durability based on laboratory testing and did not take into account catalyst degradation.	13
Table 3.1: The impedance relationships of ideal electrical elements commonly used to describe the impedance of electrochemical systems.....	61
Table 3.2. US DOE in-situ AST cycle for electrocatalyst durability. Reproduced from 231. ²³¹	66
Table 3.3. US DOE in-situ AST cycle for catalyst support durability. Reproduced from 231. ²³¹	67
Table 3.4: AST parameters for ex-situ AST potential cycle. Reproduced from 236. ²³⁶	68
Table 4.1: The ECSA, CO oxidation onset and peak potentials for Pt, PtRu, and PdIr catalysts obtained from CO-stripping voltammetry. The onset potential is defined as the potential at which the current is 10% of the maximum CO oxidation current.....	80
Table 4.2: The Tafel slope and exchange current density (j_{0-RDE}) for Pt, PdIr, Pd and Ir catalysts measured in 0.1 M HClO ₄ RDE assembly, and the exchange current density obtained from mass-transport free measurements ($j_{0-PEMFC}$). ²⁶⁸	82
Table 6.1: The ORR specific activity, mass activity, methanol oxidation peak potential (E_{peak}) and maximum methanol oxidation reaction current density (j_{max}) of supported Pt electrocatalysts.	116

Table 7.1: The average particle and crystallite size of supported Pt catalysts. ^{a)} Estimated from TEM image based on the average of 100 particles; ^{b)} Calculated from 111 signal widths of XRD using the Scherrer equation.	129
Table 7.2. The ECSA of supported Pt electrocatalysts before and after the accelerated carbon corrosion cycling (2000 cycles).	131
Table 7.3: The methanol oxidation peak potential (E_{peak}) and maximum methanol oxidation reaction current density (j_{max}) of supported Pt electrocatalysts in 1 M CH ₃ OH + 0.1 M HClO ₄ at 25°C.	135

Chapter 1

1 Introduction

1.1 Motivation

The continued exploitation of fossil fuels and the ever growing global energy demand, driven by economic and population growth, poses a significant risk of irreversible climate change. Continuous anthropogenic greenhouse gas emissions have raised atmospheric CO₂ concentrations significantly, with more than half of greenhouse gas emissions since the industrial revolution occurring in the last 40 years. Alarming, annual greenhouse gas emissions have increased by 1.0 gigatonne carbon dioxide equivalent (GtCO₂eq) per year between 2000 and 2010, compared to 0.4 GtCO₂eq per year between 1970 and 2000. If the current trend continues, global surface temperature is predicted to increase to 3.7 - 4.8 °C above pre-industrial level in 2100, which is considerably above the dangerous level at which impacts of extreme climate change can be felt (~2°C).¹

As the demand for energy continues to grow, viable fossil fuel reserves are declining. In the UK, 90% of its energy requirements depends on fossil fuels and the energy demand is projected to increase, with the transportation sector seeing the fastest growth.^{2,3} The continuing reliance on fossil fuels threatens the energy security of many nations. In order to meet total energy demands, controversial exploitation of non-ideal fossil fuel deposits in sensitive areas become necessary, resulting in an increase in financial and environmental costs in exploration and extraction activities.

Temperature change caused by anthropogenic greenhouse gas emissions can be kept to below 2°C relative to the pre-industrial level if the atmospheric CO₂ concentration level does not exceed 450 ppm by 2100. For comparison, current atmospheric CO₂ concentration is estimated to be about 430 ppm. Therefore, mitigating the effects of climate change is crucial now more than ever. By 2050, a 40 – 70% reduction in greenhouse gas emissions is necessary and by 2100 there should be zero or near zero

emission.¹ To achieve such dramatic emissions reductions, rapid improvements in energy efficiency and the adoption of zero- and low-carbon energy supply from renewables are necessary. Among the available low-carbon technologies, the polymer electrolyte membrane fuel cell (PEMFC) seems to be the most feasible solution, especially for portable and transportation applications.

1.2 Fuel cells

A fuel cell is a device that converts the chemical energy of a fuel into electrical energy via electrochemical reactions, just like a battery. However, unlike batteries, it does not get discharged, but generates electricity as long as the reactants - fuel and oxidant - are supplied. The first reference to a fuel cell can be attributed to William Grove in 1839, where he demonstrated that the gases (hydrogen and oxygen) evolved by electrolysis at platinum electrodes, which were immersed in dilute sulphuric acid, could be consumed at the same electrodes, producing electrical current.⁴

Generally, a fuel cell consists of two electrodes (anode and cathode) separated by an electrolyte, which varies depending on the system. A fuel, usually hydrogen, but other forms of hydrocarbons such as methanol can also be used, is oxidised at the anode producing positively charged ions and negatively charged electrons. Electrons liberated from the anode flow through an external electrical circuit to the cathode, whilst the positively charged ions move through the electrolyte to the cathode, completing the circuit. At the cathode, the ions and electrons react with oxygen or another oxidising agent, producing water.

Fuel cells combine many of the advantages of both conventional engines and batteries, making it a very promising technology. Some of the advantages include:

- *Low or zero greenhouse emission.* Even though hydrogen is not readily available in its pure molecular state, advances in technology means it can be produced using renewable sources such as electrolyzers, powered by wind turbines or solar photovoltaics. A fuel cell operating on hydrogen generates zero emissions at point of use and the only by-product is water.

- *High efficiency.* Fuel cells are generally more efficient than internal combustion engines (ICE) and not limited by the Carnot cycle efficiency, especially at low temperature. This is explained further in Section 1.5.
- *No moving parts.* This may result in highly reliable and long-lasting systems.
- *Modular.* Fuel cells are modular and this allows easy independent scaling between powers. Conventional batteries cannot be used for large scale applications while fuel cell applications vary from the 1 W range, such as for mobile phones, all the way up to the megawatt range (power plants).
- *Easy refuelling.* Batteries must be thrown away or recharged, while fuel cells can be quickly refuelled.

1.3 Types of fuel cells

In 1939, Francis Thomas Bacon successfully developed a 5 kW stationary fuel cell.^{5, 6} In the early 1960s, Thomas Grubb and Leonard Niedrach at General Electric Company (GE) invented the ionomer membrane technology which is now used as fuel cell electrolyte. GE went on to develop this technology with the National Aeronautics and Space Administration (NASA) and McDonnell Aircraft, leading to the first commercial use of fuel cells.⁷ Since then, interest in fuel cells has increased dramatically which lead to several breakthroughs, making fuel cell technology more feasible for wider applications. Currently there are 5 major types of fuel cells, which are classified by the type of electrolyte they use, as shown in Table 1.1 below.

Table 1.1: Major types of fuel cells

Fuel Cell Name	Fuel	Electrolyte Charge Carriers	Operating Temperature (°C)
Alkaline fuel cell (AFC)	Hydrogen	KOH solution OH ⁻	<80°C
Polymer electrolyte membrane fuel cell (PEMFC)	Hydrogen/ hydrocarbons	Polymer membrane H ⁺	<150°C
Phosphoric acid fuel cell (PAFC)	Hydrogen	Phosphoric acid H ⁺	200°C

Molten carbonate fuel cell (MCFC)	Hydrocarbons	Molten carbonate CO_3^{2-}	650 - 800°C
Solid oxide fuel cell (SOFC)	Hydrocarbons	Ceramic O_2^-	500 - 1000°C

Variants of the PEMFC which employs liquid hydrocarbons as fuels such as methanol, ethanol and formic acid are sometimes categorised as separate types of fuel cells: direct methanol fuel cell (DMFC), direct ethanol fuel cell (DEFC) and direct formic acid fuel cell (DFAFC). Alternative types of fuel cells continue to be developed, for example microbial fuel cells and solid acid fuel cells.

1.4 Introduction to PEMFC

The PEMFC employs a proton conducting polymeric membrane as its electrolyte, which separates the anode and cathode sides, as shown in Figure 1.1. The membrane, catalyst layers and the gas diffusion layers (GDL) are collectively called the membrane electrode assembly (MEA).

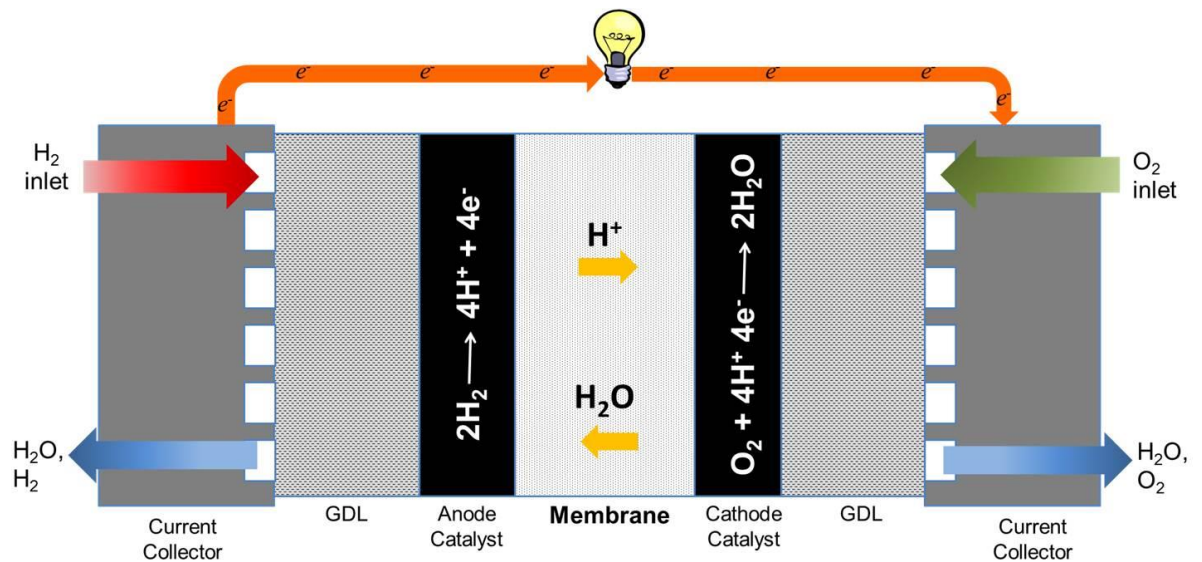


Figure 1.1: Basic operation of a typical PEMFC

At the anode catalyst layer, hydrogen is electrochemically oxidised into protons and electrons in a reaction called hydrogen oxidation reaction (HOR):

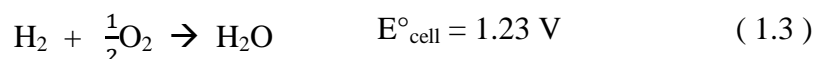


The protons are conducted through the membrane to the cathode, whereas the electrons are forced to travel in an external circuit to the cathode, because the membrane is electrically insulating.

At the cathode catalyst layer, the electrons react with oxygen and electrons in a reaction called oxygen reduction reaction (ORR):



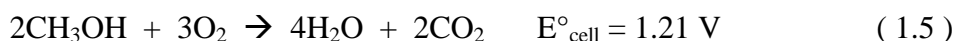
The overall reaction produces water and heat as by-products:



In the case of direct alcohol fuel cells, e.g., DMFC, the anode is supplied with a diluted methanol aqueous solution:



The overall methanol oxidation electrochemical reaction:



Both anodic and cathodic reactions require active catalyst, which occur at the interfacial area where the catalyst, gas and electrolyte meet. This interfacial area is called the *triple phase boundary* (TPB). The reactions are finite and depend on the intrinsic property and degree of utilisation of the catalyst materials.

1.5 Thermodynamics

The fuel cell is an energy conversion device and therefore its conversion efficiency is important. The enthalpy change (ΔH) corresponding to reaction (1.3) is -286 kJ mol^{-1} , where one mole of H_2 reacts with O_2 to form liquid water at 298 K and standard

atmospheric pressure. Therefore the thermal cell potential (E_t) in accordance with ΔH is given by:

$$\Delta H = nFE_t$$

$$E_t = 1.48 \text{ V} \quad (1.6)$$

Where n is the number of electrons and F is Faraday's constant, equal to $96485 \text{ C}\cdot\text{mol}^{-1}$.

The maximum energy available for conversion to electrical work is given by the Gibbs free energy change for the overall reaction, determined by the difference in the energy of formation between reactants and products. For the reaction of H_2 and O_2 to *liquid water*, the standard Gibbs free energy change at 298 K and standard atmospheric pressure is given by:

$$\Delta G^\ominus = G_{f,\text{products}}^\ominus - G_{f,\text{reactants}}^\ominus$$

$$\Delta G^\ominus = G_{f,\text{H}_2\text{O}}^\ominus - G_{f,\text{H}_2}^\ominus - G_{f,\text{O}_2}^\ominus = -237.2 - 0 - 0 = -237 \text{ kJ}\cdot\text{mol}^{-1} \quad (1.7)$$

Therefore, out of -286 kJ mol^{-1} of available energy, only $-237 \text{ kJ}\cdot\text{mol}^{-1}$ can be converted into electrical energy, which corresponds to a calculated value of $E^\ominus = 1.23 \text{ V}$ (reversible potential under standard conditions).

The Gibbs free energy change is a function of temperature and reactant concentrations or partial pressures according to:

$$\Delta G = \Delta G^\ominus + RT \ln \left(\frac{p_{\text{H}_2\text{O}}}{p_{\text{H}_2} p_{\text{O}_2}^{1/2}} \right) \quad (1.8)$$

In a reversible electrochemical system where available Gibbs free energy is converted to electrical energy, the free energy change can be described by the equation:

$$\Delta G = -nFE_{rev} \quad (1.9)$$

Substituting equation (1.9) into (1.8) gives:

$$E_{rev} = E^\ominus + \frac{RT}{nF} \ln \left(\frac{p_{H_2O}}{p_{H_2} p_{O_2}^{1/2}} \right) \quad (1.10)$$

Where E_{rev} is the Nernst equation and relates to the open circuit voltage (OCV) of a fuel cell to the temperature and concentrations partial pressures of reactants and products. Therefore, theoretically, a fuel cell operating on hydrogen and oxygen at atmospheric pressure and 80°C gives an E_{rev} of 1.18 V

The maximum theoretical efficiency (ϵ_{max}) of a fuel cell operating at standard conditions is given by the ratio of the Gibbs free energy to the enthalpy change of the overall reaction:

$$\epsilon_{max} = \frac{\Delta G^\ominus}{\Delta H} = \frac{237 \text{ kJ} \cdot \text{mol}^{-1}}{286 \text{ kJ} \cdot \text{mol}^{-1}} = 83\% \quad (1.11)$$

As ΔG^\ominus is temperature dependant, the ϵ_{max} decreases with increasing temperature. Below 700°C, the ϵ_{max} of an H₂/O₂ fuel cell is higher than the theoretical efficiency of an ideal Carnot heat engine (ICE). In practice, ICE suffers from further irreversible losses from friction, heat transfer, inefficient combustion and various other factors resulting in a typical efficiency of around 20 – 25%. Therefore between the two technologies, fuel cell remains the more efficient device.

1.6 Fuel cell polarisation curves

According to the thermodynamic analysis above, a fuel cell operating on hydrogen and oxygen at 80°C would supply current continuously while maintaining a constant voltage of 1.18 V (E_{rev}). In practice, the actual voltage is lower than this due to irreversible losses, as shown on the voltage-current (V-I) response of the cell in Figure 1.2, also known as a *polarisation curve*.

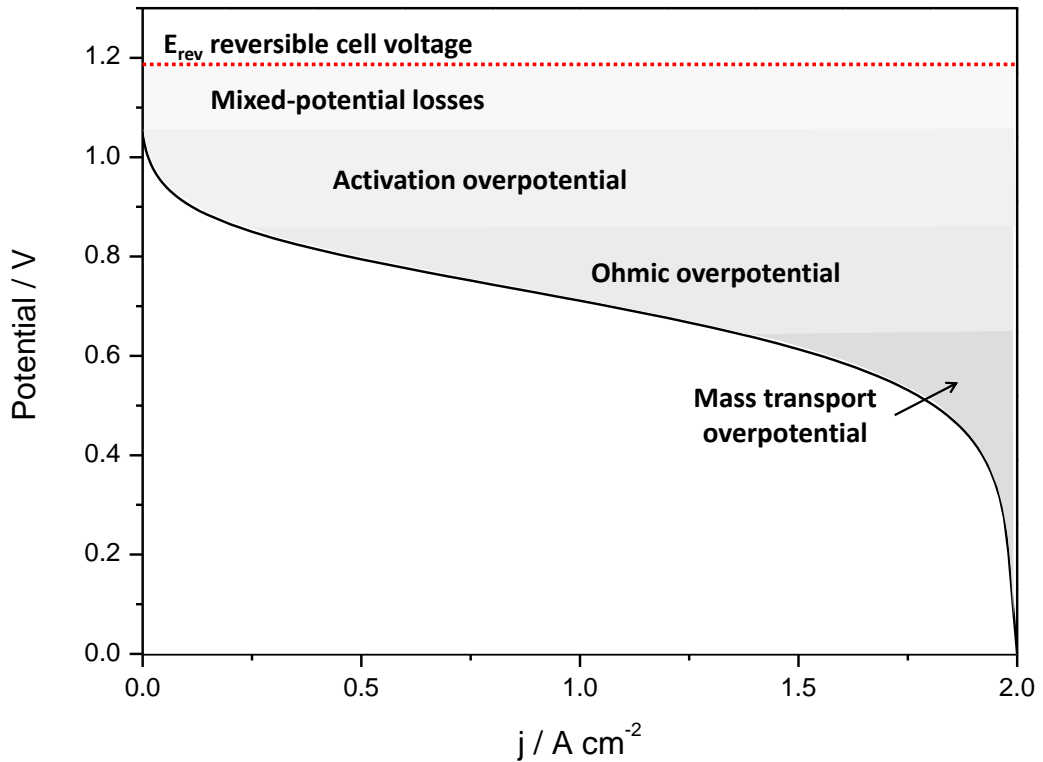
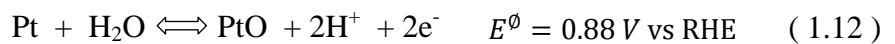


Figure 1.2: A typical PEMFC polarisation curve showing the various irreversible voltage losses.

1.6.1 Mixed-potential losses

The OCV of the PEMFC is typically around 1.0 V, which is lower than the theoretical fuel cell voltage. Even when no current is drawn, there is an irreversible voltage loss due to secondary reactions at the cathode:

1. **Mixed potential.** O_2 undergoes reversible adsorption at the surface of the Pt catalyst:



2. **Fuel crossover.** H_2 may permeate across the membrane to the cathode, where it can be directly oxidised by O_2 , resulting in mixed cathode potential. In addition, the reaction also produces peroxide radicals which damage the membrane and reduce the triple phase boundary in the catalyst layer.

1.6.2 Activation overpotential

Activation overpotential arises from the limitations on the rate of electrochemical reactions taking place at the catalyst layers. Generally, much of the activation loss is caused by the sluggish ORR at the cathode; however, activation overpotential at the anode is equally important when using fuels other than pure hydrogen.

All electrochemical reactions involve the transfer of electrons between the electrode material and the reactants. Therefore, the rate of reaction on the electrode surface can be measured by the electrical current flowing to or from the electrode. Consider a single step redox reaction involving n electrons occurring at an electrode:



In the forward direction, electrons are transferred from the electrode to the reactant, producing cathodic current i_c . In the reverse reaction, electrons are transferred from the reactant to the electrode, producing anodic current i_a . The total current (i_k) flowing at an electrode determined purely by the kinetics of reaction is given by the sum of the cathodic and anodic currents:

$$i_k = i_a - i_c \quad (1.14)$$

Similarly, when the current is normalised to the electrochemical surface area (ECSA) of the electrode, the equation above becomes:

$$j_k = j_a - j_c \quad (1.15)$$

where $j \text{ (A.cm}^{-2}\text{)} = i \text{ (A)} / A_{ECSA} \text{ (cm}^2\text{)}$.

When no net current is flowing to or from the electrode, the rate of anodic and cathodic reactions is equal and equilibrium is reached:

$$j_a = j_c = j_0 \quad (1.16)$$

where j_0 is the exchange current density, which is an intrinsic property of the electrode material and is a measure of how rapid an electrochemical reaction can occur.

The cell voltage is determined by the Nernst equation described above (1.10). The equilibrium can be shifted by changing the potential so that it becomes polarised either more positive or more negative than the reversible potential. This will generate current as the reaction proceeds to re-establish the equilibrium concentrations of O and R. The magnitude of the net current depends on the amount by which the applied potential deviates from the equilibrium potential. This applied potential is also known as *overpotential* (η):

$$\eta = E - E_{rev} \quad (1.17)$$

The relationship between current density and overpotential can be described by the classic Butler-Volmer equation:

$$j = j_0 \left(\exp \left[\frac{\alpha_a n F}{RT} \eta \right] - \exp \left[\frac{-\alpha_c n F}{RT} \eta \right] \right) \quad (1.18)$$

where the terms α_a and α_c are the transfer coefficients for the anodic and cathodic reactions respectively, and represent the fraction of additional energy (or overpotential) that goes towards the rate determining steps of the reactions. Typically, $\alpha_a + \alpha_c = 1$, so equation (1.18) becomes:

$$j = j_0 \left(\exp \left[\frac{\alpha n F}{RT} \eta \right] - \exp \left[\frac{-(1 - \alpha) n F}{RT} \eta \right] \right) \quad (1.19)$$

with $0 < \alpha < 1$. The anodic and cathodic current density can be expressed as:

$$j_a = j_0 \left(\exp \left[\frac{\alpha n F}{RT} \eta \right] \right) \quad (1.20)$$

$$j_c = -j_0 \left(\exp \left[\frac{-(1 - \alpha) n F}{RT} \eta \right] \right) \quad (1.21)$$

where the exponential term represent the rate of forward and reverse reactions. The net overall current response is illustrated in Figure 1.3. By applying a suitable overpotential η , anodic and cathodic current can be altered. The graph also shows the effect of the exchange current density on the polarisation curve. For a small exchange current density, the reaction is slow and requires a higher overpotential to reach the same current as the reaction with a large exchange current density. This is the basis for the activation losses in the PEMFC – the lower the activity of the electrocatalysts, the lower the net current achieved at a specified voltage.

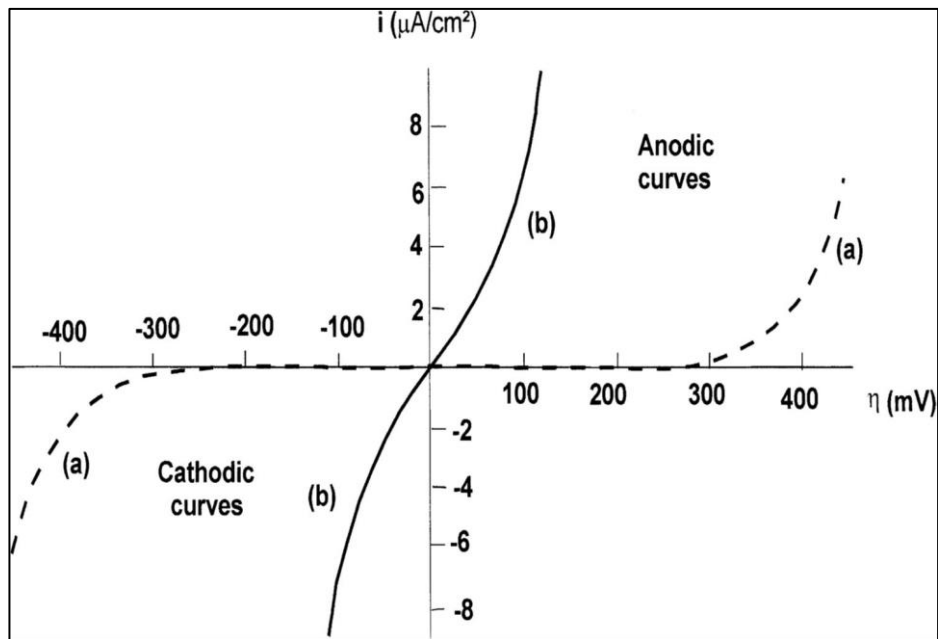


Figure 1.3: Theoretical polarisation curves according to the Butler-Volmer equation with $\alpha=0.5$ for two exchange current densities: (a) $j_0 = 10^9 \text{ A cm}^{-2}$ and (b) $j_0 = 10^{-6} \text{ A cm}^{-2}$. Reproduced from reference 5 and 6.^{8,9}

At high overpotentials ($|\eta| \geq 50 \text{ mV}$), the rate of one of the reactions becomes negligible with respect to the other and the equation reduces to:

$$j = j_0 \exp\left(\frac{-\alpha n F \eta}{RT}\right) \quad (1.22)$$

Equation (1.22) can be simplified to a linear form of $y = a + bx$ by conversion to base 10 logarithms, which gives the Tafel equation:

$$\log(j_k) = \log(j_0) - \frac{\alpha n F}{2.303 RT} \eta \quad (1.23)$$

A Tafel plot of η versus $\log|j_k|$ gives a linear line with $b = \frac{\alpha n F}{2.303 RT}$ corresponding to the Tafel slope and $a = \log(j_0)$ corresponding to the intercept at $\eta = 0$. From this, the parameters j_0 , α and n can be determined.

1.6.3 Ohmic overpotential

Ohmic loss is caused by the bulk electrical resistance of cell materials, contact resistances at interfaces between components, and the ionic resistance of the electrolyte membrane and catalyst layers. The voltage drop is described by Ohm's Law:

$$-\Delta E = \Delta I R_{\Omega} \quad (1.24)$$

where R_{Ω} is the total internal resistance. This voltage drop caused the distinctive linear drop in the middle of the polarisation curve. In fuel cell systems, the resistance comes primarily from the electrolyte.

1.6.4 Concentration overpotential

The reactant concentration at the catalyst surface depends on the current density – the higher the current density, the lower the surface reactant concentration. At very high current densities (typically above 1 A.cm⁻² in modern PEMFC), the reactant is consumed faster than it can be replenished, causing the sharp final decline in fuel cell voltage on the polarisation curve.

1.7 Commercialisation barriers

Despite the recent advances in PEMFC technology and successful commercialisation in certain specialised markets, mass-market applications in the automotive sector are yet to be realised. Mass-market commercialisation of PEMFC and hydrogen economy goes hand-in-hand, with both depending on market confidence and demand. Although hydrogen can be derived from a diverse range of clean technologies and renewables, the cost is still a major barrier. Distribution and storage of hydrogen in large volume is also

a significant challenge and huge investments (trillions of dollars) are needed to build the necessary infrastructure. Hence, the hydrogen economy will not take off until significant market in the fuel cell technology is achieved. The transition will take many years and is likely to occur in stages. Therefore, PEMFC technology needs to be reliable enough to initiate market confidence and demand.

To guarantee commercial viability, PEMFC cost and durability must be on par with conventional ICEs. As of August 2011, automotive ICEs cost between \$25-35 kW⁻¹ with operational lifetimes in excess of 5000 hours. For comparison, the cost and durability status of PEMFC system, as well as targets specified by the US Department of Energy (DOE),¹⁰⁻¹² are summarised in Table 1.2:

Table 1.2: Status and targets for PEMFC performance based on 80 kW direct hydrogen integrated PEMFC system suitable for automotive applications as reported by the US Department of Energy.¹⁰⁻¹² ^aDurability based on 10% voltage degradation in a DOE automotive drive cycles. ^bDurability based on laboratory testing and did not take into account catalyst degradation.

	Status			Target	
	2007	2010	2013	2020	2050
Stack cost (\$/kW)	50	25	27	15	-
System cost (\$/kW)	94	51	55	40	30
Durability (hours) ^a	2000 ^b	6500 ^b	2500	5000	5000

As shown above, PEMFC technology is twice as expensive with only half the durability compared to a modern ICE vehicle. For that reason, a significant cost reduction and improvements in durability is needed to compete with ICE and incentivise the hydrogen economy.

1.7.1 Cost and durability

According to the DOE cost analysis report, which looks at the breakdown of stack component cost in a high-volume manufacturing scenario (Figure 1.4),¹⁰ the catalyst is the single largest contributor to the cost of PEMFC stacks. Catalyst (primarily Pt) is

dominated by commodity cost, whereas the rest of the components' cost come from manufacturing, which are volume-sensitive. Thus, an increase in volume from 1000 to 500,000 systems increases the catalyst cost elements from 16% to 49% of the total system cost. Therefore, the highest potential for cost reduction lies in the optimisation of the catalyst component of PEMFC.

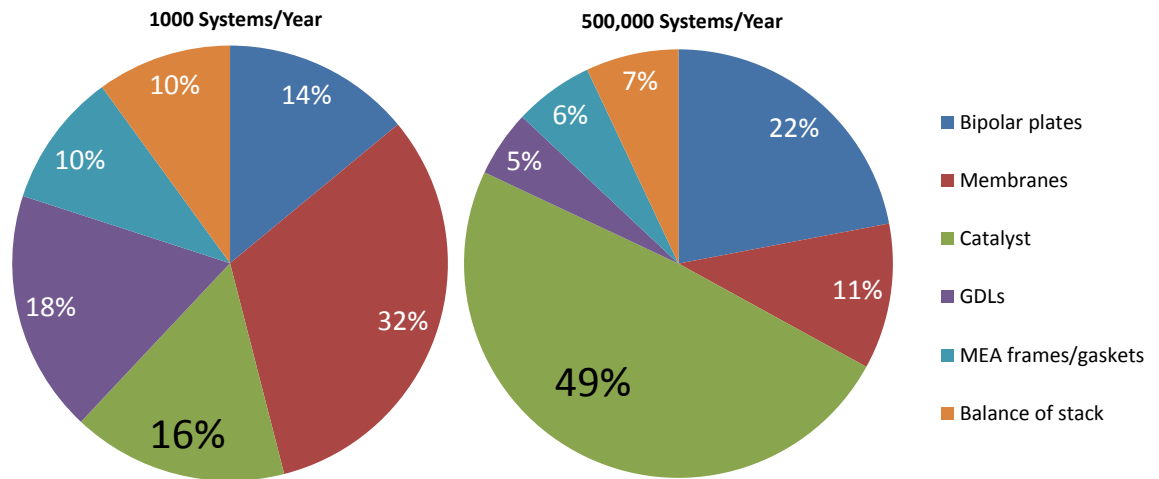


Figure 1.4. Breakdown of fuel cell stack cost based on projected scale-up of 1000 and 500,000 systems per year. Reproduced from reference 7.¹⁰

Modern ICE vehicles use platinum group metals (PGMs) in their catalytic converters and therefore the incorporation of these materials into mass-market PEMFC products should not be a barrier. According to the DOE, platinum loadings on PEMFC have reduced by more than 80% since 2005 and this trend is expected to continue, albeit at a slower rate.¹⁰

However, at present, a modern fuel cell vehicle contains 4 to 5 times more PGM catalysts than an equivalent ICE vehicle.¹³ If PEMFCs were to be widely used, it is very likely that the demand and price of Pt would increase significantly. In addition, the PEMFC is subjected to mechanical and chemical degradation, especially in automotive and portable applications, which usually have demanding start/stop cycles. The MEA presents the most challenging degradation issue affecting the long-term durability of PEMFC due to harsh operating conditions, such as fuel impurities, high humidity, low pH, elevated temperature, and dynamic loads in combination with an oxidizing or reducing environment.

Thus, to secure the viability of PEMFC technology in automotive applications, reductions in Pt loading or the use of cheaper materials, as well as improvement in durability are necessary.

1.8 Aims

This study focuses on developing alternative electrode materials for the PEMFC, with an aim to reduce catalyst cost and improve its durability.

Chapter 2 provides an overview of PEMFC catalysts layers and related issues, as well as the motivation behind the materials studied in this work. The use of low-cost, PdIr alloy as HOR anode catalyst is proposed. In addition, the use of graphitic carbon nitride as a low-cost and durable catalyst support for PEMFC is introduced.

Chapter 3 describes the methodology used in this work, including both *in-situ* and *ex-situ* electrochemical characterisation techniques. An overview of catalyst layer durability studies is provided.

Chapter 4 and 5 present the work on 1:1 PdIr as a low-cost, non-platinum anode electrocatalyst for PEMFCs. The catalyst was characterised in rotating disc-electrode configuration as well as in a real PEMFC. The durability and CO tolerance were also investigated.

Chapter 6 presents the characterisation of graphitic carbon nitride as a catalyst support. First, the durability of the material was studied in comparison to a conventional catalyst support. Platinum was then deposited on graphitic carbon nitride and the material was fully characterised via physical and electrochemical techniques. Chapter 7 presents the results on modified graphitic carbon nitrides as alternative catalyst supports.

Finally, the overall conclusions and directions for future work are highlighted in Chapter 8.

Chapter 2

2 PEMFC Catalyst Layers

Ever since the first application of proton exchange membranes in fuel cells and the successful deposition of Pt catalyst onto the membrane in the 1960s, a lot of research has gone into improving the performance and reducing PGM catalyst loading.¹⁴⁻¹⁹ The first PEMFCs utilised finely-divided Pt black, with particle size of 50 – 100 nm and physical surface area of around $10 \text{ m}^2\text{g}^{-1}$, which requires a loading of at least $4 \text{ mg}_{\text{Pt}}\text{cm}^{-2}$ to achieve decent performance. Subsequently, carbon supported electrocatalysts were introduced, which consists of smaller metal nanoparticles ($< 10 \text{ nm}$) dispersed on high surface area carbon black ($200 - 1000 \text{ m}^2\text{g}^{-1}$), allowing excellent dispersions of Pt nanoparticles and decreasing the loadings. The incorporation of proton-conducting ionomer within the catalyst layer further improved the utilisation of the catalyst, extending the triple phase boundary and converting more of the physical surfaced area to be electrochemically active.

This chapter provides an overview of the fundamental aspects of the electrochemical reactions happening at the anode (HOR or MOR) and cathode (ORR) catalyst layer in PEMFC. A review on the major durability issues affecting PEMFC catalyst layer is also presented, including the approaches used to address them.

2.1 Anode catalyst layers

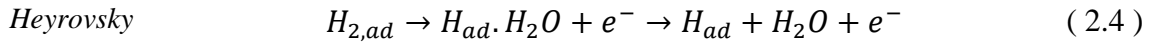
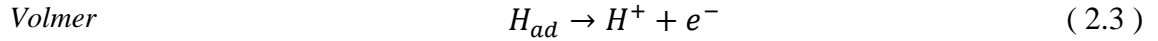
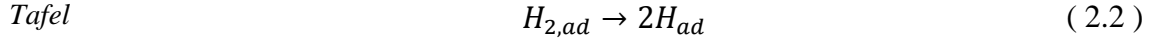
In PEMFC catalysis, most research has been focused on cathode catalysts development because the activation overpotential is mainly caused by the slow ORR kinetics. However, in some cases the HOR can also contribute to the activation overpotential, especially if there are impurities in the fuel. There are also issues with durability that is often overlooked.

The HOR may occur through a combination of several of the following steps:

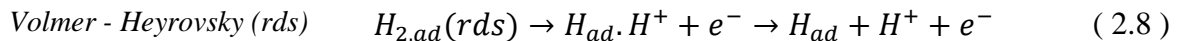
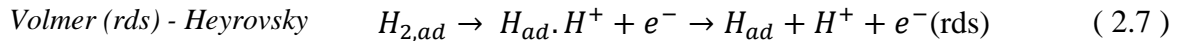
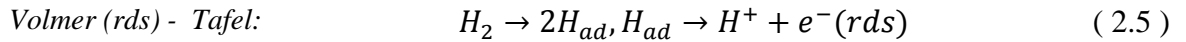
1. Adsorption step - hydrogen molecule adsorbs on the electrode surface to form surface species ($H_{2,ad}$):



2. The adsorbed hydrogen forms adsorbed H atoms (H_{ad}) through Tafel-Volmer or Heyrovsky-Volmer route:



3. Desorption step – the products desorbed and transported into the electrolytes and the rate of reaction is controlled by a rate-determining step (rds) which is sufficiently slow compared to the others. The rds step mechanisms have been identified as:



Currently Pt is the most active catalyst for the HOR and has been studied very extensively.²⁰ However, there is a lack of consensus in the literature concerning the values of the exchange current density. In a study looking at reducing Pt loading at the anode, it was found that a considerable amount of Pt could be reduced without affecting the voltage, which is contradictory to the kinetic data obtained from rotating disc-electrode (RDE) experiments.²¹ The authors found that the exchange current density obtained from the RDE experiments is 'too small' by at least a factor of 20. Further study shows that the HOR kinetics in acid much faster than the hydrogen diffusion to the surface of the electrode.²² Using a novel approach, Chen and Kucernak investigated the hydrogen oxidation electrochemical reaction using a single Pt microparticle and found that $j_0 = 20 \text{ mA cm}^{-2}$, which is in agreement with the value estimated from a real

fuel cell environment.²³ They estimated that the mass transport coefficient is about 10 cm s^{-1} and in order to achieve the same mass transport rate, the rotation speed on the RDE would have to be $4.6 \times 10^8 \text{ rpm}$, which is technically not feasible. This study has led to renewed interest to the kinetic measurements of the HOR and challenged many previous conclusions on the structural sensitivity of the HOR as well as its particle size effect.²⁴

At present, the lowest Pt catalyst loading achieved without compromising the performance is $0.15 \text{ mg}_{\text{Pt}}.\text{cm}^{-2}$.¹⁰ Despite this breakthrough, cheaper catalyst materials with better durability are needed to kick-start PEMFC commercialisation and the hydrogen economy, as discussed in Section 1.7. Figure 2.1 shows that platinum and platinum group metals are situated at the top of the HOR/HER ‘volcano plot’, indicating that they have the highest catalytic activity. The volcano plot is a useful tool for establishing and predicting reactivity trends, plotted as exchange current density versus the enthalpy of hydrogen or oxygen adsorption. The shape of the plot is based on the Sabatier principle which states that a heterogeneous catalyst must bind reaction intermediates with sufficient strength to facilitate electron transfer, but weakly enough to allow reaction products to desorb from the surface and free-up active sites for further reaction.^{25, 26} To obtain the highest catalytic activity, an intermediate value in the enthalpy of hydrogen adsorption is required so that the adsorption and desorption kinetics do not limit the overall reaction. Platinum and platinum group metals have intermediate values of hydrogen adsorption enthalpy and therefore, are the most efficient HOR catalyst among the transition metals.

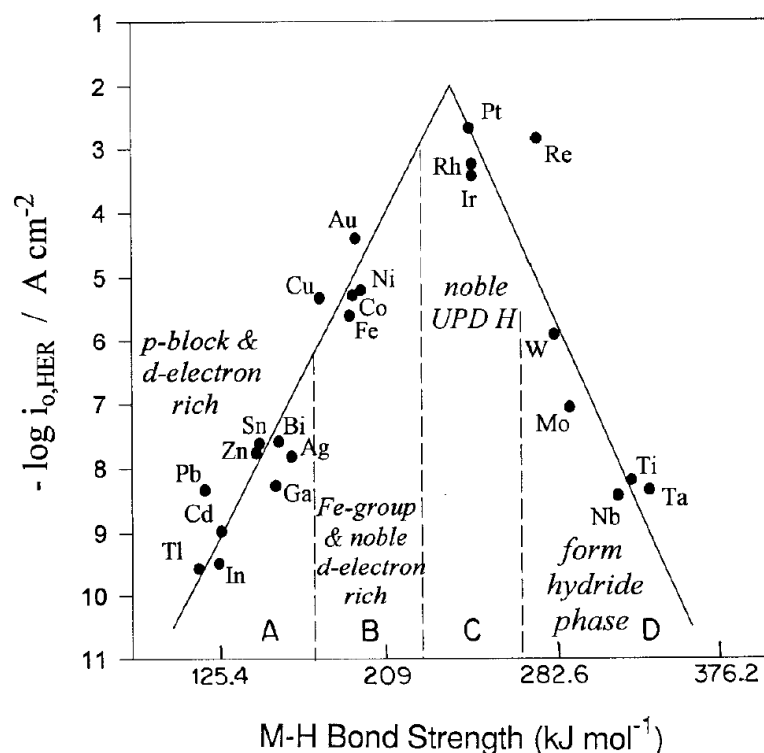


Figure 2.1: A plot of $\log j_0$ versus metal-hydrogen bond energy for various metal catalysts, showing the volcano-like dependency.²⁷

Another useful theory to predict trend reactivity among transition metals and alloys is the d -band model, which was developed by Hammer and Nørskov.²⁸⁻³⁰ The d -band model describes the bond formation at a transition metal surface, as illustrated in Figure 2.2. A transition metal surface has a continuum of energy levels with electrons filling the states from the bottom upwards and the Fermi level is the highest occupied electronic level. The valence states of transition metal surface can be divided into s and d states. An adsorbate valence states couple to the metal s -states first, leading to a shift and broadening of the adsorbate states, and then to the metal d -states. This gives rise to the formation of separate bonding and anti-bonding states, with the strength of the bonding depending on the filling of the anti-bonding states. Unfilled anti-bonding states will result in a strong bond, and vice versa.

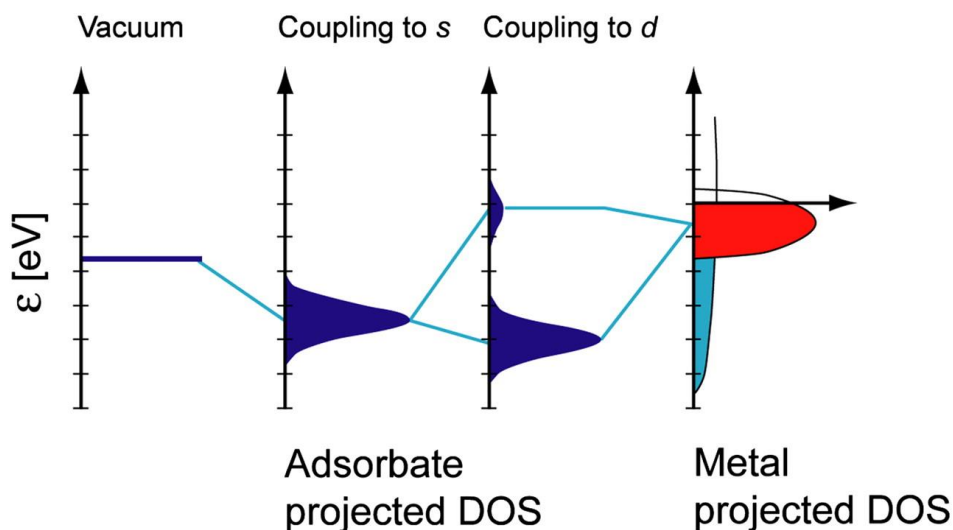


Figure 2.2: Schematic illustration of the formation of a chemical bond between an adsorbate and the s and d states of a transition metal.^{28, 29}

Unlike a molecule where the occupancy of the anti-bonding states depends on the number of electrons in the system, the occupancy of the anti-bonding states on a metal surface depends only on the energy of these states relative to the Fermi level. The anti-bonding states are always above the d -states and the energy of the d -states relative to the Fermi level varies substantially between the different transition metals. Therefore, energy of the d -states, i.e., the d -band centre, relative to the Fermi level is a good first indicator of the bond strength. The higher the d -band centre, the higher in energy the anti-bonding states are and the stronger the bond.

Based on this theory, it is possible to fine tune the d -band centre of a metal i.e., surface electronic structure, by alloying it with another metal. Recently, Yoo and Sung showed that Pd-Ir alloy could be a very good candidate for HOR anode catalyst, with activity comparable to that of Pt.³¹ The group fabricated PdIr thin film electrodes with various compositions (0, 24%, 59%, and 87% Pd) using Radio-Frequency magnetron co-sputtering method and investigated their HOR kinetics using the RDE at 273 K. They found that PdIr HOR activity showed a volcano-type dependence on the d -band vacancy, which is determined by the alloy compositions. In other words, the HOR activity depends on the strength of the PdIr-H bond interaction, which correlates to the position of the PdIr d -band centre in relation to the Fermi level. If the d -band vacancy is too big, the HOR activity decreases due to strong PdIr-H bond. It was found that the

Tafel plot and exchange current density increases in the order of $\text{Pd}_{59}\text{Ir}_{41} > \text{Pd}_{24}\text{Ir}_{59} > \text{Pd}_0\text{Ir}_{100} > \text{Pd}_{87}\text{Ir}_{13}$. This reveals a ‘volcano-like’ trend between the activity and ratio of Pd to Ir, indicating that electronic structure may play a role in the electrocatalytic reaction.

Using high-resolution photoelectron spectroscopy (HR-XPS), the authors found a linear relationship between the d -band centre of the catalyst and the percentage of Pd, as shown in Figure 2.3. As mentioned above, H_2 adsorption or desorption is the rate-determining step in the HOR. $\text{Pd}_{83}\text{Ir}_{17}$ lies at the high end of the d -band centre, which means it binds to hydrogen strongly, whereas $\text{Pd}_0\text{Ir}_{100}$ lies at the other end of the d -band centre, whereby it binds to hydrogen weakly. Both situations lead to higher H-H bond dissociation/association energy, which renders HOR to be less active. $\text{Pd}_{59}\text{Ir}_{41}$ lies close to the middle of the d -band centre and thereby a balance between H-H bond dissociation/association energy is achieved, which leads to a high HOR activity.

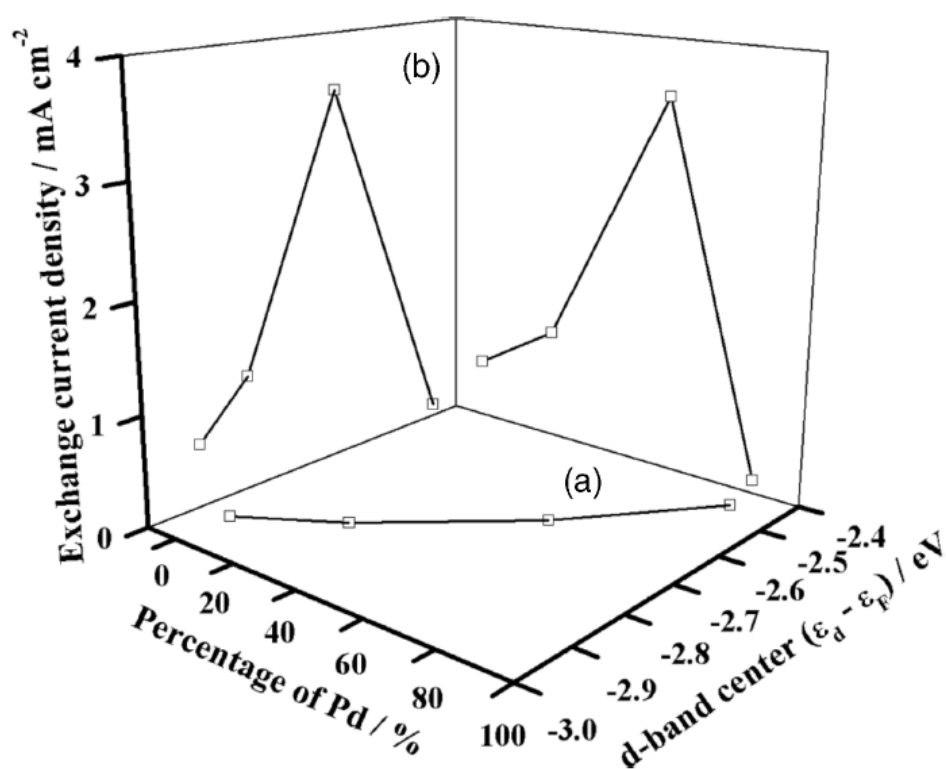


Figure 2.3: (a) Linear relationship between the d -band centre and the percentage of Pd, and (b) HOR exchange current density on PdIr electrode as a function of d -band centres and percentage of Pd.³¹

Given the linear relationship between the d -band centre and the percentage of Pd, a Pd₅₀Ir₅₀ alloy catalyst is predicted to have an optimum d -band centre and a maximum HOR activity. Many experimental studies can be found in the literature using Pd as a co-catalyst for HOR, but little work has been done on Ir.³²⁻³⁴ Both Pd and Ir are about 42% and 59% of the cost of Pt, respectively.³⁵ PdIr HOR activity for alkaline fuel cells is reported to be similar to that of pure Pt.³⁶ PdIr catalyst was also reported to have high electrocatalytic activity for ethanol oxidation in acidic medium.³⁷

2.1.1 Anode catalyst layer degradation

During fuel cell operation, one or more cells in the stack may fail. Failed cells are unable to produce the required current, but voltage produced in other cells will still be imposed on the failed cells. Such an incident can result in *voltage reversal* and may reduce the power output from the system and irreversibly damage the MEAs, flow field plates and any stack hardware in electrical contact with the plates.³⁸ It has been observed in stacks with both serial and parallel cells and is a major durability issue.

Voltage reversal can also be caused by fuel starvation at the anode. This can happen when there is a sudden change in fuel demand at start-stop, pressure-drop variations between the cells and poor water management. Figure 2.4 shows the changes in the anode and cathode potential during a *voltage reversal* experiment. When there is insufficient supply of fuel at the anode, the voltage (as indicated by **line a**) will rise to that required to oxidise water in order to sustain the stack current and the cell voltage drops sharply. Such high potentials at the anode will lead to carbon corrosion and dissolution of metal, resulting in anode catalyst layer degradation. Furthermore, the dissolved metal may be transferred from anode to cathode through the membrane, resulting in contamination and reduced catalytic activity at the cathode.

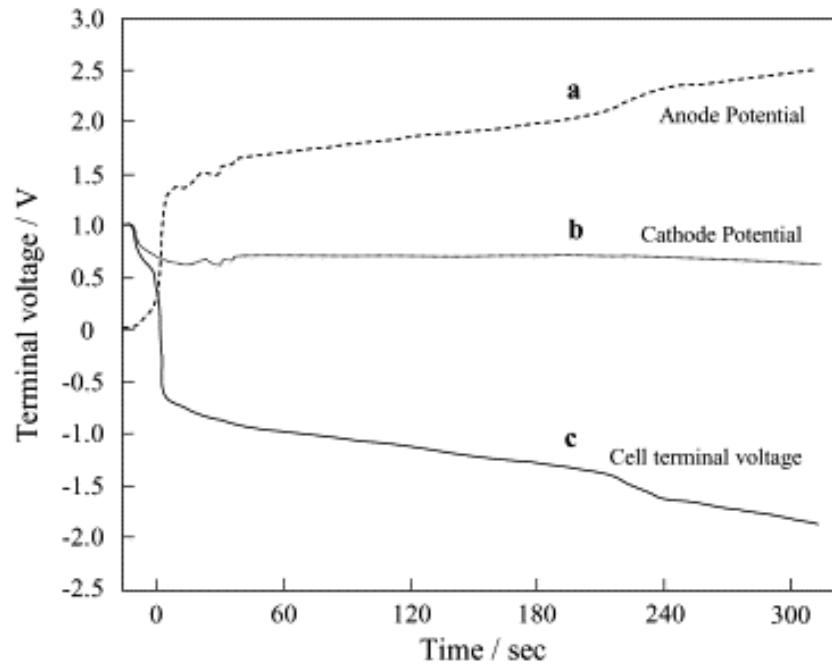


Figure 2.4: Time-dependent changes in the anode and cathode potential during a voltage reversal experiment.³⁹

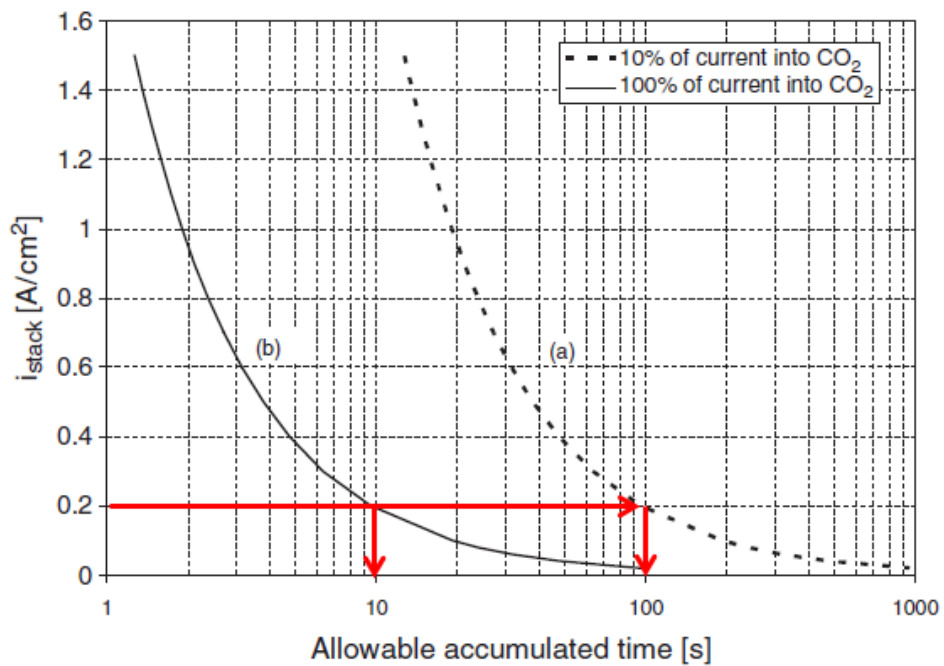


Figure 2.5: Allowable accumulated time during a voltage reversal experiment for a Pt/C catalyst at a carbon loading of 0.2 mg cm^{-2} based on two scenarios: (a) 10% of the cell current is supplied by anode carbon corrosion, and (b) 100% of the cell current is supplied by anode carbon corrosion. Note: red arrows added as guidance.⁴⁰

The extent of degradation on anode catalyst layer as a result of carbon corrosion is significant, which is often overlooked. A fuel cell operating at 0.2 A cm^{-2} would only last for 100 s if 10 % of the current is supplied by carbon oxidation, as highlighted by the arrows in Figure 2.5. In the case of 100% current supplied by carbon oxidation, the fuel cell would only last for 100 s.⁴⁰

Although voltage reversal could be prevented by advanced control strategies, imperfect system control could lead to extensive damage on the anode catalyst layer. The mitigation of the anode degradation from cell reversal could be achieved by developing stable anode electrode structure such as the use of corrosion-resistant support materials and/or the use of an additional oxygen evolution catalyst in the anode.³⁸

2.1.1.1 CO contamination

Due to the high cost and the difficulties associated with hydrogen production and storage, it is not economically practical to run PEMFCs with pure hydrogen, at least in the short term. Therefore, a hydrogen-rich reformat gas offers a more practical solution, although not without a problem. Reformat contains 1-2% CO, which in practice is removed before entering the fuel cell, but a trace amount still remains, which can have a negative effect on the performance of a PEMFC.⁴¹

CO strongly adsorbs strongly on the Pt catalyst surface, blocking much of the active sites for hydrogen adsorption and oxidation, especially for PEMFCs operating at below 100°C . This dramatically lowers the cell potential, making CO poisoning one of the most significant barriers to be overcome in the development of PEMFC systems.^{42, 43}

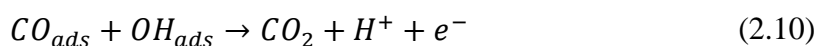
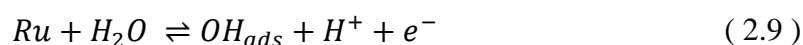
There are a number of methods to overcome CO poisoning:

- Advanced reformer design that is capable of removing the CO completely from the fuel
- Use of CO-tolerant catalysts
- Oxidant bleeding into the fuel feed for the conversion of CO to CO_2
- Use of a composite anode structure whereby the first layer is designed with CO-active catalyst and the CO-free gas then reacts with the second layer of Pt catalyst

- Higher operating temperature
- Use of membranes to separate hydrogen from impurities
- Pulsing cell voltage or current to promote CO removal on the surface

Out of all the methods mentioned above, the use of CO-tolerant catalysts is considered the most efficient and favourable way of solving the CO poisoning problems without adding to the complexity or cost of the system. The most common approach is by utilising Pt with a second metal, such as Ru, Sn, Rh, Mo, Fe, Ni and Pd, in the form of an alloy.⁴⁴ Among these alloys, PtRu is regarded as the most efficient anode electrocatalyst with enhanced CO tolerance.^{45, 46} Although the exact mechanism of CO oxidation from the PtRu surface is still debated, the following mechanisms are widely accepted:

- *Bifunctional mechanism* whereby Ru activates water to donate oxygen-containing species to promote the oxidation of CO on a neighbouring Pt atom.⁴⁷⁻⁴⁹



- *Direct mechanism (ligand/electronic)* whereby Ru alters the electronic interactions of Pt with CO, thereby weakening the Pt-CO bond and lowering the CO electrooxidation overpotential.⁵⁰⁻⁵²

It should be emphasised that CO is adsorbed on both Pt and Ru sites and therefore Ru is also a source of CO_{ads}. In the case of continuous oxidation of dissolved CO, the rate of reaction is lower due to negative reaction order with respect to CO partial pressure. This is when there is a strong adsorption of one reactant (i.e. both CO and OH compete for the same site on both Pt and Ru but CO predominates).

A totally opposite behaviour is observed for Pt₃Sn alloy. The oxidation potential of dissolved CO is shifted negatively with respect to that for PtRu (1:1) by 0.3 V and 0.45 V with respect to that for pure Pt.⁴⁵ However, the oxidation potential for adsorbed CO is in the same region as that for pure Pt. The mechanism for CO oxidation on Pt₃Sn alloys

is not fully established but is believed to be via the bifunctional mechanism.⁵³ Gasteiger et al. proposed that the high CO oxidation activity of Pt₃Sn is due to formation of weakly adsorbed state of CO, which is a consequence of the strong intermetallic bond between Pt and Sn atoms, suggesting that electronic effect also plays a role.⁵⁴ Even though Pt₃Sn alloy system is the most electroactive catalyst for the oxidation of CO, there has been no in-situ study within a fuel cell system to compare its performance with Pt and PtRu. It was reported that a Pt-Ru-Sn ternary system has an even higher CO oxidation activity than the binary systems.⁵⁵

It was reported that Pd alone has poor HOR activity,^{32, 33} the addition of even a small amount of Pt enhances its activity, similar to that of pure Pt.^{56, 57} It has been shown that the presence of Pd increases the CO tolerance of Pt and PtRu.⁵⁷⁻⁵⁹ The effect of Pd as a second metal is different than that of Ru; Pd addition decreases CO coverage on catalyst particles via the electronic effect. The use of Pt-free PdSnO₂ and PdTiO₂ as HOR catalysts has also been reported.^{60, 61} The enhancement was thought to be due to decreased Pd particle size; the oxides increased the dispersion of the Pd metal particles, and hence increased the electrochemically active surface area of the catalyst. Wang et al.⁶² found that the CO oxidation potential of Pd₅Ir in acidic medium was found to be about 0.54 V, which is significantly more negative than that of pure Pt or Pd and in the same range as that of PtRu. In this case, Ir is said to decrease the adsorption strength of CO on Pd and hence increase its CO tolerance.

2.1.2 Methanol Oxidation Reaction

The use of liquid hydrocarbons such as methanol has attracted interest due to advantages such as: easy handling and storage, no need for reforming, possibility of renewable source such as biomass, and high power density for small portable applications such as electronics. The thermodynamic potential for methanol oxidation is 0.02 V (equation (1.4), which is very close to that of hydrogen oxidation. However, this reaction is much slower than hydrogen oxidation. Although the full reaction mechanism is still unresolved, it is well known that methanol oxidation undergoes parallel pathways (Figure 2.6), as first suggested by Breiter,^{63, 64} and confirmed by a number of studies.⁶⁵⁻⁶⁸

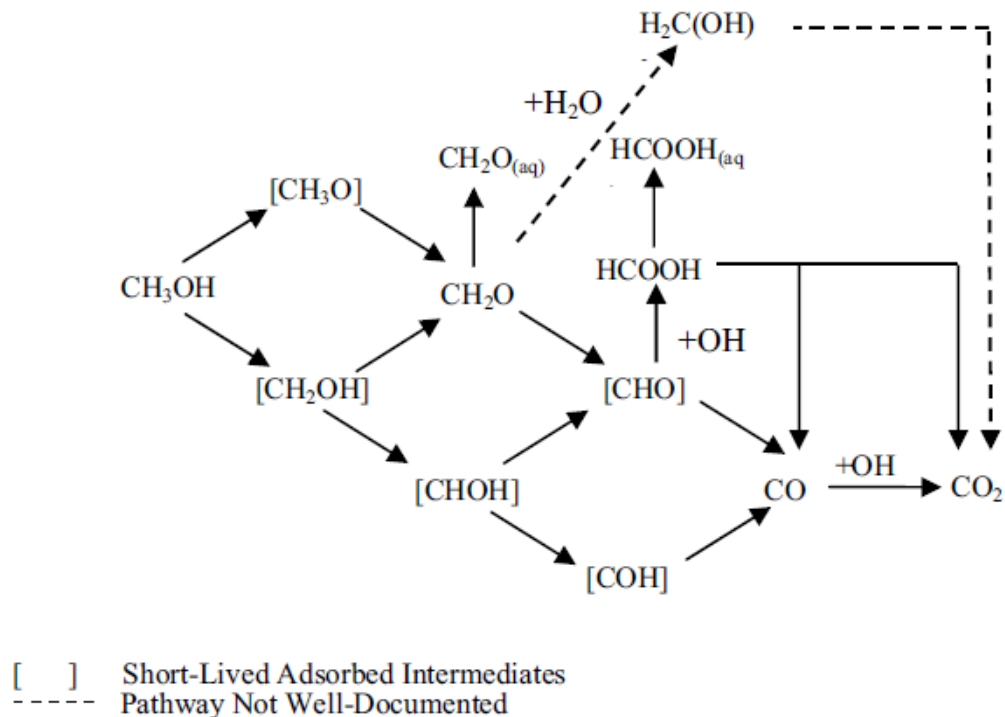


Figure 2.6: Reaction scheme of methanol oxidation reaction, showing all the possible pathways.⁶⁹

In general, a methanol oxidation catalyst is required to:

1. Dissociate the C-H bond: This involves the adsorption of methanol on the electrode and requires several neighbouring sites at the catalyst surface. It is known that hydrogen is adsorbed at low potentials and therefore methanol adsorption can only begin at potentials where enough sites become free from hydrogen. It was suggested that methanol adsorption and dissociation takes place in several steps, forming different adsorbed intermediates, as shown in Figure 2.6. One route leads to the strongly adsorbed CO_{ad} , while the other route leads to weakly adsorbed intermediates, which then generate soluble products (HCOOH , HCHO).
2. Facilitate the reaction of the adsorbed intermediates with some O-containing species to form CO_2 . The role of H_2O chemisorption and OH_{ads} formation is important for efficient removal of adsorbed intermediates.

Like CO poisoning, the most successful binary alloy catalyst for methanol oxidation is PtRu⁷⁰⁻⁷² and it is considered as the benchmark methanol oxidation catalyst. As described in Section 2.1.1.1, PtRu exhibits enhanced tolerance to CO, which is a poisoning intermediate in methanol oxidation reaction, resulting in higher MOR kinetic rate.^{70, 73}

Alloy catalysts other than PtRu were also investigated by a number of authors, particularly those which are reported to have excellent CO tolerance. For example, Pt₃Os was found to give higher current density in cyclic voltammetry and chronoamperometry experiments in comparison to PtRu (1:1).⁷⁴ The enhanced activity may be explained by both bifunctional mechanism and electronic effect. However, the experiment was conducted at low temperature and it was known that Pt rich PtRu catalyst does not give optimum performance at low temperature (<60°C) and therefore it may have not been a fair comparison. Not all CO tolerant catalysts have good MOR activity; for example, PtMo has excellent CO tolerant of Pt but worse MOR performance in comparison to both PtRu and pure Pt.^{75, 76}

The same enhanced CO tolerance was also observed for PtSn^{77, 78} but there has been a mix of reports with regards to its methanol oxidation activity. One study shows that it only has a slightly better performance than pure Pt⁷⁹, but a preliminary chronoamperometry results shows that PtSn has a higher mass specific activities at 0.5 V compared to PtRu and PtRuSn.⁸⁰ In contrast, an experiment by Gotz and Wendt at 110°C found that the order of activity for the above catalysts was PtRu > PtW > PtMo > Pt > PtSn.⁸¹ However Liu et al. reported increased power outputs for PtSn compared to Pt, although no direct comparison with PtRu was made.⁸² As all the catalysts were synthesised using different techniques, it is possible that the synthesis method had an impact on performance.

The performance of Pd-based catalyst for methanol oxidation in acidic environment is not as extensively studied. However, in alkaline environment, the addition of a second and third element has been shown to increase its performance.^{83, 84} Again, direct comparison with PtRu is usually missing from these studies.

2.2 Cathode catalyst layer

In comparison to HOR, the ORR is a relatively complex reaction involving 4 electrons and with a number of elementary steps and strongly-bound reaction intermediates. As a result, the exchange current density is one order of magnitude lower than that of the HOR.

The exact mechanism of the ORR is still not well understood and is thought to depend on the nature of the electrode material, catalyst and electrolyte. In aqueous acidic solutions, the ORR occurs mainly by two pathways:

1. The direct 4-electron reduction pathway from O_2 to H_2O :



2. The 2-electron reduction pathway from O_2 to H_2O_2 :



In fuel cells, the direct 4-electron pathway is highly preferable as it does not involve peroxide species which may accumulate in the electrolyte. However, it involves a number of steps in which O_2 has to be dissociated at the surface and recombined with hydrogen ions to form H_2O . Consequently, the reaction is very slow and a catalyst is needed.

At the current state-of-the-art technology, platinum supported on carbon black is the most efficient and practical catalyst. Figure 2.7 shows the ORR ‘volcano plot’ of various transition metal catalysts. Pt evidently has the highest activity with oxygen binding energy of $\Delta E_{O(Pt)} = +1.57$ eV. However, in-silico density functional theory (DFT) calculations shown that the optimum binding energy for maximum ORR activity is around +1.8 to +2.0 eV. Therefore, there is a considerable scope for improving ORR kinetics through the development of catalysts with oxygen binding energies 0.3 to 0.4 eV more positive than that of Pt.⁸⁵

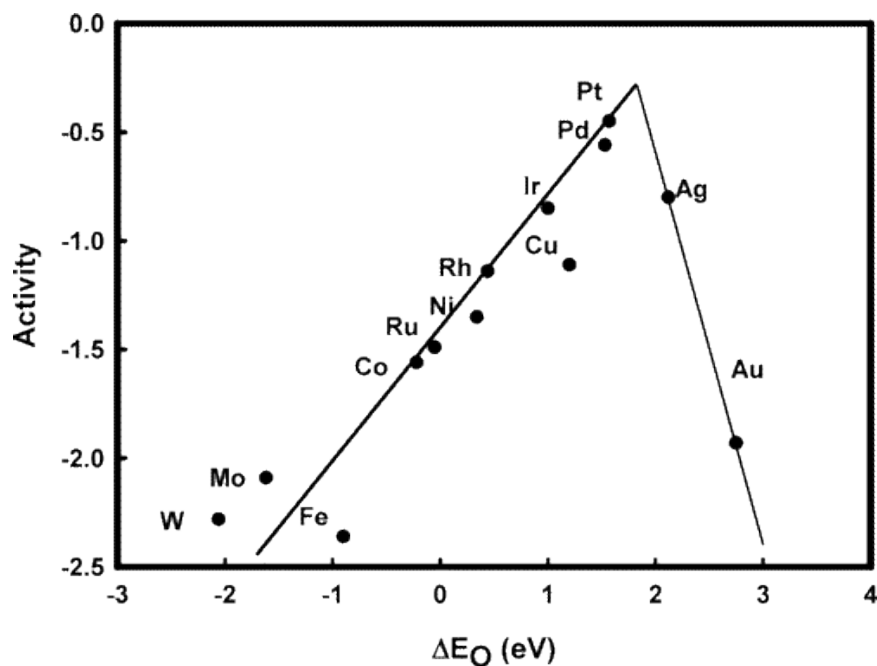


Figure 2.7: Volcano plot of oxygen reduction reaction activity plotted as a function of the oxygen binding energy (ΔE_O).⁸⁵

The most common strategy to reduce Pt catalyst loading on the cathode is by alloying it with other metal elements. The activity enhancement can be explained by the following mechanisms:

1. *The structural effect.* It was proposed that smaller Pt-M bond distances (where M is a transition metal) would provide favourable sites for the dissociative adsorption of oxygen.⁸⁶ Consequently, many studies demonstrated that Pt-M alloy, with M having smaller atomic sizes than Pt, will enter the crystal structure of Pt through substitution.⁸⁷ This results in lattice contraction and hence a decrease in Pt-M bond distance
2. *The OH_{ads} inhibition effect.* ORR reaction intermediate species such as OH or OOH are considered to be poisoning species. Pt alloys inhibit the formation of these poisoning species and thereby increase the activity of the ORR.¹⁹

3. *The electronic effect.* Alloying with transition metals cause Pt to share its *d*-electrons with the unfilled *d*-orbitals of the base metals, increasing its *d*-band vacancy or *d*-band centre, as explained in Section 2.1. This effect is considered to be the most significant in determining binding energy of adsorbates on Pt-alloy surfaces. Thus ORR activity can be enhanced if the Pt alloy can counterbalance between two opposing effects: the relatively strong adsorption energy of O₂ and reaction intermediates, and the relatively low surface oxide coverage.

Theoretical calculations and experiments have shown that Pt-M alloys supported on carbon, where M=Fe, Co, Ni, have higher activity than pure Pt.^{85, 88, 89} With regard to unsupported Pt-alloys, the most impressive performance was observed when using Pt_{0.7}Ni_{0.3}, Pt_{0.6}Co_{0.4} and Pt_{0.5}Fe_{0.5} with kinetic current densities over 10, 15, and 20 times higher than that of pure Pt.⁹⁰⁻⁹² Another advantage of alloying is it may improve catalyst stability as base metals help suppress Pt dissolution and sintering, which are the major causes of performance loss in PEMFC and described in detail below (Section 2.2.1). It was found that Pt-Co has better performance than Pt in an MEA cycling test (2400 cycles).⁹³ This may be attributed to the base metals hindering Pt mobility on carbon. In another experiment, Pt modified with gold (Au) clusters was shown to have better stability, with only 5 mV degradation and almost no loss of Pt surface area after 30,000 cycles, compared to 39 mV degradation and 45% surface area loss in Pt catalysts⁹⁴. It was found that the higher oxidation potential of Pt-Au was the major mechanism for the stabilisation effect.

Despite the positive effects of Pt-M alloys, chemical leaching of base metal elements has a detrimental effect on fuel cell performance.⁹⁵ Metal cations have a stronger affinity to the sulfonic groups in the membrane than do protons, poisoning the ion-exchange sites that are necessary for proton transfer. The effect of leaching includes increased membrane and catalyst layer resistance, decreased oxygen diffusion, and membrane degradation. In addition, it also caused the loss of the intrinsic alloying structure. Watanabe et al. found that at room temperature, the dissolution of base metals (Fe, Co, or Ni) gave rise to a Pt skin within a few monolayers of the alloy surface, modifying the electronic structure somehow and increasing its ORR activity.⁹⁶

However, at typical PEMFC operating temperature ($>60^{\circ}\text{C}$), excessive dissolution of the base metals occur, reducing the ORR activity.

2.2.1 Cathode catalyst layer degradation

Cathode catalyst layer degradation is mainly caused by loss in the electrochemical surface area of Pt or Pt alloys. The main degradation mechanisms can be broadly identified as (i) Pt dissolution; (ii) Pt nanoparticle migration and agglomeration; and (iii) carbon corrosion. These processes are interrelated and will be discussed below:

1. Pt dissolution

The dissolution of Pt in cathode catalyst layers under PEMFC operating conditions has been widely investigated and documented.⁹⁷⁻⁹⁹ It is particularly pronounced during rapid increases in cell voltage from around 0.6 V to OCV, in response to sudden reduction in current demand on the fuel cell stack (e.g. start-up and shut-down processes).

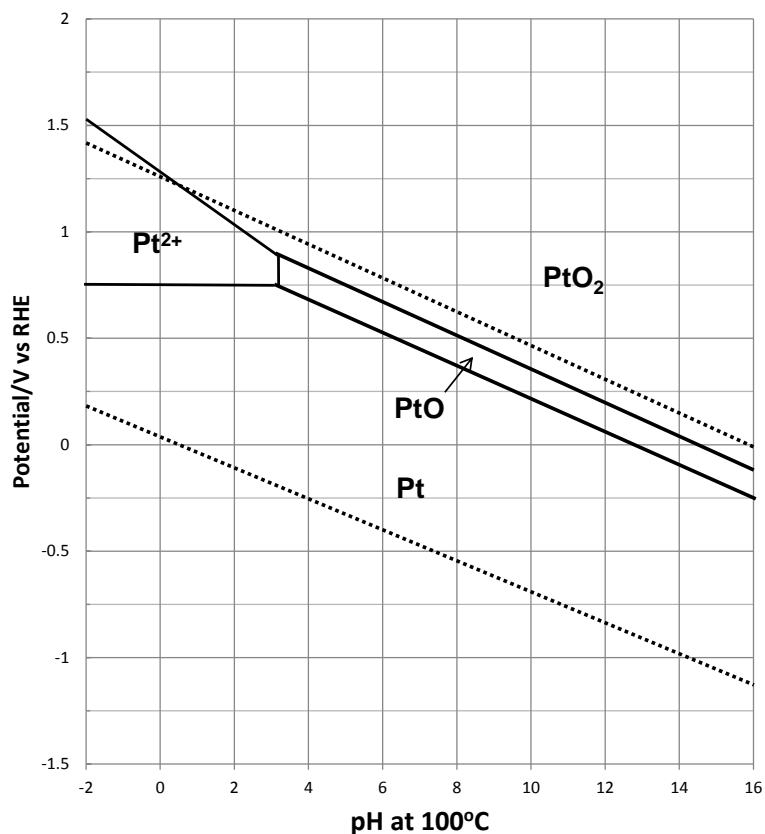


Figure 2.8: Regions of stability for platinum vs potential and pH (Pourbaix Diagram). Diagram reproduced from reference 100.¹⁰⁰

The PEMFC cathode presents an acidic and highly oxidative environment. The thermodynamic behaviour of a platinum bulk material as a function of electrolyte pH and electrode potential is guided by the potential–pH diagram, also known as the Pourbaix diagram, as shown in Figure 2.8.¹⁰¹ The Pt Pourbaix diagram indicates that at low pH, Pt will dissolve above a potential of around 1.0 V according to the surface oxidation and oxide reduction processes below:



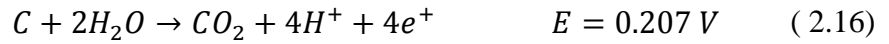
The dissolved Pt (Pt^{2+}) may be flushed out from the cell, particularly at high current densities where the flow of water from the cathode is large. Pt dissolution also caused the loss of electrochemical surface area, and hence activity, due to Pt^{2+} migrating into the ionomer membrane and/or re-depositing at the surface of existing Pt nanoparticles to form larger particles via Ostwald ripening.

2. Pt migration and agglomeration

Pt particles supported on carbon are not stationary, but can migrate across the carbon support and agglomerates to form bigger particles, resulting in loss of active surface area. The particle growth decreases the total surface tension, which is the main driving force of this process. Therefore, the interaction of Pt with carbon, as well as the interaction of Pt precursor with carbon during the catalyst formation, is crucial to the stability of the catalyst. Several strategies have been adopted to inhibit Pt migration and agglomeration such as the use of stable catalyst support, and modification of Pt deposition method to enhance metal-support interaction.

3. Carbon corrosion

Despite being the most widely used catalyst support for PEMFC, carbon support is actually thermodynamically unstable at PEMFC operating conditions. Electrochemical carbon support corrosion proceeds as in:



The reaction is almost negligibly slow at the potential at which the fuel cell operates (<1 V), provided it is constant throughout the operation. However, automotive PEMFC systems experience significant dynamic operating conditions involving an estimated 300,000 voltage cycles over the lifetime of a vehicle (5500 h), as shown in Figure 2.9.⁴⁰ Some of the conditions could result in an increase in potentials at both the anode and cathode, thus, accelerating the carbon corrosion process with detrimental effects on PEMFC performance.

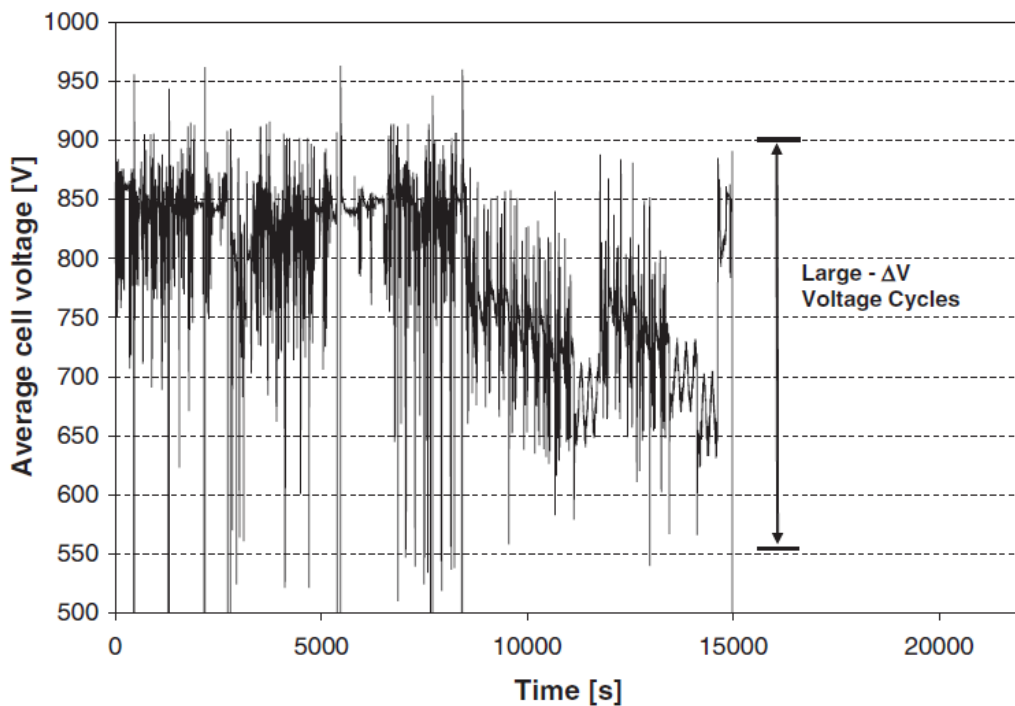


Figure 2.9. Typical automotive fuel cell vehicle drive cycle showing average cell voltage over time.⁴⁰

As carbon support corrodes, Pt nanoparticles agglomerate into larger particles and/or detach from the support material, consequently reducing the electrochemical surface area (ECSA) and catalytic activity. In the case of severe corrosion, the porous structure of the catalyst layer can be destroyed, increasing the mass transport resistance due to the blockage of gas access paths. Figure 2.10 shows a plot of the measured voltage loss versus carbon weight loss at 0.8 A cm^{-2} for a variety of carbon support materials. It shows that electrodes with commercial carbon support (Ketjen black and Vulcan) start

to degrade after just 5% loss in carbon weight. In addition, some studies suggest that carbon corrosion rate can be accelerated by the presence of Pt.^{102, 103}

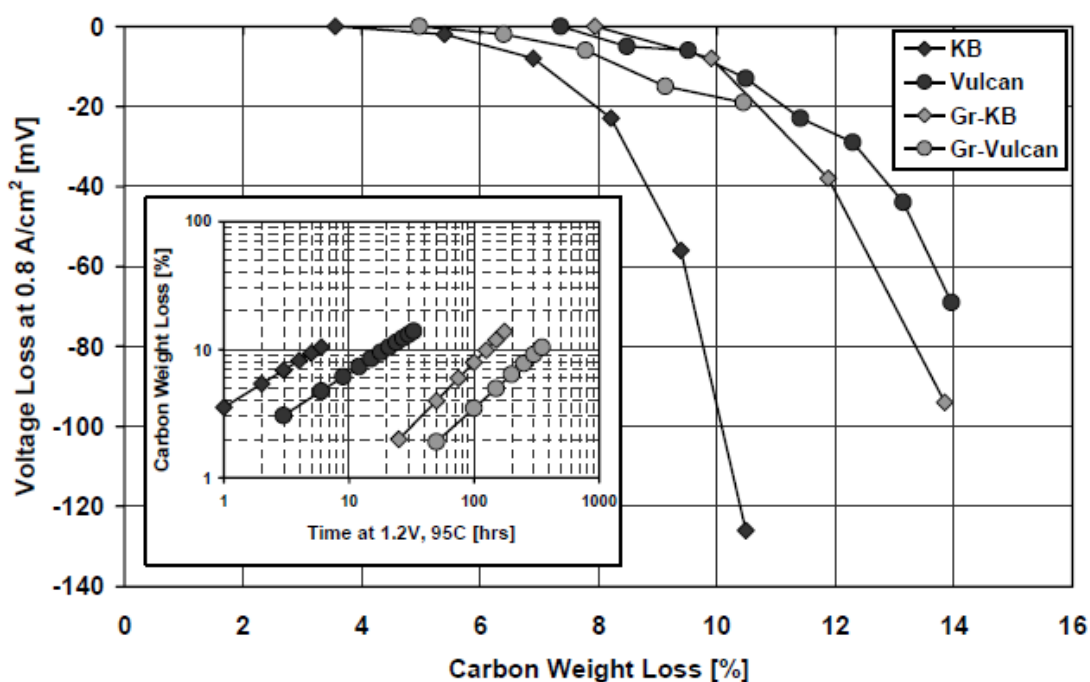


Figure 2.10: Cell voltage loss versus carbon weight loss measured at 0.8 A cm^{-2} for KB (Ketjen black), Vulcan, Gr-KB (Graphitized Ketjen black) and Gr-Vulcan (Graphitized Vulcan XC-72C). The inset shows the carbon weight loss versus time at 1.2 V.¹⁰⁴

To solve this issue, much effort has been directed towards the development of corrosion resistant catalyst supports. In recent years, numerous conductive ceramics or oxide containing composites have been studied; these include ITO, WO_3 , TiO_2 , CeO_2 and $\text{CeO}_2\text{-ZrO}_2$, WC, Ti_4O_7 , NbO_2 or Nb_2O_5 , TiN, TiB_2 and SiC.¹⁰⁵⁻¹¹⁵ Various graphitized carbon support materials with special pore structures have also been explored, such as carbon nanotubes (CNT), nanofibers (CNF), nanohorns (CNH) and nanocoils (CNC).¹¹⁶⁻¹²⁴ The graphitic structure has been shown to be effective at increasing durability due to structural electronic defects that yield higher interaction energy with the metal nanoparticle. However, its inert surface has a limited amount of active sites where the Pt nanoparticle can stably anchor. It is clear that a reasonable balance between catalyst dispersion and catalyst-support interaction is necessary to meet the fuel cell performance requirement.

2.2.1.1 Cathode failure mode

The effect of carbon corrosion on the anode is described in Section 2.1.1. The following explains the operating conditions which may cause the cathode potential range to exceed the stability region of the catalysts and carbon support:

1. *Steady-state operating conditions*

At open circuit voltage condition, i.e. when no current is drawn from the stack, the cathode potential increases to approximately 0.90 - 0.95 V. This can occur just before system shut-down and immediately after start-up, as well as in battery-fuel cell hybrid systems in which the battery provides the power during low power conditions.

2. *Transient operating conditions*

In an automotive PEMFC system, the cell voltage typically changes from 0.55 to 0.90 V. Even though one would expect little carbon corrosion at such low potentials, potential cycling can accelerate the carbon corrosion process, which is attributed to the repeated oxidation and reduction of platinum and/or carbon surface groups during the cycles.¹²⁵ It was estimated that approximately 8% carbon weight is lost over the life of a vehicle, at which electrode thinning and significant cell voltage losses can occur.⁴⁰

3. *Start/stop operating conditions*

An automotive PEMFC system undergoes an estimated 38,500 start/stop cycles over the life of a vehicle.⁴⁰ During shutdown, ambient air will diffuse into the anode originally filled with hydrogen, whereas during start-up hydrogen gas is fed into the anode initially filled with air. In both cases, an H₂/air front is created at the anode, as shown in Figure 2.11. The resulting temporary coexistence of two gases with different equilibrium potentials drives the potential in certain areas of the electrode to values substantially exceeding 1 V which can cause severe fuel cell degradation by corrosion of the carbon support material.

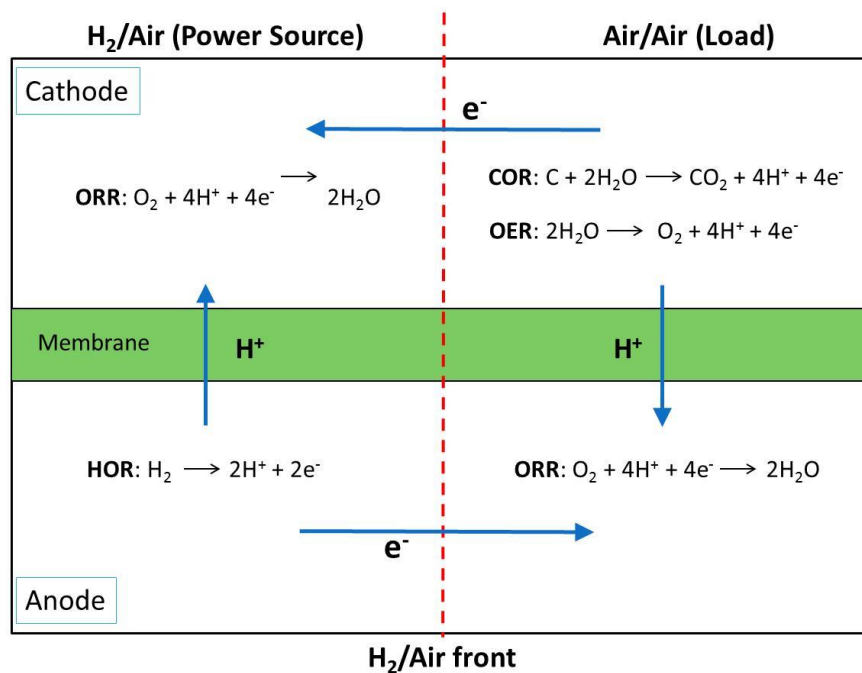


Figure 2.11: The schematic diagram of a PEMFC start-up experiencing start-up/shutdown and all electrochemical reactions involved. ORR: oxygen reduction reaction, COR: carbon oxidation reaction, HOR: hydrogen oxidation reaction and OER: oxygen evolution reaction. Reproduced from reference 104.¹⁰⁴

The mechanism leading to the increase in the potential is illustrated in Figure 2.11. The H₂/air segment on the left-hand-side generates a voltage which polarises both electrodes in the air/air segment (right-hand-side). A *reverse current* flows internally in the electrodes through the H₂/air and air/air segments such that the current in the air/air segment becomes equal to the current generated by the H₂/air segment. In other words, the H₂/air segment acts as a power source and the air/air segment acts as a load. As a consequence, the cathode reaction in the air/air segment proceeds as carbon oxidation and water hydrolysis, balanced by the ORR current on the opposing anode side.

In one start-up/shutdown experiment using a conventional carbon-support MEA with H₂/air front at the anode and air at the cathode, it was observed that the degradation rate at the cathode was about 1500 μV per cycle at 1.5 A cm⁻².¹⁰⁴ After 100 start-up/shutdown cycles, the carbon support was corroded to the point that the cell was unable to hold a positive voltage at 1.5 A cm⁻².

Several strategies have been developed to mitigate start/stop induced carbon corrosion. This includes the application of an external load to reduce voltage generated by the H₂/air segment; an increase in gas flow rate during start-up/shutdown to reduce the H₂/air front time; the use of an active oxygen evolution catalyst at the cathode to promote water hydrolysis; or the use of an alternative HOR catalyst which inhibits the oxygen reduction reaction.. Although these approaches may help to reduce carbon corrosion, their practicability depends strongly on the application of the PEMFC. Therefore, a combination of system operation mitigation strategies and corrosion resistant support material is required to meet the DOE durability targets, especially under very dynamic automotive fuel cell operation strategies.

2.3 Alternative Carbon Support

Catalyst activity and durability depends on Pt particle size and dispersion (which can be affected by the support material), as well as the interaction between the catalyst particle and the support.^{126, 127} Therefore, catalyst support plays a crucial role for optimal catalyst performance. The requirements for catalyst support materials can be summarised as: (i) high surface area for maximum catalyst dispersion, (ii) high electrochemical stability under fuel cell operating conditions, (iii) high conductivity, and (iv) porous structure for reactant gas access to the electrocatalysts.

Some commercial carbon black support materials currently used as fuel cell electrocatalyst supports include Vulcan XC-72R (Cabot Corp, 250 m² g⁻¹), Shawinigan (Chevron, 80 m² g⁻¹), Black Pearl 2000 (BP2000, Cabot Corp, 1500 m² g⁻¹), Ketjen Black (KB EC600JD & KB EC600J, Ketjen International, 1270 m² g⁻¹ and 800 m² g⁻¹, respectively) and Denka Black (DB, Denka, 65 m² g⁻¹). Despite their high surface area, carbon black has dense structure leading to mass transfer limitations and low Pt utilisation. In addition, carbon black is known to undergo electrochemical oxidation under fuel cell operating conditions, as described in Section 2.2.1.

A number of alternative carbon based materials have been investigated as catalyst supports for PEMFCs, such as carbon nanotubes (CNT), carbon nanofibers (CNF), graphene, and mesoporous carbon. These materials have high surface area, good electrical properties and theoretically are more electrochemically stable due to their

graphitic nature. The following sections summarise recent progress in these materials and discuss the problems and challenges associated with them.

2.3.1 Carbon nanotubes (CNT)

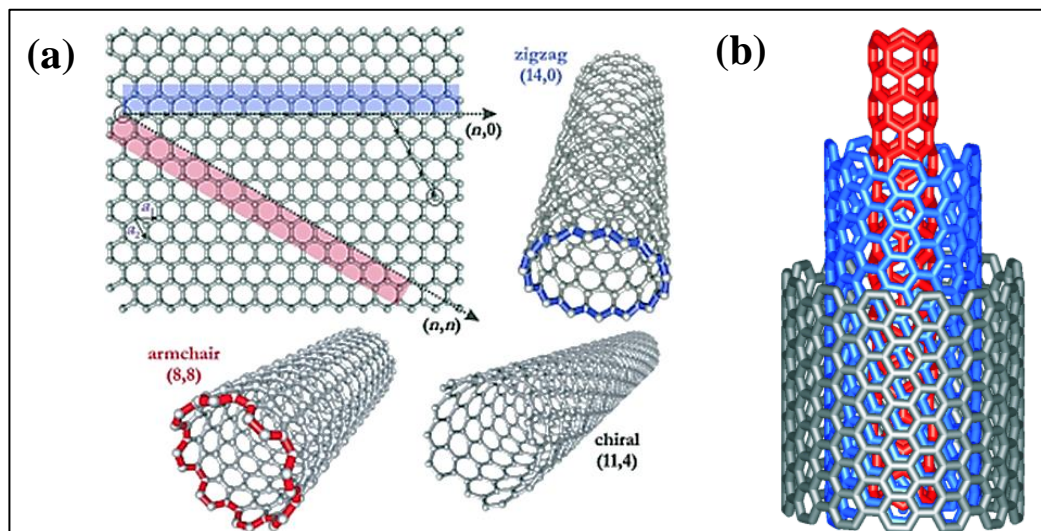


Figure 2.12: (a) Schematic illustrations of the three different structures of single-walled carbon nanotubes (SWCNTs). (b) Structure of a multi-walled carbon nanotube (MWCNT) made up of a three shells of differing chirality.¹²⁸

Carbon nanotubes are 3-D cylindrical nanostructures made up by single sheets of hexagonally arranged carbon atoms. They can be classified into single-walled (SWCNTs) or multi-walled (MWCNTs). The structure of SWCNTs is characterised by a chiral vector (m, n) : armchair ($n = m$), zigzag ($n = 0$ or $m = 0$) or chiral (any other n and m), as shown in Figure 2.12a. SWCNTs are typically semiconductors with a band gap inversely proportional to the nanotube diameter, except armchair SWCNTs which are metallic and SWCNTs with $n - m = 3k$ (where k is a non-zero integer) which are semiconductors with a small band gap. MWCNTs consist of a concentric set of cylinders with a spacing of 0.34 nm between the cylindrical walls (Figure 2.12b), resulting in a structure with relatively larger diameter than SWCNTs. MWCNTs are more conductive whereas SWCNTs have larger surface area.

CNTs have been widely studied as catalyst supports for H_2/O_2 PEMFCs or direct methanol fuel cells. They have been shown to have better performance than conventional carbon based catalysts.¹²⁹⁻¹³⁵ For example, Yan and co-workers found

improved polarisation behaviour for CNT-based MEA throughout the whole potential range compared to conventional Pt/C MEA.¹²⁹ Matsumoto et al. demonstrated that CNT-based MEA could reduce Pt usage by 60% in H₂/O₂ PEMFCs.¹³⁵ The higher performance was attributed to the unique structure of CNTs which enhances the transport of gas reactants to the catalysts, as well as its high surface area which allows good dispersion of Pt particles on the surface.

There are very few publications regarding the durability of CNTs as a catalyst support for PEMFC. Wang and co-workers found almost 90% loss of ECSA for Pt/C, while only 37% loss was observed for Pt/CNT after 168 h of oxidation treatment.¹³⁶ Shao et al. found that Pt/CNT degrades by 26.1% in terms of ECSA, compared to 49.8% for conventional Pt/C during an accelerated degradation test.¹³⁷ In another study using voltammetric and XPS analysis, Shao et al. found that CNTs are more resistant to electrochemical oxidation than carbon black, which they attributed to the unique closed structure of the CNTs. Carbon black, on the other hand, contains abundant dangling bonds and defects which are susceptible to the formation of oxides.¹³⁸ Studies by Li et al. showed that only the outside layers of MWCNTs were damaged when attacked by oxidative acids, which was attributed to the presence of defect carbons at the surface of MWCNTs. However, further in-depth oxidation must attack the intact basal planes beneath the defect carbons, which is difficult.¹³⁹ It is well-known that carbon supports with graphitic structure are more electrochemically stable. In a study comparing highly graphitized MWCNTs with normal MWCNTs, it was found that increasing the degree of graphitization leads to the increasing strength of π -sites (sp²-hybridized carbon) on the support. These π -sites act as anchoring sites for Pt and strengthen the metal-support interaction.¹⁴⁰ Although further investigations are needed, these studies suggest that CNTs could potentially provide much higher durability than carbon black.

Despite the advantages offered by CNT, there are still many challenges for its application in PEMFC. At current stage of technology, CNT synthesis techniques are costly and not suitable for large scale productions. Furthermore, due to the complex synthesis procedures, the CNT quality varies from one supplier to another and even from the same supplier at different times, making them unreliable for large-scale applications.¹⁴¹

2.3.2 Carbon nanofiber (CNF)

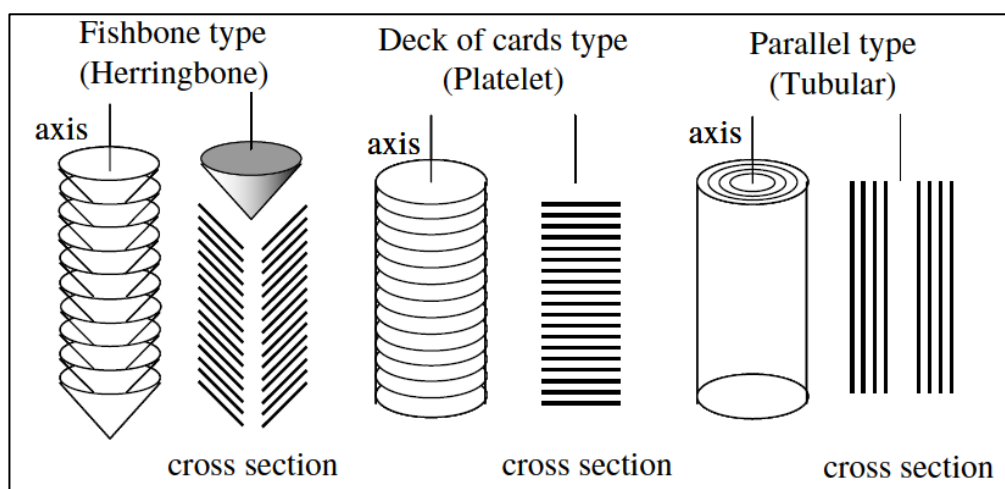


Figure 2.13: Schematic representation of the three structures of CNFs.¹⁴²

Carbon nanofibers (CNFs) consist of graphite sheets aligned in specific directions that are determined by the growth process. There are mainly three types of CNFs: herringbone, platelet, and tubular, as shown in Figure 2.13. CNTs have very thin or no hollow cavity and the diameters may go up to 500 nm and the length can go up to a few millimetres. The BET (N_2) surface areas range from 80 to 200 $m^2 g^{-1}$, depending on the structure.

The performance of CNF-based catalyst in fuel cells is well documented.¹⁴³⁻¹⁴⁶ Li et al. found that CNF-based MEA demonstrates higher PEMFC performance than carbon black-based MEA.¹⁴³ In addition, it was found that CNFs are able to maintain continuous electrical conduction path, thus high Pt utilisation, which is attributed to its unique high aspect ratio (length to diameter ratio). This implies that it is possible to reduce Pt loading in MEA using CNF as catalyst support. Unlike the CNTs (and any conventional graphite materials) where the basal plane is exposed; only the edge planes are exposed in CNFs. These edge planes provide potential anchoring sites for catalysts, leading to high dispersions of Pt nanoparticles. It was shown that 5 wt% Pt supported on platelet and ribbon type CNF, which expose mainly edge sites to the reactant, displayed comparable methanol oxidation activities to that of 25 wt% Pt on Vulcan carbon.¹⁴⁷ Furthermore, the authors found that catalysts supported on CNFs are less susceptible to CO poisoning which is believed to be linked to the fact that the metal

particles adopt specific crystallographic orientations when dispersed on the highly tailored graphite nanofiber structures. The enhancement in methanol oxidation activities in CNF-based catalysts are also supported by other studies.^{148, 149}

Like CNTs, the durability of CNF-based catalysts is less studied. Anderson et al. found that Pt supported on CNF exhibited 29% increase in ECSA after 5000 cycles (0 – 1.6 V). In comparison, Vulcan based electrode showed 41% decrease in ECSA.¹⁵⁰ Durability studies by Kang et al. showed that CNF supported PtRu anode has higher chemical and electrochemical stability compared to a commercial PtRu catalysts in DMFC.¹⁵¹

2.3.3 Ordered mesoporous carbon (OMC)

Ordered mesoporous carbon (OMC) materials have well-ordered porous structure, providing high surface area and conductivity. OMCs are prepared either by using ordered mesoporous silica templates or by templating triblock copolymer structures and the structure can be tailored by the control of synthesis parameters. For example, the BET surface area can be altered from 200 to 2000 m² g⁻¹ by changing the carbon precursor and synthesis conditions. More importantly, the three-dimensional porous structure has been shown to improve the diffusion of reactants and by-products, making it attractive as a catalyst support material.¹⁵²

The first report of the use of OMC as catalyst support can be attributed to Ryoo et al.¹⁵² The authors found that Pt supported on OMC with a BET surface area of 2000 m² g⁻¹ exhibited superior electrocatalytic mass activity toward oxygen reduction compared to Pt supported on conventional carbons. Since then, a large number of studies followed. Generally, all OMC supported catalysts presented higher metal dispersion and higher catalytic activity, both for oxygen reduction and methanol oxidation, than carbon black supported catalysts.¹⁵³⁻¹⁵⁸ Pore morphology was found to play an important role on the electrochemical performance. Song et al. prepared two kinds of mesoporous carbon materials; one is a highly ordered structure mesoporous carbon and the other is wormhole-like mesoporous carbon with a disordered three-dimensional nano-network structure. Both materials have similar pore volume, BET surface area and mesopore size but it was found that Pt on ordered structure mesoporous carbon has higher electrocatalytic activity than Pt on wormhole-like mesoporous carbon.¹⁵⁹

Limited reports have been made on the durability of OMC-based electrode. Due to the high surface area of OMC, it is expected that it is more susceptible to corrosion. One strategy is by increasing the graphitization degree of OMC. A highly graphitic ordered mesoporous carbon synthesised using a soft template was found to have better corrosion resistance than Vulcan.¹⁶⁰ However, graphitization decreases the porosity and surface area of carbon materials.

2.3.4 Graphene and Graphene oxide (GO)

Graphene, dubbed the next ‘wonder material’, was first discovered in 2004 by Geim et al.¹⁶¹ It is the thinnest known material, in the form of an atomically thin sheet of hexagonally arranged carbon atoms. Despite being atomically thin, it is stronger than steel and has excellent electrical conductivity. As such, it is widely studied for various applications including fuel cell catalysts and catalyst supports.

Theoretical calculations have shown that the highest possible surface area for a single layer graphene is $2630 \text{ m}^2 \text{ g}^{-1}$.¹⁶² However, the synthesis process is such that the product often consists of a small portion of single layer graphene and large quantities of thin graphite flakes (few to multi-layer graphene). Therefore, in a real system, the surface area is much lower due to the overlap of graphene sheets. The surface areas reported in the literature range from 270 to $1550 \text{ m}^2 \text{ g}^{-1}$ depending on the preparation route and the number of layers, but large variations were also observed within the same batch.¹⁶³

The use of a single graphene sheet as a catalytic support has not yet been reported; however, some promising results have already been obtained with ‘few-layer graphene’. It was reported that Pt or Pt-alloy catalysts supported on graphene nanosheets have high activity toward oxygen reduction and alcohol oxidation.¹⁶⁴⁻¹⁷³ Studies also shown that Pt/graphene exhibited high CO tolerance and electrochemical stability compared to a commercial catalyst.^{165, 172, 174}

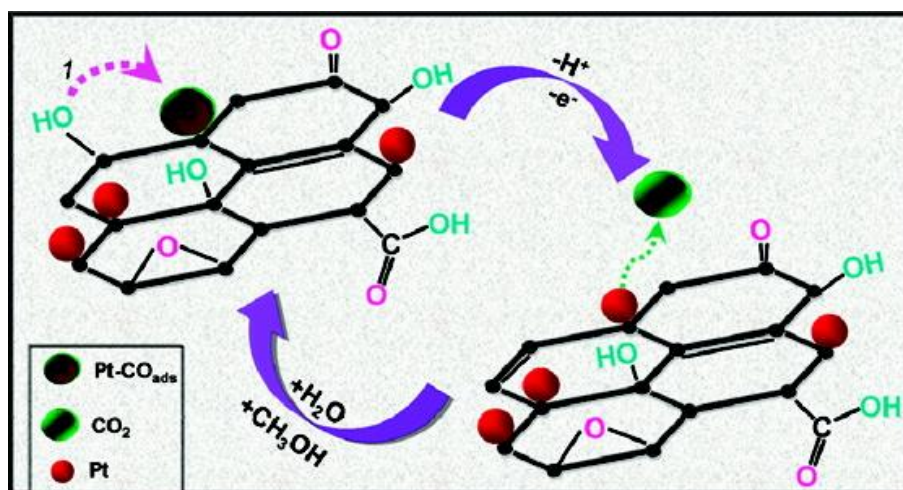
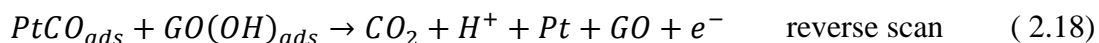
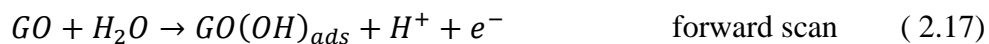


Figure 2.14: Schematic diagram explaining the conversion of adsorbed CO_{ads} species to CO_2 on Pt/GO catalysts. Diagram adapted from reference 175.¹⁷⁵

Graphene oxide (GO) has also drawn a lot of interest and attention due to its hydrophilicity and mechanical strength. GO has lower conductivity compared to graphene but it is chemically ‘tunable’, making it attractive for applications as catalyst support in fuel cells. The oxygen functional groups on the graphene structure create defects and edge planes on the surface which act as nucleation and anchoring sites for metal nanoparticles. This results in small particle size and good particle distribution leading to high ECSA and mass activity.¹⁷⁵⁻¹⁷⁹ The enhanced CO tolerance was attributed to the presence of covalently bonded oxygen functional groups and possibly a bifunctional mechanism between Pt and the GO support, as shown in Figure 2.14.¹⁷⁵ The hydrophilicity of GO promotes water activation, which readily oxidizes the adsorbed CO on Pt. The proposed mechanism is as follows:



Unfortunately, surface oxygen functional groups on carbon are also known to reduce the durability of fuel cell catalysts by promoting carbon corrosion.⁹⁹ Additionally, the complex synthesis methods mean that it is not yet suitable for large scale productions.

2.3.5 Graphitic Carbon Nitride

A growing body of literature suggests that the presence of nitrogen in carbon supports improves durability, as well as enhancing the intrinsic catalytic activity for both oxygen reduction reaction (ORR) and methanol oxidation reaction (MOR).¹⁸⁰⁻¹⁸⁵ The incorporation of nitrogen into carbon leads to a reduction in detrimental surface oxygen groups and thus provides enhanced tolerance towards oxidation.¹⁸⁶ The role of the N-surface species in catalytic enhancement is less studied and has only been hypothesized based on experimental observation and physicochemical reasoning. For example, it was suggested that C-N defects near the catalyst-particle interface adsorb oxygen containing intermediates that would otherwise block catalyst active sites, and thereby facilitate their removal and increase the rate of electrochemical reaction via bifunctional mechanism, as shown in Figure 2.15.^{186, 187} It has been shown that the N-dopant alters the catalyst electronic structure, resulting in a higher binding energy, which may decrease the specific interaction between the Pt nanoparticles and poisoning intermediates.¹⁸⁸ This is further supported by an X-ray photoelectron spectroscopy (XPS) study and theoretical calculations, where it was observed that Pt nanoparticles nucleate strongly and experience a strong ‘tethering’ effect to N atoms.^{189, 190} N-doped carbon materials also have higher specific capacitance, suggesting the presence of additional charged species within the Helmholtz layer, which might provide sites for surface groups to participate in the removal of strongly adsorbed poisoning intermediates.¹⁹¹

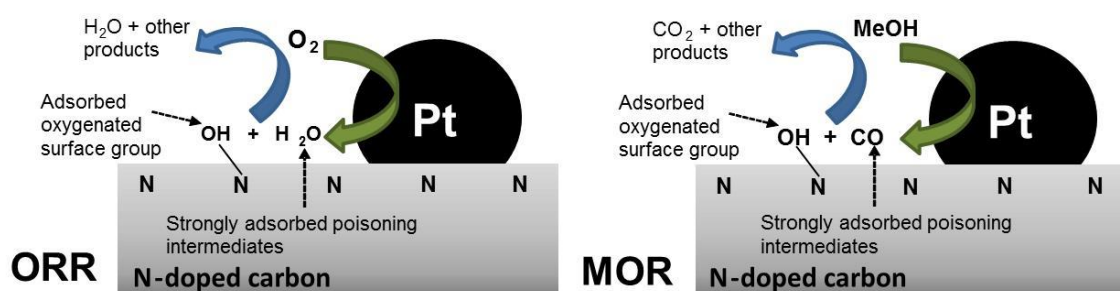


Figure 2.15: Schematic diagram of possible bifunctional ORR and MOR mechanisms involving oxophilic C–N defects near Pt/C catalyst. The adsorbed oxygen containing surface species facilitate reaction of poisoning intermediate reaction species that would otherwise block

*catalyst active sites, thereby increasing electrochemical reaction. Diagram reproduced from reference 161.*¹⁸⁶

The high electrocatalytic activity of nitrogen doped CNT was first reported by Dai et al.¹⁹² and was then confirmed by other studies.¹⁹³⁻¹⁹⁵ It was also reported that nitrogen doped OMC with moderate nitrogen content provided a high surface area and graphitic framework, leading to high electrocatalytic activity and excellent long term durability.^{196, 197} Nitrogen doped graphene (N-G) introduce disorders and defects which act as nucleation and anchoring sites for metal nanoparticles and have been shown to enhance ORR activity.^{198, 199} In addition, the incorporation of nitrogen in the C-backbone increases the conductivity. MEA fabricated using Pt/N-G as the ORR catalyst was shown to exhibit higher power density than MEA fabricated using Pt/graphene.²⁰⁰

Given the potential of N-doped carbon materials, graphitic carbon nitride could be a suitable candidate as a catalyst support for fuel cells. Polymeric solids with high N:C ratios formed by reactions of nitrogen-rich molecules were first reported by Berzelius and later studied by Liebig, Franklin, Pauling and others.^{201, 202} A fully condensed end member has the composition C_3N_4 with a planar structure related to graphite or graphene. However, most graphitic carbon nitrides are composed of C and N, along with residual amounts of H, and they are attracting new interest due to their unique structural and optoelectronic properties. The structures are based on triazine (C_3N_3) or heptazine (C_6N_7) ring units linked by -N= or -NH- bridges to form sheets or zigzag chains of monomer units linked by hydrogen bonds to give a 2D array. Typical examples include Liebig's melon, melem, or highly condensed $C_xN_yH_z$ graphitic structures formed by continued elimination of NH_3 component (Figure 2.16). Recent discussions of graphitic carbon nitride structures and their properties have been based mainly on polymerized heptazine models that are shown to more thermodynamically stable,²⁰³⁻²⁰⁵ but structures based on condensation of s-triazine rings can also be produced under different synthesis conditions and both structure types may be present.

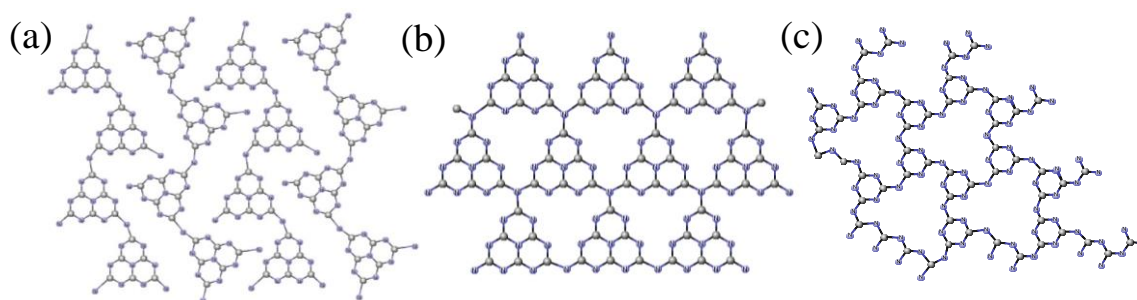


Figure 2.16. Structural motifs found in graphitic carbon nitrides. (a) Liebigs melon ($[C_6N_7(NH_2)(NH)]_n$) contains zig-zag chains of heptazine (tri-s-triazine) units linked by bridging $-NH-$ groups and decorated on their edges by $N-H$ groups, (b) fully condensed C_3N_4 layer based on heptazine units, and (c) graphitic carbon nitride based on triazine ring units.²⁰⁶

Graphitic carbon nitride is a semiconductor with a bandgap of up to 5 eV, depending on structural variations and degree of condensation of the material.²⁰⁷ The preparation method, including precursors and condensation temperature, affect the local structure, packing and defects formed during the preparation process. An ordinary polymeric carbon nitride exhibits an intrinsic band gap near 2.7 eV and optical absorption extending into the visible range,^{206, 208} although different chemical modifications may lead to a red-shift (boron and fluorine doping) or a blue-shift (sulphur doping).²⁰⁸⁻²¹⁰ These materials exhibit catalytic and photocatalytic activity and are also of interest for their intercalation, ion exchange and redox properties.^{206, 208, 209, 211-215} Because of their high nitrogen content, tunability reminiscent of polymer chemistry and facile synthesis procedure, they may provide a good balance between activity, durability and cost in PEMFC operation. However, literature data on these applications are limited.

It was reported that the fundamental ORR activity of graphitic carbon nitride in acidic medium is higher than that of pure carbon, however the current density achieved is still low for practical applications due to its low surface area.²¹⁶ Theoretical studies show that graphitic carbon nitride has poor electron transfer efficiency, but significant improvement can be achieved by blending it with high surface area carbon.²¹⁷ Since then, many studies have shown that gCNM-carbon composites could provide comparable ORR catalytic activity to that achieved by commercial Pt/C in alkaline electrolyte with enhanced durability and high carbon monoxide tolerance.²¹⁸⁻²²⁰

Although nitrogen in N-doped carbon/graphene introduces a charge carrier (n-type polaron), this charge is not necessarily localized on the nitrogen. In the case of graphitic carbon nitride, they are stoichiometric materials and contain abundant Lewis acid and base sites (terminal and bridging NH- groups and lone pairs of N in triazine/heptazine rings, respectively) that are potential anchoring sites for Pt as well as adsorption sites for CO. The first application of graphitic carbon nitride as a catalyst support can be attributed to Yu et al. in 2007 for the DMFC operation.²²¹ It was shown that PtRu supported on graphitic carbon nitride in DMFC exhibits 78-83% higher power density than on Vulcan XC-72.

2.4 Summary

This chapter provides an overview of the PEMFC catalyst layers with a focus on the challenges in the research and development of new catalysts. The use of Pd-based alloys as cheaper anode catalysts with the possibility of improved CO tolerance is proposed. PdIr alloy catalyst fabricated via magnetic co-sputtering technique was reported to have HOR activity similar to that of Pt in *ex-situ* studies. However, no further studies involving applications in a real fuel cell environment has been reported.

Catalyst layer degradation of on anode and cathode, as well as failure mechanisms is discussed. Carbon corrosion is highlighted as the main degradation mode which leads to the loss of active surface area and performance. A review on alternative carbon support was presented; although these are still in the research stage. It is clear that a balance between durability, activity and cost is needed. The applications of graphitic carbon nitride as alternative catalyst support is introduced with a view to improve the overall performance of PEMFC catalyst layers.

Chapter 3

3 Methodology: Electrochemical Characterisation Techniques

The evaluation of electrocatalyst performance is performed via *ex-situ* and *in-situ* testing. *In-situ* fuel cell testing is affected by a number of factors such as mass transport resistances and water management effects. Therefore, testing the quality of catalysts on a single-cell MEA can be unnecessarily time-consuming as it is often difficult to differentiate the contribution of each component. The initial screening is often carried out in *ex-situ* half-cell experiments which require small quantities of catalyst materials and hence higher throughput. Suitable materials are then tested *in-situ* which involves the fabrication of a single cell MEA in a PEMFC single cell. This chapter describes the techniques and limitations of both methods.

3.1 *Ex-situ* characterisation

Ex-situ electrochemical characterisation is performed using a conventional three-electrode electrochemical cell connected to a potentiostat which measures and controls the polarisation on the electrode of interest (*working electrode*). The polarisation is the potential difference between the working electrode and a *reference electrode*. For accurate measurements, it is important that the reference electrode remains at equilibrium and therefore a third electrode (*counter electrode*) is employed to pass the current. An auxiliary reaction occurs at the counter electrode so that there is no current flow between working and reference electrode. Details of the different types of *ex-situ* electrochemical techniques are discussed in the next sections.

3.1.1 Cyclic voltammetry

Cyclic voltammetry is a useful technique which allows both qualitative and quantitative information about catalysts and their electrochemical reactions to be acquired. It is performed by cycling the potential between two points and recording the current in the potential cycling region. The current represents the rate at which the anodic or cathodic reactions are taking place. The resulting current versus potential graph is called a cyclic voltammogram (CV). Figure 3.1 shows a typical CV of Pt supported on carbon black.

The whole voltammogram can be divided into six potential regions, namely:

- Hydrogen evolution region (I)
- Hydrogen adsorption region (II)
- Hydrogen desorption region (III)
- The double-layer region (IV)
- Pt oxidation region. Pt surface is oxidised to PtOH and then to PtO_x (V)
- PtO reduction to Pt (VI)

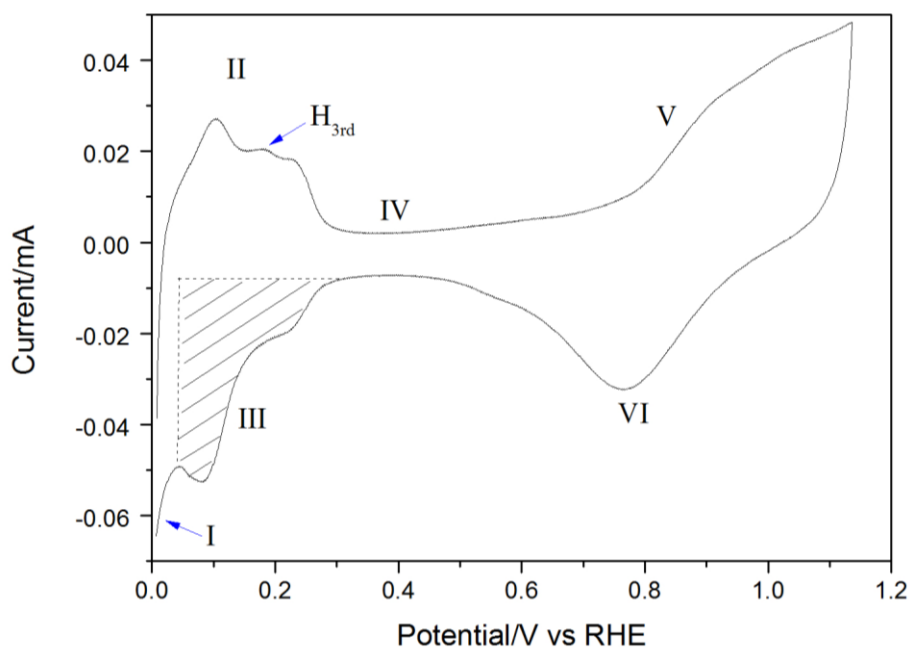


Figure 3.1: CV of Pt/C (40 wt% Alfa Aesar) at 20 mV s⁻¹ in N₂ saturated 0.1 M HClO₄. The shaded region shows the area integrated for hydrogen adsorption.

In an acidic electrolyte, H⁺ is reversibly adsorbed to form a monolayer at potentials between +0.05 and +0.4 V vs RHE via the reaction:



H_{upd} or *underpotential deposited hydrogen* refers to the adsorbed hydrogen atom on the catalyst surface. The process is reversible, with adsorption taking place on the cathodic sweep (negative-going), and desorption following when the sweep is reversed.

3.1.2 Electrochemical surface area

The electrochemical surface area (ECSA) is a quantitative measure of the surface area which is available for electron transfer. It is an important property and must be determined prior to every experiment in order to calculate and compare current densities measured for different catalysts and catalysts loadings. ECSA is usually expressed in terms of surface area per unit mass of active catalyst material in the electrode ($\text{m}^2 \text{g}^{-1}$).

There are two common methods to estimate the ECSA. The first is by measuring the integrated area of hydrogen adsorption peaks on the CV in terms of the total charge passed during the H^+ adsorption (Q_{Hads}). This is the shaded region in Figure 3.1. The ECSA of a metal catalyst is calculated using the equation:

$$ECSA (\text{m}^2 \text{g}_{Pt}^{-1}) = \left(\frac{Q_{Hads}}{Q_{density} \cdot L_{metal} \cdot A_{geo}} \right) 10^5 \quad (3.2)$$

where $Q_{density}$ is $210 \mu\text{C cm}^{-2}$ which is a well-established value for the charge required to reduce a monolayer of protons on Pt based on the assumption that one metal atom adsorbs one hydrogen atom;^{222, 223} L_{metal} is the metal loading of the working electrode in mg cm^{-2} ; and A_{geo} is the geometric surface area of the working electrode in cm^2 .

The second method for determining the ECSA is CO-stripping. In this method, the catalyst is ‘poisoned’ (surface adsorbed) with CO by purging the electrolyte with CO gas under potential control. The nature of CO adsorption is very sensitive to the surface plane, temperature and deposition potential, and therefore the charge density ($Q_{density}$) varies depending on the bonding configurations. CO molecule occupies one Pt atom in two different configurations. A linear adsorption configuration means one CO atom occupies one Pt atom and the charge density is $420 \mu\text{C cm}^{-2}$ (because two electrons are involved in CO oxidation). On the other hand, a bridge adsorption configuration corresponds to one CO atom attached to two Pt atoms, which means the charge density is $210 \mu\text{C cm}^{-2}$.^{224, 225}

The ECSA is also used to estimate the roughness factor (R_F) of an electrode. The roughness factor is a measure of the dispersion and porous structure of the catalyst and is calculated by the ratio of the catalyst surface area to the geometric surface area:

$$R_F = \frac{A_{EC}(cm^2)}{A_{geo}(cm^2)} = \frac{Q_{Hads}/Q_{density}}{A_{geo}} \quad (3.3)$$

The roughness factor for a smooth polycrystalline disk electrode is ≈ 1 and for a carbon black supported catalyst, it can vary from 1 to 10^5 , depending on the dispersion of the active components and their microstructure.

The ratio of ECSA to the physical surface area of the catalyst is known as catalyst utilisation and can be calculated by:

$$U = \frac{ECSA}{A_{phys}} \times 100\% \quad (3.4)$$

Catalyst utilisation represents the proportion of the physical catalyst surface area (A_{phys}) on the triple phase boundary (TPB) that is electrochemically active. In acidic liquid electrolyte, the entire catalyst is covered in proton-conducting medium and therefore this value is inapplicable. However, in an MEA, the catalyst depends on the proton-conducting ionomer to extend the triple phase boundary throughout the catalyst layer.

3.1.3 CO-stripping voltammetry

As mentioned in Chapter 1, H_2 -rich reformat, which is obtained through reformation of hydrocarbon fuels, is the practical choice of fuel in fuel cells. Reformate contains parts-per-million (ppm) levels of CO, even after purification steps. As CO strongly adsorbs onto the surface of many metal catalysts, it blocks the reaction sites for H_2 oxidation, thus affecting the performance. Cyclic voltammetry can be used to assess the CO tolerance of a catalyst via CO-stripping. The onset and peak potentials of the CO oxidation peak are a measure of the CO tolerance of a catalyst; low onset and peak potentials are desirable. The onset potential is also temperature dependant, with higher temperatures leading to lower onset potentials.

3.1.4 Methanol oxidation

Cyclic voltammetry can be used to evaluate the activity of a catalyst for methanol oxidation. Like CO tolerance, the method for comparing the catalytic activity of

methanol oxidation involves looking at two important features on the voltammetry: the onset and peak potentials of methanol oxidation on the anodic scan. The onset and peak potentials indicate the methanol oxidation overpotential.

3.1.5 Kinetic analysis using the rotating-disk electrode (RDE)

The rotating disk electrode (RDE) experiments enable rapid screening of catalysts without complications from *in-situ* fuel cell testing. This section describes the theory and principle of the RDE technique and how it can be used to quantitatively analyse the electrocatalytic activity of a catalyst.

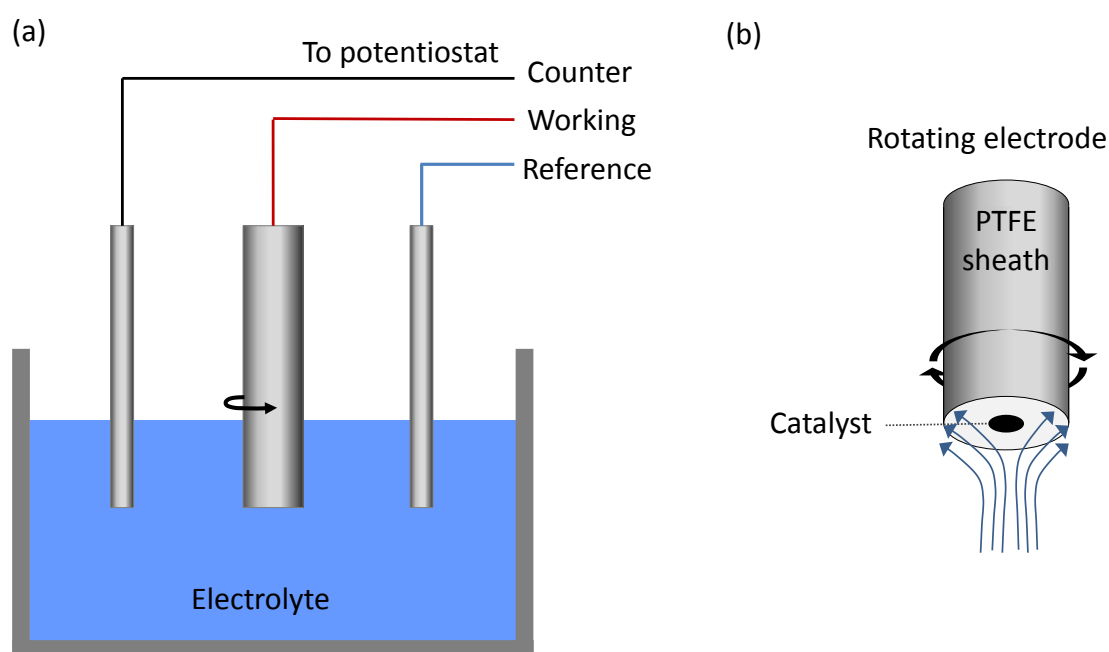


Figure 3.2: (a) Schematic of the RDE experimental setup as part of a three-electrode cell; (b) rotating electrode showing the mass transport characteristic flow lines.

An illustration of a typical RDE experimental set-up is shown in Figure 3.2. When an electrode is immersed in a stagnant electrolyte, the rate of reactions is controlled by two factors: kinetics and the transport of reactants to and from the electrode. Experimentally, it is possible to control mass transport rate so that its effect is diminished, and hence isolate the kinetic currents (i_k), by rotating the electrode with respect to the electrolyte and thereby introducing forced convection. This system is also called the hydrodynamic system.

When the electrode is rotated, the reactant is dragged to the surface of the electrode and the product is spun away leaving a fresh reaction layer on the surface of the electrode. The reactant is transported through this layer by diffusion in a laminar pattern and the net mass transport rate is now determined by both *convection* and *diffusion*, as shown in Figure 3.2b. The thickness of this layer is controlled by the angular velocity of the rotation (ω):

$$\omega(\text{rad s}^{-1}) = 2\pi f \quad (3.5)$$

where f is the number of revolutions per second. A higher angular velocity gives a thinner diffusion layer and vice versa.

In a typical RDE experiment, the potential of the working electrode is polarised linearly through a potential range of interest at several different rotation rates ω , producing a series of linear sweep voltammograms. At the reaction onset potential, the current is controlled by the reaction kinetics, which is expressed as:

$$j_k = nFA_{geo}k_f C \quad (3.6)$$

Where k_f is the rate constant and is a function of the potential. As potential is increased or decreased, the current is affected by both the reaction kinetics and the mass transport rate of the reactant (kinetic-diffusion region). Eventually, the potential is high enough that the reaction rate is determined by the mass transport rate at a given rotation rate and diffusion-limiting current plateau is achieved. This diffusion-controlled current density is described by the Levich equation²²⁶:

$$j_d = 0.62nFA_{geo}D^{\frac{2}{3}}\omega^{\frac{1}{2}}\nu^{-\frac{1}{6}}C \quad (3.7)$$

Where n is the number of electrons transferred; F is Faraday's constant (96,485 C mol⁻¹); D is the diffusion coefficient of the electrolyte (cm² s⁻¹); ν is the kinematic viscosity of the electrolyte solution (m² s⁻¹) given by the ratio of viscosity to density of the electrolyte; and C is the bulk concentration of the reactant. Throughout experiment, the electrolyte is saturated with the reactant and therefore C can be assumed to be constant.

The overall current in the entire potential sweeping region is related to the diffusion-limited current, as given by the Levich-Koutecky equation:

$$\frac{1}{j} = \frac{1}{j_k} + \frac{1}{j_d} \quad (3.8)$$

There are two methods for extracting the kinetic current density, j_k , from measured current data:

1. Substituting (3.7) into (3.8) gives a useful form of the Levich-Koutecky equation:

$$\frac{1}{j} = \frac{1}{j_k} + \frac{1}{0.62nFA_{geo}D^{\frac{2}{3}}\omega^{\frac{1}{2}}v^{-\frac{1}{6}}C} \quad (3.9)$$

Thus, plots of j^{-1} versus $\omega^{-1/2}$ at any potential within the mixed kinetic-diffusion region of the linear sweep voltammograms gives straight lines. At $\omega^{-1/2} = 0$, the rotation rate is infinite, i.e. infinite mass transport rate, and therefore extrapolation of the plots to the y-axis gives the kinetic current densities, j_k .

2. Rearranging equation (1.9) for j_k gives:

$$j_k = \frac{j \cdot j_d}{j_d - j} \quad (3.10)$$

Thus, the kinetic current density can be calculated directly from the measured current density extracted from the kinetic-diffusion region and the diffusing limited current density j_d . In the literature, 1600 rpm is the standard rotation rate used to extract the kinetic current density.^{95, 227, 228}

For more reliable comparison of catalytic activities, the kinetic current density is normalised by active surface area (ECSA) and the metal loading of the catalyst on the electrode to give *specific activities* (SA, $\mu\text{A cm}^{-2}$) and *mass activities* (MA, A g^{-1}), respectively.

Tafel analysis can be applied to the data obtained from RDE experiments, as discussed in Section 1.6.2. The linear regression of the plot of η versus $\log j_k$ gives the Tafel slope and the extrapolation of the line to 0 V gives the exchange current density (j_0).

3.2 *In-situ* characterisation

The environment in an operating PEMFC differs substantially from that of *ex-situ* tests using an electrochemical cell. Whilst *ex-situ* testing provides valuable information regarding the intrinsic properties of the catalyst, it is only by fabricating MEAs and testing them under real PEMFC operating conditions that a true property of a catalyst can be evaluated.

For an MEA evaluation, a test station is required which can measure and control the following parameters: (1) temperature, pressure, humidity and flow rates of reactants, and (2) current and voltage of the fuel cell. The fuel cell is the most important component in the system which includes current collector, flow fields and gaskets. A single cell hardware is shown in Figure 3.3. The MEA is placed in between the gaskets and screw bolts are used to compress and seal the cell assembly to the required pressure (torque).

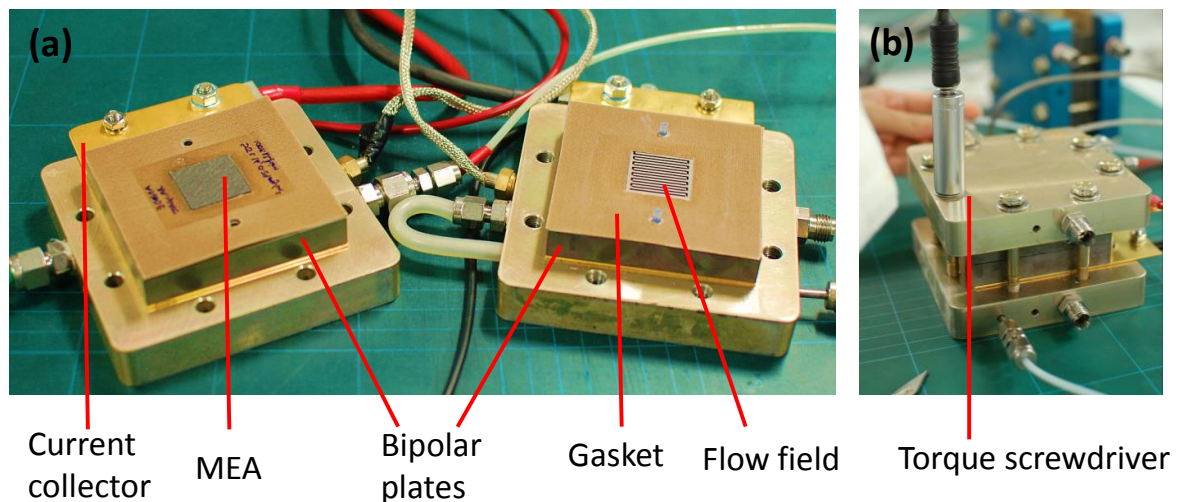


Figure 3.3. (a) A single-cell hardware (Fuel Cell Technologies) showing the different components; (b) a torque screwdriver is used to compress the cell to the required pressure.

The main difference between *in-situ* and *ex-situ* testing is the electrolyte. Liquid electrolyte provides complete wetting of the catalyst layer in which the TPB is

inapplicable, whereas in an MEA, the catalyst layer relies on ionomer (typically Nafion) and liquid water present in pores for proton conductivity and TPB. In addition, the Nafion ionomer relies on humidification of reactant gases and therefore may not be optimal. Within the MEA itself, the catalyst layer thickness is typically around $\sim 10 \mu\text{m}$, depending on composition and loading, compared to $<1 \mu\text{m}$ in RDE. Hence, MEA fabrication is very important in order to obtain the maximum possible performance of a catalyst.

3.2.1 Polarisation curve

Fuel cell performance is measured by the *polarisation curve*, which is discussed in detail in Section 1.6. The most common method for obtaining the polarisation curve is by adjusting the current density and recording the cell voltage. From the polarisation curve, the power density (cell voltage \times current density) can be plotted as a function of current density, accordingly, as shown in Figure 3.4.

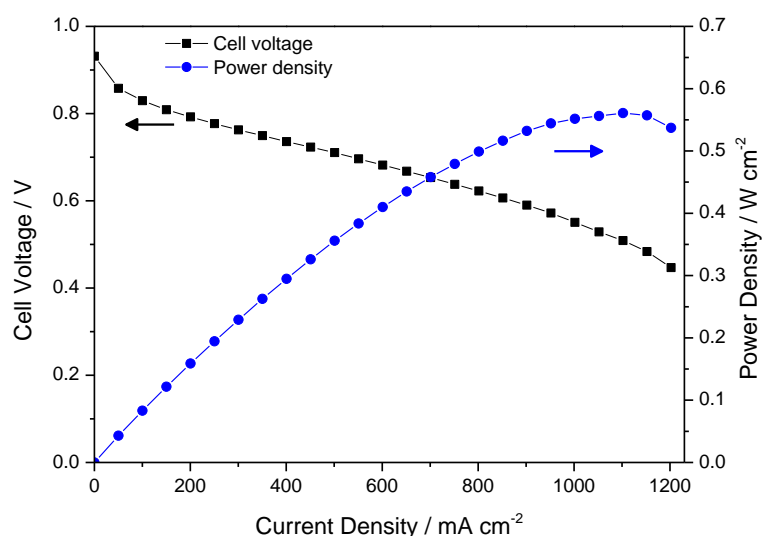


Figure 3.4: Typical polarisation curve of a PEMFC showing the cell voltage and power density as a function of current density.

The polarisation curve depends strongly on the operating conditions, such as the temperature, pressure, relative humidity and gas flow rates. Therefore, it is important to keep these parameters the same when comparing different catalysts.

3.2.2 Electrochemical Impedance Spectroscopy (EIS)

The electrochemical impedance spectroscopy (EIS) is a powerful technique for the quantitative measurement of individual losses in PEMFC performance, such as ohmic, activation and mass transport. The technique involves applying a small sinusoidal (AC) voltage or current signal of known amplitude and frequency to the cell and simultaneously recording the AC amplitude and phase response, as shown in Figure 3.5. The AC perturbation is applied over a wide range of frequencies, typically from 10 kHz to 1 Hz. The ratio and the phase-relation of the AC signal response is called the complex impedance, $\hat{Z}(\omega)$, which consists of real and imaginary components.

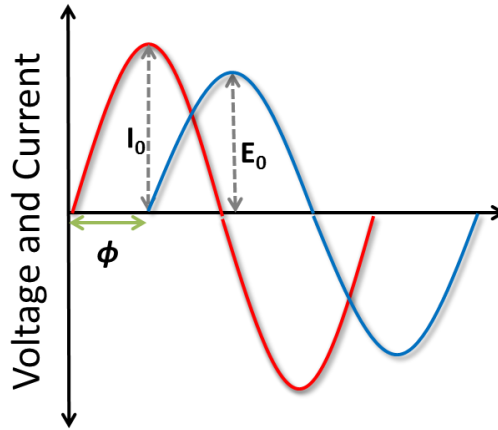


Figure 3.5: Applied sinusoidal current and resulting sinusoidal voltage response in a linear system.

In an EIS measurement, the applied current I_t and the resulting AC voltage E_t can be described mathematically as a function of time t according to equations:

$$I_t = I_0 \sin(\omega t) \quad (3.11)$$

$$E_t = E_0 \sin(\omega t - \phi) \quad (3.12)$$

Where E_0 and I_0 are the amplitude of the signals, ϕ is the phase shift with respect to the current signal, and ω is the radial frequency. Equations (3.11) and (3.12) can be expressed as complex numbers:

$$\hat{I} = I_0 e^{i\omega t} \quad (3.13)$$

$$\hat{E} = E_0 e^{i(\omega t - \phi)} \quad (3.14)$$

Where $\hat{i} \equiv \sqrt{-1}$. The impedance \hat{Z} is analogous to Ohm's Law and can be expressed as:

$$\hat{Z} = \frac{\hat{E}}{I} = \frac{E_0 e^{i(\omega t - \phi)}}{I_0 e^{i\omega t}} \quad (3.15)$$

The term $e^{i\omega t}$ cancel to give:

$$\hat{Z} = \frac{E_0}{I_0} e^{-i\phi} \quad (3.16)$$

Using Euler's relationship, $e^{i\phi} = \cos(\phi) + i\sin(\phi)$, impedance \hat{Z} can be written as a complex notation:

$$\hat{Z} = \frac{E_0}{I_0} \cos(\phi) - \hat{i} \frac{E_0}{I_0} \sin(\phi) \quad (3.17)$$

Equation (3.17) can be rewritten as:

$$\hat{Z} = Re(\hat{Z}) - \hat{i}Im(\hat{Z}) \quad (3.18)$$

Therefore, the magnitude of impedance \hat{Z} can be evaluated as:

$$|\hat{Z}| = \sqrt{Re(\hat{Z})^2 - Im(\hat{Z})^2} \quad (3.19)$$

And,

$$\phi = \tan^{-1} \left(\frac{Im(\hat{Z})}{Re(\hat{Z})} \right) \quad (3.20)$$

The complex impedance can be represented graphically in several ways; the most commonly used is a plot of $-Im(Z)$ versus $Re(Z)$, called the *Nyquist plot* (Figure 3.6).

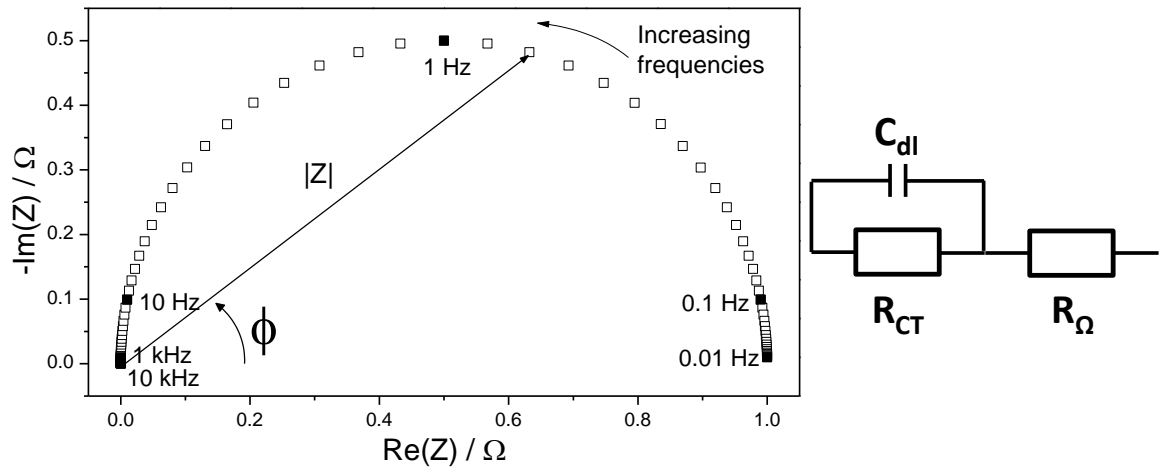


Figure 3.6. A typical Nyquist plot (left) for a Randle circuit with a resistor and capacitor in parallel (right) with frequencies between 10 kHz and 0.01 Hz

While the Nyquist plot is effective in providing insight into the possible mechanisms happening in the cell, it does not show the frequency information. Therefore, it is usually useful to indicate the frequency on the Nyquist plot. Another popular representation of the impedance data is the Bode plot, which explicitly shows the frequency-dependence of the impedance of the cell. The Bode plot displays the impedance magnitude (real or imaginary) and phase angle as a function of frequency (logarithmic scale), as shown in Figure 3.7.

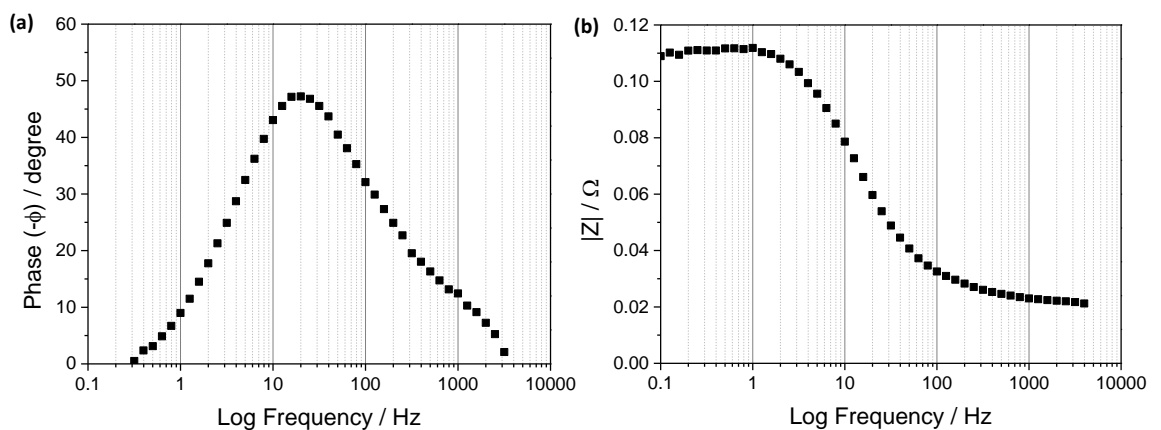
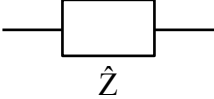
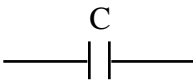
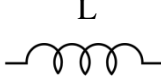


Figure 3.7: An example of the Bode plot showing the (a) phase response, and (b) magnitude response as a function of frequency.

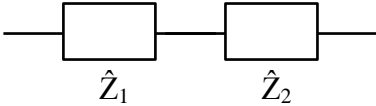
3.2.2.1 Equivalent circuits

Impedance data can be explained in terms an equivalent circuit composed of ideal resistor (R), capacitor (C), inductor (L), and distributed circuit elements.

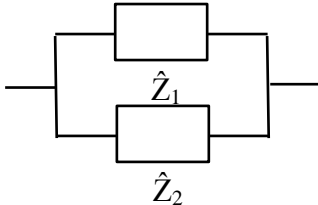
Table 3.1: The impedance relationships of ideal electrical elements commonly used to describe the impedance of electrochemical systems.

Element	Defining relationship	Equivalent circuit	Impedance
Resistor	$V = IR$		$\hat{Z} = IR$ (3.21)
Capacitor	$I = C \frac{dV}{dt}$		$\hat{Z} = \frac{1}{i\omega C}$ (3.22)
Inductor	$V = L \frac{dI}{dt}$		$\hat{Z} = i\omega L$ (3.23)

The complex voltage and current have Ohm's Law-like relationship which allows the impedance of a circuit with multiple elements to be calculated using the same rules as with multiple resistors. The total impedance of two elements in series and parallel are given by,



$\hat{Z} = \hat{Z}_1 + \hat{Z}_2$



$\frac{1}{\hat{Z}} = \frac{1}{\hat{Z}_1} + \frac{1}{\hat{Z}_2}$

In an actual electrochemical system, the reactions, processes and electrode structures are usually very complex, such that instead of behaving ideally, the circuit elements exhibit

a distribution of values. A common distributed element is the constant phase element (CPE):

$$\hat{Z}_{CPE} = \frac{1}{Q(i\omega)^n} \quad (3.24)$$

Where $0 < n < 1$, Q represents the non-ideal capacitance, and both values are assumed to be independent of frequency. The double-layer capacitance in a real electrochemical system often behaves like a CPE due to surface roughness and non-uniform current distribution.

Another common distributed circuit element is the Warburg impedance, which represents diffusion processes in the absence of migration. The Warburg circuit element can be modelled as a repeating series of identical constant phase (T) and resistive elements (R_w), also known as *transmission line*, as illustrated in Figure 3.8a. The Nyquist plot of the Warburg impedance appears as a 45° diagonal line (Figure 3.8b).

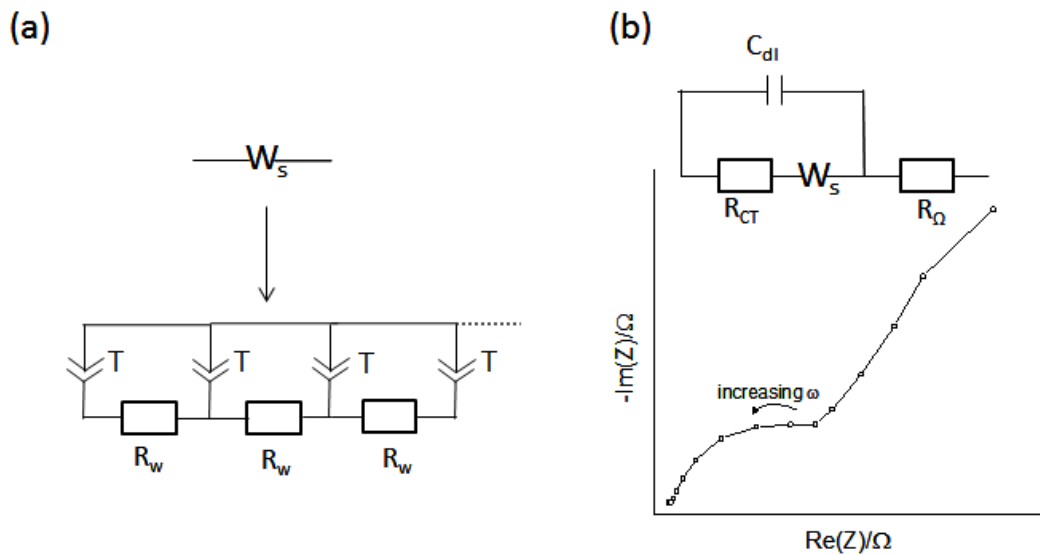


Figure 3.8: (a) Transmission line model of the Warburg circuit element and (b) typical Nyquist plot response of an equivalent circuit with Warburg impedance.

The electrochemical behaviour of an electrochemical reaction taking place at a flat electrode in a uniformly-accessible electrolyte can be modelled as a resistor (R_Ω) and capacitor (C_{dl}) in parallel, also called the Randle circuit, as illustrated in Figure 3.9(a). The R_Ω represents charge transfer required to convert the reactants to products at the

electrode surface, and the C_{dl} represents the double-layer capacitance of the electrode-electrolyte interface. The impedance response appears as a semicircle in the Nyquist plot, where it is possible to extract the charge transfer resistance from the experimental data.

Typical equivalent circuits for a PEMFC can be modelled by two parallel resistor / capacitor combinations, as shown in Figure 3.9(b). The resistive element R_{Ω} represents the Ohmic resistance (ionic and electrical) of the electrolyte membrane and connecting cables and cell components. The impedance response of a PEMFC usually appears as two semicircles with one arc representing the anode charge transfer and the other arc representing the cathode charge transfer. The semicircles also appear flattened compared to that produced by a standard parallel Randle circuit, which indicates the presence of CPE instead of a perfect capacitor. At high current densities, a third arc appears due to mass transport effects, which is represented by a lower frequency arc.

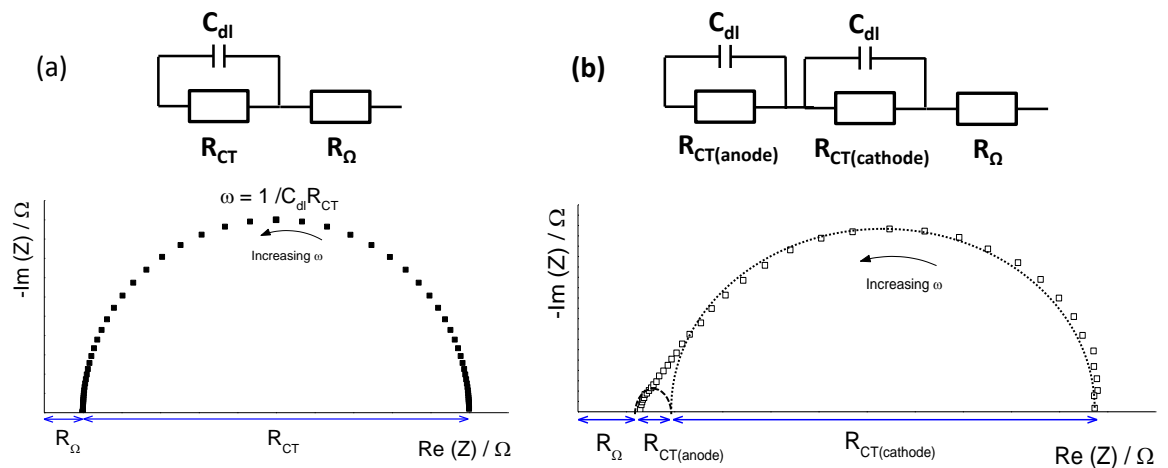


Figure 3.9: General equivalent circuit model and Nyquist plot for (a) an electrochemical interface, and (b) for a PEMFC at low current densities.

Once a suitable equivalent circuit model has been developed, a complex non-linear least-squares method is usually used to fit the model to the experimental data and calculate the values of each transfer function parameters of the circuit.

3.2.3 CO tolerance

For *in-situ* measurement of CO tolerance, the anode gas is switched to a H₂/CO mixture, with various CO concentrations depending on the system. Whilst *ex-situ* CO tolerance experiments allow quick evaluation of CO oxidation overpotential, *in-situ* experiments allow the qualitative analysis and quantification of the concentration of CO that can be tolerated for each catalyst. The effect of CO poisoning of a PEMFC with Pt/C anode is shown in Figure 3.10(a). The presence of 25 ppm CO is already detrimental to the performance of PEMFC. CO poisoning is also a transient phenomenon – it was shown that the poisoning effect of takes a significant amount of time to reach steady state, as shown in Figure 3.10(b).

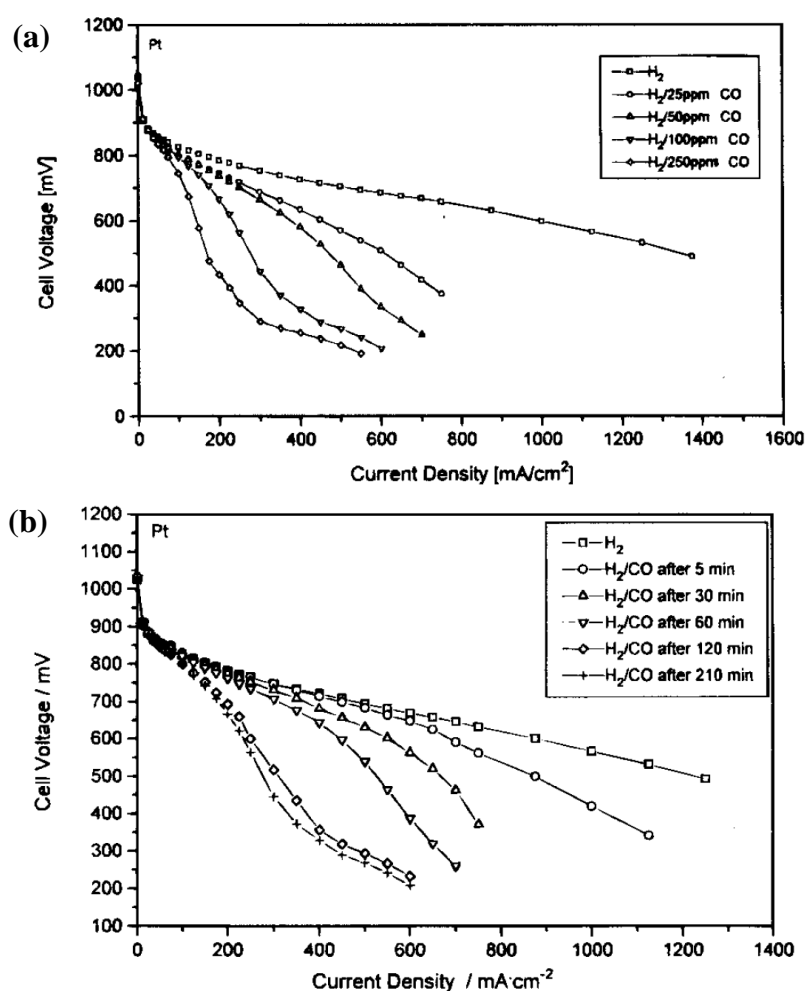


Figure 3.10: Polarisation curves of a PEMFC with Pt/Vulcan (30 wt%) anode and cathode (a) using H₂/CO fuel gas (25 to 250 ppm), and (b) in H₂/100 ppm CO during the poisoning period with steady-state achieved after 210 minutes.⁴⁸

However, it is widely known that there is discrepancy in the amount of CO that could be tolerated by catalysts, including Pt, in the literature. This may have been due to various factors such as temperature, flow rates and catalyst loading.²²⁹ It was found that lower fuel flow rates allow better CO tolerance via the oxidation of CO to CO₂ by oxygen crossover. The cathode flow rates also play an important role with higher flow rate leading to higher oxygen crossover and better CO tolerance.²³⁰ Whilst a standard experimental procedure across the literature is also needed, it is important to take these factors into account when comparing CO tolerance of various catalysts.

3.3 Durability Studies

A conventional method of testing the durability of a fuel cell requires several thousand hours under a realistic cycle. However, this type of testing is expensive with very low output and impractical for screening of new materials. Alternatively, accelerated stress test (AST) protocols can be used to induce rapid degradation of cell components and can be applied *in-situ* or *ex-situ*. It typically involves changing one or more parameters, such as potential, temperature, relative humidity, gas composition, stoichiometry and flow rate, to create specific conditions and trigger a specific degradation pathways related to a single component based on assumed but widely accepted mechanisms, while minimising degradation of other components.

As detailed in Chapter 2, carbon corrosion is the main degradation pathway, which leads to a loss in the ECSA of the electrode along with Pt dissolution. The US DOE has developed a standardised AST protocols and targets for the *in-situ* assessment of catalyst and catalyst support durability, as shown in Table 3.2 and Table 3.3.²³¹ In addition to durability testing, post-mortem analysis using physical characterisation techniques, such as XRD, SEM and TEM, is usually performed to identify the failure mechanisms.^{98, 232-235}

Table 3.2. US DOE in-situ AST cycle for electrocatalyst durability. Reproduced from 231. ²³¹

Electrocatalyst Accelerated Test Protocols and Metrics		
Cycle	Triangle sweep cycle: 50 mV s ⁻¹ between 0.6 and 1.0 V. Single cell 25 – 50 cm ²	
Total time	30000 cycles	
Cycle time	16 s	
Temperature	80°C	
Relative Humidity	100% in both anode & cathode	
Fuel/Oxidant	Hydrogen/Nitrogen	
Pressure	Atmospheric pressure	
Metric	Frequency	Target
Mass Activity (A/mg)	Beginning and end of test	≤ 40% loss of initial catalytic activity
Polarisation curve	After 0, 1000, 5000, 10000, and 30000 cycles	≤ 30 mV loss at 0.8 A cm ⁻²
ECSA		≤ 40% loss of initial area

Table 3.3. US DOE *in-situ* AST cycle for catalyst support durability. Reproduced from 231. ²³¹

Catalyst Support Accelerated Test Protocols and Metrics	
Cycle	Hold at 1.2 V for 24 h; run polarisation curve and ECSA, repeat for 400 h. Single cell 25 – 50 cm ²
Total time	Continuous operation for 400 h
Diagnostic frequency	24 h
Temperature	80°C
Relative Humidity	100% in both anode & cathode
Fuel/Oxidant	Hydrogen/Nitrogen
Pressure	150 kPa absolute
Metric	Target
Mass Activity (A/mg)	≤ 40% loss of initial catalytic activity
Polarisation curve	≤ 30 mV loss at 1.5 A cm ⁻²
ECSA	≤ 40% loss of initial area

The *in-situ* AST protocols require over 200 hours on operation, which may not always be feasible. However, there have been numerous reports of *ex-situ* AST durability studies based on the RDE in liquid electrolytes, which reduces the test duration to less than 24 hours. This involves potential cycling or hold whilst recording CV, ECSA and activity at intervals, similar to the US DOE AST protocols shown above. Ramani et al., in collaboration with Nissan North America Inc. and US DOE, have developed an *ex-situ* AST protocol which simulates the start-stop cycle in a real fuel cell system, as shown in Figure 3.11 and Table 3.4.²³⁶ They found excellent correlations between their *ex-situ* and *in-situ* results using the same catalyst. Even though no post-mortem characterisation was performed, other studies have revealed that the start-stop cycles result in severe carbon corrosion due to the high potential and temperature during the cycling.^{38, 237-241}

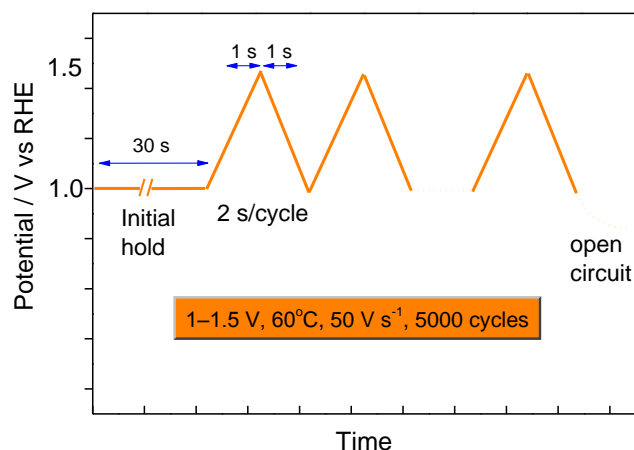


Figure 3.11. US DOE ex-situ AST potential cycle used to test catalyst durability. Reproduced from 236.²³⁶

Table 3.4: AST parameters for ex-situ AST potential cycle. Reproduced from 236.²³⁶

Temperature	60°C
Electrolyte	0.1 M HClO ₄
Dissolved gas	Nitrogen
Diagnosis	CV at 0, 10, 20, 50, 100, 200, 500, 1000, 2000, 5000 cycles

3.4 Summary

An overview of the different catalyst electrochemical characterisation techniques was presented. For the quick screening of new catalysts, *ex-situ* potential cycling and rotating-disk in a standard three-electrode electrochemical cell are often used where information such as ECSA, CO oxidation overpotential and catalyst activity can be obtained from *ex-situ* experiments. The *in-situ* evaluation of catalysts in MEA configuration involves voltage-current polarisation and impedance spectroscopy in a real fuel cell environment. From these methods, a range of information can be obtained such as polarisation curves, maximum power density, open circuit voltage, CO tolerance and reaction charge transfer resistance. Additionally, standard US DOE accelerated stress test protocols to examine catalyst and catalyst support durability in both *ex-situ* and *in-situ* configurations are presented.

Chapter 4

4 Preparation and Characterisation of Pd-alloy Anode Catalyst

In this chapter, a 1-to-1 ratio of PdIr catalyst was synthesised and characterised electrochemically in a three-electrode cell configuration using acidic electrolytes to determine its feasibility, in terms of performance and durability, as anode catalyst for PEMFC. The catalyst was also studied for its methanol oxidation reactivity.

4.1 Materials and methods

4.1.1 Hardware

Electrochemical experiments were carried out in a typical three-electrode setup consisting of working electrode, reference electrode, and counter electrode. A known amount of catalyst is deposited onto a glassy carbon working electrode, which is connected to a rotator. A platinum gauze is used as the counter electrode and a reversible hydrogen electrode (RHE) is used as the reference electrode ($E^\ominus = 0.0$ V). A separate compartment with a Luggin capillary accommodates the reference electrode. The tip of the Luggin capillary is placed close to the working electrode to minimise the impact of the uncompensated electrolyte resistance. All three electrodes are immersed in an electrolyte saturated with the reactant. Electrochemical measurements were carried out using a Metrohm Autolab PG302 potentiostat equipped with an FRA2 impedance module. The electrochemical cell was enclosed in a grounded Faraday cage. The full experimental setup is shown in Figure 4.1.

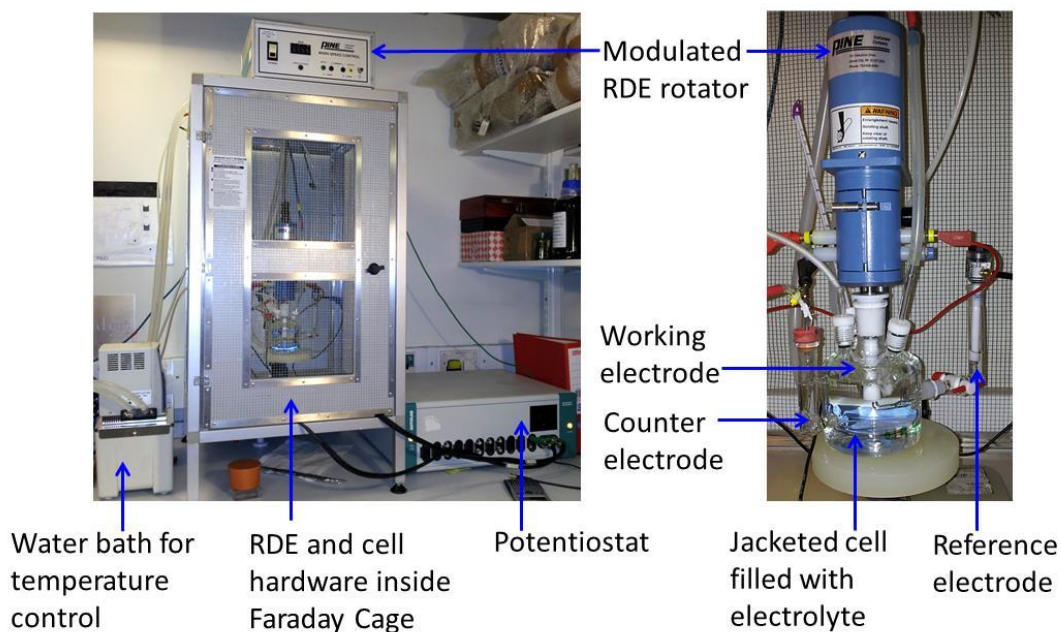


Figure 4.1: Experimental setup for ex-situ electrocatalyst characterisation

4.1.2 Materials

Pt/Vulcan (39.21 wt%, Alfa Aesar), PtRu/Vulcan (2:1, 59.8 wt%, Alfa Aesar), Pd(NO₃)₂ (>39.9% Pd, Alfa Aesar), IrCl₃ (>54.5% Ir, Alfa Aesar), RuCl₃ (>38% Ru, Alfa Aesar), Ketjen Black (Akzo Nobel), Na₂CO₃ (Sigma-Aldrich), NaH₂PO₂ (Sigma-Aldrich), HClO₄ (65% VWR Normatom), CH₃OH (VWR), C₃H₇OH (VWR Analar Normapur), N₂ (zero-grade, BOC), CO gas (Fisher Scientific), H₂ (zero-grade, BOC) and deionised water (resistivity > 18.0 MΩ cm). All chemicals and reagents were used as received without further purification.

4.1.3 Synthesis of catalysts

A low temperature chemical precipitation method has been chosen to synthesise PdIr alloy catalyst due to its simplicity, economy and low toxicity, although other methods have also been reported in the literature such as colloidal, sol-gel, micro emulsions, and electrochemical methods.²⁴²⁻²⁴⁸ PdIr/C electrocatalysts with Pd:Ir atomic ratio of 1:1 (40 wt% metal loading) was synthesised in this work. In addition, Pd/C and Ir/C were also synthesised for comparison purposes (40 wt% metal loading). Metal salts of Pd(NO₃)₂ and IrCl₃ were used as precursors. In this method, carbon black (Ketjen) was firstly dispersed in deionised water at 80°C overnight. Dissolved solutions of metal salts were

then added to the carbon slurry. Next, a solution of saturated sodium bicarbonate solution was added slowly to increase the pH to 7.0. The pH was maintained at 7.0-7.5 for 1 hour. A sodium hypophospite solution was added and the slurry was stirred for an additional hour while the temperature was maintained at 80°C. After cooling to room temperature, the slurry was filtered and washed thoroughly with deionised water. The catalysts were dried in an oven at 90°C overnight. The dried catalyst was then grinded in a pestle and mortar to give a fine powder and then reduced in a furnace under 20% H₂/80% N₂ gas flow for 1 hour at 150°C.

4.1.4 Glassware cleaning

Impurities in the electrolyte may block the active sites on the catalyst and lower the activity of the catalyst. In order to obtain reproducible measurements, the electrochemical cell and all its components such as stoppers and o-rings, must be cleaned thoroughly with deionised water to remove cationic, anionic and organic impurities. The electrochemical cell is cleaned according to the following procedures²²⁸: the cell is half-filled with concentrated H₂SO₄ and turned from side to side to ensure that the entire interior surface is wet and coated with the acid. The interior of the cell is then left soaked in the concentrated H₂SO₄ overnight. Next, the cell is rinsed with nanopure water at least 8 times and finally with the electrolyte solution. This cleaning method is performed weekly or when the system is contaminated.

4.1.5 Working electrolyte and temperature

The standard working electrolyte used in this work is 0.1 M HClO₄ which simulates a perfluoro-sulfonic acid ionomer. Older literature often describes the use of dilute H₂SO₄ as the working electrolyte. However, it has been found that Pt surfaces are highly susceptible to the adsorption of the HSO₄⁻ and SO₄²⁻ resulting in lower electrocatalytic activity in sulphuric acid.^{227, 249}

All measurements in this study are made at 25°C, unless otherwise stated. The temperature is regulated by flowing water from a water bath through the water jacket on the electrochemical cell. It is known that HClO₄ decomposes over time, especially at higher temperature, producing unwanted ions which also inhibit the activity. However,

recent work by Garsany et al. shows that the effect of temperature on the performance of Pt catalyst in HClO₄ electrolyte is insignificant.²²⁸

4.1.6 Preparation of working electrodes

Glassy carbon (GC) enclosed in PTFE (Pine Instruments) with geometric surface area of 0.196 cm² was used. Prior to every experiment, the GC electrode was polished on a microcloth (Buehler) in a “figure of eight” pattern using 1 μm and 0.05 μm alumina slurries (Buehler). The polished electrodes were rinsed with deionised water then ultrasonicated for a few minutes to remove any residual alumina.

A catalyst ink is prepared by mixing a known amount of catalyst with a known amount of solvent and Nafion (which acts as a binder). The mixture is sonicated for 30 minutes to ensure the ink is well-dispersed. The volume of ink to be deposited on the electrode is calculated by taking into account the required metal loading:

$$\text{Vol}_{\text{ink}} = \frac{\text{Required metal loading } (\mu\text{g cm}^{-2})}{\text{Ink density } (\frac{\mu\text{g}}{\mu\text{l cm}^2})} \quad (4.1)$$

A known volume of catalyst ink was deposited on the glassy carbon to produce a metal loading of 35 μg cm⁻² and dried at room temperature under ambient conditions. The ink is pipetted onto the clean polished glassy carbon electrode such that it completely covers the glassy carbon but not the Teflon. The electrode is dried at room temperature in air.

4.1.7 Reference electrode

A reversible hydrogen reference electrode (HydroFlex, Gaskatel) is employed in this study. The reference electrode is calibrated prior to every experiment to ensure that its potential does not drift. This can be done by saturating the electrolyte with H₂ and measuring the voltage of the electrode while the current is held at open circuit.

4.1.8 Physical characterisation

Low-magnification bright-field imaging was performed using Jeol JEM1010 instrument equipped with a Gatan Orius camera system and operated at 80 kV. The catalyst was

dispersed in 70% IPA under sonification and transferred to a carbon mesh TEM grid (Agar Scientific) using a micropipette under an optical microscope. Particle size analysis was done using Gatan Digital Micrograph software by measuring the longest axis of any identifiable particle in the image. Energy dispersive X-ray spectroscopy (EDX) measurements were carried using a JEOL JSM6480L scanning electron microscope equipped with an X-sight X-ray detector (Oxford Instruments) and INCA software. Synchrotron X-ray powder diffraction patterns (SXPd) were obtained using synchrotron radiation on beamline I11 at the Diamond Light Source. The data were fitted using Le Bail refinement in TOPAS software (Bruker) in order to obtain crystallographic detail such as the lattice parameter and crystallite size.

4.1.9 Electrochemical measurements

A clean electrochemical cell was filled with fresh electrolyte is 0.1 M HClO₄ and any bubbles in the Luggin capillary were removed by tipping the cell from side to side. The catalysed glassy carbon electrode was wetted with deionised water prior to experiment and mounted in an RDE assembly (Pine Instruments). The distance between the glassy carbon electrode and the tip of the Luggin capillary must be kept the same for each experiment to keep the resistance of the solution similar. Air bubbles were removed from the surface of the electrode by rotating it briefly at 2000 RPM. The cell was thermostated at 25°C using a water bath circulation heater.

The electrolyte was purged with nitrogen for 30 minutes and the electrode was electrochemically cleaned by cycling between 0.05 V – 1.0 V at 20 mV s⁻¹ for up to 20 cycles or until stable cyclic voltammograms were achieved. Electrochemical measurements were performed as follows:

- For the measurement of **ECSA**, cyclic voltammograms were recorded whilst still under N₂ purge by potential cycling between 0.05 V to 1.2 V at 20 mV s⁻¹.
- For the measurement of **CO tolerance**, the electrolyte was saturated with CO for 30 minutes while the potential of the electrode was held at 0.1 V. The gas was then switched to N₂ for 30 minutes and LSV scans were recorded from 0 to 1.2 V at 5 mV s⁻¹.

- For the measurement of **HOR activities**, the electrolyte was purged with hydrogen (ultra-high purity, BOC) for at least 30 minutes. LSV scans were recorded between 0 V to 0.4 V at rotation rates of 400, 600, 900, 1200, and 1600 RPM.
- For the measurement of **MOR activities**, the electrolyte was switched to 1 M methanol + 0.1 M HClO₄. LSV scans were recorded from 0 V to 1.2 V at 5 mV s⁻¹.

4.1.10 Durability Testing

An accelerated ex-situ stress test protocol (AST) was used for the catalyst support corrosion test. One cycle involves applying a voltage hold at 1.0 V for 30 seconds followed by two sequences of voltage cycling between 1.0 – 1.5 V at 0.5 V s⁻¹, as illustrated in Figure 3.11.

4.2 Results and discussions

4.2.1 Materials characterisation

Commercial Pt characterisation

A commercial Pt (Alfa Aesar) is used as a benchmark catalyst in this work. The catalyst morphology was analysed using TEM, as shown in Figure 4.2. The average particle size estimated from the TEM image is 4.2 nm and the quoted XRD crystallite size is 3.5 nm. Since XRD measures average crystallite size rather than particle size, which may consist of more than one crystallite, XRD crystallite size is normally smaller than TEM particle size.

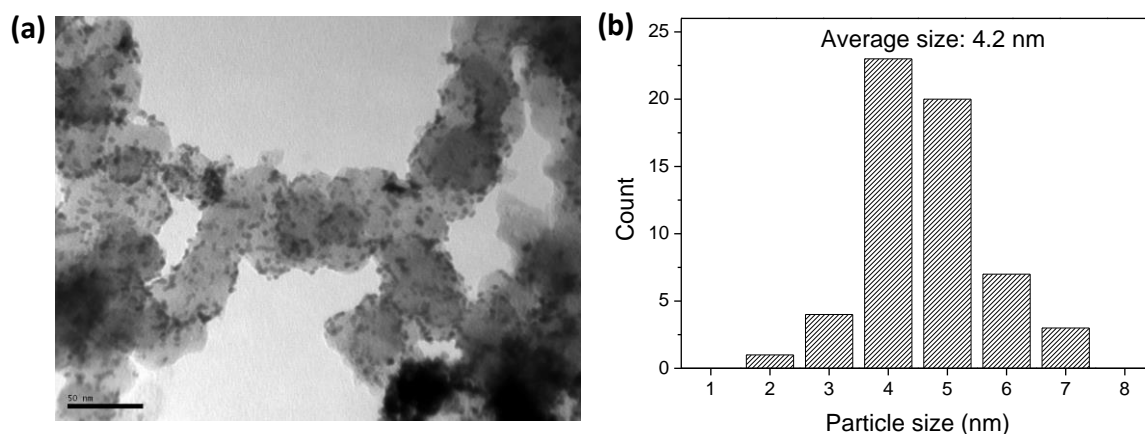


Figure 4.2: (a) TEM image of Pt supported on carbon and (b) histogram showing the particle size distribution with an average size of 4.2 nm.

The cyclic voltammogram of Pt in 0.1 M HClO₄ is shown in Figure 4.3. The hydrogen adsorption and desorption region exhibits well-defined peaks which correspond to the different crystallographic orientation of the Pt surfaces. The presence of well-defined peaks is also an indication of surface cleanliness.

The hydrogen desorption peak at 0.09 V corresponds to the weakly bonded hydrogen to Pt(110) sites whereas the peak at 0.23 V corresponds to the strongly bonded hydrogen to Pt(100) sites. The values of the potentials are close to the values given in the literature.²⁵⁰⁻²⁵³ On the anodic scan, a third hydrogen peak, H_{3rd} appears between the weakly and strongly bonded hydrogen peaks. There has been a lot of discussion on the origin of this peak. In the early studies, it was assigned by Fritz Will to the hydrogen adsorption on Pt(111).²⁵⁴ Biegler, however, concluded that it is due to hydrogen absorption²⁵⁵ but this was disputed by Kinoshita et al. because hydrogen only dissolves in Pt in very small amounts.²⁵⁶ Stonehart suggested that the peak might be due to surface diffusion and reorientation of adsorbed hydrogen and thus forming a H₃⁺ species²⁵⁷ and this was later confirmed by Sumino et al.²⁵⁸ Gomez et al. showed that Pt(110) sites are necessary for the peak to occur²⁵⁹ and this was confirmed by Frelink et al. who concluded that the peak is due to sub-surface H₂ adsorption on Pt(110) sites which are created via oxidation of the surface.²⁶⁰ This is the more likely explanation because the third hydrogen peak only appear after the potential is scanned into the Pt oxidation/reduction region.²⁶¹

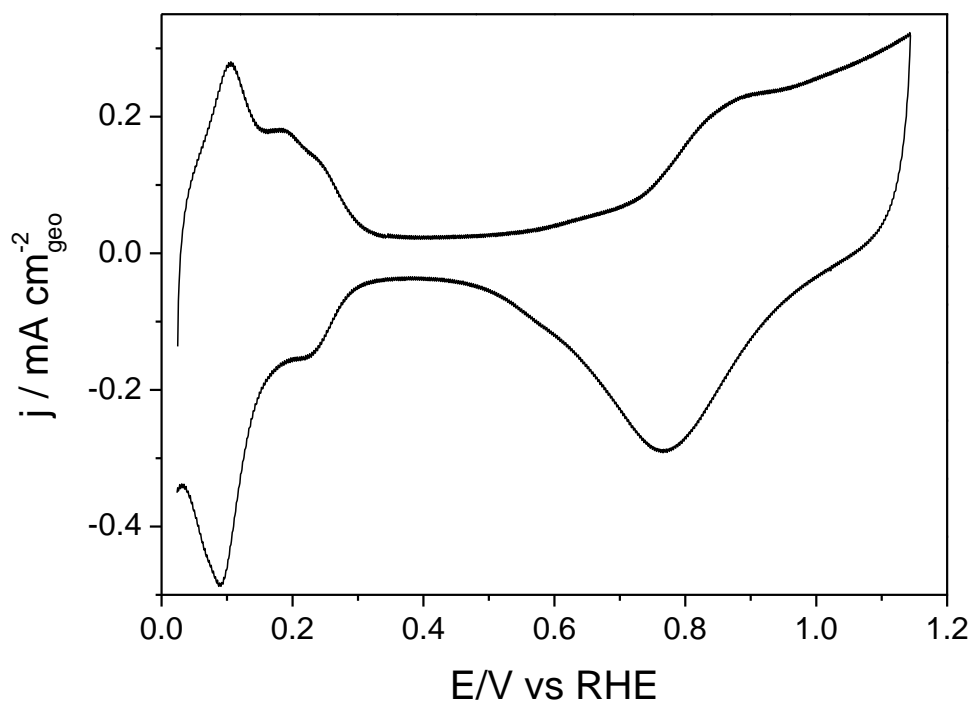


Figure 4.3: The cyclic voltammogram of Pt/C on glassy carbon in 0.1 M HClO₄ at 25°C. Scan rate: 20 mV s⁻¹

PdIr characterisation

Figure 4.4a shows the EDX analysis of the carbon supported PdIr alloy catalyst, confirming the presence of Pd, Ir and carbon. The SXPD patterns in Figure 4.4b confirm the presence of PdIr with a lattice parameter of 3.8851(1) Å, consistent with the literature value of 3.862 Å for PdIr alloy.²⁶² Both Pd and Ir have lattice parameters of 3.8898 Å and 3.8394 Å, respectively. Therefore, the absence of additional peaks in the SXPD patterns suggests that the PdIr catalyst is alloyed. The apparent crystallite size was 6.6(2) nm. The TEM image shown on Figure 4.5 shows well-dispersed PdIr nanoparticles on carbon with an average particle size of 9.6 nm, although agglomeration is also seen in the sample.

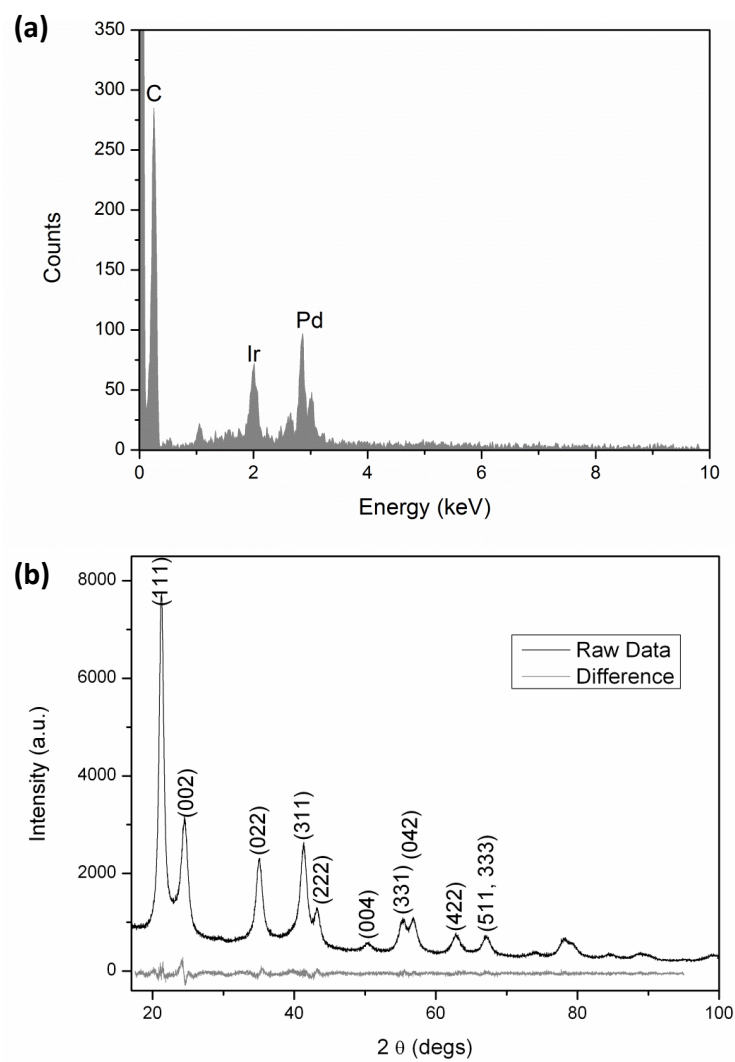


Figure 4.4: (a) EDX spectrum and (b) SXPD pattern for PdIr alloy catalyst.

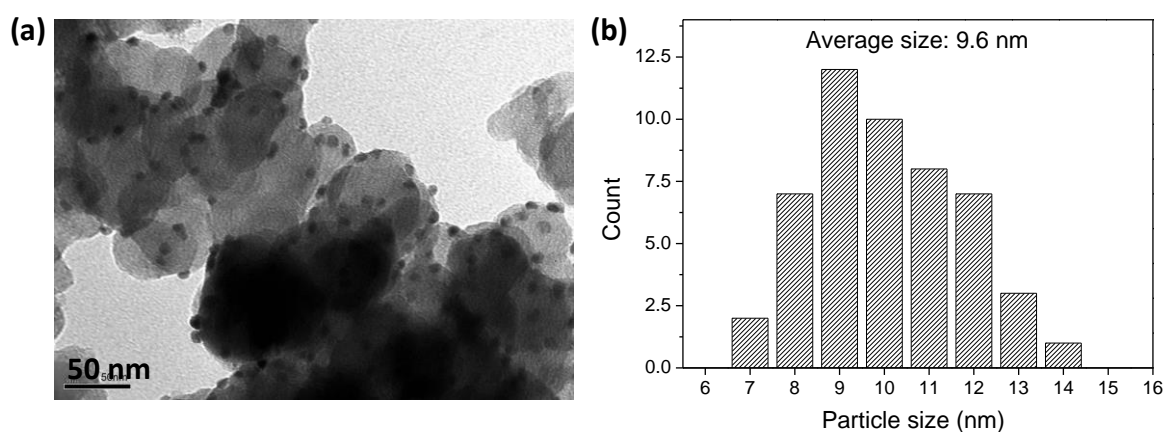


Figure 4.5: (a) TEM image of PdIr supported on carbon and (b) histogram showing the particle size distribution with an average size of 9.6 nm.

Figure 4.6 shows the CV of PdIr, Pd and Ir in 0.1 M HClO₄. The PdIr CV is distinctive from that of Pt in the hydrogen region. A sharp peak at 0.03 V is observed which can be attributed to hydrogen absorption in the β -phase on Pd – a phenomenon that is widely reported in the literature.²⁶³⁻²⁶⁵ The oxide reduction peak is observed as a single peak, rather than a mixture of Pd and Ir oxide peaks. This implies an electronic modification of the two metals due to bimetallic/alloy formation.

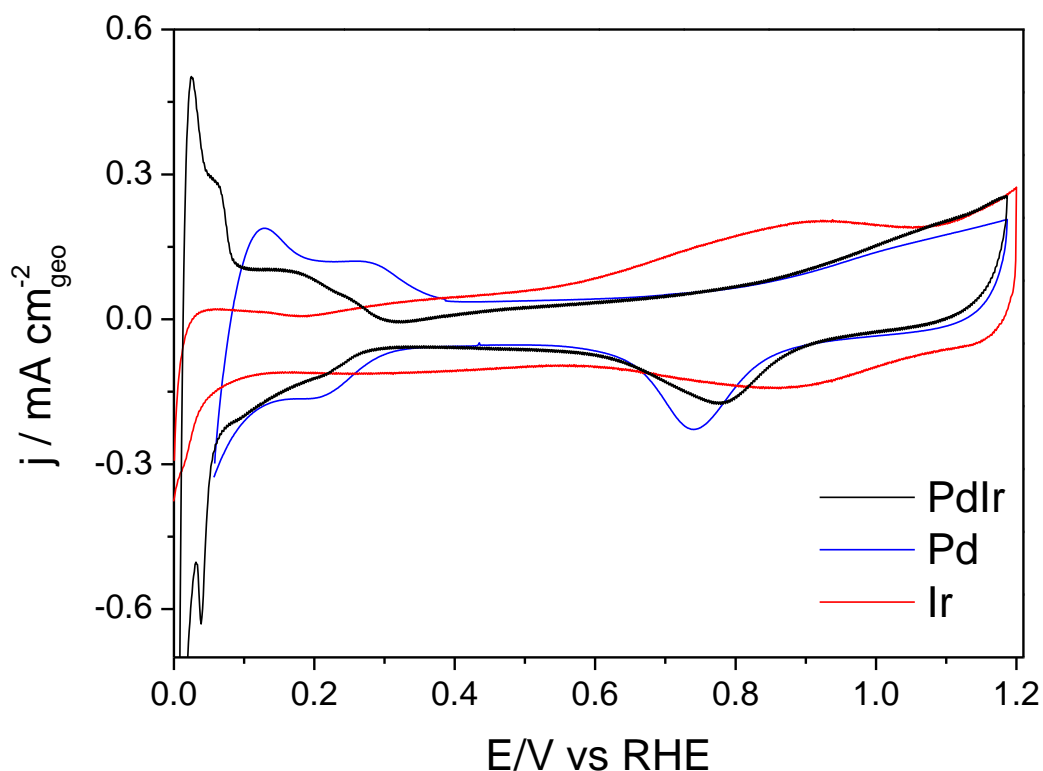


Figure 4.6: The cyclic voltammogram of PdIr, Pd and Ir in N₂-saturated 0.1 M HClO₄ at 25 °C. For clarity, the Pd cyclic voltammogram is only shown from 0.05 V. Scan rate: 20 mV s⁻¹.

The ECSA is calculated from the charge due to H_{upd}, found by integrating the hydrogen adsorption region of the CV using Equation (3.2). The hydrogen monolayer charge density $Q_{density}$ on smooth Pd and Ir surface are assumed to be 210 $\mu\text{C cm}^{-2}$ and 220 $\mu\text{C cm}^{-2}$, respectively and therefore the $Q_{density}$ of PdIr (1:1) alloy is taken as 215 $\mu\text{C cm}^{-2}$.^{63, 222} The ECSA calculated for PdIr alloy is 22.3 m² g⁻¹. The low surface area for PdIr is due to the large particle size, as seen in the TEM image, as well as the presence of agglomeration in the sample.

4.2.2 CO-stripping voltammetry

The CO-stripping voltammograms of Pt, PtRu, PdIr in 0.1 M HClO₄ are presented in Figure 4.7. It can be observed that the hydrogen desorption peaks are completely suppressed in the lower potential region for all catalysts except for PdIr. This implies that CO does not fully saturate the surface of PdIr. The same observation is reported for Pd-based alloy catalysts in literature.⁵⁷ Low CO coverage may indicate better CO tolerance as not all of the active sites of the catalysts are blocked by CO.⁵⁷ The CO oxidation peak potential for PdIr is 80 mV more negative compared to that of Pt, which could be attributed to the bifunctional effect arising from the PdIr “electronic effect”. In addition, the presence of the oxophilic Ir leads to the early formation of adsorbed hydroxides, which oxidises CO. This means that smaller driving force is needed to oxidise or remove CO from the surface of PdIr, indicating that it may have better CO tolerance than Pt.

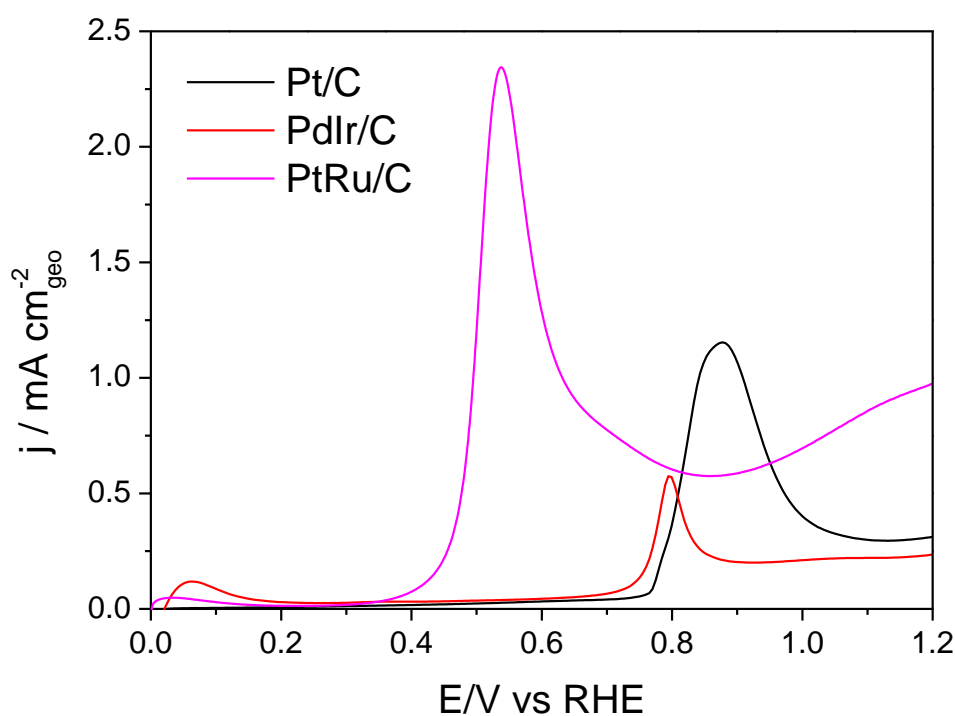


Figure 4.7: CO-stripping voltammogram of Pt, PtRu and PdIr/C, and in 0.1 M HClO₄ at 25°C.

Both Pt and PdIr have more positive CO oxidation peak compared to PtRu. The CO-tolerant PtRu shows a CO oxidation peak of 0.54 V, consistent with the value reported in the literature.^{266, 267}

The ECSA of all catalysts were measured from the CO oxidation charge after subtracting the background current of CO-free CV. The oxidation charge for one monolayer of CO on a smooth Pt or Pd surface is assumed to be $420 \mu\text{C cm}^{-2}$. The ECSA values for all catalysts are given in Table 4.1, along with CO oxidation onset potential, peak potential and average particle size. PdIr has the lowest ECSA which could be attributed to the large particle size (9.6 nm versus 4.2 nm for Pt, as shown in Chapter 4.2.1). The ECSA of PdIr obtained from CO-stripping voltammetry is lower than that obtained from H_{upd} . The ECSA obtained from CO-stripping voltammetry may likely to be an underestimation due to incomplete coverage of CO on Pd.

Table 4.1: The ECSA, CO oxidation onset and peak potentials for Pt, PtRu, and PdIr catalysts obtained from CO-stripping voltammetry. The onset potential is defined as the potential at which the current is 10% of the maximum CO oxidation current.

Catalyst	ECSA ($\text{m}^2 \text{g}^{-1}$)	Onset potential (V)	Peak potential (V)
Pt	50.2	0.78	0.88
PtRu	64.5	0.45	0.54
PdIr	20.0	0.75	0.80

4.2.3 Hydrogen Oxidation Reaction

Figure 4.8 shows the HOR linear sweep voltammogram of Pt, PdIr, Pd and Ir at 1600 rpm. The HOR activity of Pt in acid is very fast, such that it is experimentally difficult to measure using the RDE. However, the aim of this experiment is not to measure the true kinetic properties of HOR on Pt, but to define the experimental conditions for the purpose of screening and subsequently estimating the activity of newly synthesised catalysts. The final test for every suitable catalyst will be in a real PEMFC.

Pt, PdIr, and Ir reach the diffusion-limiting current around the same potential ($\sim 0.05 \text{ V}$) but the HOR current of Ir starts to decrease at $\sim 0.15 \text{ V}$ due to the early formation of adsorbed OH species (Ir is highly oxophilic).²⁶⁸ Pd exhibits a peak at around 0.25 V , which can be attributed to absorption of large amounts of hydrogen into the bulk lattice

of Pd,³¹ before diffusion limiting current is achieved at 0.30 V. This shows that Pd is kinetically controlled in a wider potential range, indicating slow reaction kinetics. In addition, hydrogen absorption into Pd bulk lattice means that less active area is available for hydrogen oxidation. Pd metal has been shown to have poor activity for the hydrogen oxidation in various literatures.^{32-34, 56, 57}

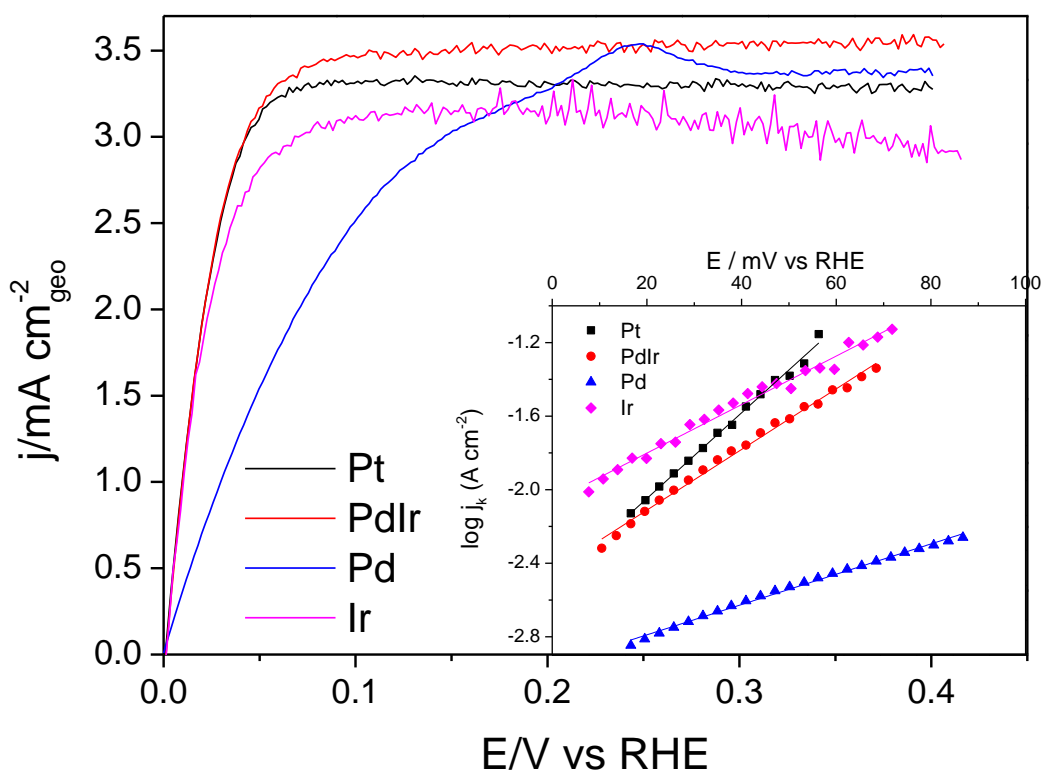


Figure 4.8: The HOR linear sweep voltammogram for carbon supported Pt, PdIr, Pd and Ir in H_2 -saturated 0.1 M $HClO_4$ at 1600 rpm. Inset: Tafel plot based on Butler-Volmer fit for each catalyst.

Tafel analysis is used to extract the kinetic parameters for each metal catalyst and the results are summarised on Table 4.2. Based on the Tafel slope, the HOR reactivity follows the orders of $Pt > Ir > Pd$, consistent with the literature.^{31, 268} The results support the early findings that both Pd and Ir alone have relatively poor HOR activity compared to Pt, but when combined as an alloy, the HOR activity is enhanced.³¹

Table 4.2: The Tafel slope and exchange current density (j_{0-RDE}) for Pt, PdIr, Pd and Ir catalysts measured in 0.1 M HClO₄ RDE assembly, and the exchange current density obtained from mass-transport free measurements ($j_{0-PEMFC}$).²⁶⁸

Catalyst	Tafel Slope (mV dec ⁻¹)	j_{0-RDE} (mA cm ⁻²)	$j_{0-PEMFC}$ (mA cm ⁻²)
Pt	28	1.64	216
PdIr	39	1.51	-
Pd	76	0.68	5.2
Ir	49	4.16	45

The exchange current densities are compared to the values obtained in the literature which uses mass-transport free measurements in a ‘H₂ pump’ configuration within a PEMFC (Table 4.2).²⁶⁸ The exchange current density found in this study is at least one order of magnitude smaller than that obtained in the literature for all catalysts, which is not surprising as the HOR in RDE is largely affected by mass-transport diffusion. Therefore, it is important to test the catalysts in an actual fuel cell before a final conclusion can be obtained.

4.2.4 Methanol oxidation reaction

Methanol oxidation voltammetry for Pt, PdIr, and PtRu are shown in Figure 4.9. It is generally accepted that low overpotential and high peak current density is an indication of good MOR activity. The current density is normalised to the ECSA of each respective catalyst due to the inherent differences in ECSA. PtRu presents the lowest methanol oxidation overpotential, as a result of its higher CO tolerance. The methanol oxidation peak for PdIr is 0.10 V more positive than Pt. The peak current density is, however, much smaller due to smaller number of active sites (ECSA). The same hydrogen desorption peak seen in CO-stripping voltammetry is observed on PdIr (inset

of Figure 4.9) indicating that not all active sites are poisoned by adsorbing intermediates.

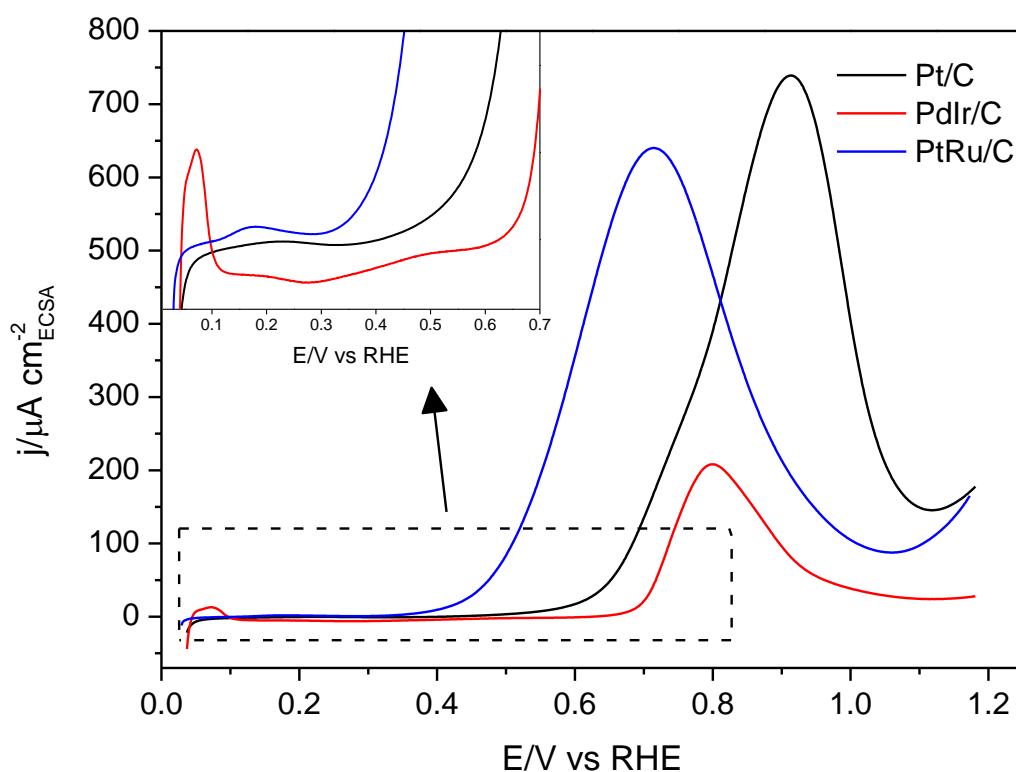


Figure 4.9: Methanol oxidation voltammogram of Pt/C, PdIr/C and PtRu/C in 1 M CH_3OH + 0.1 M HClO_4 at 25°C. Inset: Close-up of the hydrogen region showing hydrogen desorption peak for PdIr.

A comparison of a methanol oxidation reactivity of PdIr and Pd (synthesised using the same procedure) is shown in Figure 4.10. It can be seen that the addition of Ir enhances the methanol oxidation activity of Pd. Wang et al. reported that Ir is not an active metal for alcohol oxidation and therefore reducing the Ir content could enhance alcohol oxidation.⁶²

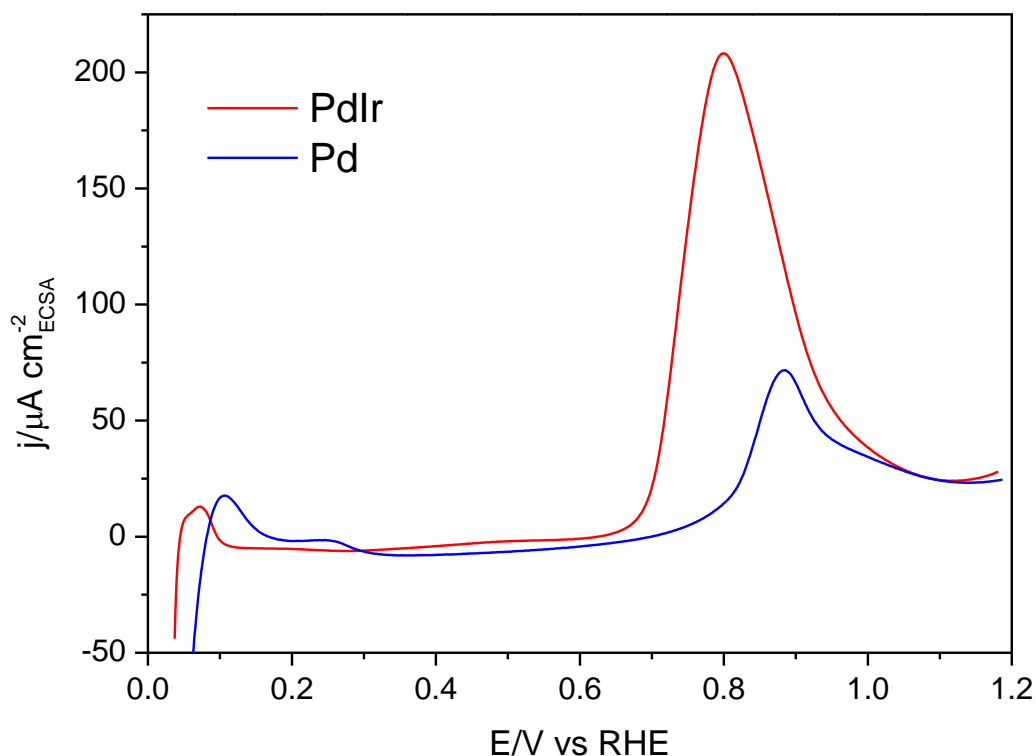


Figure 4.10: A comparison of the methanol oxidation voltammetry for PdIr and Pd in 1 M CH_3OH + 0.1 M HClO_4 at 25 °C.

4.2.5 Durability

The durability of the PdIr/Ketjen catalyst was measured using an ex-situ accelerated stress-testing protocol (AST) on the RDE. It is known that Pt catalyses the carbon corrosion therefore the measurement was benchmarked against Pt/Vulcan (Alfa Aesar). As the catalyst support is known to play an important role in durability,⁴⁰ Pt/Ketjen was also synthesised and tested for comparison. The change in CV of all three catalysts is shown in Figure 4.11. For all catalysts, the current in the hydrogen region decreases with successive cycles, indicating loss of ECSA. At the end of the 1000 cycles, commercial Pt/Vulcan exhibits a 31% decrease in ECSA. Both PdIr/Ketjen and Pt/Ketjen display significantly higher ECSA loss, with total reductions of 66% and 60% respectively. It was reported that Pd/C catalyst exhibits worse degradation compared to Pt/C due to the formation of β -hydrogen phase on Pd during the accelerated potential cycling.²⁶⁹ This was denoted by an increase in peak at around 0 V in the CV, which is not observed in this experiment. It is possible that the presence of Ir suppress the absorption of hydrogen on Pd.

Pt/Ketjen has a higher loss in ECSA compared to Pt/Vulcan; both Pt catalysts have similar particle size, which implies that the difference in durability cannot be attributed entirely to size-dependent dissolution or sintering. As seen from Figure 4.11(b), Pt/Ketjen shows a more pronounced peak in the oxide region, which is attributed to the quinone/hydroquinone oxidation reduction process on the carbon surface.²⁷⁰⁻²⁷³ The formation of surface oxygen functionalization can indicate carbon corrosions.^{272, 274} It is known that carbon corrosion is more pronounced on Ketjen due to its higher BET surface area compared to Vulcan ($800 \text{ m}^2 \text{ g}^{-1}$ vs $250 \text{ m}^2 \text{ g}^{-1}$).^{38, 104} Similar behaviour is also seen on PdIr/Ketjen CV, implying that the main degradation mechanism is carbon corrosion, although a post-mortem physical characterisation would be a more suitable method to determine the main degradation mode.

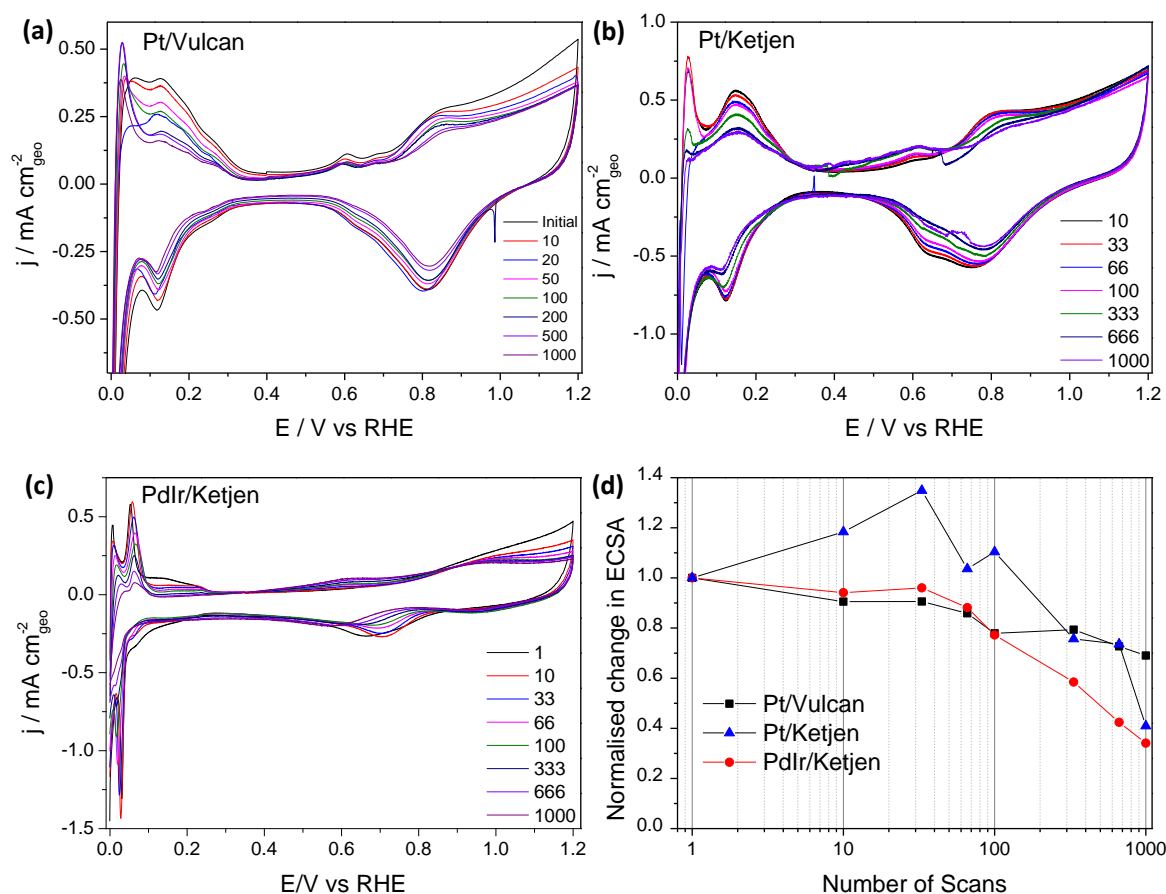


Figure 4.11: (a-c) The CV of Pt/Vulcan, Pt/Ketjen, and PdIr/Ketjen during the ex-situ AST potential cycling (1.0 – 1.5 V) and (d) the change in ECSA of the catalysts as a result of AST potential cycling.

4.3 Conclusions

In this chapter, PdIr catalyst was synthesised using a low temperature chemical precipitation method and characterised electrochemically in RDE configuration. The ECSA obtained is low due to particle agglomeration in the sample, indicating the possibility of further optimisation. Despite the low ECSA, the results from electrochemical testing suggest that the HOR activity of PdIr is almost as facile as Pt. However, the HOR activity in RDE acidic electrolyte is very fast that it is difficult to measure the true kinetics value. Therefore, the final test will be conducted in a real PEMFC, which will be discussed in the next chapter.

The CO tolerance of PdIr is slightly better than Pt, but worse than PtRu, as indicated by the CO onset potential of CO-stripping voltammetry. However, the active sites of PdIr are not 100% poisoned by CO, which suggests that these sites may be available for reaction. The methanol oxidation voltammetry results show the activity in the order of PtRu > Pt > PdIr. Ex-situ durability testing shows that PdIr have a similar durability to Pt but further experiment is needed to verify the results.

Chapter 5

5 In-situ Testing

5.1 Materials and methods

5.1.1 MEA fabrication

The catalyst ink was prepared by dispersing the catalysts in 70% IPA solution (Sigma-Aldrich) and Nafion solution, and ultrasonicated the mixture in a water bath for 30 minutes. The inks were then spray-coated onto a 2.3×2.3 cm section of GDL (Johnson Matthey). The catalyst loading was determined using a weight balance and was fixed at 0.4 mg cm^{-2} .

Commercial gas diffusion electrodes (Johnson Matthey ELE0007, $0.4 \text{ mg}_{\text{Pt}} \text{ cm}^{-2}$) were used as cathodes for all MEAs. MEAs were prepared by hot-pressing anode and cathode electrodes on either side of a Nafion 212 membrane at 130°C and 400 psi for 3 minutes. Commercial PtRu anode was prepared by spray-coating commercial PtRu (2:1, 60 wt%, Alfa Aesar) ink onto a GDL. Commercial Pt MEA was made using commercial anode and cathode GDEs.

5.1.2 Single-cell PEMFC testing

The prepared MEA (5.29 cm^2 active area) was mounted in commercial single-cell hardware (Fuel Cell Technologies Inc., USA). Single-cell testing was carried out using a Scribner 890e test stand (Scribner Associates, USA). Electrochemical impedance spectroscopy (EIS) analysis was carried out using UCL-FRA software.²⁷⁵

Prior to experimental test, the MEA was activated to ensure the membrane is sufficiently hydrated, thus reducing the Ohmic resistance and increasing the extent of the triple phase boundary. The cell temperature was set to 80°C and the anode and cathode were fed with H_2 and air at stoichiometry of 2.0 and 6.5, respectively. The activation procedure was carried out by maintaining the cell current density in sequence of 50 mA cm^{-2} , 100 mA cm^{-2} , 300 mA cm^{-2} , 500 mA cm^{-2} , and 700 mA cm^{-2} for 1 hour each or until the current density stabilised for at least 30 minutes. Following activation, the polarisation curves were recorded from OCV to 1000 mA cm^{-2} at 50 mA cm^{-2}

increments with 60 seconds at each point. EIS was applied at 100 mA cm^{-2} or 500 mA cm^{-2} at a frequency range of 0.1 Hz to 10 kHz with applied AC amplitude of 10% of the actual current. Equivalent circuit modelling was obtained using Z-view software (Scribner Associates).

CO tolerance analysis was performed by switching the anode fuel gas was to H_2/CO mixtures with CO concentrations of 25, 50, 100, and 250 ppm. The current density was held at 250 mA cm^{-2} for 120 minutes, or until steady-state is reached, before the performance data was obtained.

5.2 Results and discussions

5.2.1 Performance analysis

Figure 5.1 shows the polarisation curves of PdIr in comparison with Pd and Ir. At the activation region (0 to 100 mA cm^{-2}), PdIr and Ir have similar performance; however, PdIr gives the best overall performance. Pd performs the worst with at least 60 mV drop in performance compared to PdIr and Ir. This results suggest that the HOR activity of Pd (and Ir to a lesser degree) alone are limited, but when combined as an alloy, performance is enhanced. The enhancement is thought to be due to a decrease in PdIr *d*-band vacancy, owing to the higher binding energy of Pd- H_x ,³¹ as well as a decrease in particle size. This is in agreement with the results obtained using the RDE in Chapter 4.

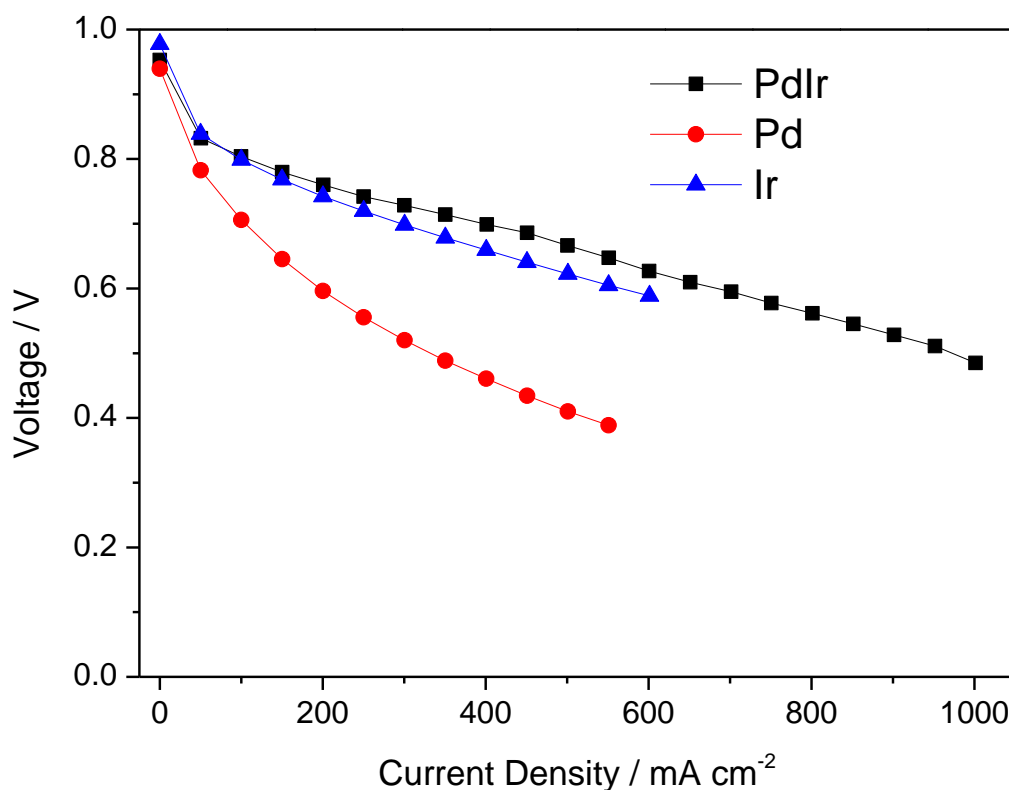


Figure 5.1: Polarisation curves of a single-cell operating at 80°C with PdIr, Pd and Ir as anode catalysts. Conditions: 5.29 cm² cell, 100% relative humidity anode and cathode, 1 atm. Load-based stoichiometry: Anode = 2.0; Cathode = 6.5 based on O₂ in air.

The performance of PdIr is compared to commercial Pt and PtRu (JM), as shown in Figure 5.2. All MEAs employ the same commercial Pt cathode GDM; therefore, the differences in performance at the activation region can be attributed to the anode catalysts. Commercial Pt gives the best overall performance, followed by PtRu and PdIr. PtRu has a similar performance to commercial Pt at the activation region, but performs worse at the Ohmic region. PdIr shows a 25 mV drop in performance, indicating that the HOR at the anode is not as facile as commercial Pt. However, after 500 mA cm⁻², the performance of PdIr MEA deteriorates further, which could be due to mass transport diffusion.

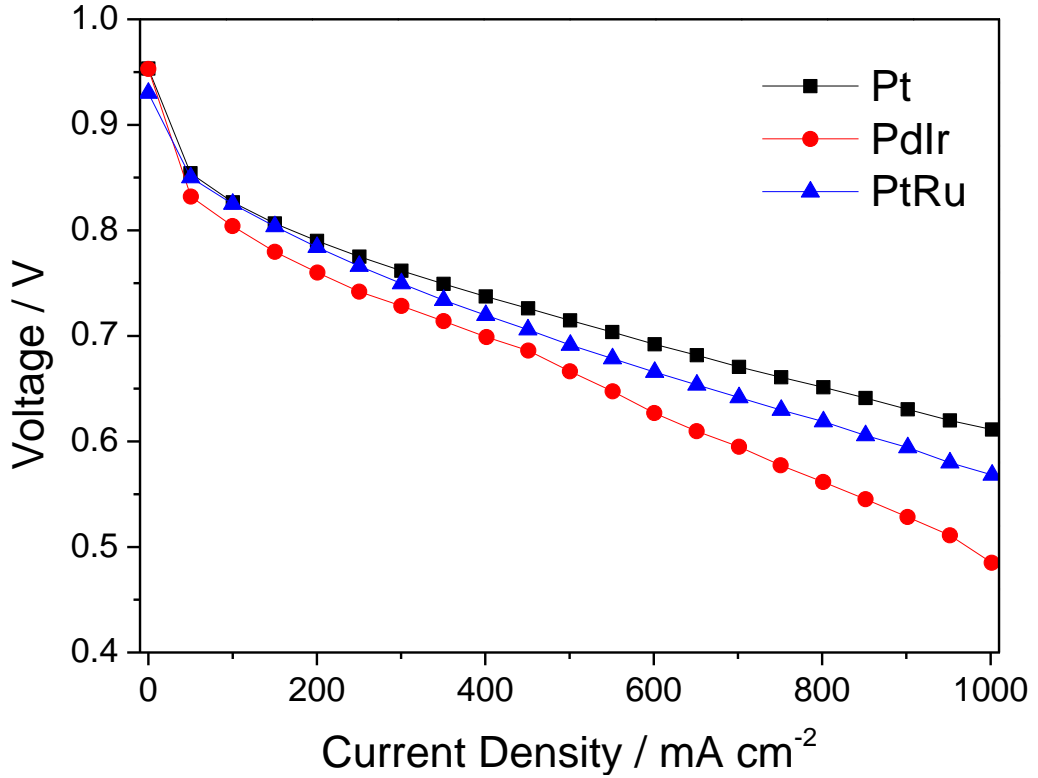


Figure 5.2: Polarisation curves of single-cell operating at 80°C with Pt (JM), PtRu (Alfa Aesar) and PdIr as anode catalysts. Conditions: 5.29 cm² cell, 100% relative humidity anode and cathode, 1 atm. Load-based stoichiometry: Anode = 2.0; Cathode = 6.5 based on O₂ in air.

Polarisation curve only shows the overall performance; therefore, EIS is used to isolate the individual components contributing to the performance of the MEAs at various regions. Figure 5.3 shows the Nyquist plot for all MEAs at the activation region (100 mA cm²).

It is generally accepted that in a PEMFC using Pt in both anode and cathode, the cathode charge transfer resistance is the dominant factor affecting the performance at the activation region due to the slow kinetics of ORR which involves the transfer of 4 electrons and the presence of strongly-bound intermediates.^{272, 276} The impedance spectrum of Pt MEA in Figure 5.3 shows a single arc due to the cathode charge transfer resistance. Similar behaviour is also seen on the impedance spectrum of PtRu MEA, although the diameter of the arc is slightly larger. On the basis that only the anode side is different in the MEAs, the change in the impedance spectra is attributed to the increase in anode charge transfer resistance.

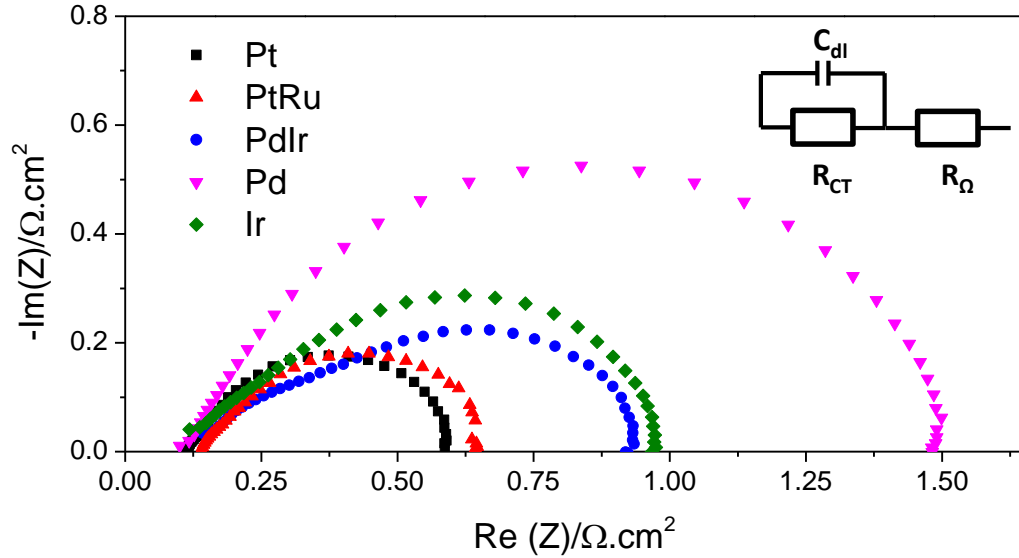


Figure 5.3: Nyquist plot showing the EIS data at 100 mA cm^{-2} for all MEAs.

Figure 5.3 shows two distinct arcs for PdIr and Ir MEAs. The first high frequency arc is attributed to the anode charge transfer resistance, whereas the low frequency arc is attributed to the cathode charge transfer resistance. This observation confirmed the earlier results that the HOR activity of anode is not as facile as initially speculated. In contrast, Pd MEA shows only a single arc. It could be that, since Pd HOR kinetics is very slow, the anode charge transfer resistance is as significant as the cathode charge transfer resistance.

The impedance spectra for all MEAs were analysed via equivalent circuit fitting and the results is presented in Figure 5.4. The anode charge transfer resistance is assumed to be negligible for Pt MEA, meaning the equivalent circuit consists of only one charge transfer resistance. The real axis intercept at high frequency corresponds to the Ohmic resistance of the cell. The Ohmic resistance measured from equivalent circuit element values at 100 mA cm^{-2} are comparable for all MEAs and correspond to the real axis intercept at high frequency on the Nyquist plot. The R_{ohm} comes from the ionic resistances of the membrane and gas diffusion media, as well as the electrical and contact resistances of the cell components and connecting leads. Since all MEAs use the same membrane and cell hardware, the Ohmic resistance is expected to be similar for all MEAs.

From Figure 5.4c, it can be seen that the cathode charge transfer resistance varies, especially on MEAs made from in-house synthesised anode catalysts, despite all MEAs using the same commercial Pt cathode. This suggests that changes at the anode side influences an alteration in the charge transfer resistance at the cathode side. This phenomenon is widely documented in the case of CO poisoning at the anode, although the change in cathode charge transfer resistance is usually small relative to the change in anode charge transfer resistance.^{277, 278} In this study, one explanation could be that the anode catalyst layer is poorly designed. In addition to the large particle size and agglomeration in the sample, the catalyst layer preparation route used in this study, such as ink composition and deposition method, is far from being optimised. This results in an uneven catalyst layer at the anode side. Considering the effective charge transfer reaction is influenced by the concentrations of the charged (protons) and uncharged species (water), inhomogeneous catalyst layer causes a local inhomogeneous distribution of protons and water molecules on the anode side. Consequently, this results in a local inhomogeneous distribution of the species, and hence, inhomogeneous local current densities at the cathode side.

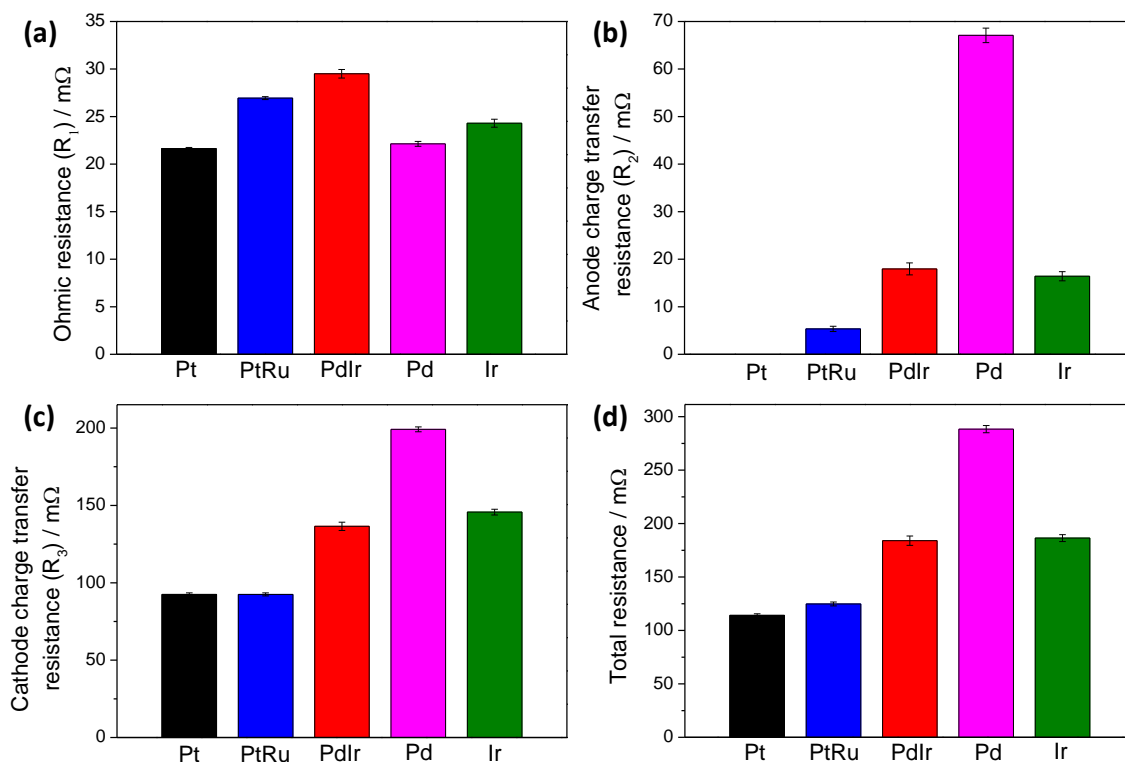


Figure 5.4: Equivalent circuit element fitted values for (a) ohmic resistance, (b) anode charge transfer resistance, (c) cathode charge transfer resistance, and (d) the sum of ohmic, cathode and anode charge transfer resistances for EIS data obtained at 100 mA cm^{-2} .

Equivalent circuit data fitting shows that Pd also significantly larger anode charge transfer resistance in comparison to other catalysts, consistent with the polarisation curves in Figure 5.1. In contrast, PdIr has a slightly higher anode charge transfer resistance compared to Ir, which is compensated by the lower cathode charge transfer resistance, thus reducing the overall resistance. In the case of Pd MEA, it is difficult to isolate the anode charge transfer resistance from the cathode charge transfer resistance since the impedance spectrum shows one big arc. Therefore, the values for Pd MEA reported in Figure 5.4 are based on the assumption that cathode charge transfer resistance is bigger than anode charge transfer resistance.

Nevertheless, even if it is assumed that the cathode charge transfer resistance is the same for all MEAs, and the increase in total charge transfer resistance is based solely on the anode charge transfer resistance, the results still demonstrate that the anode HOR

activity decreases in the order of Pt > PtRu > PdIr > Ir > Pd. The charge transfer resistance is directly related to the exchange current density (j_0) based on the equation:

$$R_{CT} = \frac{RT}{nFj_0} \quad (5.1)$$

Since exchange current density is affected by the active surface area of the catalyst, the lower ECSA of PdIr may partly contribute to the low performance.

The impedance spectra at the Ohmic region (500 mA cm^{-2}) for all MEAs are shown in Figure 5.5. At high current densities, typically above 500 mA cm^{-2} , the rate of diffusion of fuel and air within the electrodes begins to have an effect on PEMFC performance, although it is usually more prominent in the cathode. These mass transport effects due to diffusion of reactants produce a characteristic impedance response at low frequency (<100 Hz).

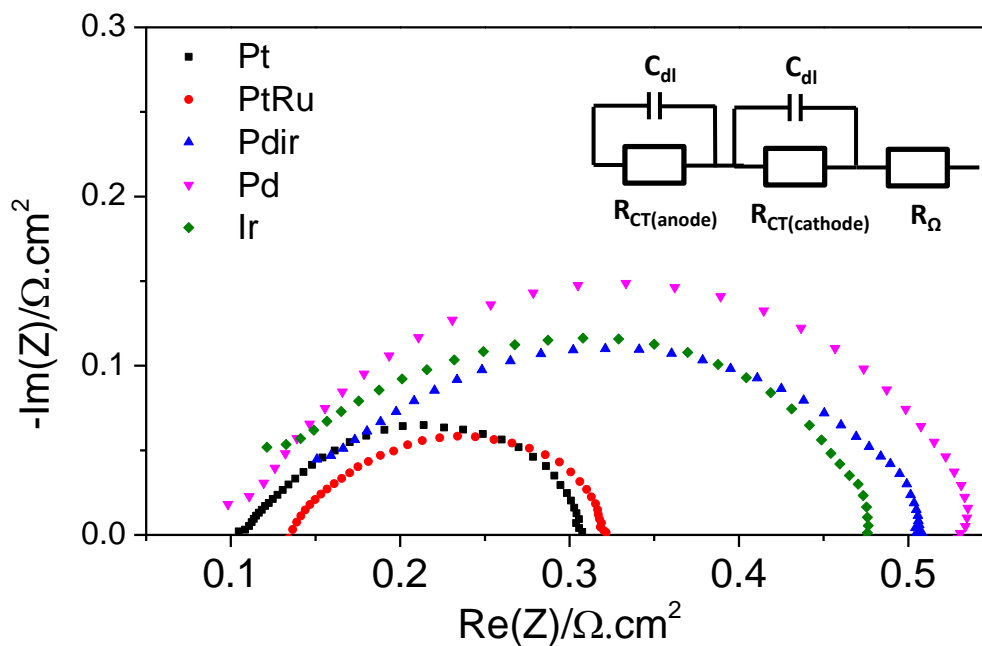


Figure 5.5: Nyquist plot showing the EIS data at 500 mA cm^{-2} for all MEAs

The mass transport resistance (R_{mt}) has very little effect on the overall performance of Pt and PtRu MEAs, but is significant for PdIr, Pd and Ir MEAs. As mentioned, PdIr, Pd and Ir catalysts have significantly larger particle size compared to commercial catalysts, resulting in uneven catalyst layer at the anode side. Therefore, the difference in mass

transport resistances may be attributed to the mass transport diffusion at the anode catalyst layer. In addition, the different GDL used in this study may partly contribute to the overall mass transport resistance. From Figure 5.5, it is clear that PtRu MEA has a comparably higher Ohmic resistance with respect to other MEAs. Seeing as all MEAs use the same cell hardware, the difference in the R_{ohm} could be due to a problem with the membrane of PtRu MEA.

5.2.2 Performance optimisation

In order to improve the performance of PdIr, an attempt was made to improve the catalyst particle dispersion and ECSA. The catalyst support material is known to have a strong influence on the properties of metal catalysts, such as metal particle size, morphology, stability and dispersion. However, it is difficult to achieve highly dispersed metal nanoparticles on carbon support, especially when the metal loading is high. Surface modification is widely used in order to introduce functional groups on the carbon surface such as doping and introducing oxygen groups by acid/base treatment.^{186, 193, 279} These functional groups act as anchoring sites for metal nanoparticles, leading to improved dispersion and size control. In addition, Pd dispersion has been shown to correlate with the amount of oxygen-containing groups present on carbon supports, which was attributed to increased interaction between Pd precursor and the surface oxygen groups.²⁸⁰⁻²⁸⁵

High metal loadings per unit area of support are usually used to minimise the thickness of catalyst layers on GDL. However, this leads to particle coalescence and formation of complex structures where the particles contact each other through grain boundaries.²⁸⁶ It has been shown that increasing metal loading on carbon support increases the particle size, and that intrinsic HOR catalytic activity decreases with increasing particle size.

Based on the above studies, 40 wt% PdIr and 20 wt% PdIr on pre-treated carbon were synthesised via the low-temperature chemical precipitation method described in Section 4.1.3. The carbon was pre-treated in 0.1 M KOH at 80°C for four hours prior to catalyst deposition. The catalysts are then compared with unoptimised PdIr catalyst, as well as commercial Pt catalyst.

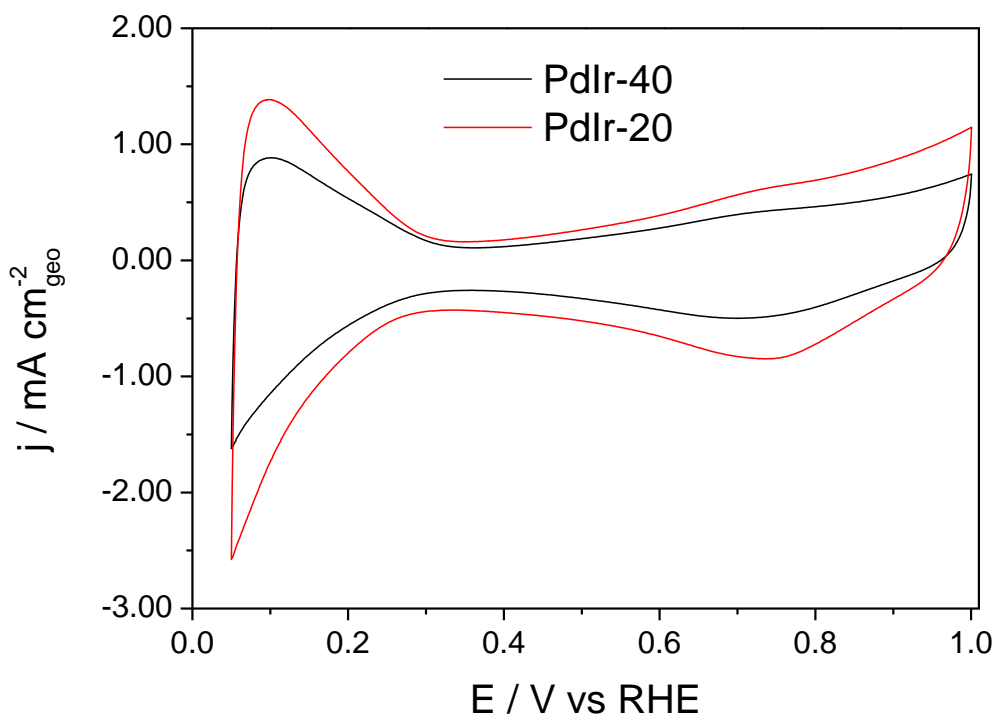


Figure 5.6: The cyclic voltammograms of PdIr-40 (40 wt% on pre-treated carbon) and PdIr-20 (20 wt% on pre-treated carbon) measured using RDE in N_2 -saturated 0.1 M $HClO_4$ electrolyte at 25°C.

First, the catalysts were analysed using cyclic voltammetry, shown in Figure 5.6. PdIr-20 (20 wt% on pre-treated carbon) has a larger double-layer capacitance, compared to PdIr-40 (40 wt% on pre-treated carbon), due to the higher amount of carbon in the sample. The ECSAs are found to be $27.4 \text{ m}^2 \text{ g}^{-1}$ and $35.0 \text{ m}^2 \text{ g}^{-1}$ for PdIr-40 and PdIr-20, respectively. For comparison, the ECSA of PdIr on untreated carbon is $22.3 \text{ m}^2 \text{ g}^{-1}$. The increase in ECSA is thought to be due to an improvement in particle dispersion, as well as reduction in particle size, as shown in Figure 5.7. Both PdIr-40 and PdIr-20 have similar average particle size (ca. 4.2 nm); however, reduction of metal loading increases the ECSA due to smaller degree of particle coalescence.

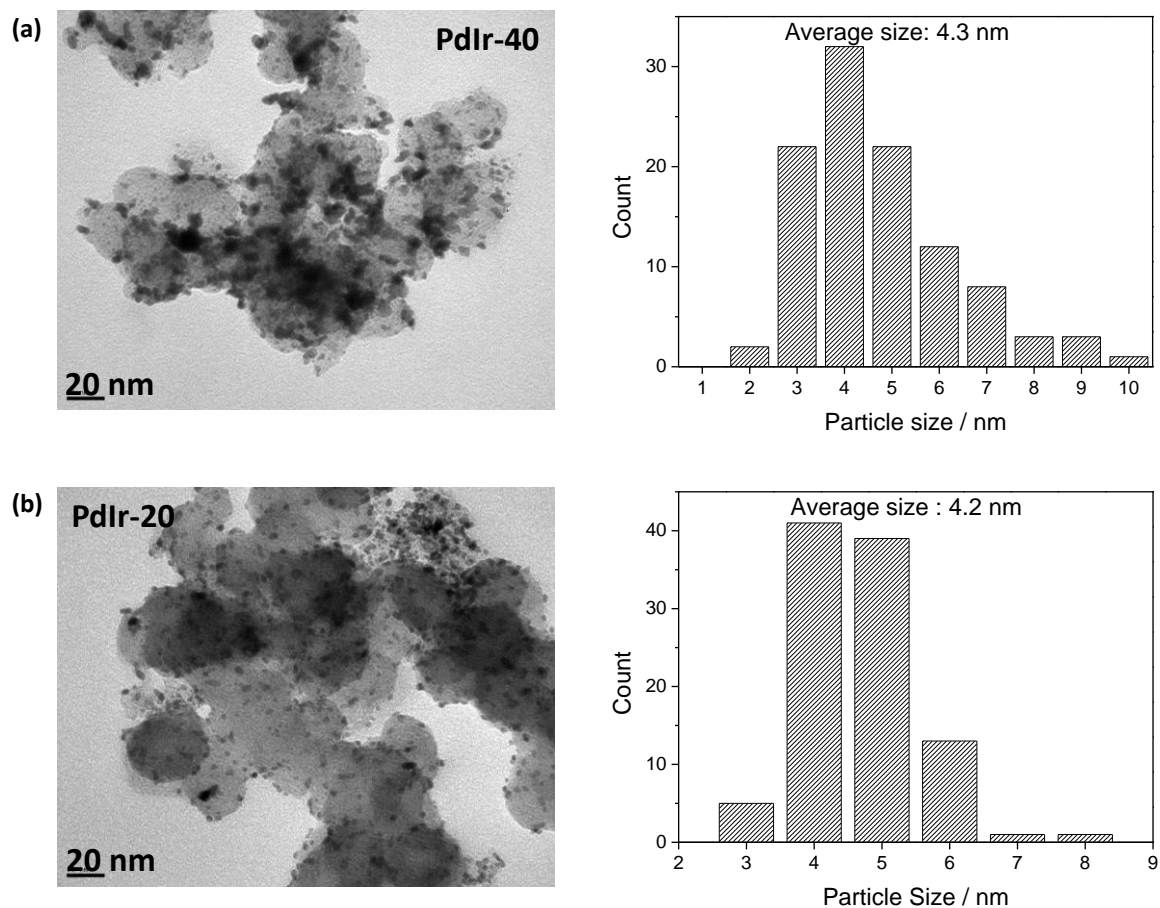


Figure 5.7. TEM images and histograms showing the particle size distribution of (a) PdIr-40 (40 wt%), and (b) PdIr-20 (20 wt%).

The polarisation curves of PdIr MEAs in comparison to commercial Pt are shown in Figure 5.8. At the activation region, all PdIr MEAs have similar performance but PdIr-20 performs slightly better than PdIr on untreated carbon and PdIr-40. The performance of PdIr-40 begins to deteriorate at the Ohmic region, possibly due to a problem with the membrane. Overall, all PdIr MEAs still perform worse than commercial Pt MEA.

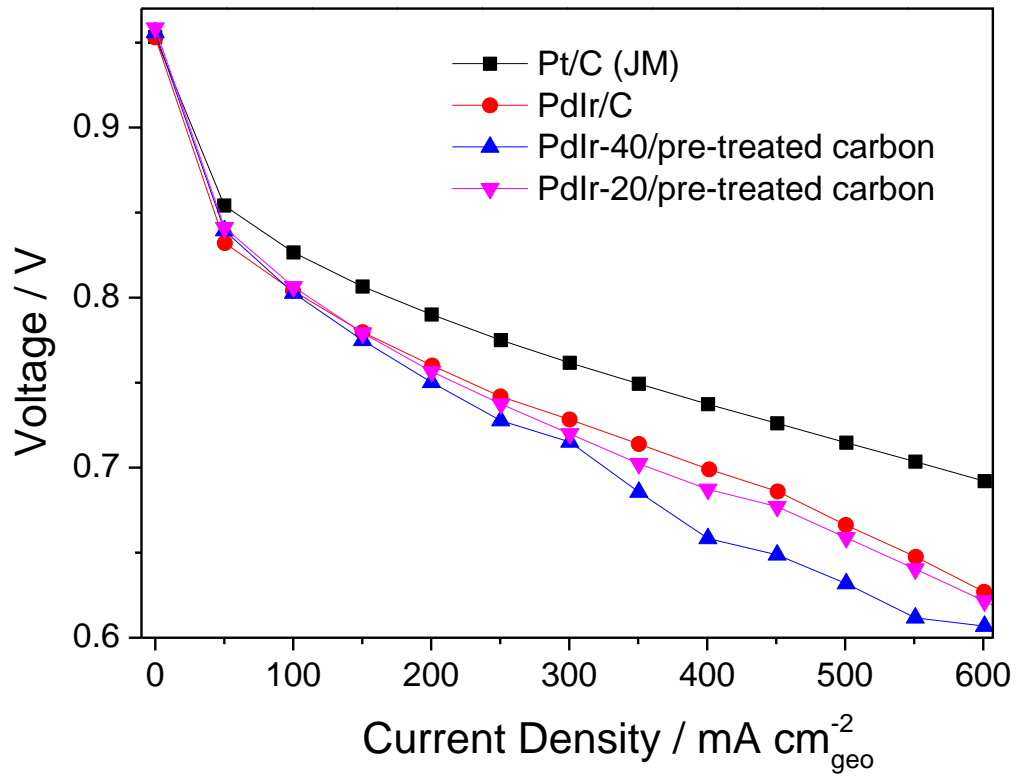


Figure 5.8: Polarisation curves of a single-cell operating at 80°C with Pt (JM) and PdIr as anode catalysts. Conditions: 5.29 cm² cell, 100% relative humidity anode and cathode, 1 atm. Load-based stoichiometry: Anode = 2.0; Cathode = 6.5 based on O₂ in air.

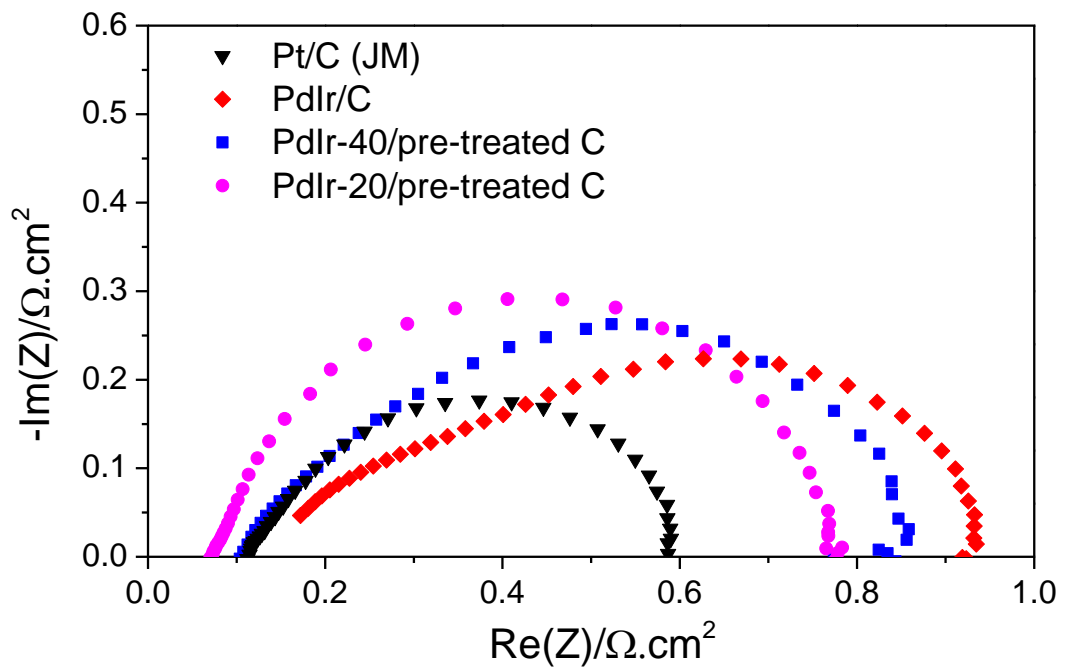


Figure 5.9: Nyquist plot of EIS data obtained at 100 mA cm⁻² for Pt and PdIr anode catalysts

The impedance spectra obtained at the activation region for Pt and PdIr MEAs are shown in Figure 5.9. From the results obtained in the previous section, it is likely that the cathode plays a significant role in reducing the overall performance of the MEAs, especially at low current density where ORR kinetics dominate. Therefore, it is necessary to separate the anode loss from the other losses using EIS. The quantification of the various losses contributing to the performance at the activation region is shown in Figure 5.10.

The cathode charge transfer resistance for all PdIr MEAs are similar, but still higher than that for Pt MEA despite using the same commercial Pt cathode. It is worth noting that the MEA fabrication method in this study is still unoptimised, which is likely to result in uneven catalyst layer at the anode side and correspondingly affecting the cathode side.

The anode charge transfer resistance decreases as ECSA increases. This shows that increasing the ECSA reduces the anode charge transfer resistance of PdIr anode catalyst. However, the total charge transfer resistances of PdIr MEAs are still higher than that for Pt MEA, which correlates with the polarisation curves data. The anode charge transfer resistance indicate that the HOR activity decreases in the order of Pt > PdIr-20 > PdIr-40 > PdI-40.

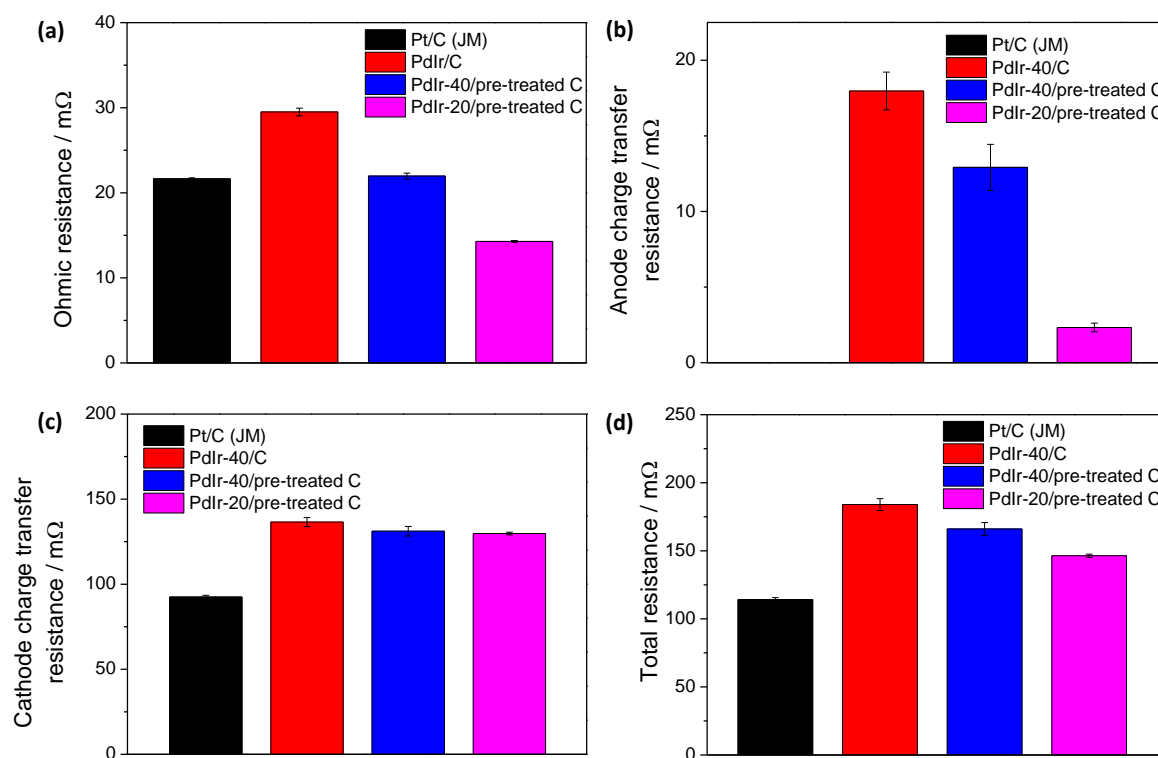


Figure 5.10 The resulting equivalent circuit element fitted values of the EIS data obtained at 100 mA cm^{-2} for Pt and PdIr anode catalyst MEAs showing the (a) ohmic resistance, (b) anode charge transfer resistance, (c) cathode charge transfer resistance, and (d) the sum of ohmic and charge transfer resistances.

The results above highlight the importance of catalyst layer design for PEMFC and the disadvantage of *in-situ* testing to screen new catalysts. The formation of the TPB is crucial in *in-situ* testing in order to maximise catalyst utilisation, which may not always be optimised for new catalysts. Catalyst utilisation relies on a number of properties such as ECSA, structure and distribution of ionomer, as well as interactions between ionomer and catalyst and catalyst support. As mentioned previously, the HOR is very fast in acidic electrolyte and therefore, RDE is not suitable. A new technique to study the kinetics of HOR catalytic activity using H_2 pump configuration with mass-transport free PEMFC based MEAs has been proposed.^{24, 268, 287} However, this technique still requires the use of optimised catalyst layer and MEA.

It is worth noting that the Pt anode used in this study is highly optimised with an ECSA in the region of $60 \text{ m}^2 \text{ g}^{-1}$,²⁷¹ twice higher than that of PdIr-20. A fair comparison would be to use in-house synthesised Pt catalyst and MEA fabricated using the same method. Nevertheless, this suggests that there is still room for improvement for PdIr catalyst. Further optimisation of the MEA preparation route, including ink composition and deposition method, is needed to achieve uniform distribution of the catalyst and ionomer layer. Optimisation of metal loading on carbon with respect to particle dispersion and morphology is also needed.

5.2.3 CO tolerance

In addition to high activity, it is highly appropriate that an anode catalyst is also CO tolerant. The CO polarisation curves for Pt and PtRu are shown in Figure 5.11. For Pt, the polarisation curves are linear at 25–50 ppm CO but two distinct slopes are seen for ≥ 100 ppm CO. Similar CO polarisation curve behaviour for Pt is observed in the literature. The two distinct slopes are speculated to be due to higher rates of CO oxidation to CO_2 at high current densities, leading to higher HOR rates. Despite the noise in the PtRu CO tolerance data, it can be clearly seen that PtRu exhibits higher performance than Pt in all CO concentrations, especially at low current densities (0 – 300 mA cm^{-2}).

The effect of CO on the catalyst performance of PdIr catalysts is shown in Figure 5.12. PdIr-40 refers to 40 wt% PdIr on untreated carbon and PdIr-20 refers to 20 wt% PdIr on pre-treated carbon. PdIr-20 exhibits the best performance at low CO concentrations (25–50 ppm); however, the performance drops significantly at higher CO concentrations (≥ 100 ppm). PdIr-1 has the worst performance, even at low CO concentration.

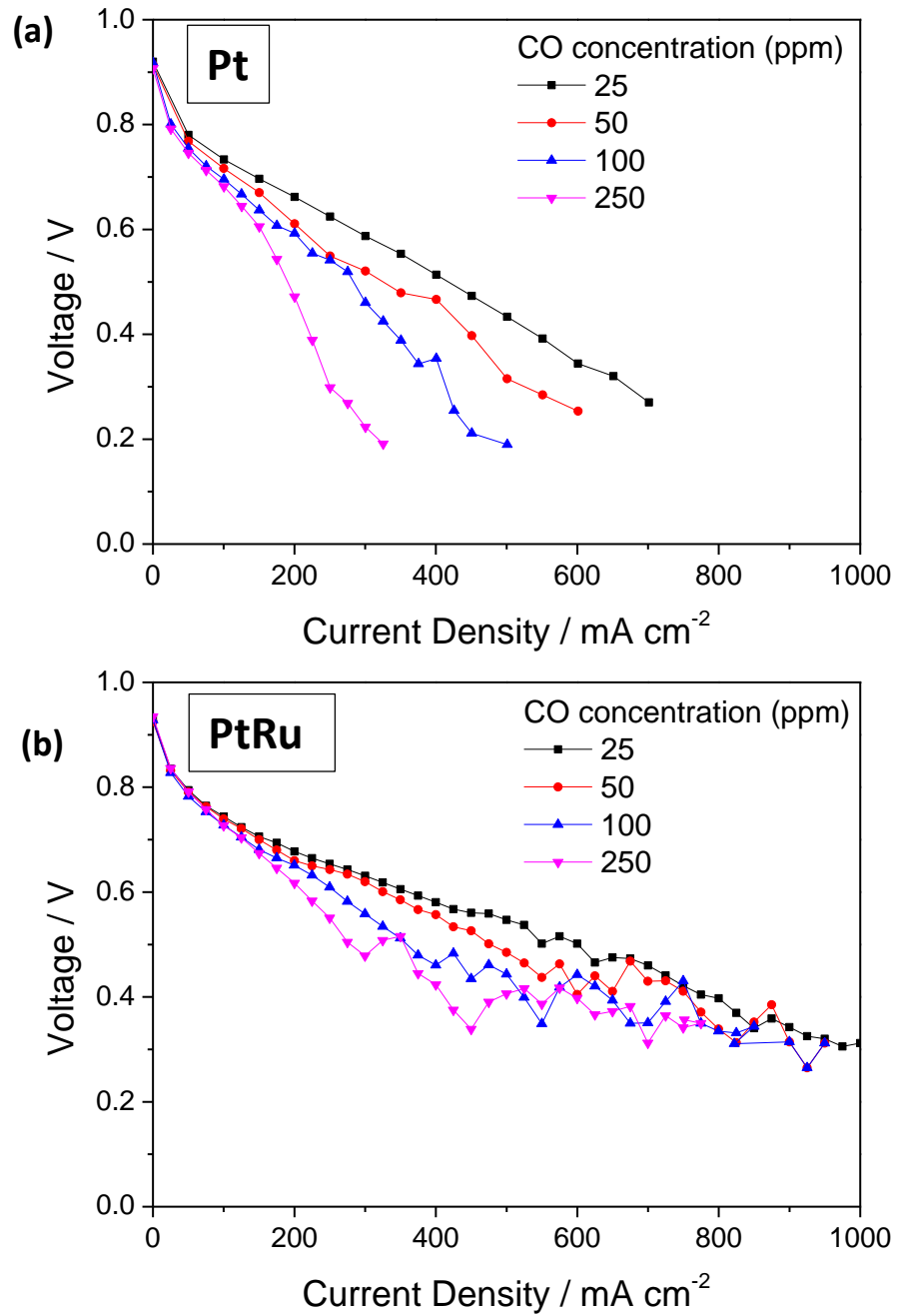


Figure 5.11: CO polarisation curves for (a) Pt and (b) PtRu MEAs operating with H₂/CO fuel with various CO concentrations in a single-cell operating at 80°C. Conditions: 5.29 cm² cell, 100% relative humidity anode and cathode, 1 atm. Stoichiometry: Anode = 2.0, constant flow rate; Cathode = 6.5 based on O₂ in air, load-based.

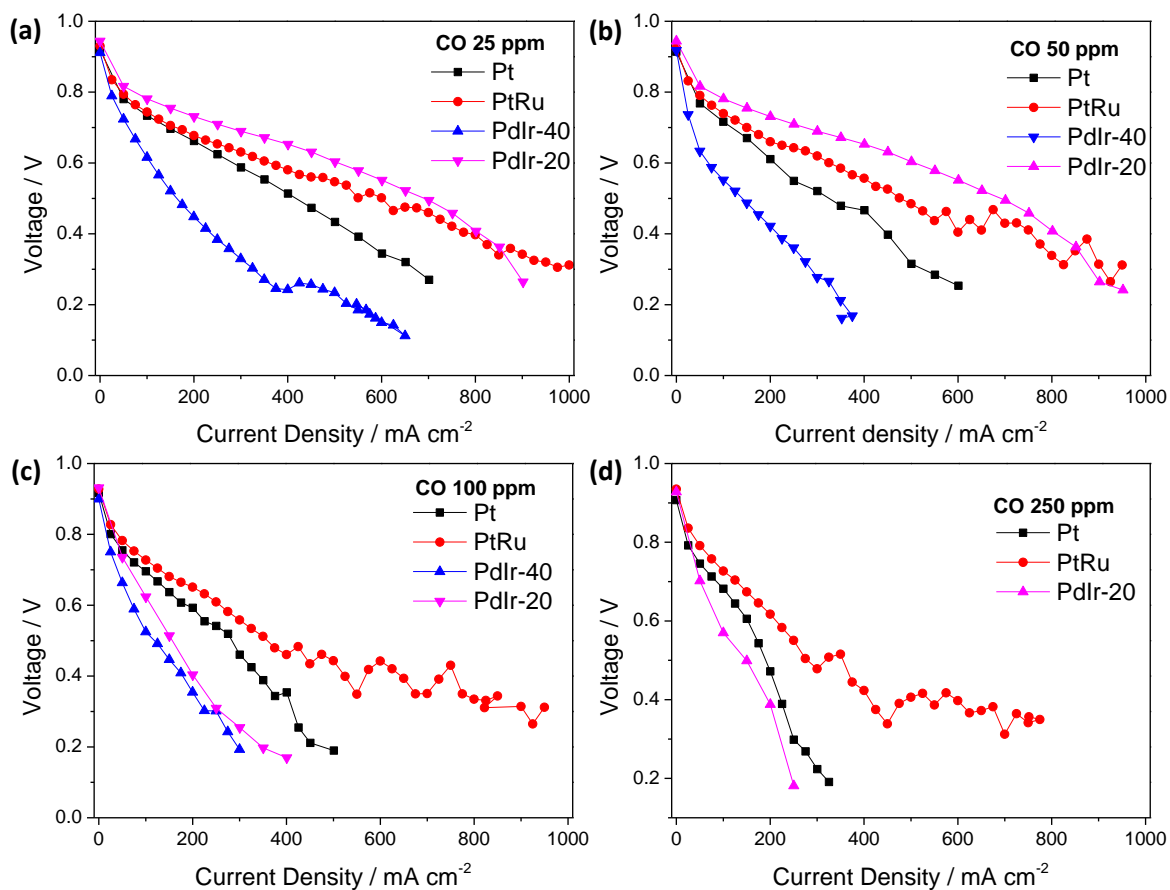


Figure 5.12: CO polarisation curves for Pt, PtRu and PdIr MEAs operating with H₂/CO fuel with various CO concentrations in a single-cell operating at 80°C. Conditions: 5.29 cm² cell, 100% relative humidity anode and cathode, 1 atm. Stoichiometry: Anode = 2.0, constant flow rate; Cathode = 6.5 based on O₂ in air, load-based.

Based on the results obtained by CO-stripping voltammetry in Chapter 5, the CO tolerance of PdIr catalyst is attributed to the low CO coverage at the hydrogen region, indicating that the availability of free sites for hydrogen adsorption and oxidation is responsible for the CO tolerance observed in the CO polarisation curves. Therefore, the ECSA plays an important role in the performance enhancement. As PdIr-40 has a very low ECSA, there may not be enough active surface area to sustain electrochemical reaction even at low CO concentrations. Similarly, at high CO concentrations, there are not enough active sites available to participate in hydrogen oxidation for PdIr-20. In PtRu, the CO tolerance is attributed to the bifunctional effect of Ru promoting the oxidation of CO on Pt, and therefore the ECSA plays a less important role.

5.3 Conclusions

The performance of PdIr (1:1, 40 wt%) as an anode catalyst was characterised in a real PEMFC. The MEAs was prepared in-house with commercial Pt electrodes used at the cathode, and compared to commercial Pt and PtRu anode electrodes. Since the cathode plays a bigger role in determining the overall performance of the MEA, EIS measurements were used to determine the HOR charge transfer resistance and exchange current density. Initial testing shows HOR activity in the order of Pt > PtRu > PdIr > Ir > Pd. EIS measurements also revealed that the cathode charge transfer resistance is consistently higher for MEA with in-house synthesised anode catalysts (PdIr, Pd and Ir). The bigger particle size and severe agglomeration seems to affect the cathode catalyst layer during MEA fabrications.

Further optimisation by pre-treating the carbon support and reducing the metal loading on carbon improves the particle dispersion, resulting in a higher ECSA. The new optimised catalyst (PdIr/C, 1:1, 20 wt%) has a lower anode charge transfer resistance. However, the performance is still worse than commercial Pt MEA. Additional optimisation of the PdIr catalyst in terms of particle size distribution and ink composition to further enhance the catalyst utilisation could offer improvement in performance.

Finally, the CO tolerance of PdIr was compared to Pt and PtRu. The results suggest that the ECSA plays an important role in the CO tolerance of PdIr catalyst. CO-stripping voltammetry in Chapter 5 shows that the surface of PdIr is not fully poisoned by CO. PdIr-20 (20 wt%) with improved ECSA has the best tolerance at low CO concentrations. However, at CO concentrations higher than 50 ppm, the CO tolerance was worse, indicating that the available unpoisoned surface area was not sufficient to maintain the reaction. PdIr-40 (40 wt%) exhibits poor performance at all CO concentrations due to its low ECSA. The results suggest that PdIr catalyst could replace Pt in applications where low level of CO is present.

Given the similar durability observed for PdIr and Pt catalyst (on the same carbon support) in *ex-situ* tests, it is likely that PdIr MEA would show similar performance degradation to Pt MEA. However, a long-term *in-situ* durability testing is required to verify the results, which is currently not possible in this work due to constraints on time and equipment.

Chapter 6

6 Alternative Catalyst Supports: Graphitic-Carbon Nitrides

6.1 Background

In addition to activity, the stability of supported electrocatalysts is another important consideration and is influenced by the following two effects: (1) stability of the support materials and the metals in electrochemical environments, and (2) interaction between the metal and the support materials. Currently, there is little work in the literature on the use of graphitic carbon nitride in electrocatalysis, although this is expected to change in the near future. The first application of graphitic carbon nitride as a catalyst support was reported by Yu et al. in 2007, where it was shown that PtRu supported on graphitic carbon nitride in DMFCs exhibits 78-83% higher power density than on Vulcan XC-72.²²¹ However, no durability studies have been performed yet. In this study, catalysed and non-catalysed polymeric carbon nitride materials (gCNM) were prepared and characterised physically and electrochemically. In addition, durability studies were performed using an accelerated stress-testing protocol.

6.2 Experimental

6.2.1 Synthesis of Graphitic Carbon Nitride

Polymeric carbon nitride (gCNM) was prepared by thermolysis and condensation reactions of a 1:1 molar ratio mixture of dicyandiamide (DCDA, $C_2N_4H_4$) and melamine ($C_3N_6H_9$) at 550°C. A finely ground sample was loaded in an alumina boat into a quartz tube in a tubular furnace under nitrogen flow. The temperature was raised to 550°C at 5°C/min for 15 h.

6.2.2 Synthesis of Pt/gCNM

The Pt catalyst was deposited onto gCNM using the ethylene glycol reduction method (*polyol method*). Ground gCNM (0.09 g) was dispersed in 200 mL of ethylene glycol (Fisher Scientific) and chloroplatinic acid (39.82% Pt basis, 0.1507 g, Sigma Aldrich) was added to the suspension. The mixture was stirred for 4 hours under inert atmosphere and then heated to 140°C for 3 hours, resulting in a dark brown mixture.

The solid product was collected via vacuum filtration and dried at 60°C in a vacuum oven. The Pt loading was fixed at 40 wt%.

6.2.3 Structural and Compositional Characterization

C, N, H analyses for gCNMs were performed using a Carlo-Erba EA1108 system. SEM was performed with a JEOL JSM-6301F field emission imaging system at 5 kV. TEM images were taken using a JEOL JEM1010 instrument operating at 80 kV, equipped with a Gatan Orius camera system. HR-TEM images were taken using JEOL CX-100 operating at 200 kV. The X-ray diffraction data were obtained using a Bruker-AXS D4 system for the support materials, and STOE powder diffractometer for the supported catalyst materials. BET measurements were carried out using a Micrometrics ASAP 2420 Surface Area / Porosity Analyser.

6.2.4 Electrochemical Characterisation

The performance of gCNM was compared to Vulcan XC-72R (Cabot corp.), whereas the performance of catalysed Pt/gCNM (40 wt% Pt/gCNM) was compared to Pt/Vulcan (40 wt%, HiSPEC 4000, Alfa Aesar). Commercially available HiSPEC4000 catalysts are platinum supported on Vulcan XC-72R carbon.²⁸⁸ Electrochemical measurements were carried out in a conventional three-electrode cell connected to an Autolab PGSTAT32 potentiostat. The electrode ink was prepared by dispersing the material in 70% isopropanol and ultrasonicated the mixture for 30 minutes. The ink was deposited on the GC and dried at room temperature, resulting in a loading of 52.5 $\mu\text{g cm}^{-2}$ for gCNM and 35 $\mu\text{g cm}^{-2}$ for Pt/gCNM. All electrochemical measurements were carried out at 25°C in 0.1 M HClO₄, except for MOR which was carried out in 1 M CH₃OH + 0.1 M HClO₄. The electrolyte was thoroughly purged with N₂ for 30 minutes prior to every experiment. All chemicals used were analytical grade and solutions were prepared with deionised water (Millipore, 18.2 M Ω .cm).

An accelerated stress testing protocol to induce carbon corrosion was used for the durability test. One cycle involves applying a voltage hold at 1.0 V for 30 seconds followed by two sequences of voltage cycling between 1.0 – 1.5 V at 0.5 V s⁻¹. The change in cyclic voltammogram (capacitance) was monitored after 1, 10, 20, 50, 100,

200, 500, 1000 and 2000 cycles. The test was conducted at 60°C in N₂ purged 0.1 M HClO₄.

6.3 Results and discussions

6.3.1 Synthesis and chemical characterisation

6.3.1.1 gCNM

Layered carbon nitride was prepared by thermolysis and condensation reactions of 1:1 molar ratio mixtures of dicyandiamide (C₂N₄H₄) and melamine (C₃N₆H₉) at 550°C for 15 h.¹¹⁶ Finely ground samples were heated in a tubular furnace under N₂ flow at 5°C per minute and allowed to cool to room temperature before being removed. Upon heating, the condensation process takes place by removal of NH₃ species leading to materials with different C:N:H stoichiometry depending on the synthesis temperature.¹¹⁶ The product obtained is pale yellow in colour and elemental analysis revealed that the material had a composition of C_{3.0}N_{5.2}H_{1.6}.

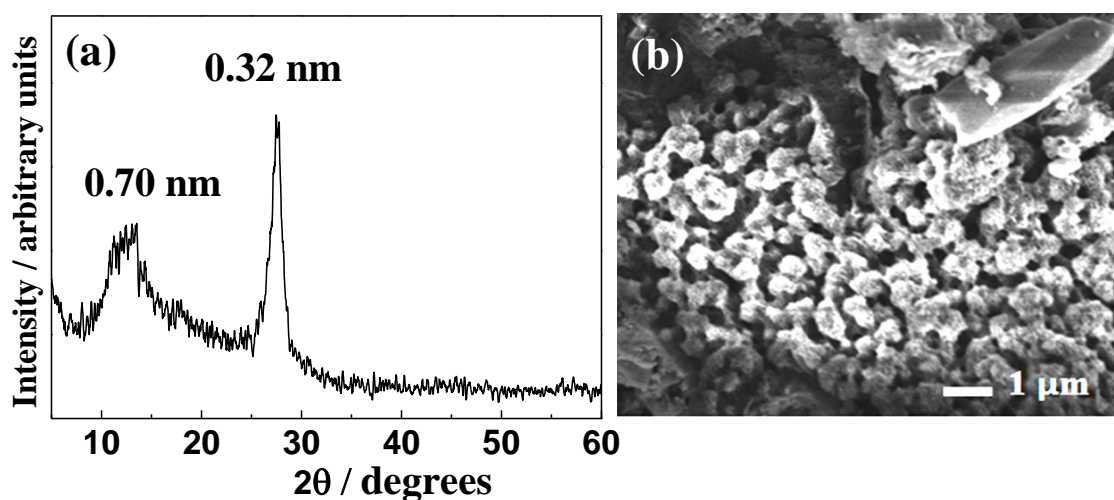


Figure 6.1: X-ray diffraction pattern (a) and SEM image (b) of a typical layered carbon nitride prepared by thermal condensation of DCDA/melamine 1:1 molar ratio.

A typical X-ray diffraction pattern (XRD) is shown in Figure 6.1(a). The strong peak at ~27.5° 2θ corresponds to a repeat distance of ~0.32 nm that correlates with the 002 reflection usually observed for graphitic materials. The feature around 12.5° 2θ

corresponds to an in-plane repeat distance of 0.70 nm that matches with the dimensions of polyheptazine or polytriazine structures within the layers.

Scanning Electron Microscope (SEM) examination indicates that gCNM exhibits a latticework of interlocking planar microstructures with individual layer thicknesses on the order of 2-3 nm that give rise to porous aggregates with pore sizes on the order of a few nm. This material is not highly condensed and its structure is believed to be close to that of Liebig's melon.²⁰¹ The aggregates are fused together to give rise to much larger pores (1-2 μm) in the resulting solid, as shown in Figure 6.1. The microstructures, with surface terminations, defects and nitrogen atoms, are believed to be beneficial for electron localisation or for anchoring active sites.²¹⁵

The BET measurements showed a surface area of 28 $\text{m}^2 \text{g}^{-1}$. Thermal gravimetric analysis (TGA) reveals that gCNM begins to decompose at above $\sim 440^\circ\text{C}$, and decomposition was complete by 670°C , indicating high thermal stability. Indeed, the thermal stability of graphitic carbon nitride is one of the highest for an organic material, although it is highly dependent on the preparation methods and degrees of polymerisation.²¹⁵

6.3.1.2 Pt/gCNM

The average particle size for Pt/gCNM is estimated to be 8.0 nm. In comparison, the average particle size of Pt/Vulcan is 4.2 nm, as shown in Figure 4.2. As gCNM has one order of magnitude less BET surface area compared to Vulcan XC-72R carbon, the same mass percentage loading of Pt nanoparticles on Vulcan XC-72R carbon result in higher Pt particle density on gCNM, which could be observed by TEM (Figure 6.2). As a result, the metal particles are in close proximity to each other, thus particle migration and sintering is greater.

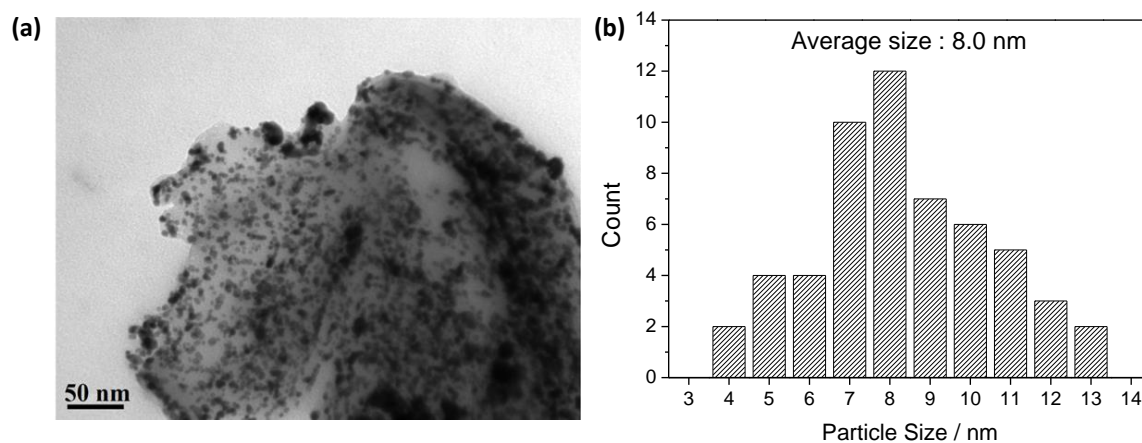


Figure 6.2: (a) TEM image and (b) particle size distribution of Pt/gCNM

Figure 6.3 shows the X-ray diffraction pattern of Pt/Vulcan and Pt/gCNM. The characteristic Pt nanoparticles peaks at $39.8^\circ 2\theta$ and $46.5^\circ 2\theta$ correspond to Pt 111 and 200 reflections, respectively. The peaks for Pt/gCNM are sharper, indicating a higher degree of crystallinity and larger particle sizes. Average Pt crystallite sizes calculated from 111 signal widths using the Scherrer equation²⁸⁹ is 8.9 nm, which is in good agreement with the TEM images.

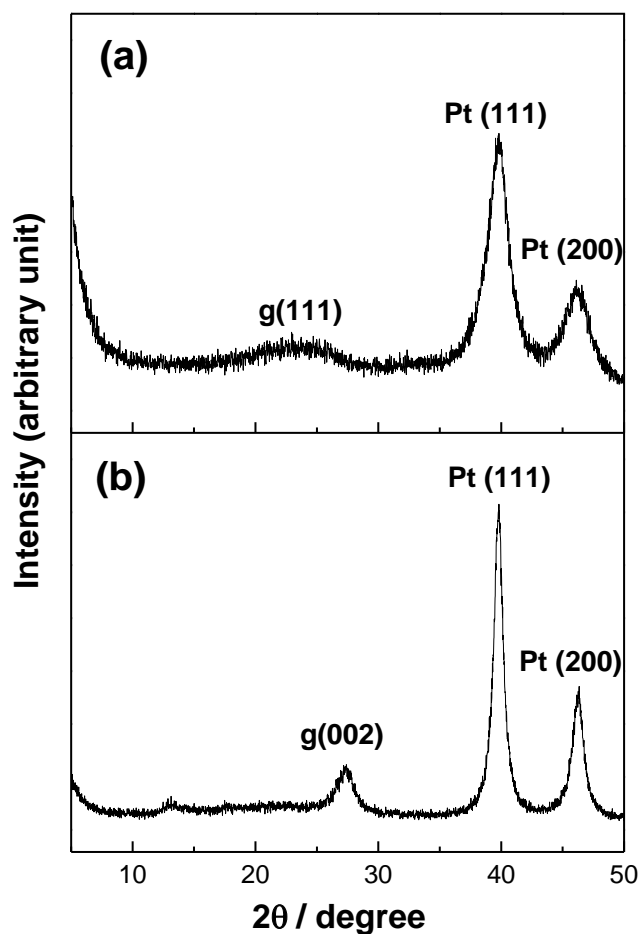


Figure 6.3: X-ray diffraction pattern of (a) Pt/Vulcan (Alfa Aesar) and (b) Pt/gCNM

6.3.2 Durability studies

The stability of the gCNM and Vulcan XC-72R carbon was determined by observing the change in double-layer capacitance in the cyclic voltammetry measurements while performing the carbon corrosion test, as shown in Figure 6.4. The capacitance was calculated at 0.40 V and normalised to the 10th scan. Capacitance increases with the number of scans due to an increase in surface area and concentration of hydrophilic carbon corrosion products with oxygen functionalities at the surface of the carbon support.^{274, 290} The presence of oxygen functionalities reduces the durability of PEMFC catalysts by promoting carbon corrosion. In addition, a more hydrophilic surface may affect water management in fuel cells and potentially contribute to performance instability and variability.

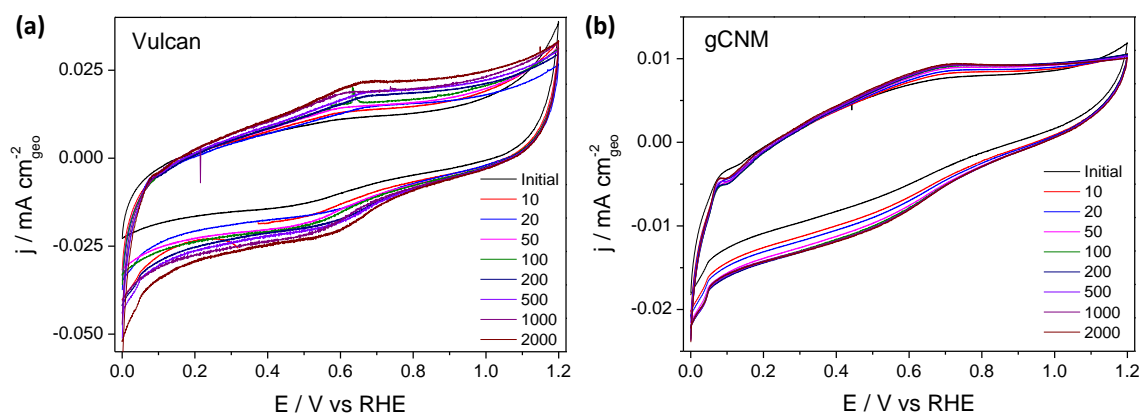


Figure 6.4: The evolution of cyclic voltammograms of (a) Vulcan, and (b) gCNM during the accelerated carbon corrosion cycling.

Figure 6.5 shows the corrosion behaviour of gCNM in comparison to Vulcan. For the first 100 cycles, both materials show a similar degree of corrosion/surface modification. However, above 100 cycles, Vulcan continues to corrode, whereas gCNM is more resistant, exhibiting a near plateau behaviour. At the end of the 2000 cycles, Vulcan shows a 166% change in capacitance whereas gCNM only shows a 133% change.

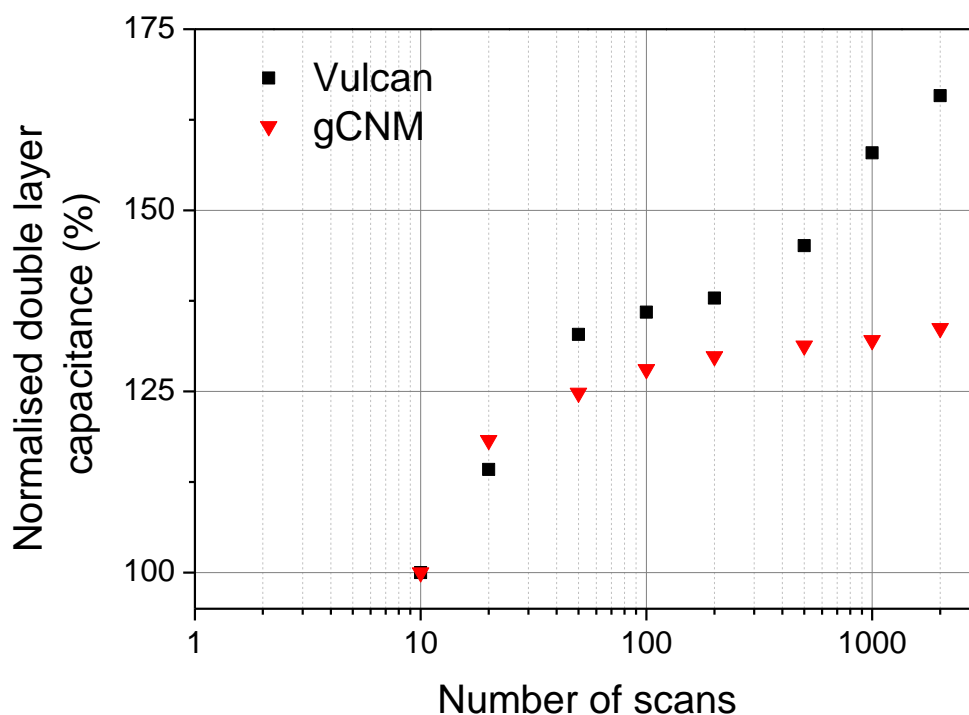


Figure 6.5: Change in double-layer capacitance (at 0.40 V) of the support materials as a result of accelerated carbon corrosion cycling.

The durability of catalysed gCNM (Pt/gCNM) is compared to Pt/Vulcan. The CVs of Pt/Vulcan and Pt/gCNM are displayed in Figure 6.6. Since the hydrogen region for Pt/gCNM is not as well defined as for Pt/Vulcan, the ECSA for Pt/gCNM is calculated from hydrogen desorption region (0.10 V to 0.40 V). The ECSA calculated for Pt/Vulcan and Pt/gCNM are $28.6 \text{ m}^2 \text{ g}^{-1}$ and $7.2 \text{ m}^2 \text{ g}^{-1}$, respectively. As expected, Pt/gCNM has a smaller ECSA due to larger particle size and agglomeration (8.0 nm compared to 4.2 nm for Pt/Vulcan). In addition, gCNM is not very soluble in the solvent, resulting in uneven electrode layer on the glassy carbon surface, which means that catalyst utilisation is very low.

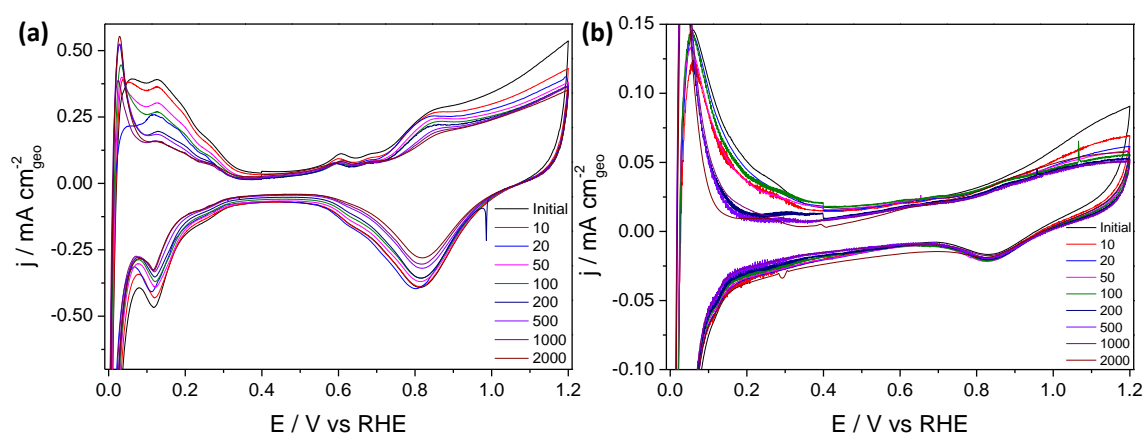


Figure 6.6: The evolution of cyclic voltammograms of (a) Pt/Vulcan, and (b) Pt/gCNM during the accelerated carbon corrosion cycling.

The degree of the catalysed carbon corrosion was evaluated using the same accelerated protocol. The CV was recorded and ECSA was calculated as part of the diagnostic, as shown in Figure 6.7. The decrease in ECSA is believed to be due to platinum agglomeration and dissolution as a result of carbon corrosion.^{274, 291, 292} After 2000 scans, the ECSA decreased by 36.3% for Pt/Vulcan and 75.6% for Pt/gCNM, despite gCNM having higher degree of corrosion tolerance. The lower durability of Pt/gCNM could be attributed to the lower ECSA and presence of agglomeration, which indicates that the catalyst deposition method is not optimized.

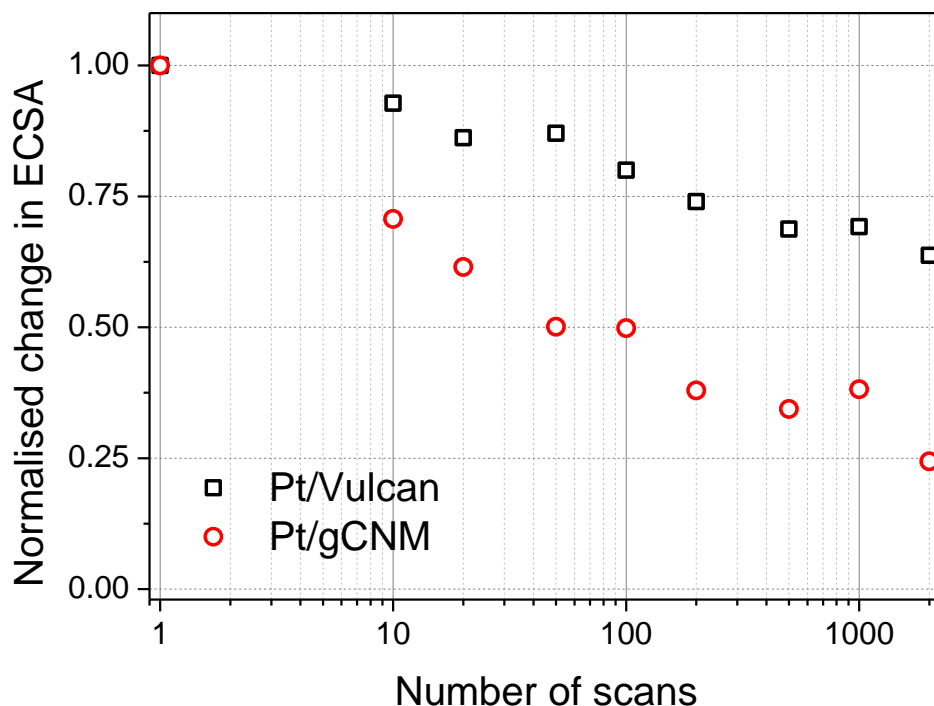


Figure 6.7. The change in ECSA (calculated from hydrogen adsorption/desorption) of the supported Pt electrocatalysts as a result of accelerated carbon corrosion cycling.

6.3.3 Electrocatalytic Activity

The catalytic activity of Pt/gCNM was examined to further investigate the potential application of gCNM in PEMFCs. It is believed that gCNM has inherent catalytic activity²⁹³ and the use of gCNM as a catalyst support has been shown to significantly improve the performance of DMFCs.²²¹

Figure 6.8(a) shows the ORR polarization curves for both Pt/Vulcan and Pt/gCNM. Both Pt/Vulcan and Pt/gCNM have similar onset potential; however, the current density for Pt/gCNM increases at a slower rate up to 2.5 mA cm^{-2} . The poor current density could be attributed to the low surface area, which limits the number of active sites, as well as the poor conductivity of gCNM. The Levich-Koutecky plot extracted from the ORR polarization curves at various rotation rates is presented in Figure 6.8(b) and the results are summarized on Table 6.1. The specific activity of Pt/gCNM is 5 times higher than that for Pt/Vulcan, which indicates that Pt/gCNM has a higher ORR activity per ECSA. The mass activity is small because of the low ECSA.

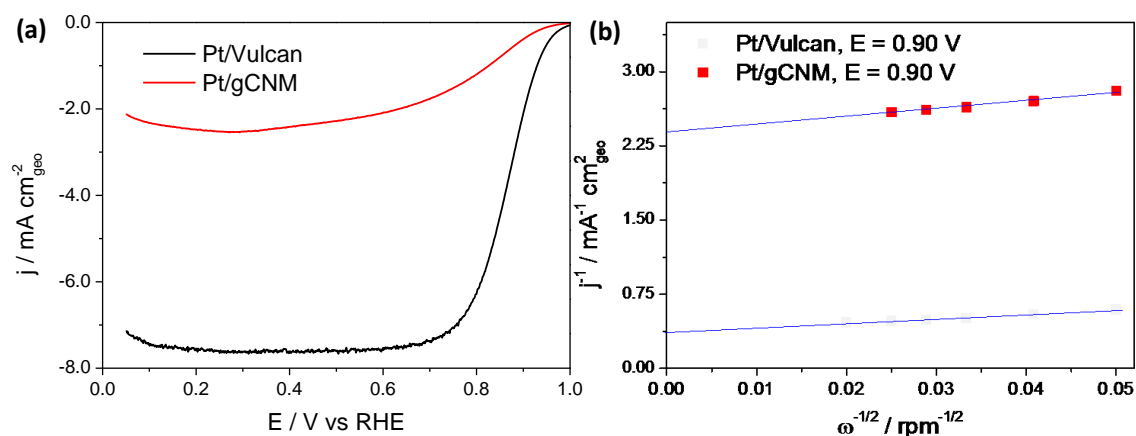


Figure 6.8. (a) Oxygen reduction reaction polarisation curves at 1600 rpm in O_2 -saturated 0.1 M $HClO_4$, and (b) Levich-Koutecky plot at 0.90 V for Pt/Vulcan and Pt/gCNM.

In order to evaluate the methanol oxidation activity, CV measurements were conducted with the Pt/Vulcan and Pt/gCNM electrode immersed in a 1 M methanol + 0.1 M $HClO_4$ solution. It is generally accepted that low overpotential and high peak current density is an indication of good MOR activity. The current density is normalised to the ECSA of each respective material due to the substantial differences in ECSA. Figure 6.9 shows that the best performance for methanol oxidation, normalised to the electrochemical surface area, is achieved on Pt/gCNM, with peak potential of 0.850 V (ca. 0.903 V for Pt/Vulcan) and peak current density of $3.21 \text{ mA cm}^{-2}_{ECSA}$, almost 4 times higher than that for Pt/Vulcan. MOR peak potential values may be influenced by particle size effects: a smaller Pt nanoparticle enhances the oxidation of poisoning intermediates and hence, decreases the peak potential.²⁹⁴ Given the difference in the particle size of both materials, with Pt/gCNM having the larger particle size, we can eliminate particle size effect on the decrease in the peak potential. This indicates that the use of gCNM as catalyst support leads to true intrinsic MOR catalytic enhancement.

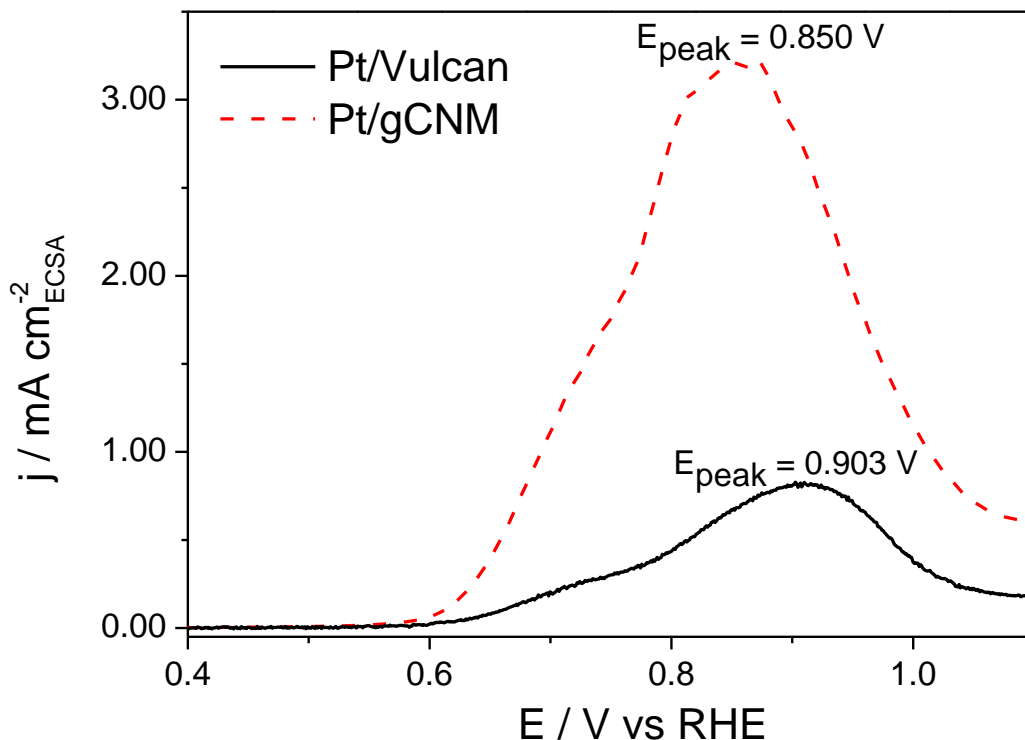


Figure 6.9. Methanol oxidation reaction of Pt/Vulcan and Pt/gCNM electrocatalyst in 1 M CH_3OH + 0.1 M HClO_4 at 25°C.

Table 6.1: The ORR specific activity, mass activity, methanol oxidation peak potential (E_{peak}) and maximum methanol oxidation reaction current density (j_{max}) of supported Pt electrocatalysts.

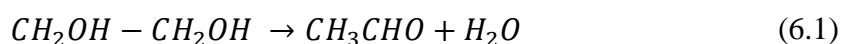
	ORR		MOR	
	Specific Activity ($\mu\text{g cm}^{-2}_{\text{ECSA}}$)	Mass Activity ($\text{A mg}^{-1}_{\text{Pt}}$)	E_{peak} (V)	j_{max} ($\text{mA cm}^{-2}_{\text{ECSA}}$)
Pt/Vulcan	396	0.15	0.903	0.821
Pt/gCNM	2050	0.02	0.850	3.21

The results suggest that gCNM has intrinsic catalytic activity for ORR and MOR, corroborating the results reported in the literature. However, the low surface area of gCNM is still a huge barrier – if the surface area can be improved, it may be a promising material as a catalyst support for fuel cells.

6.3.4 Synthesis optimisation

6.3.4.1 Higher pH conditions and low metal loading

In order to enhance catalyst utilisation of Pt on gCNM electrocatalyst, it is necessary to reduce the particle size and improve the particle dispersion on the support. In the previous section, the ethylene glycol reduction method was chosen due to its straightforwardness and has been shown to produce catalyst with narrow particle size distribution in comparison to the chemical precipitation method. Ethylene glycol has high dielectric constant and reduction ability. At high temperatures ethylene glycol decomposes to generate reducing species for the reduction of the metallic ions to metal particles.²⁹⁵ Thus, ethylene glycol acts as both a solvent and a protecting agent. Polyvinylpyrrolidone (PVP) was commonly employed as a steric stabiliser but some studies have showed that this material strongly adsorbs on Pt metals, resulting in unsupported Pt nanoparticles.²⁹⁶ It was found that the pH of the Pt precursor solution plays an important role in controlling the particle size during the synthesis – high pH (7.4 – 9.2) result in a more uniform Pt dispersion.^{295, 297, 298} The following mechanism was proposed to explain the pH effect during the formation of the Pt nanoparticles:



The acetate (CH_3COO^-) forms chelate-type complexes to the Pt via its carboxyl group and acts as a stabiliser for the Pt atoms. At low pH, this interaction is poor, resulting in agglomerated metal nanoparticles with large size and wide size distribution.²⁹⁵

Normally, high metal loading is desirable in order to produce thin electrodes. However, as shown above, gCNM has lower BET surface area and therefore the metal loading has to be reduced in order to prevent agglomeration. As such, three Pt/gCNM catalysts at various loadings (5 wt%, 10 wt% and 20 wt%) were synthesised using the same polyol method but at higher pH. 0.1 M KOH was added dropwise into the solution and maintained at pH 9 for 30 minutes, before the temperature was increased.

The resulting catalysts were examined using TEM, as shown in Figure 6.10. All metal loadings resulted in small particle size (2.7 – 3.4 nm) with narrow size distribution. At 20 wt%, the Pt nanoparticles are still agglomerated, indicating that the metal loading is still high. At 5 wt%, the loading is too low so the surface of the support is not fully coated with the Pt nanoparticles. 10 wt% appears to be the optimum metal loading with uniform dispersion of Pt nanoparticles.

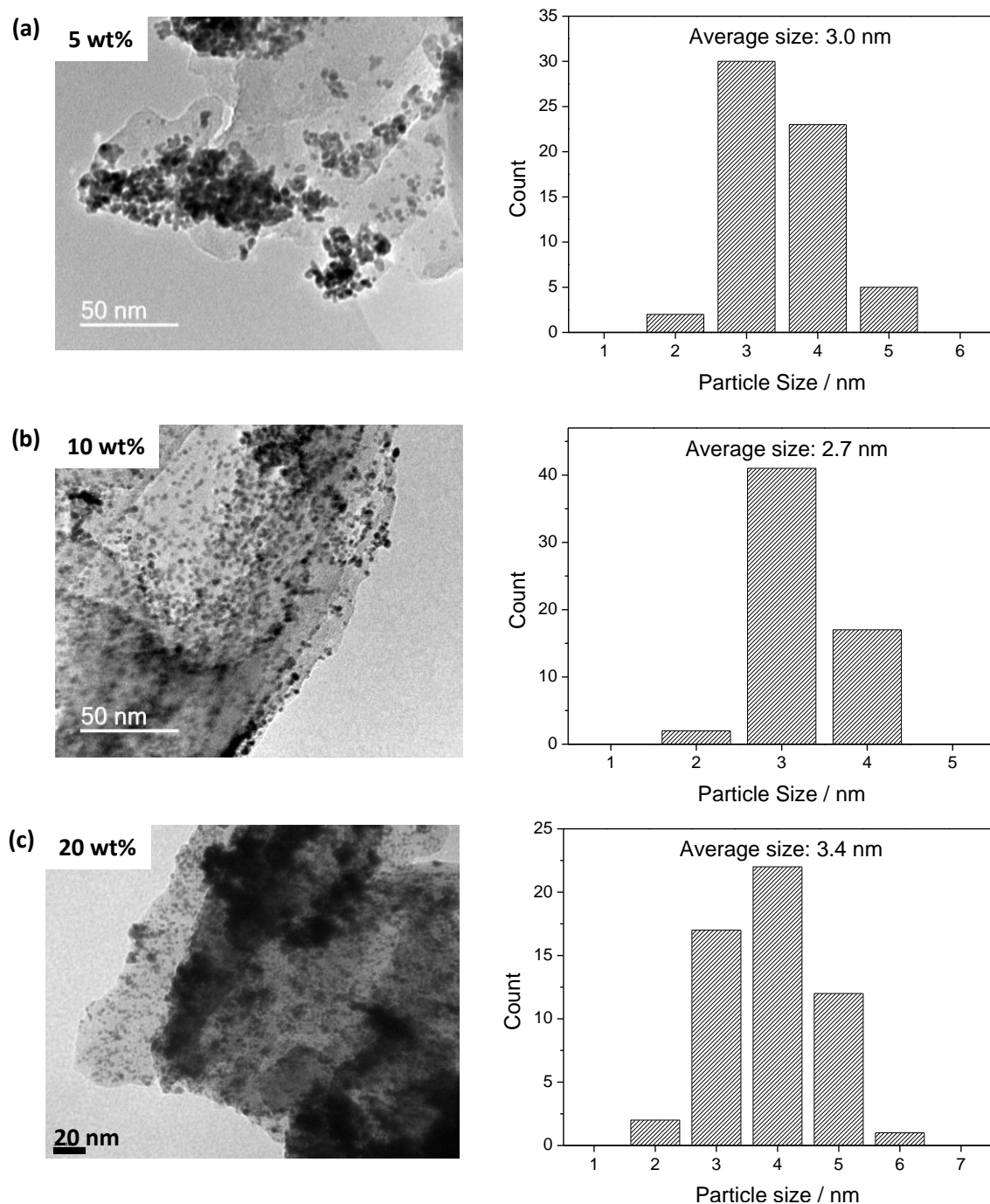


Figure 6.10. The TEM images particle size distribution of Pt/gCNM at various metal loadings: (a) 5 wt% Pt, (b) 10 wt% Pt, and (c) 20 wt% Pt.

The catalysts were then characterised electrochemically to determine their ECSA. At 20 wt%, an ECSA of $2 \text{ m}^2 \text{ g}^{-1}$ was obtained, which is much lower than at 40 wt%. Interestingly, below 10 wt% there does not appear to be any distinctive Pt peaks in the cyclic voltammogram. The reason is not clear but one explanation could be that, since gCNM has a two-dimensional structure, the catalysts are being horizontally stacked on the gCNM layers, as illustrated in Figure 6.11. This results in a loss of active sites, even at high metal loading, as most metal nanoparticles are superimposed in between the layers. At low loading, most of the metal nanoparticles will be shielded, resulting in an almost complete loss of active sites. In addition, the poor conductivity of gCNM means the buried metal nanoparticles are not accessible.

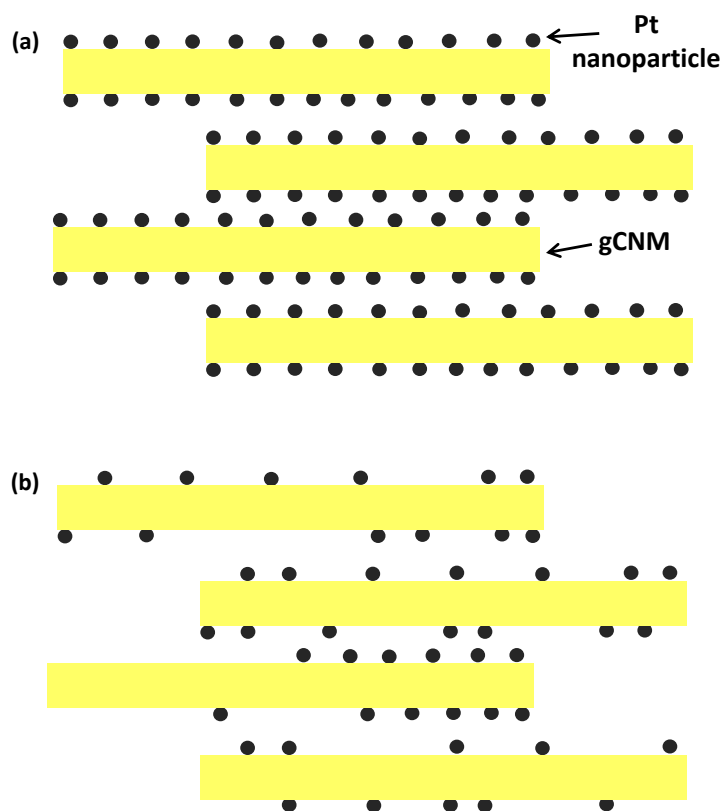


Figure 6.11. Schematic diagram of Pt/gCNM at (a) high metal loading, and (b) low metal loading.

6.3.4.2 Addition of spacer material

In light of the difficulty encountered above, a more effective strategy is required to improve catalyst utilisation on gCNM. It was reported that the addition of spacing material, such as carbon black, disrupts the horizontal stacking of graphene sheets,

making them randomly distributed.²⁹⁹ Since gCNM has the same two-dimensional structure as graphene, theoretically the same approach could be used to increase the utilisation of Pt on gCNM, as illustrated in Figure 6.12.

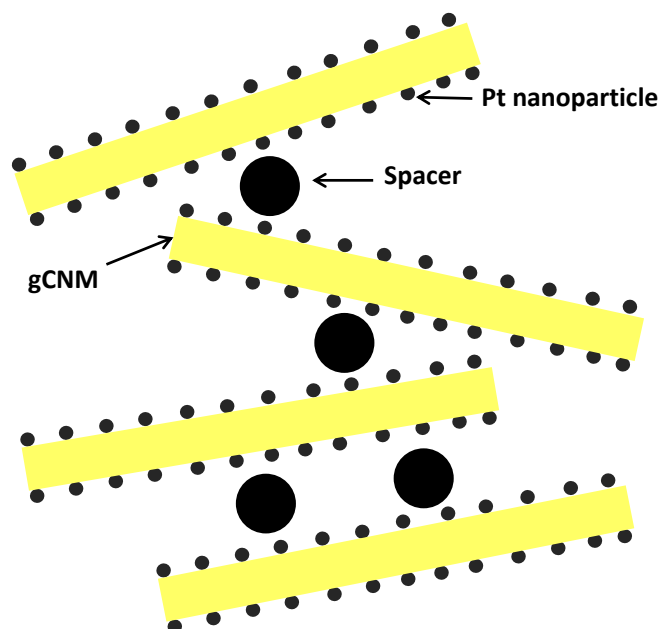


Figure 6.12. Pt supported on gCNM with the addition of spacers.

In the first set of experiments, catalyst ink was prepared by ultrasonating 10 wt% Pt/gCNM with Vulcan carbon (10 wt%) and Nafion solution in IPA. However, this resulted in two layers of slurry with well-dispersed carbon on top and Pt/gCNM in the bottom layer. Pt/gCNM was separated due to the huge difference in solubility. A second attempt was made by synthesising 10 wt% Pt on a blend of gCNM and Vulcan carbon via high pH ethylene glycol reduction method. This also resulted in two layers of catalyst ink.

6.3.4.3 Protonated gCNM

Based on the results above, it is clear that the insolubility of gCNM makes characterisation and processing difficult. One strategy to increase the solubility of gCNM is by direct protonation with strong acid. Zhang and co-workers demonstrated that adding protons to gCNM led to better degree of dispersions in aqueous solutions, a four times increase in BET surface area (8 to $30 \text{ m}^2 \text{ g}^{-1}$), as well as higher ionic conductivity.³⁰⁰

Therefore, gCNM was first stirred in HCl (37%) for 3 hours at room temperature. This changed the colour of the powder from yellow to pale yellow. Zhang reported that protonation blue-shifts the optical band gap of gCNM.³⁰⁰ Next, Pt at various loadings (10 wt% and 20 wt%) was deposited on gCNM/H⁺Cl⁻ via the ethylene glycol reduction method. The resulting catalysts were characterised using TEM and electrochemical methods.

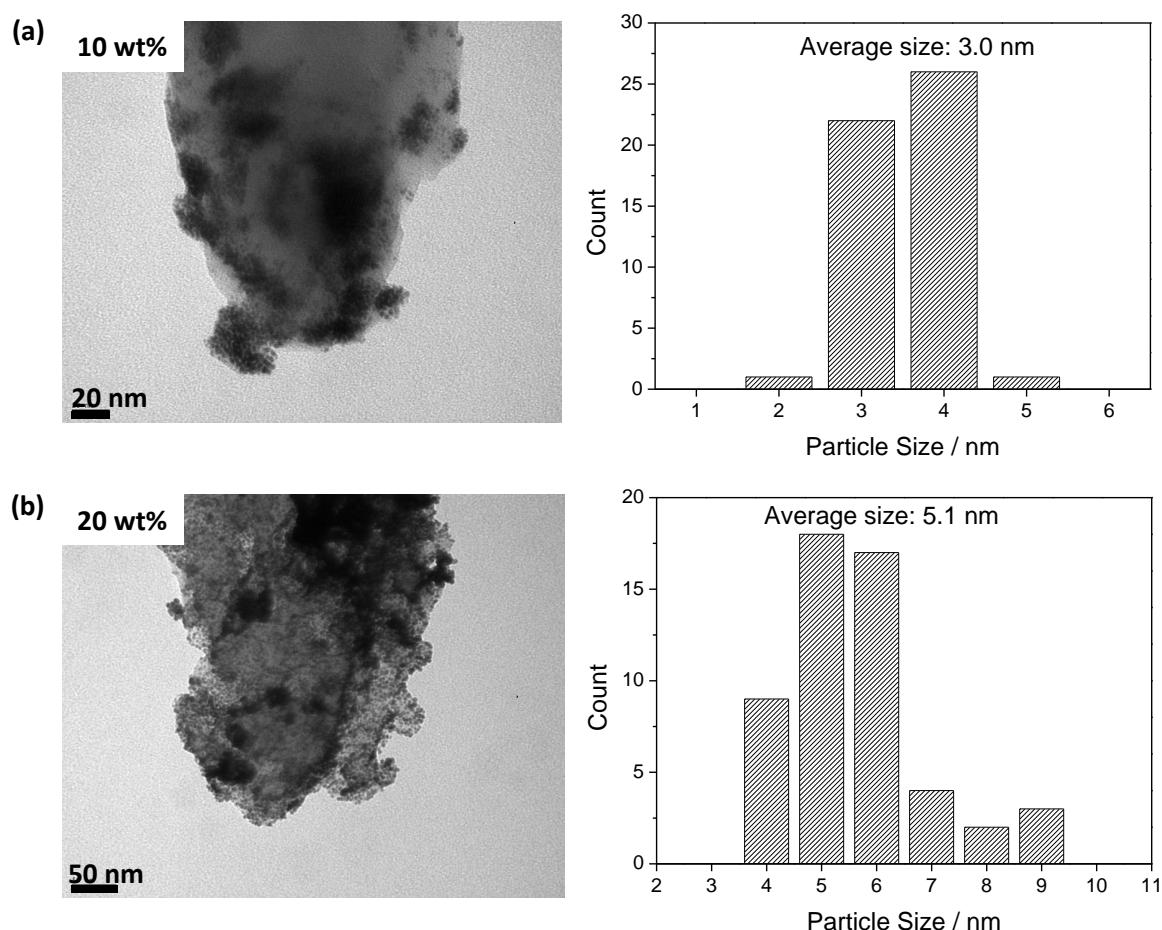


Figure 6.13. TEM image and particle size distribution of Pt/gCNM-H⁺Cl⁻ at (a) 10 wt% Pt and (b) 20 wt% Pt.

Figure 6.13 shows the TEM images of both catalysts and their particle size distribution. At 10 wt% metal loading, the average particle size is 3.0 nm with narrow particle size distribution. However, the Pt nanoparticles are not well-dispersed, with many areas uncoated and agglomeration formed at random. At 20 wt%, the average particle size is bigger and agglomeration also exists; however, the surface is fully coated with Pt. Electrochemical testing resulted in a 10 m² g⁻¹ ECSA for 20 wt% Pt/gCNM-H⁺Cl⁻,

indicating that protonation is an effective method to enhance the surface area as well as catalyst utilisation. However, no Pt peaks were found on 10 wt% Pt/gCNM-H⁺Cl⁻. It is important to note that both catalysts dispersed very well in IPA solution during the ink fabrication, indicating that the protonation was successful and the electrode quality should not be a barrier. Even though protonation increases the surface area and solubility, gCNM-H⁺Cl⁻ still retains its stacked structure, which brings us back to the first problem whereby catalyst active sites are obscured in between the gCNM sheets. Nevertheless, mixing the catalyst ink with carbon did not improve the result.

6.3.4.4 Future work: exfoliated and protonated gCNM

Even though protonation was successful in increasing catalyst utilisation, it is still far from achieving high efficiency. It is clear that a combination of strategies is required to fully utilise the potential of gCNM for electrocatalysis purposes. Recently, it was reported that it is possible to exfoliate bulk gCNM into nanosheets using a simple protocol.³⁰¹ The resulting nanosheets retain the structure of gCNM but with improved solubility and higher surface area ($\sim 384 \text{ m}^2 \text{ g}^{-1}$). SEM, TEM and AFM analysis reveal a uniform thickness of $\approx 2 \text{ nm}$ with less than 9 layers of nanosheets, with morphology similar to graphene or graphene oxide.

Therefore, for future work, it is proposed that a combination of exfoliation and protonation may offer a more successful pre-treatment route for gCNM. In addition, the inclusion of spacing materials in the catalyst ink is likely to improve the catalyst utilisation on the exfoliated and protonated gCNM.

6.4 Conclusions

Graphitic-carbon nitride materials (gCNM) are investigated for developing highly-durable catalyst supports for PEMFCs. The gCNMs are more electrochemically stable compared to conventional carbon black (Vulcan XC-72) following accelerated corrosion testing. After 2000 scans, the gCNM shows a 133% increase in double-layer capacitance compared to 166% for Vulcan. Despite the high durability, Pt/gCNM exhibits a large ECSA loss compared to Pt/Vulcan. This was attributed to the lower ECSA and presence of agglomeration on Pt/gCNM. Superior methanol oxidation and

oxidation activity is observed for Pt/gCNM on the basis of the catalyst ECSA, indicating that gCNM also acts as a co-catalyst.

However, further work is required to realize the potential of gCNM as a catalyst support. An attempt was made to reduce Pt particle size and improve particle dispersion on gCNM. This includes increasing the pH of the synthesis solution, reducing the metal loading, and pre-treating the carbon. The main difficulty encountered is the insolubility of gCNM. Nevertheless, it was shown that protonating the gCNM in acid improves the solubility as well as catalyst utilisation. For future work, a combination of exfoliation and protonation as a pre-treatment route for gCNM is proposed.

7 Modified Graphitic Carbon Nitride as Catalyst Support

7.1 Background

As mentioned in Section 2.3.5, graphitic carbon nitride is highly tunable and there are a large number of reports in the literature on the modifications of the material.²¹⁵ The second material studied in this work is a highly crystalline carbon nitride (PTI-Li⁺Cl⁻) prepared by a simple self-condensation of dicyandiamide in molten eutectic lithium chloride and potassium chloride. Chemical modification via elemental doping is also an effective way for tuning the physicochemical properties of graphitic carbon nitride,^{208, 302} and therefore, a third material – boron-doped carbon nitride (B-gCNM) – is also synthesised in this study.

7.2 Experimental

The same protocol was followed as described in Chapter 6. However, platinum loading on support was reduced to 20 wt% to reduce agglomeration.

7.2.1 Synthesis of PTI-Li⁺Cl⁻

Crystalline poly(triazine)imide (PTI/Li⁺Cl⁻) was synthesized from DCDA in molten eutectic LiCl/KCl (45:55 wt%) mixtures heated at 400°C under N₂ (g) for 6 h then sealed under vacuum and heated to 600°C for 12 h.

7.2.2 Synthesis of B-gCNM

B-doped graphitic carbon nitride (B-gCNM) was prepared by using ionic liquids. In a typical synthesis, 1-butyl-3-methylimidazolium tetrafluoroborate (BmimBF₄) was dissolved in water and stirred for 5 min. Then DCDA was added and the mixture was heated at 100°C in an oil bath until the water completely evaporated. The resulting solid was then heated in an alumina crucible for 2 h at 350°C and kept at this temperature for 4 h. Then, the temperature was raised to 550°C for another 4 h, and finally cooled to room temperature.

7.2.3 Post-mortem analysis

Following AST, the catalyst was scraped off the surface of the glassy carbon carefully by dissolving it in methanol. The catalyst was then re-deposited onto a TEM grid and TEM was applied to determine the final morphology of the catalysts.

7.3 Results and discussions

7.3.1 Synthesis and chemical characterisation

7.3.1.1 PTI-Li⁺Cl⁻

Poly(triazine) imide carbon nitride (PTI/Li⁺Cl⁻) was prepared using an ionothermal route. This method allowed us to obtain a highly crystalline carbon nitride using relatively mild conditions. In a typical synthesis, DCDA was mixed with a eutectic mixture of LiCl/KCl (45:55 wt%) and heated at 400°C for 6 h under nitrogen followed by a thermal treatment under high vacuum at 600°C for 12 h, resulting in a yellow-brown powder. The PTI-Li⁺Cl⁻ compound exhibits a sharp series of peaks in the X-ray diffraction pattern consistent with a $P6_3cm$ unit cell (Figure 7.1a).^{303, 304} The hexagonal symmetry of the PTI-Li⁺Cl⁻ can be clearly seen in the SEM images of the hexagonal-shaped crystallites (Figure 7.1b), which is consistent with the literature.^{303, 305} This material is a triazine-based (C₃N₃)₂(NH)₃·LiCl structure with Li⁺ and Cl⁻ intercalated both within and between the graphitic layers, respectively.³⁰⁴

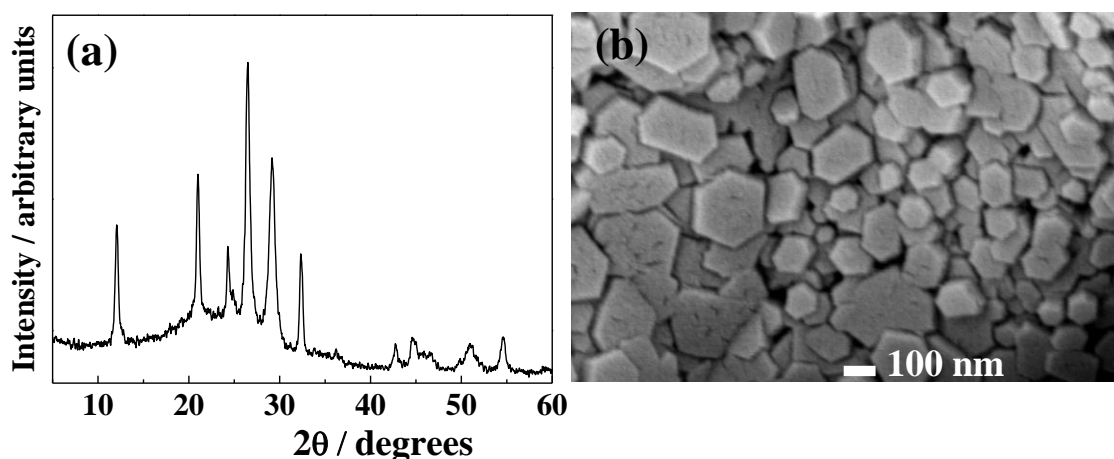


Figure 7.1. X-ray diffraction pattern (a) and SEM image (b) of a poly(triazine)imide carbon nitride prepared by ionothermal route.

The BET surface area of PTI/Li⁺Cl⁻ is reported to be ~37 m² g⁻¹, which is slightly higher than that for gCNM.³⁰⁵ Due to its highly crystalline structure, PTI/Li⁺Cl⁻ was reported to be a highly efficient photocatalyst for water splitting, especially when coated with Pt,^{305, 306} but there has not been any reports on its applications in fuel cells.

7.3.1.2 B-gCNM

1-butyl-3-methylimidazolium tetrafluoroborate (BmimBF₄) ionic liquid was used to modify the electronic structure of gCNM by substituting C ([He] 2s²2p²) by B ([He] 2s²2p¹). BmimBF₄ acts also as soft-template inducing higher porosity in the material.²⁰⁸ The X-ray diffraction pattern (Figure 7.2a) is dominated by the (002) interlayer-stacking reflection usually observed in gCNMs. The higher porosity of B-gCNM compared to gCNM and PTI-Li⁺Cl⁻ is clearly seen in the SEM images (Figure 7.2b). A homogeneous porosity with pores of about 50-75 nm were detected. These pores were considerably smaller than those observed in gCNM. The BET surface area of B-gCNM synthesised using the same method is reported to be 444 m² g⁻¹, which is significantly larger than that for gCNM.²⁰⁸ Although the use of boron-doped carbon as catalyst support has been widely studied in the literature, the use of boron-doped graphitic carbon nitride as catalyst support for fuel cells has never been studied before.

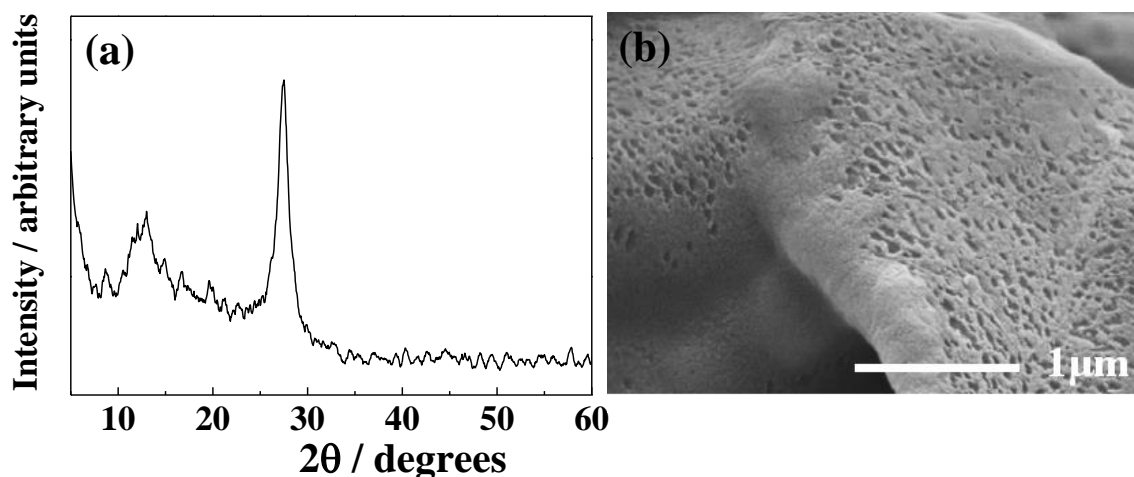


Figure 7.2. X-ray diffraction pattern (a) and SEM image (b) of B-gCNM doped with 10 wt% B.

7.3.2 Characterisation of supported catalysts

Platinum was deposited onto the supports via the ethylene glycol method. However, in this case the metal loading was reduced to 20 wt%. The materials were characterized via XRD and TEM. The XRD patterns (Figure 7.3) confirm the presence of platinum in each sample as characterized by the peaks at $39.8^\circ 2\theta$ and $46.5^\circ 2\theta$ corresponding to Pt 111 and 200 reflections, respectively.

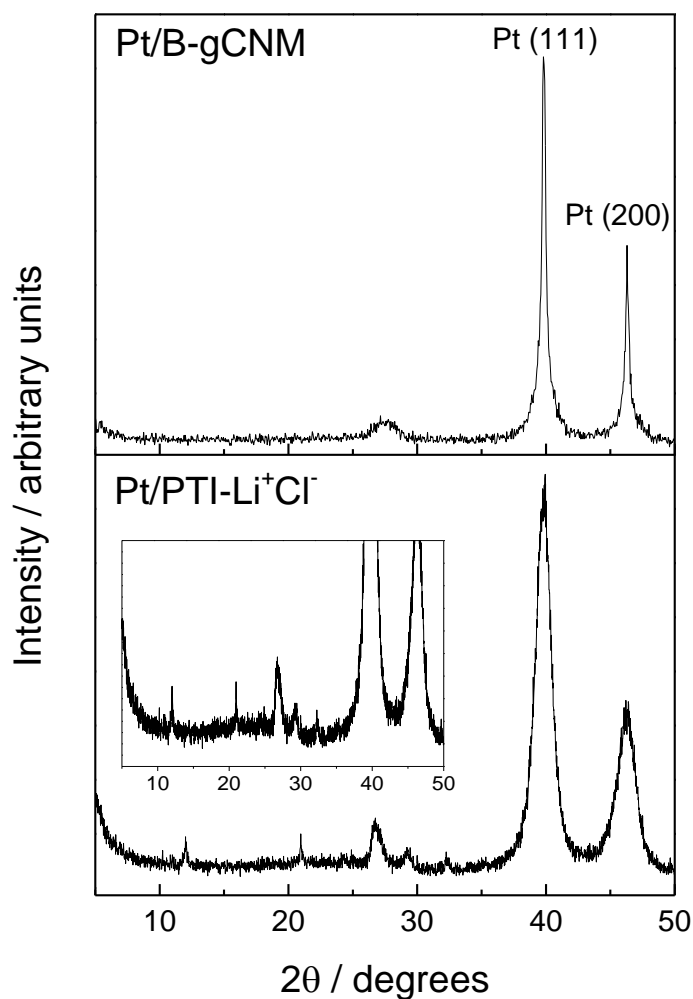


Figure 7.3. X-ray diffraction patterns of supported Pt electrocatalysts. Peaks for nanocrystalline Pt are significantly stronger than gCNM features. Inset: Magnification of the XRD pattern of Pt/PTI-Li⁺Cl⁻ confirming the presence of PTI-Li⁺Cl⁻.

The TEM images in Figure 7.4 and Figure 7.5 show both catalysts exhibit small average particle size with narrow particle size distribution. The average particle sizes of both catalysts are also smaller than that of Pt/gCNM (8.0 nm). This could be attributed to the

fact that the metal loading is lower, which means that there less particle per surface area of support, and the particles are further away from each other, and thus reducing the likelihood of particle migration and coalescence.

However, Pt particles on PTI-Li⁺Cl⁻ are more dispersed than on B-gCNM. Since [PtCl₆]²⁻ is used as a precursor for Pt deposition, it may not be deposited efficiently due to the presence of boron, which is electron deficient. Reducing the boron content or using a Pt cation precursor, depending on the composition of the material, could improve the particle dispersion

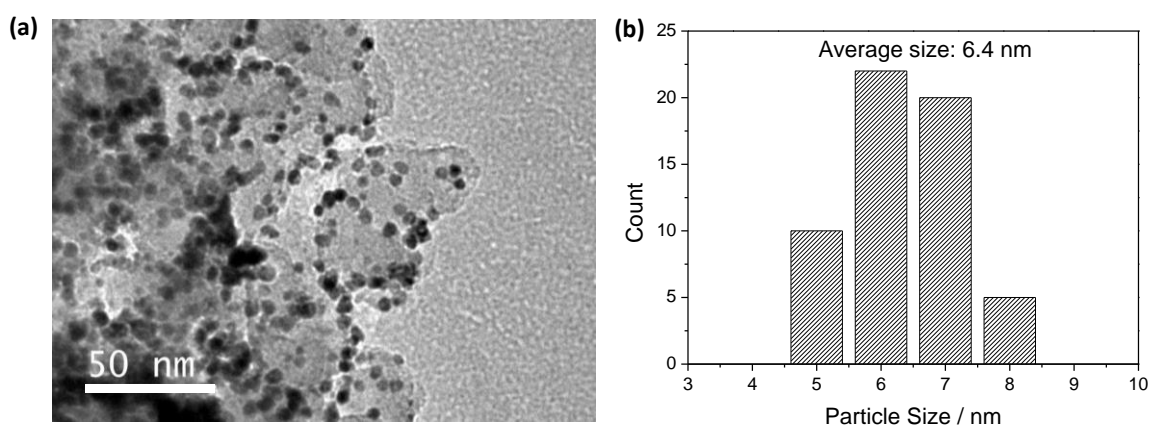


Figure 7.4. (a) HR-TEM image and (b) particle size distribution of Pt/PTI-Li⁺Cl⁻

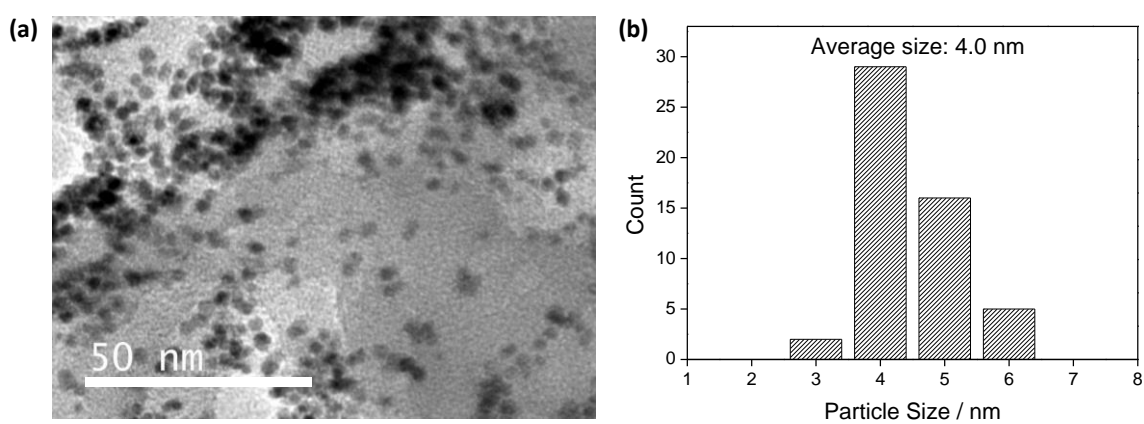


Figure 7.5. (a) HR-TEM image and (b) particle size distribution of Pt/B-gCNM

Table 7.1: The average particle and crystallite size of supported Pt catalysts. ^{a)} Estimated from TEM image based on the average of 100 particles; ^{b)} Calculated from 111 signal widths of XRD using the Scherrer equation.

	Particle size ^{a)} (nm)	Crystallite size ^{b)} (nm)
Pt/PTI-Li⁺Cl⁻	6.4	5.8
Pt/B-gCNM	4.2	3.3

7.3.3 Durability Studies

The durability of the modified graphitic carbon nitride materials were investigated in comparison to unmodified polymeric carbon nitride (gCNM). The change in capacitance as a result of carbon corrosion is shown in Figure 7.6. Both PTI-Li⁺Cl⁻ and B-gCNM have significantly higher degree of tolerance compared to gCNM. As PTI-Li⁺Cl⁻ has a higher degree of crystallinity, it is expected to exhibit higher tolerance towards carbon corrosion.⁴⁰ Despite the higher surface area of B-gCNM, it exhibits the highest durability. In addition to the terminal and bridging NH- groups, boron also acts as a Lewis acid on the surface which appears to reduce the electron density on carbon atoms, thus suppressing oxygen chemisorption. In addition, boron forms a protective layer of boron oxides on the surface, which further reinforces the inhibiting effect on corrosion.³⁰⁷⁻³⁰⁹

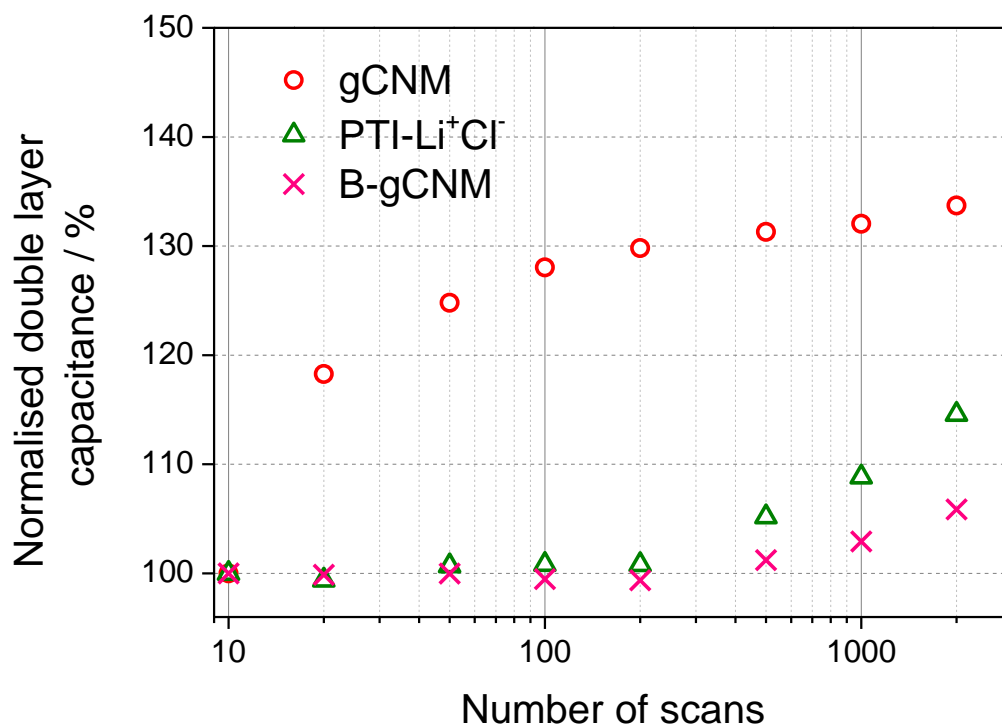


Figure 7.6. Change in double-layer capacitance (at 0.40 V) of the graphitic carbon nitride materials as a result of accelerated carbon corrosion cycling.

The durability of the materials in the presence of Pt nanoparticles was evaluated using the same accelerated protocol, with CV and ECSA recorded at regular intervals as part of the diagnostic. The results are summarized in Table 7.2. Pt/B-gCNM has a significantly lower initial ECSA compared to Pt/gCNM and Pt/PTI-Li⁺Cl⁻. This is attributed to the lower degree of particle dispersion and larger particle size, as shown in Figure 7.4(b). Pt/PTI-Li⁺Cl⁻ has the highest initial ECSA, twice larger than that for Pt/gCNM. In addition to the small particle size and enhanced particle dispersion, PTI-Li⁺Cl⁻ is more soluble in 70% IPA, owing to the presence of Li⁺ and Cl⁻, resulting in well-dispersed catalyst ink and better quality electrode.

Table 7.2. The ECSA of supported Pt electrocatalysts before and after the accelerated carbon corrosion cycling (2000 cycles).

	Initial ECSA (m² g⁻¹)	Final ECSA (m² g⁻¹)	ECSA loss (%)
Pt/gCNM	7.2	1.8	75.6
Pt/PTI-Li⁺Cl⁻	15.9	12.8	19.3
Pt/B-gCNM	1.9	0	100

Figure 7.7 shows the corrosion behaviour of the catalysed graphitic carbon nitrides as a result of accelerated stress-cycling. At the end of the 2000 cycles, Pt/B-gCNM displays the least tolerance with 100% ECSA loss, despite B-gCNM being the most durable. Pt/PTI-Li⁺Cl⁻ exhibits the highest durability at only 19.3% ECSA loss, which is even higher than the durability of commercial Pt/Vulcan (36.3% ECSA loss). From this result, it is also observed that graphitic carbon nitride supported Pt catalysts with higher initial ECSA exhibit higher electrochemical durability, indicating there is a link between good metal-support interaction and durability. Support material that provides strong adsorption and anchoring sites for the Pt nanoparticles will increase particle dispersion and limit dissolution and agglomeration processes during the accelerated test.¹⁸⁶

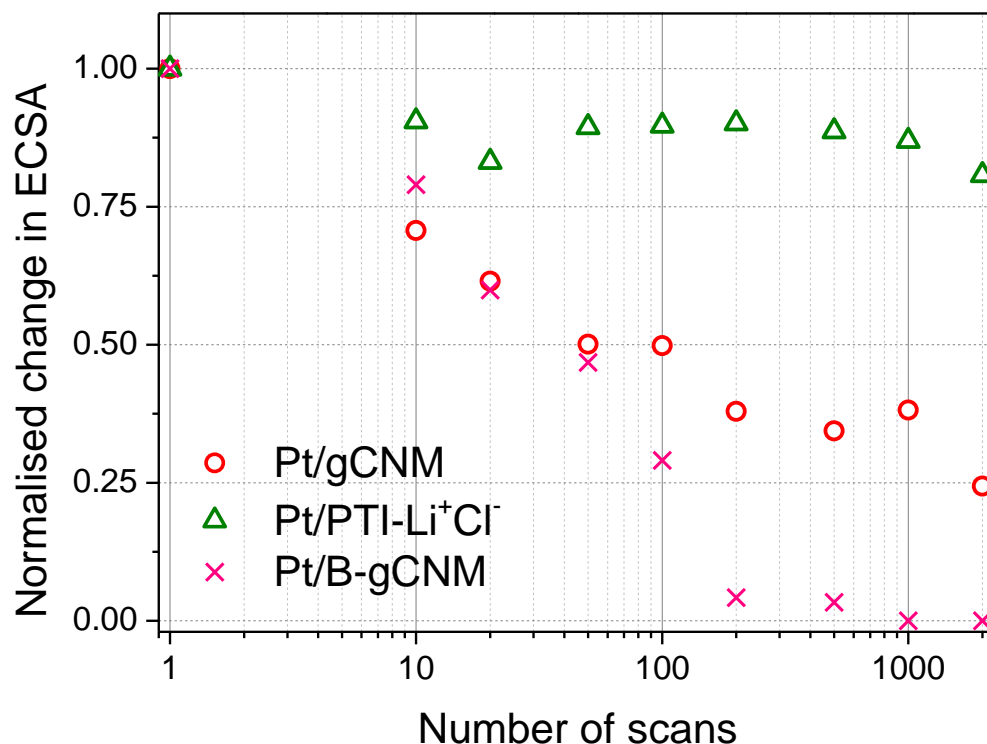


Figure 7.7. The change in ECSA (calculated from hydrogen adsorption/desorption) of the supported Pt electrocatalysts as a result of accelerated carbon corrosion cycling.

7.3.4 Post-mortem analysis

In order to study the degradation mechanism, post-mortem analysis was conducted to examine the changes in morphology after the AST test. TEM images in Figure 7.8 show significant agglomeration for Pt/gCNM and Pt/PTI-Li⁺Cl⁻. Supported Pt nanoparticles can migrate and sinter together to form agglomerates due to a reduction in the surface area of carbon support as a result of carbon corrosion. The distance between particles also play a role, smaller distance encourages particle coalescence since shorter travelling is required to establish contact. Even though gCNM and PTI-Li⁺Cl⁻ have graphitic structure and are more corrosion tolerant than commercial Vulcan carbon, they have smaller specific surface areas. This means that the same Pt metal loading on the support leads to catalysts with particles in close proximity with each other, which enhances agglomeration and coalescence.²³⁸

On the other hand, there are no metal particles seen on the post-mortem TEM image of Pt/B-gCNM following the AST test. It is not clear whether carbon support detaches along with Pt particles – further studies involving EDX to verify Pt:C elemental ratios

before and after AST testing or in-situ TEM analysis would be valuable. However, as shown in the previous section, B-gCNM is highly tolerant towards carbon corrosion, indicating that Pt dissolution is likely to be the main degradation mode and the interaction between Pt metal and B-gCNM is not as strong as initially thought.

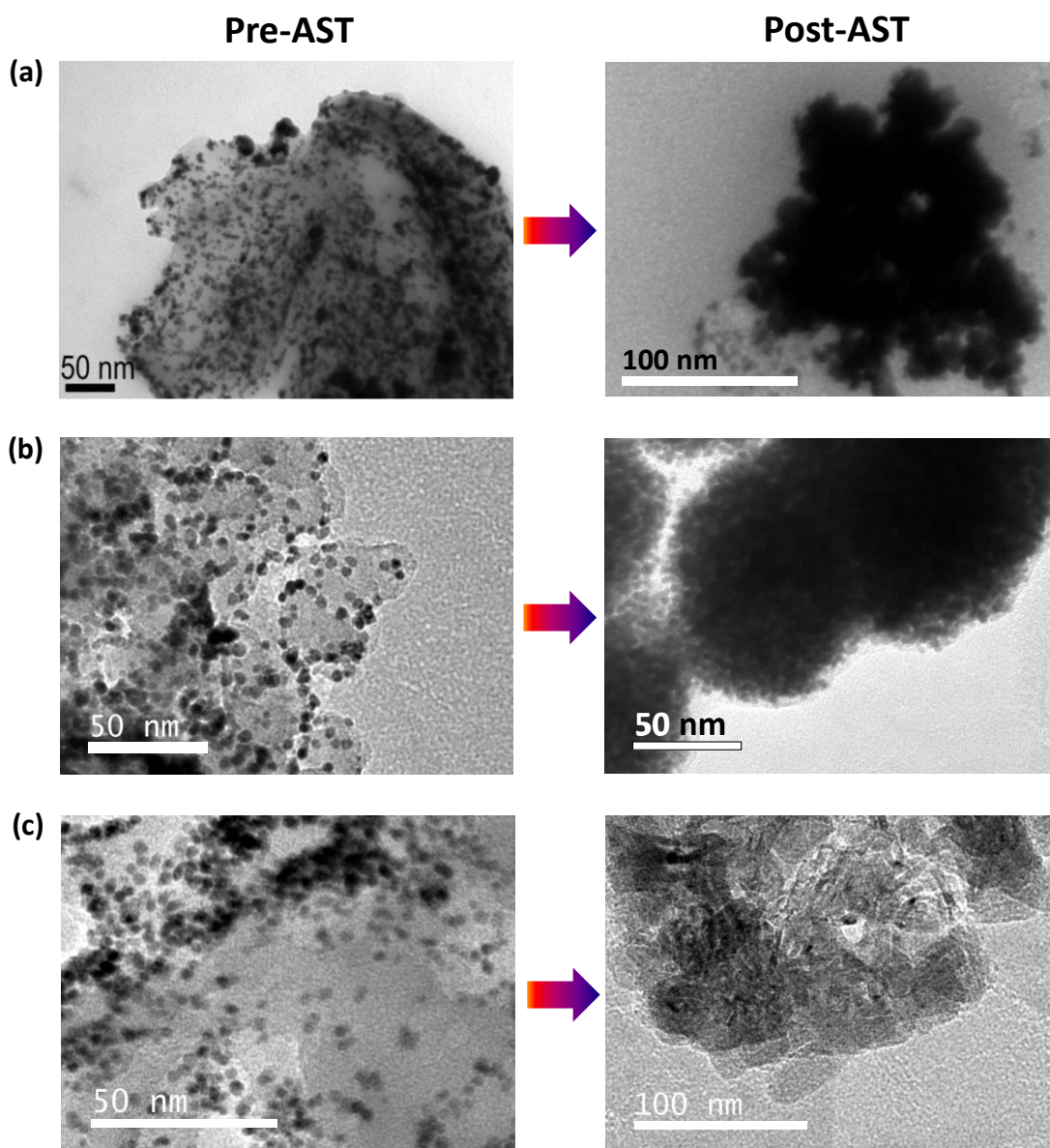


Figure 7.8. Pre and post-AST TEM images for (a) Pt/gCNM, (b) Pt/PTI-Li⁺Cl, and (c) Pt/B-gCNM.

7.3.5 Electrocatalytic activity

The catalytic activities of graphitic carbon nitride supported Pt catalysts were investigated in 1 M methanol + 0.1 M HClO₄ solution at 25°C, as shown in Figure 7.9. The current density is normalised to the ECSA of each respective material due to the differences in ECSA. The results are summarized on Table 7.3. All catalysts display similar MOR overpotential; however, Pt/PTI-Li⁺Cl⁻ exhibits significant improvement in MOR peak current density in comparison to Pt/gCNM. This can be attributed to the higher ECSA of Pt/PTI-Li⁺Cl⁻. By contrast, even though Pt/B-gCNM has the lowest ECSA, it exhibits the highest peak current density compared to all catalysts.

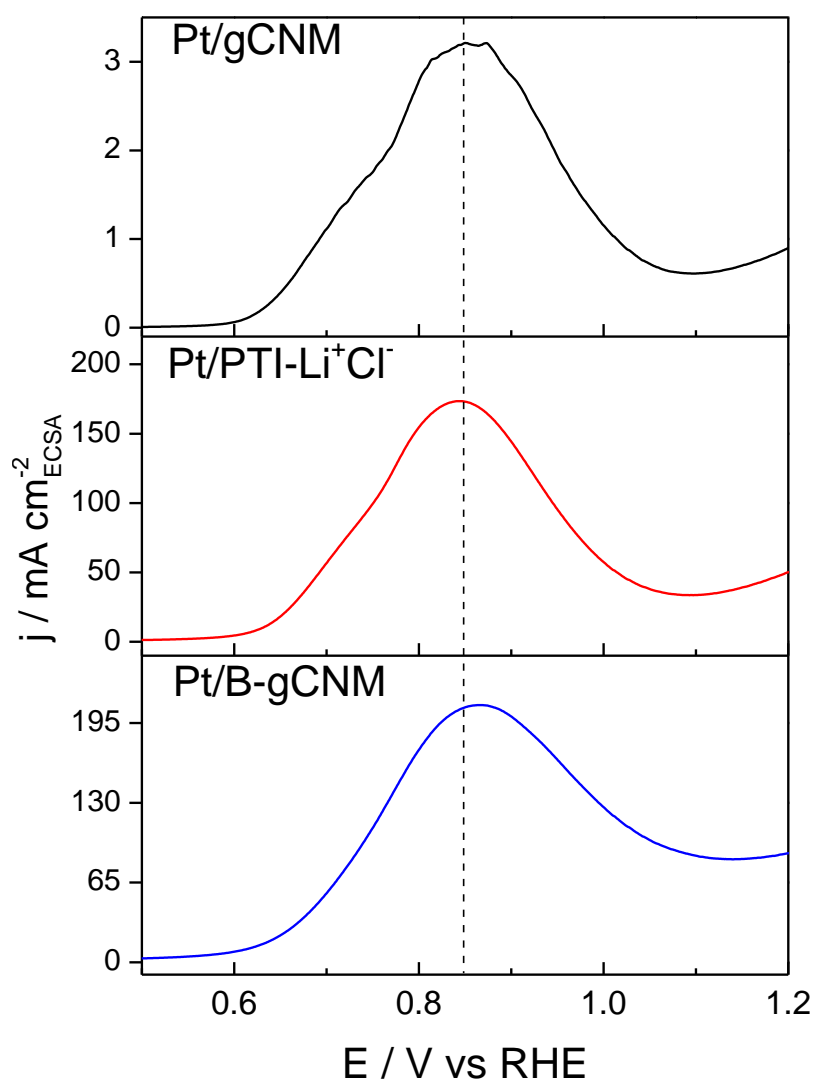


Figure 7.9. Methanol oxidation reaction of supported Pt electrocatalysts in 1 M CH₃OH + 0.1 M HClO₄ at 25°C with a scan rate of 2 mV s⁻¹.

It has been suggested that the presence of nitrogen on/within the support material could lead to intrinsic MOR catalytic enhancement.^{182, 185} As mentioned in Section 7.3.3, the presence of boron redistributes the π electrons on the carbon support, and consequently suppresses O_2 chemisorption. A similar behaviour would be expected in the case of B-doped carbon nitride. However, this same phenomenon is also responsible for a catalytic effect of CO and CO_2 desorption, which are poisoning intermediates in MOR.³⁰⁸ The net effect is a complex balance between boron content and distribution. Further work is needed to optimise the particle dispersion and ECSA on graphitic carbon nitride. Moreover, each of the graphitic carbon nitride materials has different structural properties and therefore would require a different synthesis approach.

Table 7.3: The methanol oxidation peak potential (E_{peak}) and maximum methanol oxidation reaction current density (j_{max}) of supported Pt electrocatalysts in 1 M CH_3OH + 0.1 M $HClO_4$ at 25°C.

	E_{peak} [V]	j_{max} [mA cm ⁻² _{ECSA}]
Pt/gCNM	0.850	3.21
Pt/PTI-Li⁺Cl⁻	0.842	174
Pt/B-gCNM	0.858	209

7.4 Conclusions

For the first time, modified graphitic carbon nitrides (highly crystalline PTI-Li⁺Cl⁻ and B-doped gCNM) were tested as catalyst support materials for PEMFCs. The results show that all graphitic carbon nitride materials prepared in this study exhibit significantly improved durability compared to commercial carbon black (Vulcan XC-72R) and therefore, are promising catalyst support materials for PEFC applications. Interestingly, B-gCNM and PTI/Li⁺Cl⁻ exhibit the highest stability. As shown on the X-ray diffraction patterns, B-gCNM and PTI/Li⁺Cl⁻ are more crystalline than gCNM, suggesting that crystallinity may play an important role in the stability of the material against carbon corrosion. This also suggests that the presence of dopants such as boron in B-gCNM, and Li⁺ and Cl⁻ in PTI/Li⁺Cl⁻ may enhance the stability of the support materials.

The durability of graphitic carbon nitride supported Pt electrocatalysts is highly dependent on the initial ECSA. The Pt/B-gCNM, with the lowest ECSA of all carbon nitride supported catalyst exhibits the lowest durability with a loss of 100% after 2000 cycles, despite the high corrosion tolerance of B-gCNM. The Pt/PTI-Li⁺Cl⁻ has the best durability of all Pt-supported catalyst with an ECSA loss of only 19% after 2000 scans. This value is even lower than Pt/Vulcan with an ECSA loss of 36%. The performance of PTI-Li⁺Cl⁻ is highly encouraging and worthy of further investigation.

Chapter 8

8 Conclusions and Future Work

Electrochemical energy conversion devices, such as the PEMFC, have the potential to reduce greenhouse gas emissions. However, significant work is required to improve their performance and durability, as well as reducing the overall cost, before large-scale commercialisations can be achieved. The catalyst presents the highest potential for cost reduction due to the current use of expensive Pt, and to extend durability due to the various degradation mechanisms that occur in the electrodes. This work aims to improve fuel cell electrodes via two parallel routes:

1. *The development of PdIr as anode electrocatalyst.* Previous work on Pd-based alloys has shown that electronic properties of PdIr alloy could be fine-tuned by altering the compositions. In this work, a 1:1 ratio of PdIr is expected to have an optimum *d*-band vacancy and a maximum HOR activity. The activity of PdIr electrocatalyst was investigated via *in-situ* and *ex-situ* characterization techniques, and compared to a commercially available Pt catalyst.
2. *The development of graphitic carbon nitride as alternative, low-cost, and durable catalyst supports.* For the first time, three different graphitic carbon nitride materials were characterized for their potential as catalyst support in fuel cells. The graphitic structure of the materials is expected to offer significant enhancement in durability. Based on previous work in the literature, the presence of nitrogen in materials is also expected to offer enhancement in durability and activity, especially for ORR and MOR

Chapter 4 and 5 describes the work on PdIr electrocatalysts. PdIr catalyst was prepared from a low temperature chemical precipitation method. Preliminary results from *ex-situ* tests found that the ECSA of PdIr is very low, due to the presence of agglomeration in the sample. Nevertheless, the HOR activity of PdIr was found to be comparable to that of Pt. CO-tolerance was found to be in the order of PtRu > PdIr > Pt. However, the active sites of PdIr are not 100% poisoned by CO, which may offer enhanced tolerance. MOR voltammetry tests show that even though the addition of Ir improves the activity of Pd, the activity is worse than PtRu and Pt. Under *ex-situ* AST protocol, PdIr was

found to have similar durability to Pt, with carbon corrosion as the main degradation mode.

In-situ single-cell PEMFC testing using PdIr on the anode was compared to commercial Pt and PtRu. Contrary to the findings of the *ex-situ* study, HOR activity of PdIr was found to be worse than Pt and PtRu. This was attributed to the presence of agglomeration, which reduced the formation of TPB during MEA fabrication. Improvements to the morphology and ECSA of PdIr catalyst were achieved by pre-treating the carbon support and reducing the metal loading on the carbon. The optimised PdIr catalyst was found to have higher ECSA and EIS studies reveal a decrease in anode charge transfer resistance compared to the unoptimised catalyst. However, the performance is still lower than that of commercial Pt. Further optimisation in terms of ECSA, catalyst layer design and MEA preparation route is needed to achieve similar performance to that of Pt.

In-situ CO tolerance tests suggest that ECSA plays an important role in the CO tolerance of PdIr catalyst. The unoptimised PdIr exhibited poor performance due to its low ECSA. However, PdIr with improved ECSA was found to have higher CO tolerance than Pt and PtRu at low CO concentrations (below 50 ppm CO), but worse at higher concentrations. The results suggest that the available unpoisoned surface area was not sufficient to maintain the reaction at high CO concentrations. Nevertheless, this also implies that PdIr catalyst could replace Pt or PtRu in certain applications where small concentrations of CO are present.

In terms of further work, a long-term *in-situ* durability testing, combined with post-mortem analysis, would be useful to verify the *ex-situ* results. Further enhancement in CO tolerance could be achieved by the addition of a third element, Ru. However, the balance between activity and durability needs to be weighed in the design of the new catalyst.

The work on graphitic carbon nitride materials are described in Chapter 6 and 7. Polymeric carbon nitride (gCNM) was synthesised via a simple polycondensation method and characterised. Although the use of gCNM as catalyst support has been reported in the literature, there are no further studies to explore its durability and intrinsic catalytic capacity in the same system. Following AST protocol, gCNM was

found to be more stable than a conventional carbon black (Vulcan). However, Pt/gCNM exhibits a larger ECSA loss compared to Pt/Vulcan. Superior MOR and ORR activity is observed for Pt/gCNM on the basis of the catalyst ECSA, indicating that gCNM also acts as a co-catalyst.

An attempt was made to reduce Pt particle size and improve particle dispersion on gCNM. It was shown that protonating the gCNM in acid improves the solubility as well as catalyst utilisation. For future work, a combination of exfoliation and protonation as a pre-treatment route for gCNM is proposed.

Modified graphitic carbon nitride (highly crystalline PTI-Li⁺Cl⁻ and B-doped gCNM) were prepared and tested as catalyst support materials for PEMFCs. Currently, no studies exist in the literature on the use of both materials in electrocatalysis. The results show that both materials exhibit significantly improved durability compared to gCNM and Vulcan, possibly due to enhanced crystallinity in the structure. The presence of dopants such as boron in B-gCNM, and Li⁺ and Cl⁻ in PTI/Li⁺Cl⁻ may also contribute to the enhanced stability.

It was found that the durability of graphitic carbon nitride supported Pt electrocatalysts may be dependent on the initial ECSA. The Pt/B-gCNM, which has the lowest ECSA, exhibits the lowest durability with a complete loss of surface area at the end of AST cycles. On the other hand, Pt/PTI-Li⁺Cl⁻ which has the highest ECSA, has the highest durability with only 19% ECSA loss. This value is even lower than Pt/Vulcan with an ECSA loss of 36%. The performance of PTI/Li⁺Cl⁻ is highly encouraging and worthy of further investigations, such as further ECSA and morphological optimization as well as *in-situ* testing.

References

1. United Nation Intergovernmental Panel on Climate Change. Climate Change 2014: Mitigation of Climate Change. <http://www.ipcc.ch/> (accessed 24-04-2014).
2. UK Department of Energy & Climate Change. Energy Consumption in the UK. 2014.
3. Davis, S. J.; Caldeira, K.; Matthews, H. D., Future CO₂ Emissions and Climate Change from Existing Energy Infrastructure. *Science* **2010**, 329 (5997), 1330-1333.
4. Grove, W. R., On Voltaic Series and the Combination of Gases by Platinum. *London and Edinburgh Philosophical Magazine Journal Science* **1839**, 14 (86).
5. Bacon, F. T.; Fry, T. M., Review Lecture: The Development and Practical Application of Fuel Cells. *Proceedings of the Royal Society of London. A. Mathematical and Physical Sciences* **1973**, 334 (1599), 427-452.
6. Williams, K. R., Francis Thomas Bacon. 21 December 1904-24 May 1992. *Biographical Memoirs of Fellows of the Royal Society* **1994**, 39, 2-18.
7. Warshay, M.; Prokopius, P. R., The fuel cell in space: yesterday, today and tomorrow. *Journal of Power Sources* **1990**, 29 (1-2), 193-200.
8. Bard, A. J.; Faulkner, L. R., *Electrochemical Methods: Fundamentals and Applications*. Wiley: 2000.
9. Pham, V. N.; Boyer, D.; Chouliaras, G.; Savvaidis, A.; Stavrakakis, G.; Le Mouél, J. L., Sources of anomalous transient electric signals (ATESs) in the ULF band in the Lamia region (central Greece): electrochemical mechanisms for their generation. *Physics of the Earth and Planetary Interiors* **2002**, 130 (3-4), 209-233.
10. US Department of Energy. Fuel Cell System Cost - 2013. http://www.hydrogen.energy.gov/pdfs/13012_fuel_cell_system_cost_2013.pdf.
11. US Department of Energy. Fuel Cell Stack Durability. http://www.hydrogen.energy.gov/pdfs/11003_fuel_cell_stack_durability.pdf.
12. US DRIVE partnership. Fuel Cell Technical Team Roadmap. http://www1.eere.energy.gov/vehiclesandfuels/pdfs/program/fctt_roadmap_june2013.pdf.
13. Carter, D. The Cost of Platinum in Fuel Cell Electric Vehicles 2013. <http://www.fuelcelltoday.com/analysis/analyst-views/2013/13-11-06-the-cost-of-platinum-in-fuel-cell-electric-vehicles> (accessed 24-04-2014).
14. Petrow, H. G.; Allen, R. J. Finely particulated colloidal platinum compound and sol for producing the same, and method of preparation of fuel cell electrodes and the like employing the same US Patent 4,044,193, 1974.

15. Raistrick, I. D. Electrode assembly for use in a solid polymer electrolyte fuel cell US Patent 4,876,115, 1989.
16. Wilson, M. S. Membrane catalyst layer for fuel cells. US Patent 5,211,984, 1991.
17. Springer, T. E.; Wilson, M. S.; Gottesfeld, S., Modeling and Experimental Diagnostics in Polymer Electrolyte Fuel Cells. *Journal of The Electrochemical Society* **1993**, *140* (12), 3513-3526.
18. Mukerjee, S.; Srinivasan, S.; Soriaga, M. P.; McBreen, J., Role of Structural and Electronic Properties of Pt and Pt Alloys on Electrocatalysis of Oxygen Reduction: An In Situ XANES and EXAFS Investigation. *Journal of The Electrochemical Society* **1995**, *142* (5), 1409-1422.
19. Mukerjee, S.; Srinivasan, S., Enhanced electrocatalysis of oxygen reduction on platinum alloys in proton exchange membrane fuel cells. *Journal of Electroanalytical Chemistry* **1993**, *357* (1-2), 201-224.
20. Marković, N. M.; Ross Jr, P. N., Surface science studies of model fuel cell electrocatalysts. *Surface Science Reports* **2002**, *45* (4-6), 117-229.
21. Gasteiger, H. A.; Panels, J. E.; Yan, S. G., Dependence of PEM fuel cell performance on catalyst loading. *Journal of Power Sources* **2004**, *127* (1-2), 162-171.
22. Sheng, W.; Gasteiger, H. A.; Shao-Horn, Y., Hydrogen Oxidation and Evolution Reaction Kinetics on Platinum: Acid vs Alkaline Electrolytes. *Journal of The Electrochemical Society* **2010**, *157* (11), B1529.
23. Chen, S.; Kucernak, A., Electrocatalysis under Conditions of High Mass Transport: Investigation of Hydrogen Oxidation on Single Submicron Pt Particles Supported on Carbon. *The Journal of Physical Chemistry B* **2004**, *108* (37), 13984-13994.
24. Neyerlin, K. C.; Gu, W.; Jorne, J.; Gasteiger, H. A., Study of the Exchange Current Density for the Hydrogen Oxidation and Evolution Reactions. *Journal of The Electrochemical Society* **2007**, *154* (7), B631-B635.
25. Nørskov, J. K.; Bligaard, T.; Logadottir, A.; Bahn, S.; Hansen, L. B.; Bollinger, M.; Bengard, H.; Hammer, B.; Sljivancanin, Z.; Mavrikakis, M.; Xu, Y.; Dahl, S.; Jacobsen, C. J. H., Universality in Heterogeneous Catalysis. *Journal of Catalysis* **2002**, *209* (2), 275-278.
26. Bligaard, T.; Nørskov, J. K., Chemical Bonding at Surfaces and Interfaces. Nilsson, A.; Pettersson, L. G. M.; Nørskov, J. K., Eds. Elsevier: 2007; pp 255-321.
27. Conway, B. E.; Jerkiewicz, G., Relation of energies and coverages of underpotential and overpotential deposited H at Pt and other metals to the 'volcano curve' for cathodic H₂ evolution kinetics. *Electrochimica Acta* **2000**, *45* (25-26), 4075-4083.

28. Hammer, B.; Nørskov, J. K., Electronic factors determining the reactivity of metal surfaces. *Surface Science* **1995**, *343* (3), 211-220.
29. Nilsson, A.; Pettersson, L. G. M.; Hammer, B.; Bligaard, T.; Christensen, C. H.; Nørskov, J. K., The electronic structure effect in heterogeneous catalysis. *Catalysis Letters* **2005**, *100* (3-4), 111-114.
30. Nørskov, J. K.; Abild-Pedersen, F.; Studt, F.; Bligaard, T., Density functional theory in surface chemistry and catalysis. *Proceedings of the National Academy of Sciences* **2011**, *108* (3), 937-943.
31. Yoo, S. J.; Sung, Y.-E., Design of Palladium-Based Alloy Electrocatalysts for Hydrogen Oxidation Reaction in Fuel Cells. In *Fuel Cell Science: Theory, Fundamentals, and Biocatalysis*, Wieckowski, A.; Nørskov, J. K., Eds. Wiley & Sons: Canada, 2010; pp 132-143.
32. Grigoriev, S.; Lyutikova, E.; Martemianov, S.; Fateev, V.; Lebouin, C.; Millet, P., Pd-based electrocatalysts for PEM applications. In *16th World Hydrogen Energy Conference*, Lyon, France, 2006.
33. Garcia, A. C.; Paganin, V. A.; Ticianelli, E. A., CO tolerance of PdPt/C and PdPtRu/C anodes for PEMFC. *Electrochimica Acta* **2008**, *53* (12), 4309-4315.
34. Antolini, E., Palladium in fuel cell catalysis. *Energy & Environmental Science* **2009**, *2* (9), 915.
35. Johnson Matthey PGM Price Tables. <http://www.platinum.matthey.com/prices/price-tables> (accessed 24th June 2014).
36. Gibbs, C.; Liu, F.; Papageorgopoulos, D. Improvements in or relating to catalysts for fuel cells. GB2481309, 2011.
37. Shen, S. Y.; Zhao, T. S.; Xu, J. B., Carbon-supported bimetallic PdIr catalysts for ethanol oxidation in alkaline media. *Electrochimica Acta* **2010**, *55* (28), 9179-9184.
38. Ralph, T. R.; Hudson, S.; Wilkinson, D. P., Electrocatalyst Stability In PEMFCs And The Role Of Fuel Starvation And Cell Reversal Tolerant Anodes. *ECS Transactions* **2006**, *1* (8), 67-84.
39. Taniguchi, A.; Akita, T.; Yasuda, K.; Miyazaki, Y., Analysis of electrocatalyst degradation in PEMFC caused by cell reversal during fuel starvation. *Journal of Power Sources* **2004**, *130* (1-2), 42-49.
40. Yu, P. T.; Gu, W.; Zhang, J.; Makharia, R.; Wagner, F. T.; Gasteiger, H. A., Carbon-Support Requirements for Highly Durable Fuel Cell Operation. In *Polymer Electrolyte Fuel Cell Durability*, Buchi, F. N.; Inaba, M.; Schmidt, T. J., Eds. Springer: 2009; pp 41-42.
41. Springer, T. E.; Rockward, T.; Zawodzinski, T. A.; Gottesfeld, S., Model for Polymer Electrolyte Fuel Cell Operation on Reformate Feed: Effects of CO, H₂

Dilution, and High Fuel Utilization. *Journal of The Electrochemical Society* **2001**, *148* (1), A11-A23.

42. Gottesfeld, S.; Pafford, J., A New Approach to the Problem of Carbon Monoxide Poisoning in Fuel Cells Operating at Low Temperatures. *Journal of The Electrochemical Society* **1988**, *135* (10), 2651-2652.

43. Ye, S., CO-tolerant Catalysts. In *PEM Fuel Cell Electrocatalysts and Catalyst Layers - Fundamentals and Applications*, Zhang, J., Ed. Springer: 2008; p 759.

44. Thompsett, D., Pt alloys as oxygen reduction catalysts. In *Handbook of Fuel Cells*, John Wiley & Sons, Ltd: 2010.

45. Gasteiger, H. A.; Markovic, N. M.; Ross, P. N., H₂ and CO Electrooxidation on Well-Characterized Pt, Ru, and Pt-Ru. 2. Rotating Disk Electrode Studies of CO/H₂ Mixtures at 62°C. *J. Phys. Chem* **1995**, *99* (45), 16757-16767.

46. Spendelow, J. S.; Babu, P. K.; Wieckowski, A., Electrocatalytic oxidation of carbon monoxide and methanol on platinum surfaces decorated with ruthenium. *Current Opinion in Solid State and Materials Science* **2005**, *9* (1-2), 37-48.

47. Gasteiger, H. A.; Markovic, N.; Ross, P. N.; Cairns, E. J., Carbon monoxide electrooxidation on well-characterized platinum-ruthenium alloys. *J. Phys. Chem* **1994**, *98* (2), 617-625.

48. Oetjen, H.-F.; Schmidt, V. M.; Stimming, U.; Trila, F., Performance Data of a Proton Exchange Membrane Fuel Cell Using H₂/CO as Fuel Gas. *Journal of The Electrochemical Society* **1996**, *143* (12), 3838-3842.

49. Friedrich, K. A.; Geyzers, K. P.; Linke, U.; Stimming, U.; Stumper, J., CO adsorption and oxidation on a Pt(111) electrode modified by ruthenium deposition: an IR spectroscopic study. *Journal of Electroanalytical Chemistry* **1996**, *402* (1-2), 123-128.

50. Camara, G. A.; Giz, M. J.; Paganin, V. A.; Ticianelli, E. A., Correlation of electrochemical and physical properties of PtRu alloy electrocatalysts for PEM fuel cells. *Journal of Electroanalytical Chemistry* **2002**, *537* (1-2), 21-29.

51. Igarashi, H.; Fujino, T.; Zhu, Y.; Uchida, H.; Watanabe, M., CO Tolerance of Pt alloy electrocatalysts for polymer electrolyte fuel cells and the detoxification mechanism. *Physical Chemistry Chemical Physics* **2001**, *3* (3), 306-314.

52. Buatier de Mongeot, F.; Scherer, M.; Gleich, B.; Kopatzki, E.; Behm, R. J., CO adsorption and oxidation on bimetallic Pt/Ru(0001) surfaces – a combined STM and TPD/TPR study. *Surface Science* **1998**, *411* (3), 249-262.

53. Koper, M. T. M., Electrocatalysis on bimetallic and alloy surfaces. *Surface Science* **2004**, *548* (1-3), 1-3.

54. Gasteiger, H. A.; Marković, N. M.; Ross, P. N., Structural effects in electrocatalysis: electrooxidation of carbon monoxide on Pt₃Sn single-crystal alloy surfaces. *Catalysis Letters* **1996**, *36* (1), 1-8.
55. Morimoto, Y.; Yeager, E. B., CO oxidation on smooth and high area Pt, Pt-Ru and Pt-Sn electrodes. *Journal of Electroanalytical Chemistry* **1998**, *441* (1-2), 77-81.
56. Cho, Y.-H.; Choi, B.; Cho, Y.-H.; Park, H.-S.; Sung, Y.-E., Pd-based PdPt(19:1)/C electrocatalyst as an electrode in PEM fuel cell. *Electrochemistry Communications* **2007**, *9* (3), 378-381.
57. Papageorgopoulos, D. C.; Keijzer, M.; Veldhuis, J. B. J.; de Bruijn, F. A., CO Tolerance of Pd-Rich Platinum Palladium Carbon-Supported Electrocatalysts. *Journal of The Electrochemical Society* **2002**, *149* (11), A1400-A1404.
58. Long, J. W.; Stroud, R. M.; Swider-Lyons, K. E.; Rolison, D. R., How To Make Electrocatalysts More Active for Direct Methanol Oxidation: Avoid PtRu Bimetallic Alloys! *The Journal of Physical Chemistry B* **2000**, *104* (42), 9772-9776.
59. He, C.; Kunz, H. R.; Fenton, J. M., Evaluation of Platinum-Based Catalysts for Methanol Electro-oxidation in Phosphoric Acid Electrolyte. *Journal of The Electrochemical Society* **1997**, *144* (3), 970-979.
60. Takeguchi, T.; Anzai, Y.; Kikuchi, R.; Eguchi, K.; Ueda, W., Preparation and Characterization of CO-Tolerant Pt and Pd Anodes Modified with SnO₂ Nanoparticles for PEFC. *Journal of The Electrochemical Society* **2007**, *154* (11), B1132-B1137.
61. Muhamad, E. N.; Takeguchi, T.; Wang, G.; Anzai, Y.; Ueda, W., Electrochemical Characteristics of Pd Anode Catalyst Modified with TiO₂ Nanoparticles in Polymer Electrolyte Fuel Cell. *Journal of The Electrochemical Society* **2009**, *156* (1), B32-B37.
62. Wang, X.; Tang, Y.; Gao, Y.; Lu, T., Carbon-supported Pd-Ir catalyst as anodic catalyst in direct formic acid fuel cell. *Journal of Power Sources* **2008**, *175* (2), 784-788.
63. Breiter, M. W., Dissolution and adsorption of hydrogen at smooth Pd wires at potentials of the alpha phase in sulfuric acid solution. *Journal of Electroanalytical Chemistry and Interfacial Electrochemistry* **1977**, *81* (2), 275-284.
64. Breiter, M. W., Role of adsorbed species for the anodic methanol oxidation on platinum in acidic electrolytes. *Discussions of the Faraday Society* **1968**, *45* (0), 79-86.
65. Batista, E. A.; Malpass, G. R. P.; Motheo, A. J.; Iwasita, T., New mechanistic aspects of methanol oxidation. *Journal of Electroanalytical Chemistry* **2004**, *571* (2), 273-282.
66. Hamnett, A., Mechanism and Electrocatalysis in the Direct Methanol Fuel Cell. *Catalysis Today* **2007**, *38*, 445-457.

67. T, I., Electrocatalysis of methanol oxidation. *Electrochimica Acta* **2002**, *47* (22–23), 3663-3674.
68. Cao, D.; Lu, G. Q.; Wieckowski, A.; Wasileski, S. A.; Neurock, M., Mechanisms of Methanol Decomposition on Platinum: A Combined Experimental and ab Initio Approach. *The Journal of Physical Chemistry B* **2005**, *109* (23), 11622-11633.
69. Gyenge, E., Electrocatalytic Oxidation of Methanol, Ethanol and Formic Acid. In *PEM Fuel Cell Electrocatalysts and Catalyst Layers: Fundamentals and Applications*, Zhang, J., Ed. Springer: 2008; pp 172-201.
70. Gasteiger, H. A.; Markovic, N.; Ross, P. N.; Cairns, E. J., Methanol electrooxidation on well-characterized platinum-ruthenium bulk alloys. *J. Phys. Chem* **1993**, *97* (46), 12020-12029.
71. Gasteiger, H. A.; Marković, N.; Ross Jr, P. N.; Cairns, E. J., Electro-oxidation of small organic molecules on well-characterized PtRu alloys. *Electrochimica Acta* **1994**, *39* (11–12), 1825-1832.
72. Díaz, V.; Ohanian, M.; Zinola, C. F., Kinetics of methanol electrooxidation on Pt/C and PtRu/C catalysts. *International Journal of Hydrogen Energy* **2010**, *35* (19), 10539-10546.
73. Anderson, A. B.; Grantscharova, E., Catalytic Effect of Ruthenium in Ruthenium-Platinum Alloys on the Electrooxidation of Methanol. Molecular Orbital Theory. *J. Phys. Chem* **1995**, *99* (22), 9149-9154.
74. Huang, J.; Yang, H.; Huang, Q.; Tang, Y.; Lu, T.; Akins, D. L., Methanol Oxidation on Carbon-Supported Pt-Os Bimetallic Nanoparticle Electrocatalysts. *Journal of The Electrochemical Society* **2004**, *151* (11), A1810-A1815.
75. Mukerjee, S.; Urian, R. C., Bifunctionality in Pt alloy nanocluster electrocatalysts for enhanced methanol oxidation and CO tolerance in PEM fuel cells: electrochemical and in situ synchrotron spectroscopy. *Electrochimica Acta* **2002**, *47* (19), 3219-3231.
76. Mylswamy, S.; Wang, C. Y.; Liu, R. S.; Lee, J. F.; Tang, M. J.; Lee, J. J.; Weng, B. J., Anode catalysts for enhanced methanol oxidation: An in situ XANES study of PtRu/C and PtMo/C catalysts. *Chemical Physics Letters* **2005**, *412* (4–6), 444-448.
77. Arenz, M.; Stamenkovic, V.; Blizanac, B. B.; Mayrhofer, K. J.; Markovic, N. M.; Ross, P. N., Carbon-supported Pt–Sn electrocatalysts for the anodic oxidation of H₂, CO, and H₂/CO mixtures.: Part II: The structure–activity relationship. *Journal of Catalysis* **2005**, *232* (2), 402-410.
78. Radmilovic, V.; Richardson, T. J.; Chen, S. J.; Ross Jr, P. N., Carbon-supported Pt–Sn electrocatalysts for the anodic oxidation of H₂, CO, and H₂/CO mixtures. Part I. Microstructural characterization. *Journal of Catalysis* **2005**, *232* (1), 199-209.

79. Colmati, F.; Antolini, E.; Gonzalez, E. R., Pt–Sn/C electrocatalysts for methanol oxidation synthesized by reduction with formic acid. *Electrochimica Acta* **2005**, *50* (28), 5496-5503.
80. Neto, A. O.; Dias, R. R.; Tusi, M. M.; Linardi, M.; Spinacé, E. V., Electro-oxidation of methanol and ethanol using PtRu/C, PtSn/C and PtSnRu/C electrocatalysts prepared by an alcohol-reduction process. *Journal of Power Sources* **2007**, *166* (1), 87-91.
81. Götz, M.; Wendt, H., Binary and ternary anode catalyst formulations including the elements W, Sn and Mo for PEMFCs operated on methanol or reformat gas. *Electrochimica Acta* **1998**, *43* (24), 3637-3644.
82. Liu, Z.; Guo, B.; Hong, L.; Lim, T. H., Microwave heated polyol synthesis of carbon-supported PtSn nanoparticles for methanol electrooxidation. *Electrochemistry Communications* **2006**, *8* (1), 83-90.
83. Liu, Z.; Zhang, X.; Hong, L., Physical and electrochemical characterizations of nanostructured Pd/C and PdNi/C catalysts for methanol oxidation. *Electrochemistry Communications* **2009**, *11* (4), 925-928.
84. Bianchini, C.; Shen, P. K., Palladium-based electrocatalysts for alcohol oxidation in half cells and in direct alcohol fuel cells. *Chemical reviews* **2009**, *109* (9), 4183-206.
85. Nørskov, J. K.; Rossmeisl, J.; Logadottir, A.; Lindqvist, L.; Kitchin, J. R.; Bligaard, T.; Jónsson, H., Origin of the Overpotential for Oxygen Reduction at a Fuel-Cell Cathode. *The Journal of Physical Chemistry B* **2004**, *108* (46), 17886-17892.
86. Jalan, V.; Taylor, E. J., Importance of Interatomic Spacing in Catalytic Reduction of Oxygen in Phosphoric Acid. *Journal of The Electrochemical Society* **1983**, *130* (11), 2299-2302.
87. Min, M.-k.; Cho, J.; Cho, K.; Kim, H., Particle size and alloying effects of Pt-based alloy catalysts for fuel cell applications. *Electrochimica Acta* **2000**, *45* (25–26), 4211-4217.
88. Stassi, A.; D'urso, C.; Baglio, V.; Di Blasi, A.; Antonucci, V.; Arico, A. S.; Castro Luna, A. M.; Bonesi, A.; Triaca, W. E., Electrocatalytic behaviour for oxygen reduction reaction of small nanostructured crystalline bimetallic Pt–M supported catalysts. *Journal of Applied Electrochemistry* **2006**, *36* (10), 1143-1149.
89. Stamenkovic, V. R.; Fowler, B.; Mun, B. S.; Wang, G.; Ross, P. N.; Lucas, C. A.; Marković, N. M., Improved Oxygen Reduction Activity on Pt₃Ni(111) via Increased Surface Site Availability. *Science* **2007**, *315* (5811), 493-497.
90. Ralph, T. R.; Hogarth, M. P., Catalysis for low temperature fuel cells. *Platinum Metals Review* **2002**, *46* (1), 3-14.

91. Toda, T.; Igarashi, H.; Watanabe, M., Enhancement of the electrocatalytic O₂ reduction on Pt–Fe alloys. *Journal of Electroanalytical Chemistry* **1999**, *460* (1–2), 258-262.
92. Toda, T.; Igarashi, H.; Uchida, H.; Watanabe, M., Enhancement of the Electroreduction of Oxygen on Pt Alloys with Fe, Ni, and Co. *Journal of The Electrochemical Society* **1999**, *146* (10), 3750-3756.
93. Yu, P.; Pemberton, M.; Plasse, P., PtCo/C cathode catalyst for improved durability in PEMFCs. *Journal of Power Sources* **2005**, *144* (1), 11-20.
94. Zhang, J.; Sasaki, K.; Sutter, E.; Adzic, R. R., Stabilization of Platinum Oxygen-Reduction Electrocatalysts Using Gold Clusters. *Science* **2007**, *315* (5809), 220-222.
95. Gasteiger, H. A.; Kocha, S. S.; Sompalli, B.; Wagner, F. T., Activity benchmarks and requirements for Pt, Pt-alloy, and non-Pt oxygen reduction catalysts for PEMFCs. *Applied Catalysis B: Environmental* **2005**, *56* (1-2), 9-35.
96. Wakabayashi, N.; Takeichi, M.; Uchida, H.; Watanabe, M., Temperature Dependence of Oxygen Reduction Activity at Pt–Fe, Pt–Co, and Pt–Ni Alloy Electrodes. *The Journal of Physical Chemistry B* **2005**, *109* (12), 5836-5841.
97. Borup, R.; Meyers, J.; Pivovar, B.; Kim, Y. S.; Mukundan, R.; Garland, N.; Myers, D.; Wilson, M.; Garzon, F.; Wood, D.; Zelenay, P.; More, K.; Stroh, K.; Zawodzinski, T.; Boncella, J.; McGrath, J. E.; Inaba, M.; Miyatake, K.; Hori, M.; Ota, K.; Ogumi, Z.; Miyata, S.; Nishikata, A.; Siroma, Z.; Uchimoto, Y.; Yasuda, K.; Kimijima, K.-i.; Iwashita, N., Scientific Aspects of Polymer Electrolyte Fuel Cell Durability and Degradation. *Chemical reviews* **2007**, *107* (10), 3904-3951.
98. Ferreira, P. J.; la O', G. J.; Shao-Horn, Y.; Morgan, D.; Makharia, R.; Kocha, S.; Gasteiger, H. A., Instability of Pt/C Electrocatalysts in Proton Exchange Membrane Fuel Cells: A Mechanistic Investigation. *Journal of The Electrochemical Society* **2005**, *152* (11), A2256-A2271.
99. Yu, X.; Ye, S., Recent advances in activity and durability enhancement of Pt/C catalytic cathode in PEMFC: Part II: Degradation mechanism and durability enhancement of carbon supported platinum catalyst. *Journal of Power Sources* **2007**, *172* (1), 145-154.
100. Lee, J. B., Elevated Temperature Potential-pH Diagrams for the Cr-H₂O, Ti-H₂O, Mo-H₂O, and Pt-H₂O Systems. *Corrosion* **1981**, *37* (8), 467-481.
101. Pourbaix, M. J. N.; Muyllder, J. V.; Zoubov, N. d., Electrochemical Properties of the Platinum Metals. *Platinum Metals Review* **1959**, *3* (3), 100-106.
102. Roen, L. M.; Paik, C. H.; Jarvi, T. D., Electrocatalytic Corrosion of Carbon Support in PEMFC Cathodes. *Electrochemical and Solid-State Letters* **2004**, *7* (1), A19-A22.

103. Siroma, Z.; Ishii, K.; Yasuda, K.; Miyazaki, Y.; Inaba, M.; Tasaka, A., Imaging of highly oriented pyrolytic graphite corrosion accelerated by Pt particles. *Electrochemistry Communications* **2005**, *7* (11), 1153-1156.
104. Yu, P. T.; Gu, W.; Makharia, R.; Wagner, F. T.; Gasteiger, H. A., The Impact of Carbon Stability on PEM Fuel Cell Startup and Shutdown Voltage Degradation. *ECS Transactions* **2006**, *3* (1), 797-809.
105. Avasarala, B.; Murray, T.; Li, W.; Haldar, P., Titanium nitride nanoparticles based electrocatalysts for proton exchange membrane fuel cells. *Journal of Materials Chemistry* **2009**, *19* (13), 1803-1805.
106. Chhina, H.; Campbell, S.; Kesler, O., An oxidation-resistant indium tin oxide catalyst support for proton exchange membrane fuel cells. *Journal of Power Sources* **2006**, *161* (2), 893-900.
107. Ioroi, T.; Siroma, Z.; Fujiwara, N.; Yamazaki, S.-i.; Yasuda, K., Sub-stoichiometric titanium oxide-supported platinum electrocatalyst for polymer electrolyte fuel cells. *Electrochemistry Communications* **2005**, *7* (2), 183-188.
108. Lu, H.; Mu, S.; Cheng, N.; Pan, M., Nano-silicon carbide supported catalysts for PEM fuel cells with high electrochemical stability and improved performance by addition of carbon. *Applied Catalysis B: Environmental* **2010**, *100* (1-2), 190-196.
109. Rajeswari, J.; Viswanathan, B.; Varadarajan, T. K., Tungsten trioxide nanorods as supports for platinum in methanol oxidation. *Materials Chemistry and Physics* **2007**, *106* (2-3), 168-174.
110. Ruettinger, W.; Liu, X.; Farrauto, R. J., Mechanism of aging for a Pt/CeO₂-ZrO₂ water gas shift catalyst. *Applied Catalysis B: Environmental* **2006**, *65* (1-2), 135-141.
111. Sakurai, H.; Akita, T.; Tsubota, S.; Kiuchi, M.; Haruta, M., Low-temperature activity of Au/CeO₂ for water gas shift reaction, and characterization by ADF-STEM, temperature-programmed reaction, and pulse reaction. *Applied Catalysis A: General* **2005**, *291* (1-2), 179-187.
112. Sasaki, K.; Zhang, L.; Adzic, R. R., Niobium oxide-supported platinum ultra-low amount electrocatalysts for oxygen reduction. *Physical Chemistry Chemical Physics* **2008**, *10* (1), 159-167.
113. Shen, P. K.; Yin, S.; Li, Z.; Chen, C., Preparation and performance of nanosized tungsten carbides for electrocatalysis. *Electrochimica Acta* **2010**, *55* (27), 7969-7974.
114. von Kraemer, S.; Wikander, K.; Lindbergh, G.; Lundblad, A.; Palmqvist, A. E. C., Evaluation of TiO₂ as catalyst support in Pt-TiO₂/C composite cathodes for the proton exchange membrane fuel cell. *Journal of Power Sources* **2008**, *180* (1), 185-190.
115. Yin, S.; Mu, S.; Pan, M.; Fu, Z., A highly stable TiB₂-supported Pt catalyst for polymer electrolyte membrane fuel cells. *Journal of Power Sources* **2011**, *196* (19), 7931-7936.

116. Antolini, E., Carbon supports for low-temperature fuel cell catalysts. *Applied Catalysis B: Environmental* **2009**, *88* (1–2), 1-24.
117. He, D.; Mu, S.; Pan, M., Perfluorosulfonic acid-functionalized Pt/carbon nanotube catalysts with enhanced stability and performance for use in proton exchange membrane fuel cells. *Carbon* **2011**, *49* (1), 82-88.
118. Hyeon, T.; Han, S.; Sung, Y.-E.; Park, K.-W.; Kim, Y.-W., High-Performance Direct Methanol Fuel Cell Electrodes using Solid-Phase-Synthesized Carbon Nanocoils. *Angewandte Chemie International Edition* **2003**, *42* (36), 4352-4356.
119. Sano, N.; Ukita, S.-i., One-step synthesis of Pt-supported carbon nanohorns for fuel cell electrode by arc plasma in liquid nitrogen. *Materials Chemistry and Physics* **2006**, *99* (2–3), 447-450.
120. Serp, P.; Corrias, M.; Kalck, P., Carbon nanotubes and nanofibers in catalysis. *Applied Catalysis A: General* **2003**, *253* (2), 337-358.
121. Sevilla, M.; Lota, G.; Fuertes, A. B., Saccharide-based graphitic carbon nanocoils as supports for PtRu nanoparticles for methanol electrooxidation. *Journal of Power Sources* **2007**, *171* (2), 546-551.
122. Wildgoose, G. G.; Banks, C. E.; Compton, R. G., Metal Nanoparticles and Related Materials Supported on Carbon Nanotubes: Methods and Applications. *Small* **2006**, *2* (2), 182-193.
123. Yoshitake, T.; Shimakawa, Y.; Kuroshima, S.; Kimura, H.; Ichihashi, T.; Kubo, Y.; Kasuya, D.; Takahashi, K.; Kokai, F.; Yudasaka, M.; Iijima, S., Preparation of fine platinum catalyst supported on single-wall carbon nanohorns for fuel cell application. *Physica B: Condensed Matter* **2002**, *323* (1–4), 124-126.
124. Zhang, S.; Shao, Y.; Yin, G.; Lin, Y., Carbon nanotubes decorated with Pt nanoparticles via electrostatic self-assembly: a highly active oxygen reduction electrocatalyst. *Journal of Materials Chemistry* **2010**, *20* (14), 2826-2830.
125. Ball, S. C.; Hudson, S. L.; Thompsett, D.; Theobald, B., An investigation into factors affecting the stability of carbons and carbon supported platinum and platinum/cobalt alloy catalysts during 1.2 V potentiostatic hold regimes at a range of temperatures. *Journal of Power Sources* **2007**, *171* (1), 18-25.
126. Chen, W. X.; Lee, J. Y.; Liu, Z., Microwave-assisted synthesis of carbon supported Pt nanoparticles for fuel cell applications. *Chemical Communications* **2002**, *0* (21), 2588-2589.
127. Zhou, J.; Zhou, X.; Sun, X.; Li, R.; Murphy, M.; Ding, Z.; Sun, X.; Sham, T.-K., Interaction between Pt nanoparticles and carbon nanotubes – An X-ray absorption near edge structures (XANES) study. *Chemical Physics Letters* **2007**, *437* (4–6), 229-232.
128. Balasubramanian, K.; Burghard, M., Chemically Functionalized Carbon Nanotubes. *Small* **2005**, *1* (2), 180-192.

129. Wang, X.; Waje, M.; Yan, Y., CNT-Based Electrodes with High Efficiency for PEMFCs. *Electrochemical and Solid-State Letters* **2005**, *8* (1), A42-A44.
130. Li, W.; Liang, C.; Zhou, W.; Qiu, J.; Zhou; Sun, G.; Xin, Q., Preparation and Characterization of Multiwalled Carbon Nanotube-Supported Platinum for Cathode Catalysts of Direct Methanol Fuel Cells. *The Journal of Physical Chemistry B* **2003**, *107* (26), 6292-6299.
131. Li, W.; Liang, C.; Zhou, W.; Qiu, J.; Li, H.; Sun, G.; Xin, Q., Homogeneous and controllable Pt particles deposited on multi-wall carbon nanotubes as cathode catalyst for direct methanol fuel cells. *Carbon* **2004**, *42* (2), 436-439.
132. Li, W.; Liang, C.; Qiu, J.; Zhou, W.; Han, H.; Wei, Z.; Sun, G.; Xin, Q., Carbon nanotubes as support for cathode catalyst of a direct methanol fuel cell. *Carbon* **2002**, *40* (5), 791-794.
133. Li, W.; Wang, X.; Chen, Z.; Waje, M.; Yan, Carbon Nanotube Film by Filtration as Cathode Catalyst Support for Proton-Exchange Membrane Fuel Cell. *Langmuir* **2005**, *21* (21), 9386-9389.
134. Mahesh, M. W.; Xin, W.; Wenzhen, L.; Yushan, Y., Deposition of platinum nanoparticles on organic functionalized carbon nanotubes grown in situ on carbon paper for fuel cells. *Nanotechnology* **2005**, *16* (7), S395.
135. Matsumoto, T.; Komatsu, T.; Arai, K.; Yamazaki, T.; Kijima, M.; Shimizu, H.; Takasawa, Y.; Nakamura, J., Reduction of Pt usage in fuel cell electrocatalysts with carbon nanotube electrodes. *Chemical Communications* **2004**, (7), 840-841.
136. Wang, X.; Li, W.; Chen, Z.; Waje, M.; Yan, Y., Durability investigation of carbon nanotube as catalyst support for proton exchange membrane fuel cell. *Journal of Power Sources* **2006**, *158* (1), 154-159.
137. Shao, Y.; Yin, G.; Gao, Y.; Shi, P., Durability Study of Pt/C and Pt/CNTs Catalysts under Simulated PEM Fuel Cell Conditions. *Journal of The Electrochemical Society* **2006**, *153* (6), A1093-A1097.
138. Shao, Y.; Yin, G.; Zhang, J.; Gao, Y., Comparative investigation of the resistance to electrochemical oxidation of carbon black and carbon nanotubes in aqueous sulfuric acid solution. *Electrochimica Acta* **2006**, *51* (26), 5853-5857.
139. Li, L.; Xing, Y., Electrochemical Durability of Carbon Nanotubes in Noncatalyzed and Catalyzed Oxidations. *Journal of The Electrochemical Society* **2006**, *153* (10), A1823-A1828.
140. Wang, J.; Yin, G.; Shao, Y.; Wang, Z.; Gao, Y., Investigation of Further Improvement of Platinum Catalyst Durability with Highly Graphitized Carbon Nanotubes Support. *The Journal of Physical Chemistry C* **2008**, *112* (15), 5784-5789.
141. Giles, J., Growing nanotech trade hit by questions over quality. *Nature* **2004**, *432* (7019), 791-791.

142. Lee, K.; Zhang, J.; Wang, H.; Wilkinson, D. P., Progress in the synthesis of carbon nanotube- and nanofiber-supported Pt electrocatalysts for PEM fuel cell catalysis. *Journal of Applied Electrochemistry* **2006**, *36* (5), 507-522.
143. Li, W.; Waje, M.; Chen, Z.; Larsen, P.; Yan, Y., Platinum nanoparticles supported on stacked-cup carbon nanofibers as electrocatalysts for proton exchange membrane fuel cell. *Carbon* **2010**, *48* (4), 995-1003.
144. Zheng, J.-S.; Zhang, X.-S.; Li, P.; Zhu, J.; Zhou, X.-G.; Yuan, W.-K., Effect of carbon nanofiber microstructure on oxygen reduction activity of supported palladium electrocatalyst. *Electrochemistry Communications* **2007**, *9* (5), 895-900.
145. Zheng, J.-S.; Zhang, X.-S.; Li, P.; Zhou, X.-G.; Yuan, W.-K., Microstructure effect of carbon nanofiber on electrocatalytic oxygen reduction reaction. *Catalysis Today* **2008**, *131* (1-4), 270-277.
146. Zheng, J.-S.; Wang, M.-X.; Zhang, X.-S.; Wu, Y.-X.; Li, P.; Zhou, X.-G.; Yuan, W.-K., Platinum/carbon nanofiber nanocomposite synthesized by electrophoretic deposition as electrocatalyst for oxygen reduction. *Journal of Power Sources* **2008**, *175* (1), 211-216.
147. Bessel, C. A.; Laubernds, K.; Rodriguez, N. M.; Baker, R. T. K., Graphite Nanofibers as an Electrode for Fuel Cell Applications. *The Journal of Physical Chemistry B* **2001**, *105* (6), 1115-1118.
148. Steigerwalt, E. S.; Deluga, G. A.; Lukehart, C. M., Pt-Ru/Carbon Fiber Nanocomposites: Synthesis, Characterization, and Performance as Anode Catalysts of Direct Methanol Fuel Cells. A Search for Exceptional Performance. *The Journal of Physical Chemistry B* **2002**, *106* (4), 760-766.
149. Guo, J.; Sun, G.; Wang, Q.; Wang, G.; Zhou, Z.; Tang, S.; Jiang, L.; Zhou, B.; Xin, Q., Carbon nanofibers supported Pt-Ru electrocatalysts for direct methanol fuel cells. *Carbon* **2006**, *44* (1), 152-157.
150. Andersen, S. M.; Borghei, M.; Lund, P.; Elina, Y.-R.; Pasanen, A.; Kauppinen, E.; Ruiz, V.; Kauranen, P.; Skou, E. M., Durability of carbon nanofiber (CNF) & carbon nanotube (CNT) as catalyst support for Proton Exchange Membrane Fuel Cells. *Solid State Ionics* **2013**, *231* (0), 94-101.
151. Kang, S.; Lim, S.; Peck, D.-H.; Kim, S.-K.; Jung, D.-H.; Hong, S.-H.; Jung, H.-G.; Shul, Y., Stability and durability of PtRu catalysts supported on carbon nanofibers for direct methanol fuel cells. *International Journal of Hydrogen Energy* **2012**, *37* (5), 4685-4693.
152. Joo, S. H.; Choi, S. J.; Oh, I.; Kwak, J.; Liu, Z.; Terasaki, O.; Ryoo, R., Ordered nanoporous arrays of carbon supporting high dispersions of platinum nanoparticles. *Nature* **2001**, *412* (6843), 169-172.

153. Ding, J.; Chan, K.-Y.; Ren, J.; Xiao, F.-s., Platinum and platinum–ruthenium nanoparticles supported on ordered mesoporous carbon and their electrocatalytic performance for fuel cell reactions. *Electrochimica Acta* **2005**, *50* (15), 3131-3141.
154. Joo, S. H.; Pak, C.; You, D. J.; Lee, S.-A.; Lee, H. I.; Kim, J. M.; Chang, H.; Seung, D., Ordered mesoporous carbons (OMC) as supports of electrocatalysts for direct methanol fuel cells (DMFC): Effect of carbon precursors of OMC on DMFC performances. *Electrochimica Acta* **2006**, *52* (4), 1618-1626.
155. Su, F.; Zeng, J.; Bao, X.; Yu, Y.; Lee, J. Y.; Zhao, X. S., Preparation and Characterization of Highly Ordered Graphitic Mesoporous Carbon as a Pt Catalyst Support for Direct Methanol Fuel Cells. *Chemistry of Materials* **2005**, *17* (15), 3960-3967.
156. Choi, W. C.; Woo, S. I.; Jeon, M. K.; Sohn, J. M.; Kim, M. R.; Jeon, H. J., Platinum Nanoclusters Studied in the Microporous Nanowalls of Ordered Mesoporous Carbon. *Advanced Materials* **2005**, *17* (4), 446-451.
157. Chai, G. S.; Yoon, S. B.; Yu, J.-S.; Choi, J.-H.; Sung, Y.-E., Ordered Porous Carbons with Tunable Pore Sizes as Catalyst Supports in Direct Methanol Fuel Cell. *The Journal of Physical Chemistry B* **2004**, *108* (22), 7074-7079.
158. Joo, J. B.; Kim, P.; Kim, W.; Kim, J.; Yi, J., Preparation of mesoporous carbon templated by silica particles for use as a catalyst support in polymer electrolyte membrane fuel cells. *Catalysis Today* **2006**, *111* (3–4), 171-175.
159. Song, S.; Liang, Y.; Li, Z.; Wang, Y.; Fu, R.; Wu, D.; Tsiakaras, P., Effect of pore morphology of mesoporous carbons on the electrocatalytic activity of Pt nanoparticles for fuel cell reactions. *Applied Catalysis B: Environmental* **2010**, *98* (3–4), 132-137.
160. Shanahan, P. V.; Xu, L.; Liang, C.; Waje, M.; Dai, S.; Yan, Y. S., Graphitic mesoporous carbon as a durable fuel cell catalyst support. *Journal of Power Sources* **2008**, *185* (1), 423-427.
161. Novoselov, K. S.; Geim, A. K.; Morozov, S. V.; Jiang, D.; Zhang, Y.; Dubonos, S. V.; Grigorieva, I. V.; Firsov, A. A., Electric Field Effect in Atomically Thin Carbon Films. *Science* **2004**, *306* (5696), 666-669.
162. Peigney, A.; Laurent, C.; Flahaut, E.; Bacsá, R. R.; Rousset, A., Specific surface area of carbon nanotubes and bundles of carbon nanotubes. *Carbon* **2001**, *39* (4), 507-514.
163. Machado, B. F.; Serp, P., Graphene-based materials for catalysis. *Catalysis Science & Technology* **2012**, *2* (1), 54-75.
164. Singh, R. N.; Awasthi, R., Graphene support for enhanced electrocatalytic activity of Pd for alcohol oxidation. *Catalysis Science & Technology* **2011**, *1* (5), 778-783.

165. Kou, R.; Shao, Y.; Wang, D.; Engelhard, M. H.; Kwak, J. H.; Wang, J.; Viswanathan, V. V.; Wang, C.; Lin, Y.; Wang, Y.; Aksay, I. A.; Liu, J., Enhanced activity and stability of Pt catalysts on functionalized graphene sheets for electrocatalytic oxygen reduction. *Electrochemistry Communications* **2009**, *11* (5), 954-957.
166. Soin, N.; Roy, S. S.; Lim, T. H.; McLaughlin, J. A. D., Microstructural and electrochemical properties of vertically aligned few layered graphene (FLG) nanoflakes and their application in methanol oxidation. *Materials Chemistry and Physics* **2011**, *129* (3), 1051-1057.
167. Zhang, S.; Shao, Y.; Liao, H.-g.; Liu, J.; Aksay, I. A.; Yin, G.; Lin, Y., Graphene Decorated with PtAu Alloy Nanoparticles: Facile Synthesis and Promising Application for Formic Acid Oxidation. *Chemistry of Materials* **2011**, *23* (5), 1079-1081.
168. Liu, S.; Wang, J.; Zeng, J.; Ou, J.; Li, Z.; Liu, X.; Yang, S., "Green" electrochemical synthesis of Pt/graphene sheet nanocomposite film and its electrocatalytic property. *Journal of Power Sources* **2010**, *195* (15), 4628-4633.
169. Xu, C.; Wang, X.; Zhu, J., Graphene–Metal Particle Nanocomposites. *The Journal of Physical Chemistry C* **2008**, *112* (50), 19841-19845.
170. Dong, L.; Gari, R. R. S.; Li, Z.; Craig, M. M.; Hou, S., Graphene-supported platinum and platinum–ruthenium nanoparticles with high electrocatalytic activity for methanol and ethanol oxidation. *Carbon* **2010**, *48* (3), 781-787.
171. Li, Y.; Tang, L.; Li, J., Preparation and electrochemical performance for methanol oxidation of Pt/graphene nanocomposites. *Electrochemistry Communications* **2009**, *11* (4), 846-849.
172. Shao, Y.; Zhang, S.; Wang, C.; Nie, Z.; Liu, J.; Wang, Y.; Lin, Y., Highly durable graphene nanoplatelets supported Pt nanocatalysts for oxygen reduction. *Journal of Power Sources* **2010**, *195* (15), 4600-4605.
173. Hu, Y.; Zhang, H.; Wu, P.; Zhang, H.; Zhou, B.; Cai, C., Bimetallic Pt-Au nanocatalysts electrochemically deposited on graphene and their electrocatalytic characteristics towards oxygen reduction and methanol oxidation. *Physical Chemistry Chemical Physics* **2011**, *13* (9), 4083-4094.
174. Yoo, E.; Okada, T.; Akita, T.; Kohyama, M.; Honma, I.; Nakamura, J., Sub-nano-Pt cluster supported on graphene nanosheets for CO tolerant catalysts in polymer electrolyte fuel cells. *Journal of Power Sources* **2011**, *196* (1), 110-115.
175. Sharma, S.; Ganguly, A.; Papakonstantinou, P.; Miao, X.; Li, M.; Hutchison, J. L.; Delichatsios, M.; Ukleja, S., Rapid Microwave Synthesis of CO Tolerant Reduced Graphene Oxide-Supported Platinum Electrocatalysts for Oxidation of Methanol. *The Journal of Physical Chemistry C* **2010**, *114* (45), 19459-19466.

176. Qiu, J.-D.; Wang, G.-C.; Liang, R.-P.; Xia, X.-H.; Yu, H.-W., Controllable Deposition of Platinum Nanoparticles on Graphene As an Electrocatalyst for Direct Methanol Fuel Cells. *The Journal of Physical Chemistry C* **2011**, *115* (31), 15639-15645.
177. Li, Y.; Gao, W.; Ci, L.; Wang, C.; Ajayan, P. M., Catalytic performance of Pt nanoparticles on reduced graphene oxide for methanol electro-oxidation. *Carbon* **2010**, *48* (4), 1124-1130.
178. Ha, H.-W.; Kim, I. Y.; Hwang, S.-J.; Ruoff, R. S., One-Pot Synthesis of Platinum Nanoparticles Embedded on Reduced Graphene Oxide for Oxygen Reduction in Methanol Fuel Cells. *Electrochemical and Solid-State Letters* **2011**, *14* (7), B70-B73.
179. Chen, X.; Wu, G.; Chen, J.; Chen, X.; Xie, Z.; Wang, X., Synthesis of “Clean” and Well-Dispersive Pd Nanoparticles with Excellent Electrocatalytic Property on Graphene Oxide. *J Am Chem Soc* **2011**, *133* (11), 3693-3695.
180. Chetty, R.; Kundu, S.; Xia, W.; Bron, M.; Schuhmann, W.; Chirila, V.; Brandl, W.; Reinecke, T.; Muhler, M., PtRu nanoparticles supported on nitrogen-doped multiwalled carbon nanotubes as catalyst for methanol electrooxidation. *Electrochimica Acta* **2009**, *54* (17), 4208-4215.
181. Kundu, S.; Nagaiah, T. C.; Xia, W.; Wang, Y.; Dommele, S. V.; Bitter, J. H.; Santa, M.; Grundmeier, G.; Bron, M.; Schuhmann, W.; Muhler, M., Electrocatalytic Activity and Stability of Nitrogen-Containing Carbon Nanotubes in the Oxygen Reduction Reaction. *The Journal of Physical Chemistry C* **2009**, *113* (32), 14302-14310.
182. Lei, Z.; An, L.; Dang, L.; Zhao, M.; Shi, J.; Bai, S.; Cao, Y., Highly dispersed platinum supported on nitrogen-containing ordered mesoporous carbon for methanol electrochemical oxidation. *Microporous and Mesoporous Materials* **2009**, *119* (1-3), 30-38.
183. Ozaki, J.-i.; Anahara, T.; Kimura, N.; Oya, A., Simultaneous doping of boron and nitrogen into a carbon to enhance its oxygen reduction activity in proton exchange membrane fuel cells. *Carbon* **2006**, *44* (15), 3358-3361.
184. Wu, G.; Li, D.; Dai, C.; Wang, D.; Li, N., Well-Dispersed High-Loading Pt Nanoparticles Supported by Shell-Core Nanostructured Carbon for Methanol Electrooxidation. *Langmuir* **2008**, *24* (7), 3566-3575.
185. Roy, S. C.; Christensen, P. A.; Hamnett, A.; Thomas, K. M.; Trapp, V., Direct Methanol Fuel Cell Cathodes with Sulfur and Nitrogen-Based Carbon Functionality. *Journal of The Electrochemical Society* **1996**, *143* (10), 3073-3079.
186. Zhou, Y.; Neyerlin, K.; Olson, T. S.; Pylypenko, S.; Bult, J.; Dinh, H. N.; Gennett, T.; Shao, Z.; O'Hayre, R., Enhancement of Pt and Pt-alloy fuel cell catalyst activity and durability via nitrogen-modified carbon supports. *Energy & Environmental Science* **2010**, *3* (10), 1437-1446.

187. Olson, T. S.; Pylypenko, S.; Fulghum, J. E.; Atanassov, P., Bifunctional Oxygen Reduction Reaction Mechanism on Non-Platinum Catalysts Derived from Pyrolyzed Porphyrins. *Journal of The Electrochemical Society* **2010**, *157* (1), B54-B63.
188. Zhou, Y.; Pasquarelli, R.; Holme, T.; Berry, J.; Ginley, D.; O'Hayre, R., Improving PEM fuel cell catalyst activity and durability using nitrogen-doped carbon supports: observations from model Pt/HOPG systems. *Journal of Materials Chemistry* **2009**, *19* (42), 7830-7838.
189. Sun, C.-L.; Chen, L.-C.; Su, M.-C.; Hong, L.-S.; Chyan, O.; Hsu, C.-Y.; Chen, K.-H.; Chang, T.-F.; Chang, L., Ultrafine Platinum Nanoparticles Uniformly Dispersed on Arrayed CNx Nanotubes with High Electrochemical Activity. *Chemistry of Materials* **2005**, *17* (14), 3749-3753.
190. Holme, T.; Zhou, Y.; Pasquarelli, R.; O'Hayre, R., First principles study of doped carbon supports for enhanced platinum catalysts. *Physical Chemistry Chemical Physics* **2010**, *12* (32), 9461-9468.
191. Wiggins-Camacho, J. D.; Stevenson, K. J., Effect of Nitrogen Concentration on Capacitance, Density of States, Electronic Conductivity, and Morphology of N-Doped Carbon Nanotube Electrodes. *The Journal of Physical Chemistry C* **2009**, *113* (44), 19082-19090.
192. Gong, K.; Du, F.; Xia, Z.; Durstock, M.; Dai, L., Nitrogen-Doped Carbon Nanotube Arrays with High Electrocatalytic Activity for Oxygen Reduction. *Science* **2009**, *323* (5915), 760-764.
193. Chen, Z.; Higgins, D.; Tao, H.; Hsu, R. S.; Chen, Z., Highly Active Nitrogen-Doped Carbon Nanotubes for Oxygen Reduction Reaction in Fuel Cell Applications. *The Journal of Physical Chemistry C* **2009**, *113* (49), 21008-21013.
194. Tang, Y.; Allen, B. L.; Kauffman, D. R.; Star, A., Electrocatalytic Activity of Nitrogen-Doped Carbon Nanotube Cups. *J Am Chem Soc* **2009**, *131* (37), 13200-13201.
195. Viswanathan, B., Architecture of carbon support for Pt anodes in direct methanol fuel cells. *Catalysis Today* **2009**, *141* (1-2), 52-55.
196. Liu, R.; Wu, D.; Feng, X.; Müllen, K., Nitrogen-Doped Ordered Mesoporous Graphitic Arrays with High Electrocatalytic Activity for Oxygen Reduction. *Angewandte Chemie International Edition* **2010**, *49* (14), 2565-2569.
197. Datta, K. K. R.; Balasubramanian, V. V.; Ariga, K.; Mori, T.; Vinu, A., Highly Crystalline and Conductive Nitrogen-Doped Mesoporous Carbon with Graphitic Walls and Its Electrochemical Performance. *Chemistry – A European Journal* **2011**, *17* (12), 3390-3397.
198. Qu, L.; Liu, Y.; Baek, J.-B.; Dai, L., Nitrogen-Doped Graphene as Efficient Metal-Free Electrocatalyst for Oxygen Reduction in Fuel Cells. *ACS Nano* **2010**, *4* (3), 1321-1326.

199. Geng, D.; Chen, Y.; Chen, Y.; Li, Y.; Li, R.; Sun, X.; Ye, S.; Knights, S., High oxygen-reduction activity and durability of nitrogen-doped graphene. *Energy & Environmental Science* **2011**, *4* (3), 760-764.
200. Imran Jafri, R.; Rajalakshmi, N.; Ramaprabhu, S., Nitrogen doped graphene nanoplatelets as catalyst support for oxygen reduction reaction in proton exchange membrane fuel cell. *Journal of Materials Chemistry* **2010**, *20* (34), 7114-7117.
201. Liebig, J., Über einige Stickstoff - Verbindungen. *Annalen der Pharmacie* **1834**, *10* (1), 1-47.
202. Franklin, E. C., The Ammono Carbonic Acids. *J. Am. Chem. Soc.* **1922**, *44* (3), 486-509.
203. Komatsu, T., Prototype carbon nitrides similar to the symmetric triangular form of melon. *Journal of Materials Chemistry* **2001**, *11* (3), 802-803.
204. Kroke, E.; Schwarz, M.; Horath-Bordon, E.; Kroll, P.; Noll, B.; Norman, A. D., Tri-s-triazine derivatives. Part I. From trichloro-tri-s-triazine to graphitic C₃N₄ structures. *New Journal of Chemistry* **2002**, *26* (5), 508-512.
205. Kroke, E.; Schwarz, M., Novel group 14 nitrides. *Coordination Chemistry Reviews* **2004**, *248* (5-6), 493-532.
206. Jorge, A. B.; Martin, D. J.; Dhanoa, M. T. S.; Rahman, A. S.; Makwana, N.; Tang, J.; Sella, A.; Corà, F.; Firth, S.; Darr, J. A.; McMillan, P. F., H₂ and O₂ Evolution from Water Half-Splitting Reactions by Graphitic Carbon Nitride Materials. *The Journal of Physical Chemistry C* **2013**, *117* (14), 7178-7185.
207. Deifallah, M.; McMillan, P. F.; Corà, F., Electronic and Structural Properties of Two-Dimensional Carbon Nitride Graphenes. *The Journal of Physical Chemistry C* **2008**, *112* (14), 5447-5453.
208. Wang, Y.; Zhang, J.; Wang, X.; Antonietti, M.; Li, H., Boron- and Fluorine-Containing Mesoporous Carbon Nitride Polymers: Metal-Free Catalysts for Cyclohexane Oxidation. *Angew. Chem. Int. Ed.* **2010**, *49* (19), 3356-3359.
209. Wang, Y.; Di, Y.; Antonietti, M.; Li, H.; Chen, X.; Wang, X., Excellent Visible-Light Photocatalysis of Fluorinated Polymeric Carbon Nitride Solids. *Chemistry of Materials* **2010**, *22* (18), 5119-5121.
210. Liu, G.; Niu, P.; Sun, C.; Smith, S. C.; Chen, Z.; Lu, G. Q.; Cheng, H.-M., Unique Electronic Structure Induced High Photoreactivity of Sulfur-Doped Graphitic C₃N₃. *J Am Chem Soc* **2010**, *132* (33), 11642-11648.
211. Kohl, S. W.; Weiner, L.; Schwartzburd, L.; Konstantinovski, L.; Shimon, L. J. W.; Ben-David, Y.; Iron, M. A.; Milstein, D., Consecutive Thermal H₂ and Light-Induced O₂ Evolution from Water Promoted by a Metal Complex. *Science* **2009**, *324* (5923), 74-77.

212. Liu, H.; Jiang, T.; Han, B.; Liang, S.; Zhou, Y., Selective Phenol Hydrogenation to Cyclohexanone Over a Dual Supported Pd–Lewis Acid Catalyst. *Science* **2009**, *326* (5957), 1250-1252.
213. Su, F.; Mathew, S. C.; Lipner, G.; Fu, X.; Antonietti, M.; Blechert, S.; Wang, X., mpg-C₃N₄-Catalyzed Selective Oxidation of Alcohols Using O₂ and Visible Light. *J. Am. Chem. Soc.* **2010**, *132* (46), 16299-16301.
214. Wang, X.; Maeda, K.; Thomas, A.; Takanabe, K.; Xin, G.; Carlsson, J. M.; Domen, K.; Antonietti, M., A metal-free polymeric photocatalyst for hydrogen production from water under visible light. *Nature Material* **2009**, *8* (1), 76-80.
215. Wang, Y.; Wang, X.; Antonietti, M., Polymeric Graphitic Carbon Nitride as a Heterogeneous Organocatalyst: From Photochemistry to Multipurpose Catalysis to Sustainable Chemistry. *Angewandte Chemie International Edition* **2012**, *51* (1), 68-89.
216. Lyth, S. M.; Nabae, Y.; Moriya, S.; Kuroki, S.; Kakimoto, M.-a.; Ozaki, J.-i.; Miyata, S., Carbon Nitride as a Nonprecious Catalyst for Electrochemical Oxygen Reduction. *The Journal of Physical Chemistry C* **2009**, *113* (47), 20148-20151.
217. Zheng, Y.; Jiao, Y.; Chen, J.; Liu, J.; Liang, J.; Du, A.; Zhang, W.; Zhu, Z.; Smith, S. C.; Jaroniec, M.; Lu, G. Q.; Qiao, S. Z., Nanoporous Graphitic-C₃N₄@Carbon Metal-Free Electrocatalysts for Highly Efficient Oxygen Reduction. *J Am Chem Soc* **2011**, *133* (50), 20116-20119.
218. Yang, S.; Feng, X.; Wang, X.; Müllen, K., Graphene-Based Carbon Nitride Nanosheets as Efficient Metal-Free Electrocatalysts for Oxygen Reduction Reactions. *Angewandte Chemie International Edition* **2011**, *50* (23), 5339-5343.
219. Qiu, K.; Guo, Z. X., Hierarchically porous graphene sheets and graphitic carbon nitride intercalated composites for enhanced oxygen reduction reaction. *Journal of Materials Chemistry A* **2014**, *2* (9), 3209-3215.
220. Lyth, S. M.; Nabae, Y.; Islam, N. M.; Kuroki, S.; Kakimoto, M.; Miyata, S., Electrochemical Oxygen Reduction Activity of Carbon Nitride Supported on Carbon Black. *Journal of The Electrochemical Society* **2011**, *158* (2), B194-B201.
221. Kim, M.; Hwang, S.; Yu, J.-S., Novel ordered nanoporous graphitic C₃N₄ as a support for Pt-Ru anode catalyst in direct methanol fuel cell. *Journal of Materials Chemistry* **2007**, *17* (17).
222. Woods, R., Hydrogen adsorption on platinum, iridium and rhodium electrodes at reduced temperatures and the determination of real surface area. *Journal of Electroanalytical Chemistry and Interfacial Electrochemistry* **1974**, *49* (2), 217-226.
223. Clavilier, J.; Armand, D.; Wu, B. L., Electrochemical study of the initial surface condition of platinum surfaces with (100) and (111) orientations. *Journal of Electroanalytical Chemistry and Interfacial Electrochemistry* **1982**, *135* (1), 159-166.
224. Rush, B. M.; Reimer, J. A.; Cairns, E. J., Nuclear Magnetic Resonance and Voltammetry Studies of Carbon Monoxide Adsorption and Oxidation on a Carbon-

Supported Platinum Fuel Cell Electrocatalyst. *Journal of The Electrochemical Society* **2001**, *148* (2), A137-A148.

225. Rodes, A.; Gómez, R.; Feliu, J. M.; Weaver, M. J., Sensitivity of Compressed Carbon Monoxide Adlayers on Platinum(111) Electrodes to Long-Range Substrate Structure: Influence of Monoatomic Steps. *Langmuir* **1999**, *16* (2), 811-816.

226. Bard, A. J., *Electrochemical methods: fundamentals and applications*. 2006.

227. Paulus, U. A.; Schmidt, T. J.; Gasteiger, H. A.; Behm, R. J., Oxygen reduction on a high-surface area Pt/Vulcan carbon catalyst: a thin-film rotating ring-disk electrode study. *Journal of Electroanalytical Chemistry* **2001**, *495* (2), 134-145.

228. Garsany, Y.; Baturina, O.; Swider-Lyons, K.; Kocha, S., Experimental Methods for Quantifying the Activity. *Analytical Chemistry* **2010**, *82*, 6321–6328.

229. Zawodzinski, T. A.; Karuppaiah, C.; Uribe, F.; Gottesfeld, S. In *Aspects of CO tolerance in polymer electrolyte fuel cells: some experimental findings*, Proceedings of the Electrochemical Society, 1997; pp 139-146.

230. Zhang, J.; Thampan, T.; Datta, R., Influence of Anode Flow Rate and Cathode Oxygen Pressure on CO Poisoning of Proton Exchange Membrane Fuel Cells. *Journal of The Electrochemical Society* **2002**, *149* (6), A765-A772.

231. US Department of Energy. USCAR Fuel Cell Tech Team Cell Component Accelerated Stress Test Protocols For PEM Fuel Cells.

232. Shao-Horn, Y.; Ferreira, P.; la O', G. J.; Morgan, D.; Gasteiger, H. A.; Makharia, R., Coarsening of Pt Nanoparticles in Proton Exchange Membrane Fuel Cells upon Potential Cycling. *ECS Transactions* **2006**, *1* (8), 185-195.

233. Yasuda, K.; Taniguchi, A.; Akita, T.; Ioroi, T.; Siroma, Z., Platinum dissolution and deposition in the polymer electrolyte membrane of a PEM fuel cell as studied by potential cycling. *Physical Chemistry Chemical Physics* **2006**, *8* (6), 746-752.

234. Yasuda, K.; Taniguchi, A.; Akita, T.; Ioroi, T.; Siroma, Z., Characteristics of a Platinum Black Catalyst Layer with Regard to Platinum Dissolution Phenomena in a Membrane Electrode Assembly. *Journal of The Electrochemical Society* **2006**, *153* (8), A1599-A1603.

235. Wang, Z.-B.; Zuo, P.-J.; Wang, X.-P.; Lou, J.; Yang, B.-Q.; Yin, G.-P., Studies of performance decay of Pt/C catalysts with working time of proton exchange membrane fuel cell. *Journal of Power Sources* **2008**, *184* (1), 245-250.

236. Ramani, V. K.; Prakash, J., Synthesis and Characterization of Mixed-Conducting Corrosion Resistant Oxide Supports. 2012.

237. Yoda, T.; Uchida, H.; Watanabe, M., Effects of operating potential and temperature on degradation of electrocatalyst layer for PEFCs. *Electrochimica Acta* **2007**, *52* (19), 5997-6005.

238. Meier, J. C.; Galeano, C.; Katsounaros, I.; Witte, J.; Bongard, H. J.; Topalov, A. A.; Baldizzone, C.; Mezzavilla, S.; Schüth, F.; Mayrhofer, K. J. J., Design criteria for stable Pt/C fuel cell catalysts. *Beilstein Journal of Nanotechnology* **2014**, *5*, 44-67.
239. Wang, J.; Yin, G.; Shao, Y.; Zhang, S.; Wang, Z.; Gao, Y., Effect of carbon black support corrosion on the durability of Pt/C catalyst. *Journal of Power Sources* **2007**, *171* (2), 331-339.
240. Kim, J.; Lee, J.; Tak, Y., Relationship between carbon corrosion and positive electrode potential in a proton-exchange membrane fuel cell during start/stop operation. *Journal of Power Sources* **2009**, *192* (2), 674-678.
241. Gu, W.; Carter, R. N.; Yu, P. T.; Gasteiger, H. A., Start/Stop and Local H₂ Starvation Mechanisms of Carbon Corrosion: Model vs. Experiment. *ECS Transactions* **2007**, *11* (1), 963-973.
242. Rodriguez, P.; Tichelaar, F. D.; Koper, M. T. M.; Yanson, A. I., Cathodic Corrosion as a Facile and Effective Method To Prepare Clean Metal Alloy Nanoparticles. *J. Am. Chem. Soc.* **2011**, *133* (44), 17626-17629.
243. Watanabe, M.; Uchida, M.; Motoo, S., Preparation of highly dispersed Pt + Ru alloy clusters and the activity for the electrooxidation of methanol. *Journal of Electroanalytical Chemistry and Interfacial Electrochemistry* **1987**, *229* (1-2), 395-406.
244. Teranishi, T.; Hosoe, M.; Tanaka, T.; Miyake, M., Size Control of Monodispersed Pt Nanoparticles and Their 2D Organization by Electrophoretic Deposition. *The Journal of Physical Chemistry B* **1999**, *103* (19), 3818-3827.
245. Xiong, L.; Manthiram, A., Catalytic activity of Pt-Ru alloys synthesized by a microemulsion method in direct methanol fuel cells. *Solid State Ionics* **2005**, *176* (3-4), 385-392.
246. Rojas, S.; García-García, F. J.; Järas, S.; Martínez-Huerta, M. V.; Fierro, J. L. G.; Boutonnet, M., Preparation of carbon supported Pt and PtRu nanoparticles from microemulsion: Electrocatalysts for fuel cell applications. *Applied Catalysis A: General* **2005**, *285* (1-2), 24-35.
247. Shimazu, K.; Weisshaar, D.; Kuwana, T., Electrochemical dispersion of Pt microparticles on glassy carbon electrodes. *Journal of Electroanalytical Chemistry and Interfacial Electrochemistry* **1987**, *223* (1-2), 223-234.
248. He, Z.; Chen, J.; Liu, D.; Tang, H.; Deng, W.; Kuang, Y., Deposition and electrocatalytic properties of platinum nanoparticles on carbon nanotubes for methanol electrooxidation. *Materials Chemistry and Physics* **2004**, *85* (2-3), 396-401.
249. Markovic, N.; Gasteiger, H.; Ross, P. N., Kinetics of Oxygen Reduction on Pt(hkl) Electrodes: Implications for the Crystallite Size Effect with Supported Pt Electrocatalysts. *Journal of The Electrochemical Society* **1997**, *144* (5), 1591-1597.

250. Woodard, F. E.; Scortichini, C. L.; Reilley, C. N., Hydrogen chemisorption and related anion effects on Pt(110) electrodes. *Journal of Electroanalytical Chemistry and Interfacial Electrochemistry* **1983**, *151* (1–2), 109-131.
251. Furuya, N.; Koide, S., Hydrogen adsorption on platinum single-crystal surfaces. *Surface Science* **1989**, *220* (1), 18-28.
252. Yamamoto, K.; Kolb, D. M.; Kötzt, R.; Lehmpfuhl, G., Hydrogen adsorption and oxide formation on platinum single crystal electrodes. *Journal of Electroanalytical Chemistry and Interfacial Electrochemistry* **1979**, *96* (2), 233-239.
253. Santos, E.; Leiva, E. P. M.; Vielstich, W.; Linke, U., Comparative study of CO adsorbates for different structures of platinum surfaces. *Journal of Electroanalytical Chemistry and Interfacial Electrochemistry* **1987**, *227* (1–2), 199-211.
254. Will, F. G., Hydrogen Adsorption on Platinum Single Crystal Electrodes. *Journal of The Electrochemical Society* **1965**, *112* (4), 451-455.
255. Biegler, T., Search for surface structural effects in electrocatalysis. I. Smooth platinum electrodes. *Australian Journal of Chemistry* **1973**, *26* (12), 2571-2585.
256. Kinoshita, K.; Lundquist, J.; Stonehart, P., Hydrogen adsorption on high surface area platinum crystallites. *Journal of Catalysis* **1973**, *31* (3), 325-334.
257. Stonehart, P., Surface interactions affecting quasi-equilibrium adsorption. *Electrochimica Acta* **1970**, *15* (12), 1853-1864.
258. Sumino, M. P.; Shibata, S., Specific adsorption of hydrogen on polycrystalline platinum electrode. *Electrochimica Acta* **1992**, *37* (14), 2629-2635.
259. Gómez, R.; Clavilier, J., Electrochemical behaviour of platinum surfaces containing (110) sites and the problem of the third oxidation peak. *Journal of Electroanalytical Chemistry* **1993**, *354* (1–2), 189-208.
260. Frelink, T.; Visscher, W.; van Veen, J. A. R., The third anodic hydrogen peak on platinum; Subsurface H₂ adsorption. *Electrochimica Acta* **1995**, *40* (5), 545-549.
261. Loo, B. H.; Furtak, T. E., Intrinsic heterogeneity in the multiple states of adsorbed hydrogen on polycrystalline platinum. *Electrochimica Acta* **1980**, *25* (5), 505-508.
262. Raub, E., A note on the origins of volume 1 of the Journal of the less-common metals. *Journal of the Less Common Metals* **1984**, *100* (0), iv-vi.
263. Gabrielli, C.; Grand, P. P.; Lasia, A.; Perrot, H., Investigation of Hydrogen Adsorption and Absorption in Palladium Thin Films: II. Cyclic Voltammetry. *Journal of The Electrochemical Society* **2004**, *151* (11), A1937-A1942.
264. Czerwiński, A.; Marassi, R.; Zamponi, S., The absorption of hydrogen and deuterium in thin palladium electrodes: Part I. Acidic solutions. *Journal of Electroanalytical Chemistry and Interfacial Electrochemistry* **1991**, *316* (1–2), 211-221.

265. Birry, L.; Lasia, A., Effect of crystal violet on the kinetics of H sorption into Pd. *Electrochimica Acta* **2006**, *51* (16), 3356-3364.
266. L, G. C.; A, K., Determination of the Platinum and Ruthenium Surface Areas in Platinum-Ruthenium Alloy Electrocatalysts by Underpotential Deposition of Copper. *J. Phys. Chem. B* **2002**, *106*, 1036-1047.
267. Crabb, E. M.; Ravikumar, M. K.; Thompsett, D.; Hurford, M.; Rose, A.; Russell, A. E., Effect of Ru surface composition on the CO tolerance of Ru modified carbon supported Pt catalysts. *Physical Chemistry Chemical Physics* **2004**, *6* (8), 1792-1798.
268. Durst, J.; Siebel, A.; Simon, C.; Hasche, F.; Herranz, J.; Gasteiger, H. A., New insights into the electrochemical hydrogen oxidation and evolution reaction mechanism. *Energy & Environmental Science* **2014**, *7* (7), 2255-2260.
269. Tang, Y.; Mu, S.; Yu, S.; Zhao, Y.; Wang, H.; Gao, F., In Situ and Ex Situ Studies on the Degradation of Pd/C Catalyst for Proton Exchange Membrane Fuel Cells. *Journal of Fuel Cell Science and Technology* **2014**, *11* (5), 051004-051004.
270. Kangasniemi, K. H.; Condit, D. A.; Jarvi, T. D., Characterization of Vulcan Electrochemically Oxidized under Simulated PEM Fuel Cell Conditions. *Journal of The Electrochemical Society* **2004**, *151* (4), E125-E132.
271. Kinoshita, K.; Bett, J. A. S., Potentiodynamic analysis of surface oxides on carbon blacks. *Carbon* **1973**, *11* (4), 403-411.
272. von Deak, D.; Biddinger, E.; Ozkan, U., Carbon corrosion characteristics of CN x nanostructures in acidic media and implications for ORR performance. *Journal of Applied Electrochemistry* **2011**, *41* (7), 757-763.
273. Tarasevich, M. R.; Bogdanovskaya, V. A.; Zagudaeva, N. M., Redox reactions of quinones on carbon materials. *Journal of Electroanalytical Chemistry and Interfacial Electrochemistry* **1987**, *223* (1-2), 161-169.
274. Young, A. P.; Stumper, J.; Gyenge, E., Characterizing the Structural Degradation in a PEMFC Cathode Catalyst Layer: Carbon Corrosion. *Journal of The Electrochemical Society* **2009**, *156* (8), B913-B922.
275. Meyer, Q.; Barass, S.; Curnick, O.; Reisch, T.; Brett, D. J. L., A Multichannel Frequency Response Analyser for Impedance Spectroscopy on Power Sources. *J. Electrochem. Sci. Eng.* **2013**, *3* (3), 107-114.
276. Das, P. K.; Li, X.; Liu, Z.-S., Analytical approach to polymer electrolyte membrane fuel cell performance and optimization. *Journal of Electroanalytical Chemistry* **2007**, *604* (2), 72-90.
277. Wagner, N.; Gülzow, E., Change of electrochemical impedance spectra (EIS) with time during CO-poisoning of the Pt-anode in a membrane fuel cell. *Journal of Power Sources* **2004**, *127* (1-2), 341-347.

278. Boaventura, M.; Sander, H.; Friedrich, K. A.; Mendes, A., The influence of CO on the current density distribution of high temperature polymer electrolyte membrane fuel cells. *Electrochimica Acta* **2011**, *56* (25), 9467-9475.
279. Huang, H.; Wang, X., Recent progress on carbon-based support materials for electrocatalysts of direct methanol fuel cells. *Journal of Materials Chemistry A* **2014**, *2* (18), 6266-6291.
280. Radkevich, V. Z.; Senko, T. L.; Wilson, K.; Grishenko, L. M.; Zaderko, A. N.; Diyuk, V. Y., The influence of surface functionalization of activated carbon on palladium dispersion and catalytic activity in hydrogen oxidation. *Applied Catalysis A: General* **2008**, *335* (2), 241-251.
281. Suh, D. J.; Park, T. J.; Ihm, S. K., Characteristics of carbon-supported palladium catalysts for liquid-phase hydrogenation of nitroaromatics. *Industrial & Engineering Chemistry Research* **1992**, *31* (8), 1849-1856.
282. Dong Jin, S.; Tae-Jin, P.; Son-Ki, I., Effect of surface oxygen groups of carbon supports on the characteristics of Pd/C catalysts. *Carbon* **1993**, *31* (3), 427-435.
283. Gurevich, S. V.; Simonov, P. A.; Lisitsyn, A. S.; Likholobov, V. A.; Moroz, E. M.; Chuvilin, A. L.; Kolomiichuk, V. N., Influence of carbon support pretreatment on properties of Pd/C catalysts. *React Kinet Catal Lett* **1990**, *41* (1), 211-216.
284. Ryndin, Y. A.; Alekseev, O. S.; Simonov, P. A.; Likholobov, V. A., Supported metallic catalysts obtained by anchoring metal complexes on carbon supports. *Journal of Molecular Catalysis* **1989**, *55* (1), 109-125.
285. Dubois, V.; Dal, Y.; Jannes, G., Active carbon surface oxidation to optimize the support functionality and metallic dispersion of a Pd/C catalyst. In *Studies in Surface Science and Catalysis*, 2002; Vol. 143, pp 993-1002.
286. Gleiter, H., Materials with ultrafine microstructures: Retrospectives and perspectives. *Nanostructured Materials* **1992**, *1* (1), 1-19.
287. Wang, X.; Ahluwalia, R. K.; Steinbach, A. J., Kinetics of Hydrogen Oxidation and Hydrogen Evolution Reactions on Nanostructured Thin-Film Platinum Alloy Catalyst. *Journal of The Electrochemical Society* **2013**, *160* (3), F251-F261.
288. Cells, J. M. F. HiSPEC Fuel Cell Catalysts. http://www.jmfuelcells.com/documents/fuel_cells/documents_library/4_hispec_catalyst_product_range (accessed 30-09-2014).
289. Patterson, A. L., The Scherrer Formula for X-Ray Particle Size Determination. *Physical Review* **1939**, *56* (10), 978-982.
290. Bleda-Martínez, M. J.; Maciá-Agulló, J. A.; Lozano-Castelló, D.; Morallón, E.; Cazorla-Amorós, D.; Linares-Solano, A., Role of surface chemistry on electric double layer capacitance of carbon materials. *Carbon* **2005**, *43* (13), 2677-2684.

291. Shao, Y.; Yin, G.; Wang, Z.; Gao, Y., Proton exchange membrane fuel cell from low temperature to high temperature: Material challenges. *Journal of Power Sources* **2007**, *167* (2), 235-242.
292. Sun, X.; Li, R.; Villers, D.; Dodelet, J. P.; Désilets, S., Composite electrodes made of Pt nanoparticles deposited on carbon nanotubes grown on fuel cell backings. *Chemical Physics Letters* **2003**, *379* (1–2), 99-104.
293. Zheng, Y.; Jiao, Y.; Chen, J.; Liu, J.; Liang, J.; Du, A.; Zhang, W.; Zhu, Z.; Smith, S. C.; Jaroniec, M.; Lu, G. Q.; Qiao, S. Z., Nanoporous graphitic-C₃N₄@carbon metal-free electrocatalysts for highly efficient oxygen reduction. *J Am Chem Soc* **2011**, *133* (50), 20116-9.
294. Mayrhofer, K. J. J.; Blizanac, B. B.; Arenz, M.; Stamenkovic, V. R.; Ross, P. N.; Markovic, N. M., The Impact of Geometric and Surface Electronic Properties of Pt-Catalysts on the Particle Size Effect in Electrocatalysis. *The Journal of Physical Chemistry B* **2005**, *109* (30), 14433-14440.
295. Li, X.; Chen, W.-X.; Zhao, J.; Xing, W.; Xu, Z.-D., Microwave polyol synthesis of Pt/CNTs catalysts: Effects of pH on particle size and electrocatalytic activity for methanol electrooxidation. *Carbon* **2005**, *43* (10), 2168-2174.
296. Chen, W. X.; Lee, J. Y.; Liu, Z., Microwave-assisted synthesis of carbon supported Pt nanoparticles for fuel cell applications. *Chemical Communications* **2002**, (21), 2588-2589.
297. Bock, C.; Paquet, C.; Couillard, M.; Botton, G. A.; MacDougall, B. R., Size-Selected Synthesis of PtRu Nano-Catalysts: Reaction and Size Control Mechanism. *J Am Chem Soc* **2004**, *126* (25), 8028-8037.
298. Yang, J.; Deivaraj, T. C.; Too, H.-P.; Lee, J. Y., Acetate Stabilization of Metal Nanoparticles and Its Role in the Preparation of Metal Nanoparticles in Ethylene Glycol. *Langmuir* **2004**, *20* (10), 4241-4245.
299. Park, S.; Shao, Y.; Wan, H.; Rieke, P. C.; Viswanathan, V. V.; Towne, S. A.; Saraf, L. V.; Liu, J.; Lin, Y.; Wang, Y., Design of graphene sheets-supported Pt catalyst layer in PEM fuel cells. *Electrochemistry Communications* **2011**, *13* (3), 258-261.
300. Zhang, Y.; Thomas, A.; Antonietti, M.; Wang, X., Activation of Carbon Nitride Solids by Protonation: Morphology Changes, Enhanced Ionic Conductivity, and Photoconduction Experiments. *J Am Chem Soc* **2008**, *131* (1), 50-51.
301. Yang, S.; Gong, Y.; Zhang, J.; Zhan, L.; Ma, L.; Fang, Z.; Vajtai, R.; Wang, X.; Ajayan, P. M., Exfoliated Graphitic Carbon Nitride Nanosheets as Efficient Catalysts for Hydrogen Evolution Under Visible Light. *Advanced Materials* **2013**, *25* (17), 2452-2456.
302. Wang, Y.; Li, H.; Yao, J.; Wang, X.; Antonietti, M., Synthesis of boron doped polymeric carbon nitride solids and their use as metal-free catalysts for aliphatic C-H bond oxidation. *Chemical Science* **2011**, *2* (3), 446-450.

303. Wirnhier, E.; Döblinger, M.; Gunzelmann, D.; Senker, J.; Lotsch, B. V.; Schnick, W., Poly(triazine imide) with Intercalation of Lithium and Chloride Ions [(C₃N₃)₂(NH_xLi_{1-x})₃LiCl]: A Crystalline 2D Carbon Nitride Network. *Chemistry – A European Journal* **2011**, *17* (11), 3213-3221.
304. Bojdys, M. J.; Müller, J.-O.; Antonietti, M.; Thomas, A., Ionothermal Synthesis of Crystalline, Condensed, Graphitic Carbon Nitride. *Chemistry – A European Journal* **2008**, *14* (27), 8177-8182.
305. Schwinghammer, K.; Tuffy, B.; Mesch, M. B.; Wirnhier, E.; Martineau, C.; Taulelle, F.; Schnick, W.; Senker, J.; Lotsch, B. V., Triazine-based Carbon Nitrides for Visible-Light-Driven Hydrogen Evolution. *Angewandte Chemie International Edition* **2013**, *52* (9), 2435-2439.
306. Ham, Y.; Maeda, K.; Cha, D.; Takanebe, K.; Domen, K., Synthesis and Photocatalytic Activity of Poly(triazine imide). *Chemistry – An Asian Journal* **2013**, *8* (1), 218-224.
307. Acharya, C. K.; Li, W.; Liu, Z.; Kwon, G.; Heath Turner, C.; Lane, A. M.; Nikles, D.; Klein, T.; Weaver, M., Effect of boron doping in the carbon support on platinum nanoparticles and carbon corrosion. *Journal of Power Sources* **2009**, *192* (2), 324-329.
308. Radovic, L. R.; Karra, M.; Skokova, K.; Thrower, P. A., The role of substitutional boron in carbon oxidation. *Carbon* **1998**, *36* (12), 1841-1854.
309. Yang, L.; Jiang, S.; Zhao, Y.; Zhu, L.; Chen, S.; Wang, X.; Wu, Q.; Ma, J.; Ma, Y.; Hu, Z., Boron-Doped Carbon Nanotubes as Metal-Free Electrocatalysts for the Oxygen Reduction Reaction. *Angewandte Chemie International Edition* **2011**, *50* (31), 7132-7135.